School of Pharmacy and Biomedical Sciences

Molecular Dynamics Simulation of the Permeation of Lipid-Conjugated Peptides through the Stratum Corneum

Lanie Ruiz Perez

0000-0001-5931-8783

This thesis is presented for the Degree of

Doctor of Philosophy

of

Curtin University

August 2021

Declaration

To the best of my knowledge and belief this thesis contains no material previously published by any other person except where appropriate acknowledgement has been made. Similarly, this thesis contains no material which has been accepted for the award of any other degree of diploma in any university person except where appropriate acknowledgement has been made.

Signature _____

Date: 24-08-2021

Abstract

The development of transdermal delivery applications has been limited to only a few drugs with low molecular weight (MW) despite its appeal as an alternative route for the delivery of drugs. Some of the challenging factors delaying the development of these applications are related to the barrier function of the skin. The stratum corneum (SC) is the upper layer of the skin and is the *locus* of the barrier function of the skin, i.e. it is the rate-limiting step of the transdermal permeation of drug molecules. The SC features a unique intercellular lipid matrix (ICLM), a highly organized supramolecular structure featuring hundreds of lipid species. Understanding of the lipid composition, structural arrangement and properties of the ICLM-SC has steadily increased in recent years. Similarly, an increasing body of experimental work reveals the existence of key molecular descriptors which could be employed to predict the transdermal permeability of drug candidates. However the unequivocal elucidation of the supramolecular arrangement of lipids in the ICLM-SC and a high-resolution understanding of their interactions with bioactive molecules (e.g. drug molecules) remains a difficult task. The estimation of permeability coefficients and the mechanism of permeation of bioactive molecules using theoretical approaches such as molecular dynamics (MD) simulations represents an attractive approach for the rational design of transdermal drug delivery applications.

The first aim of this thesis was to estimate permeability coefficients reliably and efficiently from atomistic MD simulations. The recently developed, Selective replica exchange with solute tempering (REST3) was employed for the prediction of the permeability coefficient and free energy of binding of the Ala-Trp dipeptide to a mode; pf the ICLM-SC. By comparison with experimental data, we demonstrated that in combination with conventional umbrella sampling (US), REST3 yielded satisfactory estimations and converges fast. US-REST3 was then used to predict the permeability coefficients of a series of small bioactive molecules and their derivatives across the same model bilayer. The second aim of this thesis was to investigate the molecular interactions that explain the permeability enhancement observed with lipid-conjugation strategy. For this, the permeation of a series of small bioactive molecules and their lipid-conjugated derivatives was simulated across the model bilayer. Our findings suggest that a subtle balance between hydrophobic and hydrophilic interactions determines the outcome of the lipid conjugation of small biomolecules. Lastly, the third aim of this thesis was to investigate the molecular interactions that determine distinct permeability response of bioactive molecules differing only in

their stereochemistry. For this we simulate the permeation of two epimers of the lipid conjugated AAPV tetrapeptide across the model lipid bilayer. Results indicate that the difference in permeability observed for the epimers is caused by the free energy contribution of their interactions with the hydrophobic core of the bilayer.

Attribution Statement

As part of the research during my PhD, I have co-authored two manuscripts that are closely related to the work presented in this thesis. The first manuscript is a review paper titled "Molecular Dynamics Simulation of Small Molecules Interacting with Biological Membranes" (C. Martinotti, L. Ruiz-Perez, E. Deplazes, R. L. Mancera, *ChemPhysChem* **2020**, *21*, 1486.). This review paper contains content that is included in the Literature Review chapter. I am joint-first author of this publication with Carlo Martinotti (CM). Dr Evelyne Deplazes (ED) and Professor Ricardo L Mancera (RLM) were crucial in planning the outline and scope of the manuscript and provided invaluable help with editing the manuscript. My contribution to published manuscript is described in the table below.

Section	Contribution
1.1. MODEL MEMBRANE SYSTEMS	Paragraphs describing the thermophysical phase of model lipid bilayers, and creation of associated figure depicting the melting from gel to liquid phase.
1.2. MEMBRANE BINDING AND PERMEATION	Description of permeation by the inhomogeneous solubility diffusion model. Creation of the associated image of the four-region model using a structure file of a phospholipid membrane provided by ED.
2. EXPERIMENTAL CHARACTERISATION OF SMMI	Description of a range of biophysical methods to study the behaviour of model lipid bilayers and changes upon interactions with small molecules. Except for NMR and SPR, which were described by ED.
3.1. COMMON QUANTITIES IN MOLECULAR DYNAMICS SIMULATIONS	Description of the equation to estimate permeability coefficients and description of the multiple ways to calculate diffusion coefficients. Previous equations were described by CM.
3.2.1. SURFACE BINDING OF SMALL MOLECULES AND ITS EFFECT ON THE MEMBRANE	Description of simulations studying the effects of solvents and alcohols on lipid bilayers. Descriptions of studies of bilayers in the gel phase, their phase transition and the interdigitation phase, and creation of associated figure. Description of

	simulations of saccharides interacting with lipid bilayers was provided by RLM and CM.
3.2.2. DIFFUSION AND PERMEATION OF SMALL MOLECUES	Discussion of seminal works describing molecular mechanisms of permeability.
3.3.1. UMBRELLA SAMPLING	Discussion about the limitations of the COM distance used as RC and discussion of approaches to address such limitations.
3.3.2. MD SIMULATIONS OF SMMI USING UMBRELLA SAMPLING AND RELATED METHODS	Entire section.
3.3.4. SIMULATING PERMEATION USING METADYNAMICS	Selection of suitable references and summarizing them.
3.3.8. OTHER WAYS TO ENHANCE SAMPLING	Entire section
4. CONCLUSIONS AND OUTLOOK	Entire section

The second manuscript includes research on the testing and validation of the enhanced sampling method that was used for all the simulations conducted in this thesis. The title of this manuscript is "Selective replica-exchange with solute tempering (REST3) for the prediction of the interactions of small molecules with lipid bilayers" (revised version currently under review at J Chem Theory Comput). CM, ED and RLM are also co-authors of this manuscript. CM contributed to the development, and testing of the method based on an idea developed by RLM. RLM and ED contributed to the outline of the manuscript and edited the different versions of the manuscript. My contribution as second author is listed in the table below and can be thought of as a summary of the contents of Chapter 3 in this thesis, i.e. the work related to conducting and analysing the simulations of the Ala-Trp dipeptide interacting with the SC model bilayer.

Section	Subsections
3.2. Permeation of Ala-Trp dipeptide across a model of the stratum corneum (Methods)	o System setting and equilibration o Umbrella sampling simulations o US-REST3 simulations o Potential of mean force calculations o Permeability coefficients from MD simulations

	o Configurational space of Ala-Trp
4.2. Interactions between the Ala-Trp dipeptide and the lipid layers of the stratum corneum (Results and discussion)	o Permeability coefficient of Ala-Trp o Potential of mean force profile of Ala-Trp o Configurational sampling of the Ala-Trp dipeptide

I, Lanie Ruiz Perez, author of this document, declare that all the material that has been taken from the manuscripts described above was conceptualized and written by me.

Signature _____

I, Carlo Martinotti, as co-author of both manuscritps described above, endorse that the material used by the PhD candidate in this thesis is an accurate reflection of her contributions.

Signature _____

I, Evelyne Deplazes , as co-author of both manuscritps described above, endorse that the material used by the PhD candidate in this thesis is an accurate reflection of her contributions.

Signature _____

I, Ricardo L. Mancera, as co-author of both manuscritps described above, endorse that the material used by the PhD candidate in this thesis is an accurate reflection of her contributions.

Signature _____

Copyright Statement

I have obtained permission from the copyright owners to use any third-party copyright material reproduced in this thesis, or to use any of my own published work in which the copyright is held by another party. The supporting documents are presented in the appendix titled "Copyright of Figures".

Funding Source Acknowledgment

Acknowledgement of Country

We acknowledge that Curtin University works across hundreds of traditional lands and custodial groups in Australia, and with First Nations people around the globe. We wish to pay our deepest respects to their ancestors and members of their communities, past, present, and to their emerging leaders. Our passion and commitment to work with all Australians and peoples from across the world, including our First Nations peoples are at the core of the work we do, reflective of our institutions' values and commitment to our role as leaders in the Reconciliation space in Australia.

Acknowledgments

It takes a village. The completion of my PhD journey as an international student is one of the most joyful and proud moments of my life. This achievement does not only belong to me as I have been supported in many ways by my family and close friends. I was fortunate to grow up with parents that demonstrated the value and virtue of choosing a professional career based on one's interests and approaching that choice with a passion that leads to excellence. With their advice and their example they inspired me to excel and find a rewarding academic path into the biological and biomedical sciences.

I want to thank my supervisor, Professor Ricardo Mancera, for accepting me into his research group, where I encountered amazingly talented friends. It has been a real pleasure and an honour to grow alongside the other students in the Biomolecular modelling Research group. I want to thank them for demonstrating kindness, empathy, patience, courage and resilience, and for taking the time to share their knowledge and personal time with me. They have been consistently the first to celebrate the wins and the first to offer support through hardships. I also want to thank Dr Evelyne Deplazes for her generosity and invaluable practical and personal advice. I thank them all for helping me navigate and recover numerous times in this journey.

My support network extends beyond university as I've been incredibly lucky to find friends to share interests and hobbies. Their company has kept me healthy, sane, excited and entertained. I want to thank Josh Shubert and Megan McKee for their generosity in sharing their loving families and lovely friends with me, and for inviting me to join them in adventures, celebrations, parties and very scenic trips. Serendipity led me to experience even more kindness and generosity from Australians when I met Jacque and Mark Hagan. On behalf of my family, I want to thank them for adopting me as their own, for maintaining their trust in me and my abilities, for their patience during the most difficult times of this journey, and for facilitating all the other aspects of my life when I needed to concentrate on my academic endeavours. Not content with keeping me alive, they managed to spoil me with delicious food, worldly conversations and access to pristine locations in WA. Even more, they introduced me to their incredible friends who also have adopted me as their own. Special thanks to Caryl and Steve Baily for their advice, for the hugs and for spoiling me in the warmth of their loving home.

A million thanks to my global village! I aspire to live a life that honours your contributions to mine.

Table of Contents

List of Figures

List of Tables

Abbreviations

5-ALA	5-aminolevulinic acid
AA	All-atom
AAPV	HNE inhibitor tetrapeptide
APL	Area per lipid
CEMOVIS	Cryo-electron microscopy of the vitreous section
CER	Ceramide
CG	Coarse grain
CHOL	Cholesterol
CIP	Cahn-Ingold-Prelog
COM	Centre of mass
DLPC	1,2-dilauroyl-sn-glycero-3-phosphocholine
DMPC	1,2-dimyristoyl-sn-glycero-3-phosphocholine
DOPC	1,2-dioleoyl-sn-glycero-3-phosphocholine
DPPC	1,2-dipalmitoyl-sn-glycero-3-phosphocholine
DPPE	1,2-dipalmitoyl-sn-glycero-3-phosphoethanolamine
EM	Electron microscopy
FDA	Food and Drug Administration of the United States of America
ff	Force field
FFA	Free fatty acid
FITR	Fourier-transform infrared spectroscopy
GMP	Glycerol monopalmitate
HNE	Human neutrophil elastase
IACT	Integrated autocorrelation time
ICLM	Intercellular lipid matrix
ITC	Isothermal titration calorimetry
Laa	Lipoamino acid
LJ	Lennard-Jones
LPP	Long periodicity phase
LUV	Large unilamellar vesicle
MD	Molecular dynamics
MW	Molecular weight
NMR	Nuclear magnetic resonance
PAMPA	Parallel artificial membrane permeability assay
PDT	Photodynamic therapy
PME	Particle mesh Ewald

PMF	Potential of mean-force
POPC	1-palmitoyl-2-oleoyl-sn-glycero-3-phosphocholine
PpIX	Protoporphyrin-IX
Pro-Leu-Gly	Melanostatin
QM	Quantum mechanics
QSAR	Quantitative structure-activity relationship
RC	Reaction coordinate
RDF	Radial distribution function
REST	Replica exchange with solute tempering
REST3	Selective replica-exchange with solute tempering
S	Order parameter
SAXS	Small-angle X-ray scattering
SC	*Stratum corneum*
SMMI	Small molecule- membrane interaction
SPC	Single point charge
SPP	Short periodicity phase
TEWL	Trans-epidermal water loss
T_m	Transition temperature
UA	United atom
US	Umbrella sampling
Val-Trp	Dipeptide 2
VMD	Visual molecular dynamics
WAXS	Wide-angle X-ray scattering
WHAM	Weighted histogram analysis method

1 Introduction

1.1 The nearly impermeable nature of the skin: The *stratum corneum.*

Dermal and transdermal delivery of active compounds is highly relevant for the pharmaceutical and cosmeceutical industries. Both dermal and transdermal delivery require the translocation of active compounds across the outer layers of the skin (1). In the case of transdermal delivery, to reach the viable tissue underneath and, in the case of dermal delivery, to act on the layers of the skin. The transdermal drug-delivery route offers many advantages in comparison to its more common counterparts (oral administration or intravenous-intramuscular route), especially for drugs requiring prolonged low dosage, systemic dosage, or for drugs targeting the skin (2, 3). The advantages of transdermal drug delivery include being safe and non-invasive, the possibility to be self-administered and, more importantly, overcoming the metabolic steps associated with the oral uptake of active compounds, which often renders them inactive.

Despite the clear opportunities and potential benefits from the use of transdermal drug delivery, by 2019 the Food and Drug Administration (FDA) of the United States of America had 30 drugs approved or under research for commercial use in transdermal applications (GDUFA Research Report) (4), and by Dec 2020, had 18 generics listed as approved dermal delivery systems. These figures are small in comparison to the universe of FDA-approved drugs under other drug delivery administration routes. One molecular descriptor of these approved transdermal drugs is their low molecular weight (MW) (lower than 500 Da) (5). This scenario is the result of the challenges in obtaining drug candidates with properties that allow their skin penetration while retaining their activity (6). Challenges in the field of transdermal drug delivery occur mostly in the drug development stage and include: i) the *nearly impermeable* nature of the skin, which prevents drug candidates from reaching their site of action, in particular those with higher MW; and ii) the lack of agreement in experimental permeability measurements obtained from different methods and sample types, which hinders the reliability of accurate predictive *in silico* tools (7).

The first challenge is related to the main function of the skin, which is to protect the interior of the body from potentially hazardous environmental conditions. In acting as a barrier, the skin regulates water loss and prevents the penetration of exogenous

compounds (8). The vascular network that serves the skin gives rise to the second function of the skin, which is to maintain the homeostasis of the body in the form of heat regulation, blood pressure regulation and excretory roles (9).

The skin is a stratified organ featuring both viable and non-viable cells. The deepest layer of the human epidermis is the *stratum basale*, a single layer of germinative cells. The main function of the *stratum basale* is to give origin to the cells that will follow a differentiation path into corneocytes as they are pushed outwards, until they eventually desquamate. In the epidermis, the early stages of differentiation involve increasing their content of keratin in the cytoplasm, but also changing shape and dehydrating (9, 10). Their increased keratin content originates the name of keratinocytes to most cells forming the epidermis (Box 1, Figure 1.1.1).

Keratinocytes are organised in layers displaying a gradient of increasing dehydration and keratin content in the outward direction. The last differentiation step converts keratinocytes into the non-viable corneocytes that form the outer layer of the skin: the *stratum corneum* (SC). This step involves loss of their nucleus, cessation of all metabolic processes, and excretion of sphingosine and other lipids into the intercellular space. Corneocytes are flat shaped cells featuring an extremely dehydrated interior filled with keratin granules. The excretion of lipids and the marked dehydration of corneocytes confer special features to the SC, which led to the conceptualization of it as a "brick and mortar" structure, where the corneocytes are the bricks and the intercellular lipid matrix (ICLM) is the mortar (see box 2 in Figure 1.1.1).

Some of the skin appendages (e.g. hair follicles and sweat glands) are transversal to its layers. This is a convenient route by which exogenous compounds could reach the inner layers of the skin. However, the surface area that these structures cover is negligible with respect to area of the main layered structure. Thus, it is accepted that any exogenous compound has to translocate across the layers of the skin. Furthermore, experiments suggest that exogenous compounds that do translocate across the skin have to diffuse through the ICLM as opposed to traversing into the corneocytes. Therefore, there is agreement that the main route of translocation of exogenous compounds across the skin is a route across the ICLM-SC.

The lipids in the ICLM-SC secreted from the interior of the keratinocytes are arranged into several stacked lipid bilayers (lamellae) in a very ordered and dehydrated state (see box 3 in Figure 1.1.1). Understanding the molecular interactions between exogenous compounds (e.g. drug candidates) and the ICLM-SC is of particular interest for the cosmeceutical and pharmaceutical industries, since this is the rate-limiting step for drug delivery.

Figure 1.1.1. Schematic representation of the layers of human skin (1). Representation of the SC as 'brick and mortar' (2). Representation of the lamellae in the intercellular lipid matrix (ICLM) of the SC (3). Representation of lamellar and lateral organization found in human stratum corneum (Right panel). Reprinted from Ref. (11). Copyright © 1969, Elsevier (CC-BY).
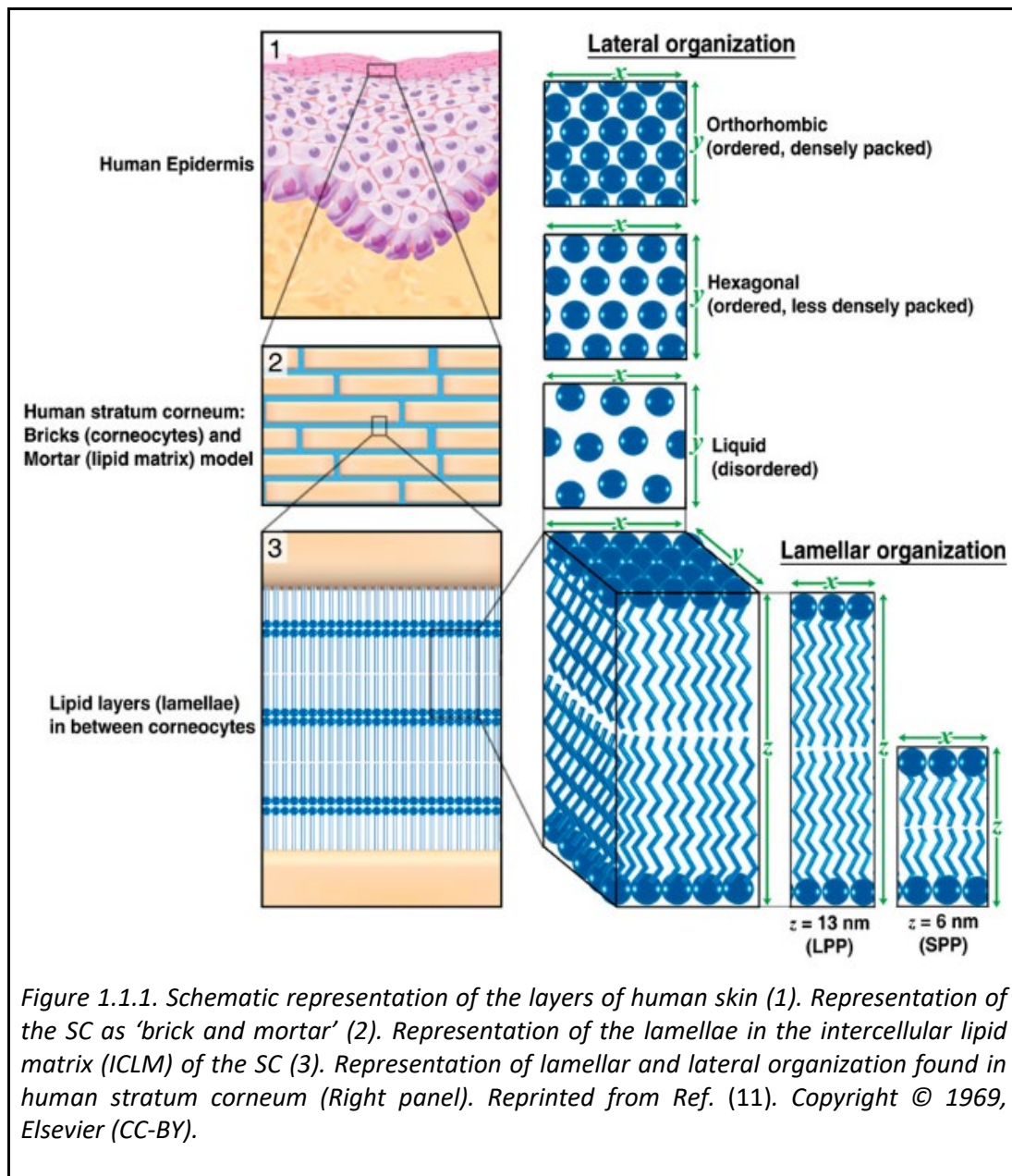
1.2 Composition of intercellular lipid matrix (ICLM) of the SC.

The very unique lamellar organization of the ICLM-SC is directly related to its lipid composition. The three main lipid classes found in the ICLM-SC are ceramides, cholesterol and free fatty acids. The exact molecular arrangement of these lipids to form the lamellae (and individual lipid bilayers) is still debated. The molecular models that have been proposed to describe said molecular arrangement will be presented and discussed in depth in Chapter 2 (Literature Review).

1.2.1 Ceramides (CER)

Figure 1.2.1. Schematic structure of ceramides. Red sections indicate the regions where ceramides show structural differences. Reprinted from Ref. (11)*. Copyright © 1969, Elsevier*
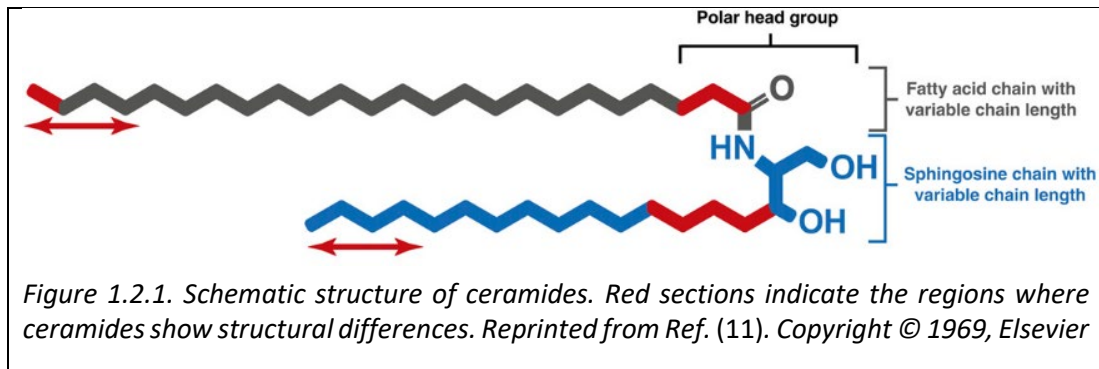
Ceramides are a type of sphingolipids responsible for the gel-phase and slow dynamics of the lipid bilayers found in the ICLM-SC. Ceramides are in fact a diverse group of lipids that bear one sphingosine moiety and one fatty acid moiety, covalently bound by one amide bond (Figure 1.2.1). The different lengths of these moieties confer the characteristic of asymmetric lipid tails. Ceramides have been classified according to the order of elution using chromatography purification. In this classification ceramides are numbered according to their polarity: the least polar ceramides elute the fastest (e.g., CER 1) and the most polar ceramides (retained for longer) elute the slowest (e.g., CER 6) (12).

Figure 1.2.2. Current classification of ceramides. Reprinted from Ref. (13) *2017. © 2020 Sciendo (CC BY-NC-ND 4.0).*
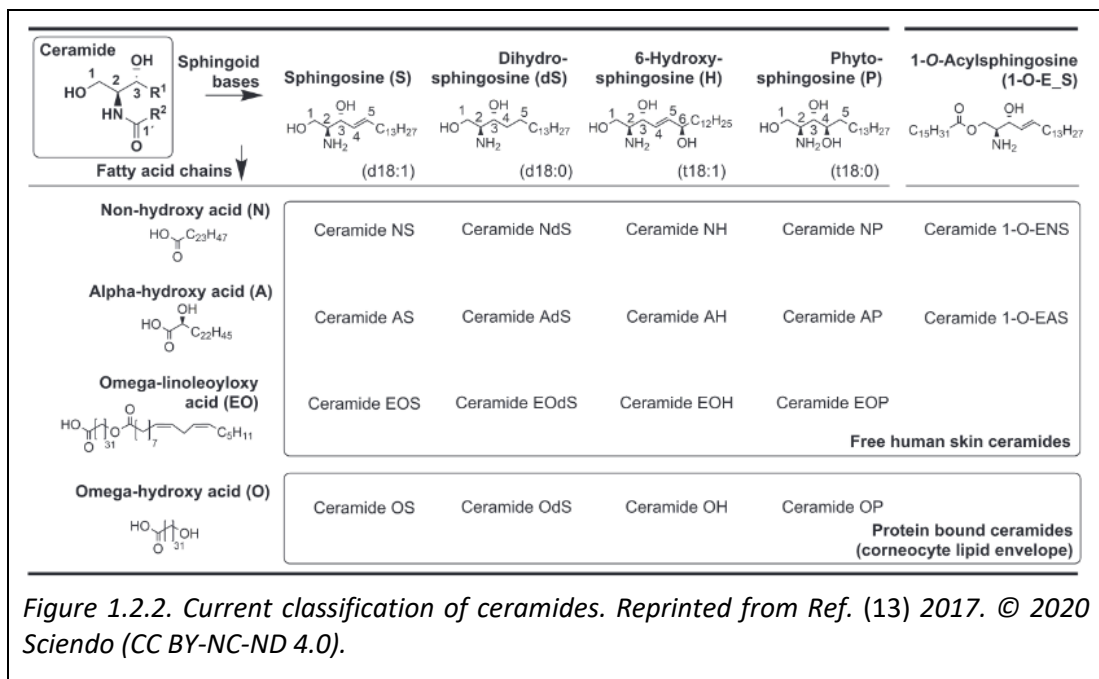
The current classification of ceramides found in human SC is illustrated in (Figure 1.2.2) and categorizes them into in a more informative and precise way. This nomenclature system was proposed in 1993 by Motta et al. (14) and it assigns

subclasses of ceramides according to the combination of functional groups in the sphingosine backbone (i.e., the five columns in Figure 1.2.2) and in the fatty acid moiety (i.e. the four rows in Figure 1.2.2), (11). This nomenclature system is completed by indicating the length of the fatty acid hydrocarbon tails and the position of unsaturation (if any).

The major drawback of the early nomenclature is that ceramides from different subclasses could elute together (given similar polarity and MW). This resulted in the underestimation of ceramide diversity and the presence of *hidden* subclasses in subsequent permeability and structural determination experiments. Two well documented examples exist: CER2 included ceramides with a non-hydroxyl fatty acid moiety (N) linked to either sphingosine (S) or dihydrosphingosine backbones (dS) (15); and similarly for CER5 with the alpha-hydroxyl fatty acid moiety (A) (16).

With improvements in purification procedures (17–19), ceramide subclasses were discovered in human SC and added to the classification (Figure 1.2.2). For example, Schreiner et al. (20) reported 7 CER subclasses in 2000, and Janssens et al. reported 12 in 2012 (11). For the same reason, the relative abundance of ceramide subclasses in the SC has been updated over time, having a direct impact on the diversity of ceramides considered in experiments with model lipid bilayers, and in the detail of molecular models that have been proposed. Similarly, the tail-length polydispersity within ceramide subclasses could be better documented (18, 21, 22). These developments resulted in an understanding of the delicate balance of lipid components that is required for a healthy barrier function of the skin (23, 24), and how it changes with age (20). For example an impaired barrier function in atopic eczema patients is correlated with imbalance in the proportion of short-chain ceramides (11, 25). Similarly, the lamellar arrangement of the ICLM presents distinct features in healthy and diseased skin (10, 26), with a key role of the omega-esterified ceramides (row 3 in Figure 1.2.2) in the healthy barrier function (27–29).

1.2.2 Cholesterol (CHOL)

The relative abundance of cholesterol and cholesterol sulphate (Figure 1.2.3) in the ICLM-SC is notably higher than in plasma membranes. Cholesterol molecules are planar rigid molecules that can perform two activities (30): they can increase the order of disordered liquid-phase bilayers (e.g. plasma membranes mainly composed of phospholipids), and they can also fluidize bilayers in the gel-phase, conferring plasticity (e.g. ceramide-rich lipid bilayers like the lamella of ICLM-SC). The role of cholesterol sulphate appears to be to increase the miscibility of cholesterol in lipid mixtures (containing ceramides) so that it does not separate into crystalline domains at high relative compositions (31).

Figure 1.2.3. Structure of cholesterol (CHOL), cholesterol sulphate (CHOL-S) and lignoceric acid (FFA C24). Reprinted from PubChem database.
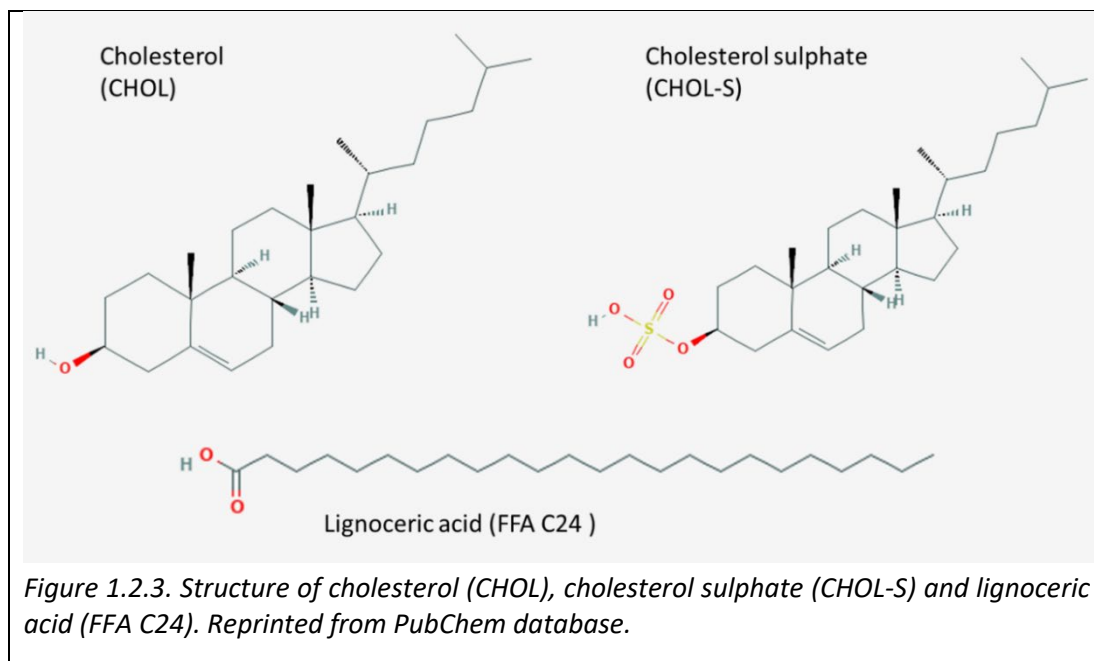
1.2.3 Free Fatty Acids (FFAs)

The free fatty acids (FFA) found in the ICLM-SC mainly feature long-chain saturated hydrocarbon tails. The tail-length distribution ranges from 16 to 30 carbons long, with the most prevalent being C24 (8, 32) (tetracosanoic acid or lignoceric acid) (Figure 1.2.3). This distribution is referred to as the tail-length polydispersity, and it seems to play a key role in the dense packing of lipids (typically in the gel-phase) and in the barrier properties of the SC (33). At physiological pH (7.4), a large fraction of FFA will be ionized; however, the pH of the skin (5) indicates the existence of neutral FFA. The ionization state of FFA has effects in their ability to interact with the head groups of other lipids in the mixture (31).

1.2.4 Gradients in the SC

The overall composition of the SC is well described. However, there are gradients of pH, hydration and composition along the depth dimension. This translates into differences in the molecular arrangement and dynamics of lamella.

The hydration gradient refers to the upper layers of the SC, which are very dehydrated in contrast to maximum hydration at the boundary with the viable tissue. The exact distribution of this increased water content in the ICLM is a matter of debate given experimental and simulation studies reporting lack of swelling of model membranes upon increased water content (28, 34).

As mentioned above, the pH gradient has a direct effect on the ionization state of the FFA fraction, which in turn affects structural properties of the lipid bilayers. The SC is acidic in the upper layers with a pH of 5. With increased depth the pH reaches 7.4 at the boundary with the viable tissue.

The relative abundance of lipid classes also changes along the depth profile. This prevents agreement to a single composition that unequivocally represents the barrier function of the skin. Historically two options have appeared to capture the molar ratio of the three major lipid classes that can better represent the barrier function of the skin. Some studies favour an equimolar molar ratio, where ceramides, cholesterol and free fatty acids are represented in equal parts in the mixture (31, 35). The second option is a 2:2:1 molar ratio, supported by Norlen and collaborators (26, 36).

1.3 Approaches and challenges in enhancing permeability across the skin.

The enhancement of transdermal delivery of novel drugs and active compounds is a very active research field (1, 37, 38). The variety of naturally occurring skin peptides with local activity highlights the range of therapeutic opportunities to be explored in dermal drug delivery applications. Targeting these active peptides directly to their site of activity has immediate applications in wound healing, modulation of inflammation in diseased skin, and in decreasing sings of skin ageing (39, 40). However, their molecular descriptors (e.g. MW and flexibility) are often incompatible with dermal permeation.

The three main challenges in transdermal drug delivery are overcoming the barrier function of the skin, maintaining the activity of the drug (or drug candidate) during its translocation into the skin, and the addition of other compounds to the formulation to stabilize, preserve or deliver the active compound in a safe way. The approaches to enhance transdermal delivery can thus be categorised into i) strategies that act on the skin (disabling, altering or bypassing it), and ii) strategies that act on the drug candidate by either changing its physicochemical properties or the physicochemical properties of the formulation. An example of the first category is the use of chemical permeation enhancers to alter the molecular arrangement of the ICLM-SC (41).

1.3.1 Altering the skin's barrier

Approaches to altering the skin's barrier include physical techniques that bypass the SC either with microneedles that reach into the deeper layers of the skin (42), or with dermal (laser or thermal) ablation to impair the physical barrier by partly removing its upper layers (3, 43). Other strategies employ external energy sources to actively push the molecule deeper into the skin (e.g. sonophoresis, iontophoresis, electrophoresis) (40, 44).

1.3.2 Altering the drug candidate

The underlying proposition of this group of approaches is that the molecular interactions between the drug candidate and the ICLM-SC play the central role in determining the drug's permeability. In principle, enhancing transdermal drug delivery reduces to finding a combination of ideal physicochemical properties that favour permeation but retain activity of the drug candidate.

Approaches like encapsulation of the active compound in delivery vehicles such as liposomes (45, 46), and the formulation with other compounds that act as penetration enhancers (38, 47, 48) are designed to optimize the absorption of the drug candidate by masking its unfavourable interactions with the barrier or rate-limiting step. For example, an "ethanol/water binary vehicle with lauric acid appears to be a good candidate as a vehicle for transdermal therapeutic systems for hydrophilic drugs"(49).

In contrast, the chemical modification of the drug candidate itself can be targeted to the functional groups of the drug molecule that directly interact with the barrier to its absorption. One well-documented example is the transdermal application of the drug propranolol in the form of acyl-esterified pro-drugs. In this case, all the prodrugs had increased permeability but there was not a clear trend in regards to the acyl-chain length (50, 51). Lipid conjugation is a promising alternative involving chemical modification of the drug candidate.

1.3.3 Lipid conjugation

Lipid conjugation involves chemically linking a lipid moiety to a drug candidate with the aim of changing its physicochemical properties (in particular, its hydrophobicity). Lipid conjugates have been shown to exhibit superior permeability across biological lipid bilayers, suggesting potential applications for enhanced delivery of drugs, peptides, antimicrobials and vaccines (52–54). Lipid conjugation is also employed in commercially available cosmeceutical products. An example is palmitoyl

pentapeptide-4 (Matrixyl®: Sederma/Procter & Gamble), in which the active peptide is covalently linked to a fatty acid (palmitic acid or C15).

In 2003 an experimental study of the permeation of the Phe-Gly dipeptide across rat skin showed that the conjugation of the parent dipeptide with either butyric acid (C4), caproic acid (C6) or octanoic acid (C8) enabled transdermal permeation (i.e. no permeation of parent peptide was observed) whilst increasing the stability of the dipeptide. The permeation of the C6 acyl derivative was found to be highest of the set of lipid conjugates, suggesting that there is not a linear relationship with hydrophobicity and the existence of an optimal value above which permeability does not improve anymore (54). Similar findings were observed for Ala-Ala-Pro-Val (AAPV), a naturally occurring tetrapeptide with inhibitory activity against the human neutrophil elastase (HNE). Experimental evidence showed that lipid conjugation of the tetrapeptide AAPV enhances its skin permeation and reduces its degradation (55, 56). In that study, lipid conjugation of the tetrapeptide was achieved by the addition of a modified amino acid bearing a hydrocarbon tail in the place of the side chain, i.e. a lipoamino acid (Laa) (56). Three Laa moieties were tested (C6, C8, C10) and it was found that permeation reaches a maximum at a specific tail length (C8), such that if the tail length is further increased, the permeability decreases (54, 56). Furthermore, the process of synthesizing a Laa yields two stereoisomers depending on the absolute 3D configuration (R or S) of the chiral centre of the alpha carbon. For the AAPV tetra peptide, the enhancement of permeation was shown to be dependent on the stereochemistry of the added Laa, with a preference for the R configuration (56, 57). This will be discussed in detail in the Literature Review (section 2.4.1.1). The chirality of the lipids forming the ICLM-SC has been proposed as one source of stereo-selectivity for the transdermal permeability of small drug molecules, as described in the review of Afouna et al. (58).

Given the non-linear relationship between hydrophobicity and transdermal permeability of lipid conjugated bioactive peptides, and the effects of stereo-selective interactions playing a role in their transdermal permeability, studies that investigate the molecular mechanisms of these two factors can inform rational drug design for the optimal pairing of a drug candidate and a lipid moiety with the aim of maximizing its permeability across the skin.

1.4 Permeability

As previously stated, the second challenge in the development of transdermal drug delivery applications is the lack of agreement in experimental permeability measurements obtained from different methods and sample types. In the context of

cell biology, *permeability* is commonly assumed to be an *active* process of translocation of molecules across a lipid bilayer (typically a plasma membrane, which is a phospholipid bilayer). This process is deemed to be *active* because of the role of transmembrane proteins that facilitate the translocation of the molecule of interest. However, in this work the use of the word *permeability* refers to the non-facilitated process of translocation of molecules across a lipid bilayer, which is commonly referred to as *passive diffusion*. As will be explained below, the *permeability* of small molecules across lipid bilayers is conceptualized from the mass transport equations that describe the *passive diffusion* of molecules in the direction of a concentration gradient, and the movement of each molecule in 3D space as conceptualized from Brownian dynamics of rigid particles in a dilute system.

1.4.1 Mass transport

The key concept in the theory of mass transport is the *potential* given by a concentration gradient (ΔC), which makes the molecules move or *diffuse* in the direction from the higher to the lower concentration. The flux (J) of a substance across a barrier separating two chambers is the diffusion of molecules from one chamber to the other. It is defined as the mass of the substance that translocates across the barrier in a given time ($g.cm^{-2}.s^{-1}$) and given a particular concentration gradient. The flux J then is directly related to the permeability coefficient (P) of the substance of interest (59), as described in Equation 1.1:

$$P = \frac{J}{A \times \Delta C}$$
Equation 1.1

Early estimates of the permeability of small molecules across lipid bilayers were obtained using the Meyer-Overton rule. This is a simple equation (Equation 1.2) that relates the permeability coefficient to the partition coefficient (K) (59):

$$P = \frac{KD}{h}$$
Equation 1.2

Here, D is the diffusivity and h is the thickness of the barrier. The partition coefficient measures the ability of a substance to translocate from a hydrophilic phase (e.g., an aqueous solution) to an organic phase (e.g., the hydrophilic interior of a lipid bilayer). It is defined as the ratio of the equilibrium concentrations of a solute in the organic and aqueous phases and is a function of the *hydrophobicity* of a substance. The partition coefficient is commonly measured in octanol/water systems ($K_{octanol/water}$) to represent partitioning into a plasma membrane.

The Meyer-Overton rule led to the simplistic paradigm that increased hydrophobicity results in increased partition to the organic phase, which in turn favours permeability.

In fact, the hydrophobicity and $K_{octanol/water}$ are common molecular descriptors used for the prediction of the permeability of a substance, as will be discussed further below. However, the permeation process involves molecular interactions that mediate the flux of a substance across a lipid bilayer and, therefore, approximating it to the translocation into a bulk organic phase (partition) is an oversimplification.

The diffusivity of the substance of interest refers to the ability of molecules to move or *diffuse* in solution. The thickness of the barrier (h) that separates two compartments with different concentrations can be a lipid bilayer. One can appreciate how (Equation 1.2) reduces the effect of the interaction with a lipid bilayer to a single geometric parameter, and how it includes two molecular descriptors to characterize the permeant substance.

1.4.2 Stereoselectivity and permeability

The chirality of a molecule is a property that refers to the absolute configuration of said molecule in 3D space (given a carbon with four different substituents). Chirality is another molecular property that has effects on the permeability of a molecule across a lipid bilayer (60–62). Permeants with chiral centres will have to interact with biologically relevant lipids (which also have chiral centres) and this generates selectivity (63). It has been proposed that chiral-chiral interactions can be favourable for one isomer and less favourable for the other. In other words, the interaction of chiral small molecules with lipids bilayers is a source of chiral discrimination in biological systems, and one that has direct implications for biochemistry during the origins of life (64, 65). However, the effect of chiral selectivity (or stereoselectivity) is not as *intuitive* as other molecular descriptors like hydrophobicity, partition coefficient or MW, and is difficult to measure. Gaining understanding of the molecular mechanisms that rationalize stereoselectivity in biomolecular interactions could provide valuable approaches for drug development as a whole (not only in the context of transdermal applications) (66). This will be presented in detail in Chapter 5 (section 5.1).

As discussed above in the context of lipid conjugation, when presented with diastereoisomers of the lipid conjugated AAPV tetra peptide (Laa-AAPV), lipid bilayers in the SC can favour the permeability of one isomer more than the other. This is not an isolated effect, as other studies have reported stereoselectivity in the context of enhancement of transdermal permeability (58, 67, 68). The paucity of studies stresses the gap in understanding and evidences the value of tools to predict the permeability of molecules with very similar physicochemical properties, e.g., between diastereoisomers.

Molecular dynamics (MD) simulations are perfectly suited for providing mechanistic information about the interactions of molecules. Studies of chiral effects, in particular the optical properties of stereoisomers and their interaction with solvents, suggest the existence of different molecular arrangements in the vicinity of the chiral molecule depending on its chirality (69–72). In fact, at least two studies have demonstrated the ability of MD simulations to reproduce enantioselectivity in biomolecules: one demonstrates the resolution of MD simulation in separating the preferential insertion depth of the drug into the lipid bilayer (73), and the other demonstrates the resolution of MD simulation in linking conformational differences to permeability differences of a cyclic decapeptide (74). These studies will be discussed in detail in Chapter 5 (section 5.1.6).

1.4.3 Experimental measures of permeability

There is a notable variety of experimental methods that have been developed to measure permeability given the wide range of application of permeability coefficients across lipid bilayers in the biological sciences. The pharmaceutical, bioprocessing and molecular biology fields benefit from measuring, understanding and predicting permeability. This variety of methods generates a challenge in extrapolating permeation measurements across different types of samples, given that results can differ in orders of magnitude depending on sample type and preparation. As a rule of thumb, *in vivo* studies of permeability across the skin produce lower measures than *ex vivo* studies (75), and *in-vitro* and *in silico* studies with their reduced complexity models make comparisons of permeability coefficients even more remote (76).

1.4.3.1   Trans-epidermal water loss (TEWL)

This measurement is obtained with a Tewameter® and is a gold-standard marker for the barrier function of the skin *in-vivo* (11, 20). In healthy barrier function, water loss is modulated to fulfil the other functions of the skin (excretory and temperature regulation). This is also a measure of the integrity of an *ex vivo* sample (30, 77). If the tissue is intact, it will reflect a low TEWL and can better represent the barrier function of the skin when presented with other substances. TEWL measurements are also conducted for testing and characterizing model membranes mounted on porous supports (27) (*see* below).

1.4.3.2   In-vivo measures

These measures involve the recruitment of volunteers or patients for the subsequent application of the active molecule to the skin in an established skin section of constant area (usually the forearm, where the skin is uniform), following standard guidelines for topical dermatological dosage (78). Depending on the formulation of the active molecule, its application to the skin can be done with one of the following

delivery methods: cloth, solution, lotion, cream, gel, patch, ointment or film (slow release). The monitoring of the penetration of the active molecule is performed by physically removing the upper layers of the SC. This is achieved by sequentially tape-stripping the skin and extracting the active molecule from the tape (79).

1.4.3.3 Ex-vivo measures

Franz diffusion cell assays are used to obtain permeability measurements by monitoring the time evolution of the flux of a permeant substance across a section of known area. For these assays, a skin sample separates donor and acceptor chambers. The donor chamber contains a known concentration of permeant, whilst the acceptor chamber is monitored over time for changes in the concentration of the permeant (Figure 1.4.1). The assay returns a plot of the cumulative amount of permeant vs time (Figure 1.4.2), from which the steady state flux and permeability coefficient can be estimated.

Figure 1.4.1. Sketch of typical Franz diffusion cell assay. Reprinted from Ref. (80). Copyright © 2010, American Association of Pharmaceutical Scientists.
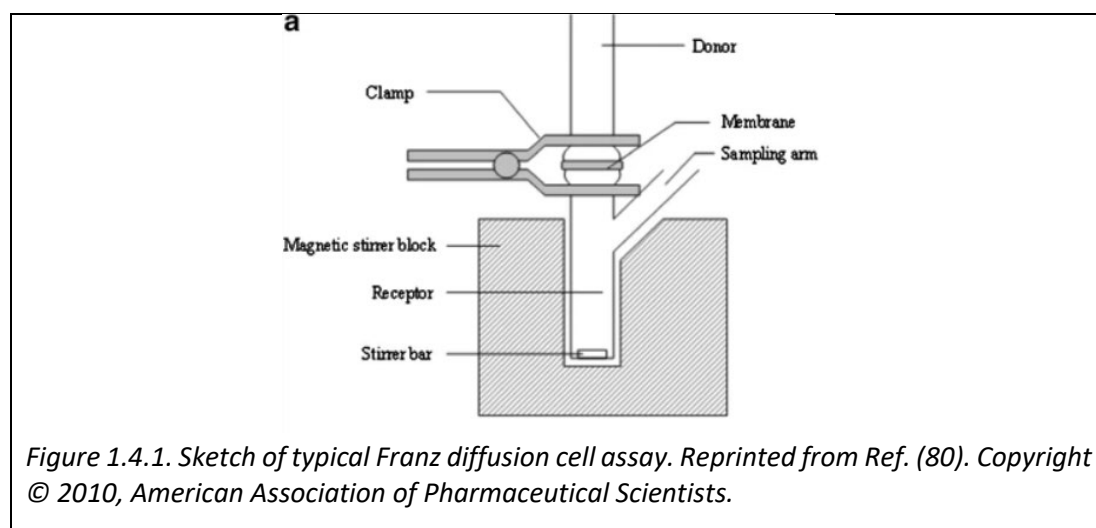
To obtain *ex vivo* permeability measurements, typically piglet, mice, rat or human excised skin is used. The skin sample is typically treated for a few reasons: to sterilize, to remove hair, to remove the tissue from underneath (dermis), or to freeze. Sometimes the skin is treated (protease digestion) to separate the SC from the rest of the epidermis. All of the above can affect the structural properties of the SC and dramatically bias the permeability measurements obtained from these samples. This is clearly illustrated in the work of Yamamoto et al., who observed that permeation profiles over time and the permeability values (and the ranking of permeability) changes when intact rat skin is used in comparison with stripped rat skin (54). Other sources of variability arise from skin inter-individual variation due to age, gender, and ethnicity, and even intra-individual differences in skin according to the region of the body from which the sample is collected (26, 75, 81).

Figure 1.4.2. Changes in permeation profiles of a parent Phe-Gly dipeptide, and three of its acyl-derivatives according to the treatment of the sample in the Franz diffusion cell assay: intact skin (left) and stripped skin (right). Reprinted from Ref. (54). Copyright © 2002 Elsevier Science B.V. All rights reserved.
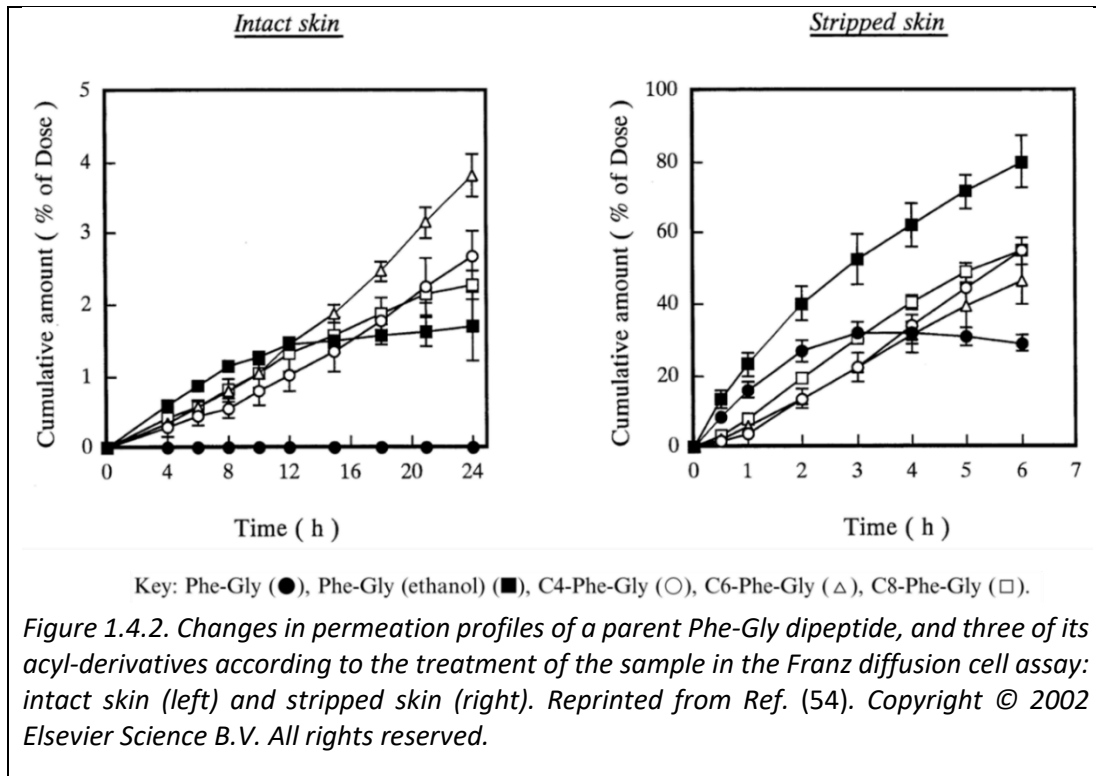
Lastly, parameters related to how the assay is conducted can add to the variability of permeability measurements taken from Franz diffusion cell assays (80). The prolonged exposure to unnatural hydration during the assay also alters the integrity of the skin's barrier (82). An alternative is to use permeability assays like the one depicted in Figure 1.4.3.

Figure 1.4.3. Experimental setting for permeability measurements across a SC substitute. Note that the donor compartment does not contain an aqueous solution. Reprinted from Ref. (83). Copyright © 1969, Elsevier. (CC-BY).
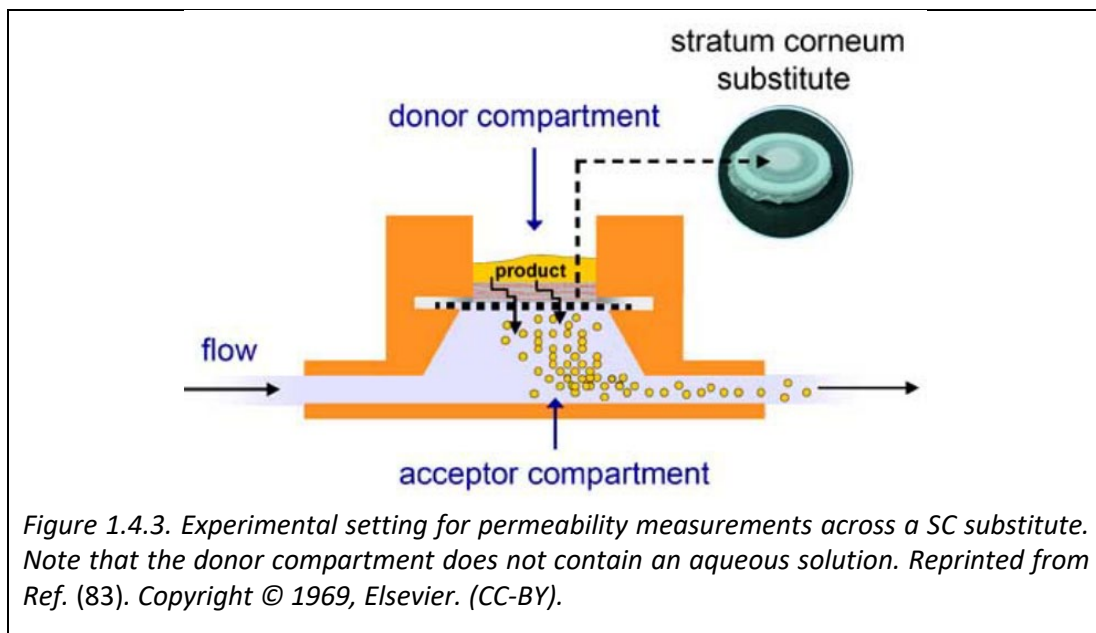
Despite its wide use, Franz diffusion cell assays are still both costly and time consuming (≈30 hours per assay) given that permeation across intact skin is very slow. Reproducibility across laboratories can be challenging and extrapolation of results to human *in vivo* permeability is difficult because of the known issues mentioned above. Perhaps the biggest obstacle in the sustained use of *ex-vivo* samples relates to the ethical concerns associated with using animal or human samples for conducting experiments (84).

1.4.3.1   In-vitro measures

Alternatives to the use of *ex-vivo* samples can be categorized into tissue culture and model membranes. For transdermal applications, reconstructed epidermis is a type of tissue culture aimed to mimic the skin. However it has been found to be more permeable than skin in in-vivo measurements (82).

Model membranes have been developed and tested for their ability to reproduce relevant SC properties. These models simplify the complexity of the ICLM-SC by including only its most abundant components and assembling them into a single planar lipid bilayer (15, 85–88). The parallel artificial membrane permeation assay (PAMPA) allows the measurement of permeability across a lipid bilayer separating two solutions with different concentrations of the permeant (59). Similar to the Franz cell assay, in PAMPA the changes in the concentration of the permeant indicate the flux of the permeant across the lipid bilayer, from which the permeability coefficient is estimated. Given the nature of lipid bilayers, the choice of lipid composition, lipid diversity and hydration of the model lipid bilayers have a significant effect on permeability estimates. Therefore, optimizing these parameters is non-trivial. Overall, the inherent simplification of model lipid bilayers is an obstacle for direct extrapolation to *in vivo* permeability (89, 90).

Using model membranes offers the possibility of measuring thermodynamic parameters of their interaction with permeants. These include association and dissociation constants, and binding affinity. Other available measures refer to the ability to locate the preferential site of interaction (inside the membrane) and the effects of the interaction on the organization and dynamics of the membrane. The possibility of formulating the composition of the model membrane provides an opportunity to study the roles of different types of lipids, not only in the properties of the membrane, but also in the interaction with the permeant (e.g. for permeation). I co-first authored an extensive review paper that contains a discussion of the physicochemical and thermodynamical properties of interest for small molecule – membrane interactions (SMMI). In that review, we presented the properties that can be obtained using a number of experimental methods (91). Parts of said discussion will be presented in Chapter 2 (Literature Review) of this thesis.

1.4.4 In-silico estimation: Predictive models

Quantitative structure-activity relationship (QSAR) models provide an alternative for estimating permeability across the skin. In principle, the only information required to build a predictive model is a robust set of active compounds (the drug candidates) with available and accurate experimental data about their physicochemical properties and their activity (in this case, their permeability) (7, 92). In practice, however, this is hard to achieve because the chemical space of physicochemical properties of drug candidates is very large to be systematically explored. Therefore, it is common practice to narrow it down using a training set of molecules with similar activity (and structural similarity) and with available experimental permeability data. Using this information as input, a mathematical model is built relating their molecular descriptors (e.g., MW, hydrophobicity/polarity, partition coefficient, number of rotatable bonds, etc.) to their activity, in this case permeability across the skin (93). Later, the model can be used to predict the permeability of a new compound using as input only its molecular descriptors. After the seminal work of Pugh et al. (94), several studies explored the estimation of permeability of small molecules (95–97) and cosmetic ingredients (98) across the skin. It is noteworthy that the hydrophobicity of a drug candidate is often used as a strong predictor of transdermal penetration (97), which can be explained considering Equation 1.2.

The limitations of QSAR models are related to the robustness of the test set and the reproducibility of the permeability data. On the one hand, the narrow chemical space represented in the training set can bias the estimates of the model (93). On the second hand, the variability associated with experimental permeability data poses an obstacle for the finer resolution of estimates (e.g., two diastereoisomers of a drug candidate that have almost identical molecular descriptors). In the best of cases, where a quantitative model is able to differentiate two drug candidates that share most of their physicochemical properties (but show very different permeability values), the model will fail to explain the molecular mechanism behind the observed differences.

1.5 Molecular dynamics (MD) simulations of permeation.

Unlike experimental measurements and *in silico* predictions, molecular dynamics (MD) simulations provide a method to obtain unmatched time and spatial resolution of the permeation process. MD simulation approaches are able to predict the free energy change and the associated permeability coefficient, plus provide detailed

information about the molecular mechanism of interaction between the drug candidate and the lipid bilayer (99–101).

In MD simulations atoms are represented as particles, forces are treated by empirical potentials and dynamics are approximated by Newtonian physics. The energy of the system is determined by a potential energy function accounting for bonded (chemical bond stretching, bending and torsion) and non-bonded (van der Waals and electrostatic) interactions. This potential energy function is defined as a function of the coordinates of the atoms in the system (r), and is solved for every atom pair in each discrete time step, with the resulting forces and velocities used to calculate new positions by solving Newton's equations of motion iteratively (102). The result is a continuous simulation trajectory that allows the *observation* of a molecular system evolving in time, in other words, the *observation* of molecular translations and rotations, and the changes in molecular conformations. Based on the equations of statistical thermodynamics, with sufficient sampling of these *observations,* it is possible to compute average structural, dynamic and thermodynamic properties that no other experimental method or combination of experimental methods can provide.

From the definition given above, one can realize that the calculation of pairwise (combinatorial) interaction of atoms in a moderately-sized biomolecular system (of the order of $\approx 10^4$ to 10^5 atoms) quickly becomes a huge computational task. However, with the steep increase in computational power and development of more efficient algorithms and computer codes, the main limitations of MD simulation are not always related to the computational effort that it requires. Instead, given the larger systems and longer time scales in a typical, average biomolecular MD simulation system, the main current limitations are related to the accuracy and reliability of the calculations, which translates to the identification of propagation of errors and other artefacts that can bias the estimates. For the calculation of dynamical properties like the diffusion coefficient, these errors and artefacts are related to the system size and simulation boundary issues (103, 104). Another challenge is the assessment of convergence of computed thermodynamic properties (e.g. free energy in a membrane simulation) (105), and the sufficient sampling of relevant (i.e. usually rare or high energy) molecular events.

Aside from the current challenges of biomolecular simulations, all MD simulation estimates are also dependent on the description of particles forming molecules (ranging from electrons to atoms to groups of atoms) and the degree of approximation in the description of their interactions. This is another non-trivial issue known as the choice of *force field*. Different force fields make different approximations for a trade-off between accuracy of estimates and efficiency in the use of computational resources (106, 107). Often structural or dynamic features of a system can vary according to the choice of force field (107–109). In light of this,

several approaches have been developed to accurately represent groups of biomolecules: structured proteins, intrinsically disordered proteins, lipids, solvents, carbohydrates, etc. These have evolved and been parametrized to accurately reproduce key structural and dynamical characteristics of each group. In practice, the problem reduces to finding a force field that adequately describes all molecules in the system and their interactions.

1.5.1 The sampling problem

MD simulation estimates are strongly dependent on the ability to sample efficiently the molecular events being considered, and this is known as *the sampling problem* (100, 110). This is of particular relevance for the study of permeation across biological membranes given the slow rates at which it happens in comparison to the time scale accessible by MD simulation (in the order of microseconds). Simulating the diffusion and permeation of small molecules through an intact lipid bilayer with unbiased MD simulation techniques would require very long simulations. Even in the case of water, which has a high flux across lipid membranes (compared to other small molecules), simulations of a few microseconds or more are required to obtain reliable predictions of permeability coefficients (111).

Several methods have been developed to overcome the sampling problem of unbiased (conventional) MD simulations (111, 112), which have been recently reviewed (111, 113, 114). Umbrella sampling (US) is one of the most common enhanced sampling methods and is indeed the most extensively used to characterise the permeation of small molecules across lipid bilayers (111, 115).

1.5.2 Permeability coefficients from MD

To simulate the permeation process, US requires the definition of a reaction coordinate (RC) that represents the progression of the translocation of the solute from one side of the lipid bilayer to the other. In practice one needs to define a series of N overlapping intervals that, when combined, cover the entire RC or path of translocation (111).

US adds a new energy term to the potential energy function (E), the biasing potential (ω), which restrains the location of the solute at a given interval of the RC. The typical approach to US consists of setting up N independent simulations (referred to as 'windows'). In each window the biasing potential is centred at a discrete value along the RC, in the form of a simple harmonic potential. In practice, the US approach is based on probing the free energy of the system at a series of positions of the permeant, typically the insertion depth along an axis normal to the bilayer plane (z-

axis), which altogether represents the entire translocation (steps 1 to 5 in Figure 1.5.1). The weighted histogram analysis method (WHAM) is commonly used to retrieve the unbiased probability distributions and their associated free energy estimates into a global free energy profile ($\Delta G(z)$) (116), which is then used to calculate the permeability coefficient according to Equation 1.3:

$$\frac{1}{P} = \int_{z_1}^{z_2} \frac{e^{\Delta G(z)/RT}}{D_i(z)} dz \qquad \text{Equation 1.3}$$

Here D(z) is the diffusivity profile (i.e. the diffusion coefficient as a function of the RC), also calculated from MD simulations (117, 118).

US works under a few assumptions: the permeant molecule is relatively rigid, symmetrical and very small in comparison to the bilayer; and the bilayer is homogeneous and not perturbed significantly by the insertion of the molecule. If these assumptions are met, the free energy is safely assumed to be a function of the RC only.

Figure 1.5.1. Schematic of umbrella sampling (US). Adapted from Ref. (119). Copyright © 2011 John Wiley & Sons, Inc.
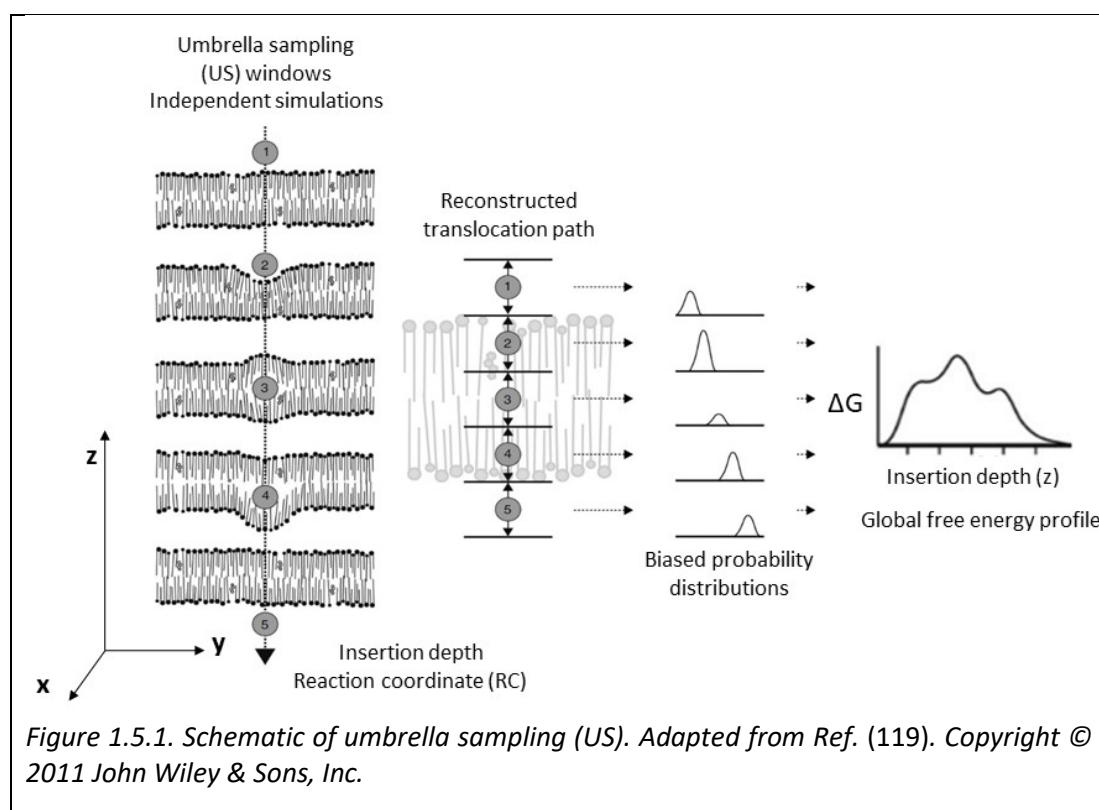
US is a well-established method for determining the free energy profile of molecules interacting with lipid bilayers, and for the subsequent estimation of permeability coefficients (120–124). However, in biologically relevant systems most of the above assumptions are not met. Firstly, as adequately explained by the *inhomogeneous diffusion solubility-model*, (120, 121) lipid bilayers are not uniform along the insertion

19

depth. This means that the bilayer presents distinct regions (layers) of characteristic resistance to permeation. Secondly, most lipid bilayers are made of multiple lipid species, which increases the number of permeant-to-lipid species interactions that need to be sampled. Thirdly, permeant molecules (except water and other small solvents) of interest are not small or rigid. The larger the permeant molecule, the more degrees of freedom (DOF) that need to be properly sampled (125). These additional DOFs can be considered as geometric parameters, such as the orientation/rotation of the permeant and chemical parameters such as dihedral angles and formation of internal hydrogen-bonds (117, 124). Insufficient sampling of all of the above can bias the free energy profile. As indicated by Equation 1.3, this yields errors in the estimates of the permeability coefficient.

The sampling problem arises from the permeant *locking* into a particular configuration as a result of its interactions with lipids, partly because the dynamics of lipids are slower than the dynamics in an aqueous solution. Furthermore, the slower dynamics of lipid bilayers in the gel state (e.g., the SC) add to the challenge of sufficient sampling because all events will occur at a slower rate than phospholipid bilayers in the fluid state.

The newly developed selective replica exchange with solute tempering (REST3) method is a convenient method to enhance sampling of configurational space of the permeant when coupled to the US approach. The derivation of the method is described in the manuscript titled *Selective replica-exchange with solute tempering (REST3) for the prediction of the interactions of small molecules with lipid bilayers*. I am the second author of said work and my contribution is the validation of the method with the estimation of permeability of the Ala-Trp dipeptide across a SC model bilayer. This will be explained in detail in Chapter 3 of this thesis. Briefly, the REST3 approach enhances sampling by selectively modifying (*tempering*) the non-bonded interactions of the permeant molecule with its environment, such that it can be "*released*" from those configurations (in which it was "*locked*") and visit other possible configurations faster (Figure 1.5.2).

Figure 1.5.2. Schematic of US-REST3. Several US windows cover the coordinate of the insertion depth (orange box). For each of these windows, a replica exchange scheme is applied whereby the non-bonded interactions between the permeant and the rest of the simulation system are progressively downscaled (blue box).
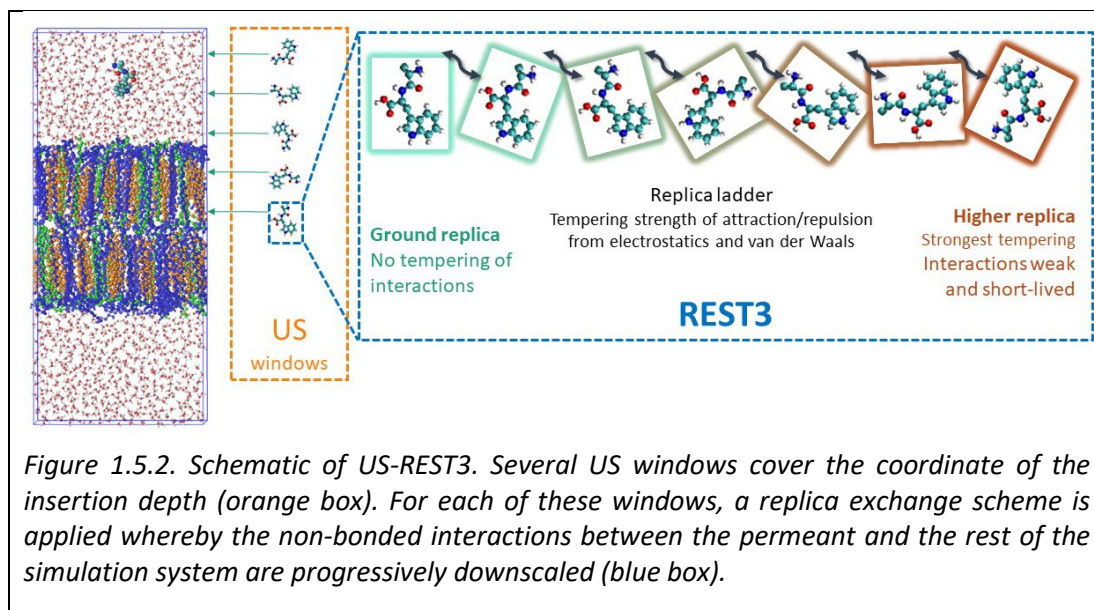
In practice, several copies of the system (replicas) are run in parallel at different tempering factors (as a ladder), while exchange of structures is periodically attempted between neighbouring replicas following the exchange rules of the original REST method. Thus, configurations found in the *strongly tempered* replicas can migrate to the un-tempered simulation (the so-called ground replica), where they would be rarely observed otherwise (126, 127). Because this enhanced sampling method is based on US, the WHAM method can be used to compute the free energy changes ($\Delta G(z)$), which is a requirement for the calculation of the permeability coefficient (91) as indicated in Equation 1.3.

1.6 Synopsis of the thesis.

This thesis presents an investigation of the interactions of the lipid barrier of the outer layer of the skin with small active compounds including peptides, peptide-like molecules, and their Laa-conjugated derivatives using molecular dynamics (MD) simulations. Understanding of said interactions and the prediction of permeability estimates of these small molecules across the skin barrier is important for rational drug design for transdermal drug delivery applications. One of the main challenges in the simulation of small molecule-membrane interactions (SMMI) is related to the sufficient sampling of relevant states of a process that occurs at longer the timescales than the simulations. This is an issue because sufficient sampling is a requisite of reliable free energy estimates. In this work, these challenges are addressed by studying the interactions of a selected group of bioactive molecules with an established molecular model of the ICLM-SC using a novel enhanced sampling approach based on conventional umbrella sampling (US).

Chapter 2 contains a review of the literature, which begins with a brief section introducing pre-requisite concepts about the structural and thermodynamic properties of lipid bilayers. The following section presents a discussion about the challenges in the characterization of the supramolecular arrangement of the ICLM-SC. The discussion begins with the distinctive structural characteristics that have been revealed from a range of experiments and ends by presenting the models that have been proposed to explain said structural characteristics. The third section of the chapter provides a discussion of selected MD simulation studies of permeation of small molecules across lipid bilayers. The discussion is guided by the mechanistic insights gained from MD simulation studies using enhanced sampling methods. The end of the section details selected MD simulation studies of the permeation of small molecules across the different models of ICLM-SC bilayers.

Chapter 3 presents the validation of the enhanced sampling approach which is latter used for the simulation of permeation of small molecules across the ICLM-SC model bilayer. The enhanced sampling approach combines US and REST3 to improve sampling of the configurations of the small permeant molecule at all depths sampled with US. The test case chosen to conduct this test was the Ala-Trp dipeptide. The choice was guided by the availability of experimental values of permeability and free energy of binding to model lipid bilayers featuring a similar composition to the MD model chosen for this work. This enabled direct comparison of the predicted permeability value obtained from US-REST3 against experimental observations. The chapter also describes the generation of starting configurations for US, the assessment of convergence based on free energy profiles, the optimization of replica ladders for different sections of the simulation system and the calculation of diffusion coefficients.

Chapters 4 and 5 contain a two-part investigation of the effects of Laa conjugation of short peptides on their ability to interact with and permeate across the SC. In Chapter 4, the focus is on identifying the optimal lipid-tail length of the Laa that maximises permeability across the skin. For this aim, the interaction of nine small molecules with a SC model bilayer was simulated using the US-REST3 enhanced sampling approach. These small molecules are divided into three groups that are analysed independently: the parent molecule and two lipid-conjugated versions of the parent molecule with lipid lengths of either 4 carbons (C4Laa) or 8 carbons (C8Laa). The three parent molecules are 5-aminolevulinic acid (5-ALA), Val-Trp dipeptide (Dipeptide 2) and Pro-Leu-Gly tripeptide (Melanostatin). The choice of these three parent molecules was made in consideration of their skin activity, the availability of experimental permeability data and their small MW. Results are discussed using the predicted free energy and diffusivity profiles, and the predicted permeability coefficients.

In Chapter 5, the focus is on characterising the distinct permeability of lipid-conjugated peptides according to the stereochemistry of the chiral centre in the Laa moiety. The basic concepts in chirality and stereo selectivity of biomolecular interactions are presented in the introduction of the chapter. This is followed by a discussion of research describing stereoselectivity in the interaction of small molecules with lipid bilayers, including the lipid bilayers of the ICLM-SC. This section summarizes key findings and outlines the gap in the understanding and prediction of stereoselective interactions with lipid bilayers. The aim of the chapter is to address the distinct interaction of the two diastereoisomers of the (C8Laa) lipid-conjugated Ala-Ala-Pro-Val tetra peptide (AAPV) with a SC model bilayer. The simulations were conducted and analysed in the same manner as described in the previous chapter. Four properties are presented and analysed: the free energy profile, the diffusivity profile, the permeability coefficients, and the hydrogen-bonding interactions. The difference in the predicted transdermal permeation between the two diastereoisomers is discussed.

Lastly, Chapter 6 summarizes key findings of this research and outlines future avenues of research in the field of estimation of permeability coefficients using MD simulations of biomolecules.

2 Literature Review

Lipid bilayers constitute the semi-permeable membranes present in all living organisms. The most common lipid bilayers are plasma membranes, which protect the cell from the external environment. These are made of glycerol-phospholipids, sphingolipids, and sterols, varying in proportion depending on the type of cell. It is thus not surprising that most MD simulation studies in the field of small molecules interacting with biological membranes (SMMI) feature glycerol-phospholipid bilayers. Nonetheless, there is active research of lipid bilayers of the ICLM-SC. Detailed understanding of the interplay between the composition, structure, and function of the ILCM-SC will better inform of i) the aetiology of skin conditions, and ii) of ways to enhance drug delivery into or across the skin.

This chapter introduces pre-requisite concepts related to the characterization of lipid bilayers. The main body of the literature review is divided into two sections. The first section discusses experimental works contributing to the resolution of the structural arrangement of the lipid bilayers in the ICLM-SC. The second section presents MD simulation as an ideal tool to elucidate the molecular mechanisms of SMMI occurring in the ICLM-SC.

2.1 Concepts in the study of lipid bilayers.

Lipids are amphiphilic biomolecules featuring both a hydrophobic and a hydrophilic region. This characteristic confers them the ability to interact with other lipids to spontaneously self-assemble into supramolecular arrangements stabilized by favourable intermolecular interactions. On the one hand, the hydrophobic effect drives the hydrophobic regions into close contact. On the other hand, the hydrophilic regions interact strongly with water (and other polar molecules in the solvent), forming a network of hydrogen-bonds. Lipid bilayers are the most common supramolecular arrangement of lipids in an aqueous environment. In fact, every living organism has at least one type of lipid bilayer to enclose the contents of the cell (the plasma membrane). This remarks two of the main functions of lipid bilayers: i) to provide a physical barrier to compartmentalize cells and cell organelles, and ii) to regulate the transport of substances across the barrier such that cell (or organelle) metabolic processes can occur in a controlled manner (91).

Lipid bilayers are described by a set of many interrelated physicochemical properties. However, there are three common descriptors of lipid bilayers (Figure 2.1.1). Bilayer

thickness is defined as the distance separating head groups across opposite leaflets (i.e. along the normal to the membrane plane). Experimentally, the inter-bilayer distance can be measured by small-angle X-ray scattering (SAXS), as it is related to the lamellar repeat (stacking) distance. The area per lipid (APL) refers to the area that a single lipid molecule covers on the plane of the membrane interface and can be estimated with wide-angle X-ray scattering (WAXS), as it is related to the lateral arrangement of the lipids, i.e. the packing of lipids in a lattice (i.e. the volume per lipid) and their rotational freedom. The order of the lipid tails refers to the collective alignment of the hydrocarbon tails to an axis of reference (normal to the membrane plane). It is measured by the order parameter (S_{CH}), which is defined as the orientation of the C–H bond vector with respect to the bilayer normal and measured for every carbon in the lipid tail with NMR experiments (91).

These three bilayer properties have an interplay such that changes in one drive changes in the others. Similarly, they are linked with many other physical properties, like the mass density profile, the bending modulus, area compressibility, etc. The extent of interrelation of these properties is evidenced in the phase of a bilayer, which is determined by the order of the lipid tails, the fluidity of the bilayer and the mass density profile. The phases of lipid bilayers range from stiffer (and densely packed) to more fluid (and lightly packed). Phases include sub-gel, gel, rippled, liquid ordered, and liquid disordered. Each phase has a characteristic combination of the structural descriptors mentioned above (Figure 2.1.1). In the fluid phase, lipid tails have high mobility and low lipid tail order. In contrast, in the gel phase lipid tail mobility is lower and is accompanied by an increase in lipid tail order (91).

Figure 2.1.1. Schematic of the gel to fluid phase transition and the associated changes in bilayer thickness, area per lipid (APL) and order parameters. Reprinted from Ref. (91). © 2020 Wiley-VCH Verlag GmbH & Co. KGaA, Weinheim
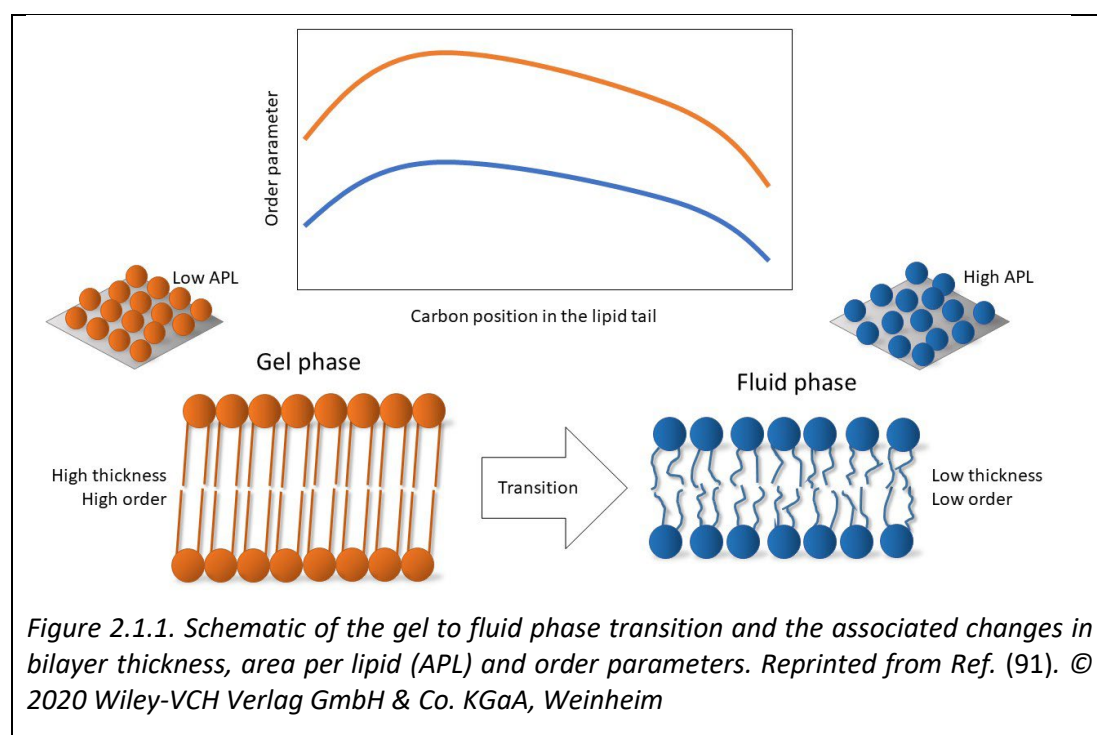
The composition of the membrane in terms of the number of components (lipid species) and their relative abundance (e.g. molar ratio) have effects on the phase of bilayers. Each lipid species features distinct functional groups in the hydrophobic and hydrophilic regions, giving rise to distinct interaction patterns between lipids, and hence changes in bilayer properties. In general, the hydrophobic region features hydrocarbon chains (i.e. so-called lipid tails) ranging in length and degree of unsaturation. An increase in the former results in increased bilayer thickness, whereas an increase in the latter results in a decrease in the order parameter. The hydrophilic region of lipids (commonly known as the head groups) features distinct polar functional groups, ranging in charge and MW (e.g. from glycerol to choline to polysaccharides). The network of hydrogen-bonds across these polar headgroups and their interactions with water determines the ability to bind small molecules and other ligands at the bilayer interface. Thus, the combination of lipid species (in a particular proportion) generates distinct biological membranes that perform specialized functions. For example, a Gram-negative cell wall features an asymmetric lipid bilayer with lipopolysaccharides in the outer leaflet (conferring its rigidity). Eukaryotic cell membranes, composed mainly of phospholipids, behave as fluid mosaics of lipid rafts and transmembrane proteins. In addition, the lipid bilayers of the ICLM-SC, composed mainly of sphingosine-based lipids (instead of phospholipids) feature a dense and dehydrated barrier to exogenous compounds (91).

Lastly, the properties of lipid bilayers will change if subjected to changes in physicochemical conditions of the surrounding environment e.g. pH, temperature, hydration, or concentration of solvents and solutes. A phase transition is indication of a concerted change in bilayer properties, arising from rearrangements in bilayer structure and changes in stability. In Figure 2.1.1, the bilayer in the gel-state features high order of the lipid tails, higher thickness and small APL. After the phase transition, the bilayer features increased APL, reduced thickness and lower order of the lipid tails. Characterizing the temperature at which such transitions occur is common practice in the biophysical study of lipid bilayers. In fact, the transition temperature (T_m) is commonly used to indicate the stability of a lipid bilayer (91). The higher the transition temperature, the more energy it is required to break the intermolecular interactions that confer the current bilayer properties, i.e. the more stable the bilayer. For most cell membranes the bilayer integrity is associated with the fluid phase (liquid ordered or liquid disordered) and thus a phase transition away from this phase is deleterious. In contrast, the integrity of the barrier function of the ICLM-SC is associated with the gel-like state. Hence, changes in bilayer properties towards increased fluidity, increased APL or reduced order parameters are associated with an impaired barrier function.

2.2 The elusive supramolecular structure of the lipid bilayers in the ICLM-SC.

A suitable molecular model of the ICLM-SC must reproduce experimental information about its supramolecular arrangement and its barrier properties. First, it should reproduce the structural features observed in experiments, which have proven difficult to characterize unequivocally. Second, it should reproduce the barrier properties of the skin in terms of TEWL as well as in terms of permeability, retention and stereoselectivity of small molecules. The main components of the ICLM-SC are ceramides (CERs), cholesterol (CHOL) and free fatty acids (FFAs), which were introduced in section 1.2 of the Introduction chapter. In this section, the interplay between the relative abundance of these components, the diversity of functional groups within each lipid class, and the supramolecular structure of the lipid bilayers is discussed.

The gel phase in the ICLM-SC has been extensively described and is a key structural feature that contributes to the barrier function with its slower dynamics compared to the fluid phase (128). Its mass density profile displays two characteristic density regions in the hydrophobic core. The first one is located below the head groups and has high-density and high order of the acyl chains. The second one is the low-density hydrophobic region and has lower density and less ordered acyl chains. This region includes the interdigitating region which is located around the centre plane and is characterized by the interaction of opposing leaflets (129). This section also presents the different molecular models of the ICLM-SC that have been proposed to represent the findings obtained from decades of experimental information.

In the ICLM-SC, the vertical dimension corresponds to the stacking axis of lamellae and features two well-described phases according to the periodicity of density peaks in X-ray diffraction studies: the short periodicity phase (SPP) and the long periodicity phase (LPP) (10). It appears that both contribute towards the integrity of the barrier function; however, the LPP has proven harder to reproduce experimentally and appears to contribute more to the barrier function of the skin (28). Hexagonal and orthorhombic lateral packing are found in the ICLM-SC, and some studies suggest that they might co-exist. Figure 2.2.1 summarizes the vertical and lateral supramolecular arrangements that have been found in the ICLM-SC through X-ray diffraction studies. In view of this variety of arrangements, there is debate over the molecular model that can best explain these properties.

Studies investigating the composition and lateral/lamellar arrangements of the ICLM-SC have been conducted with different samples, such as human or pig skin *ex vivo*, human skin *in vivo*, reconstituted model membranes using lipids extracted from

human or pig skin, and model membranes made of synthetic lipids. These studies are often complicated to extrapolate to the properties of the skin because of the different combinations of lipid diversity and molar ratio used in the mixtures, which affects the structural characteristics revealed by each type of sample (128). For example, observations obtained with a lipid mixture that only produces a SPP with a hexagonal lateral phase will not correspond to the characteristics of the ICLM-SC. This is of particular relevance in the case of phase transitions of model lipid bilayers due to their thermal memory (130).

Figure 2.2.1. The supramolecular arrangement in the vertical (lamellar) and lateral dimension of the ICLM-SC. Reprinted from Ref. (83). International Public License (CC-BY 4.0).
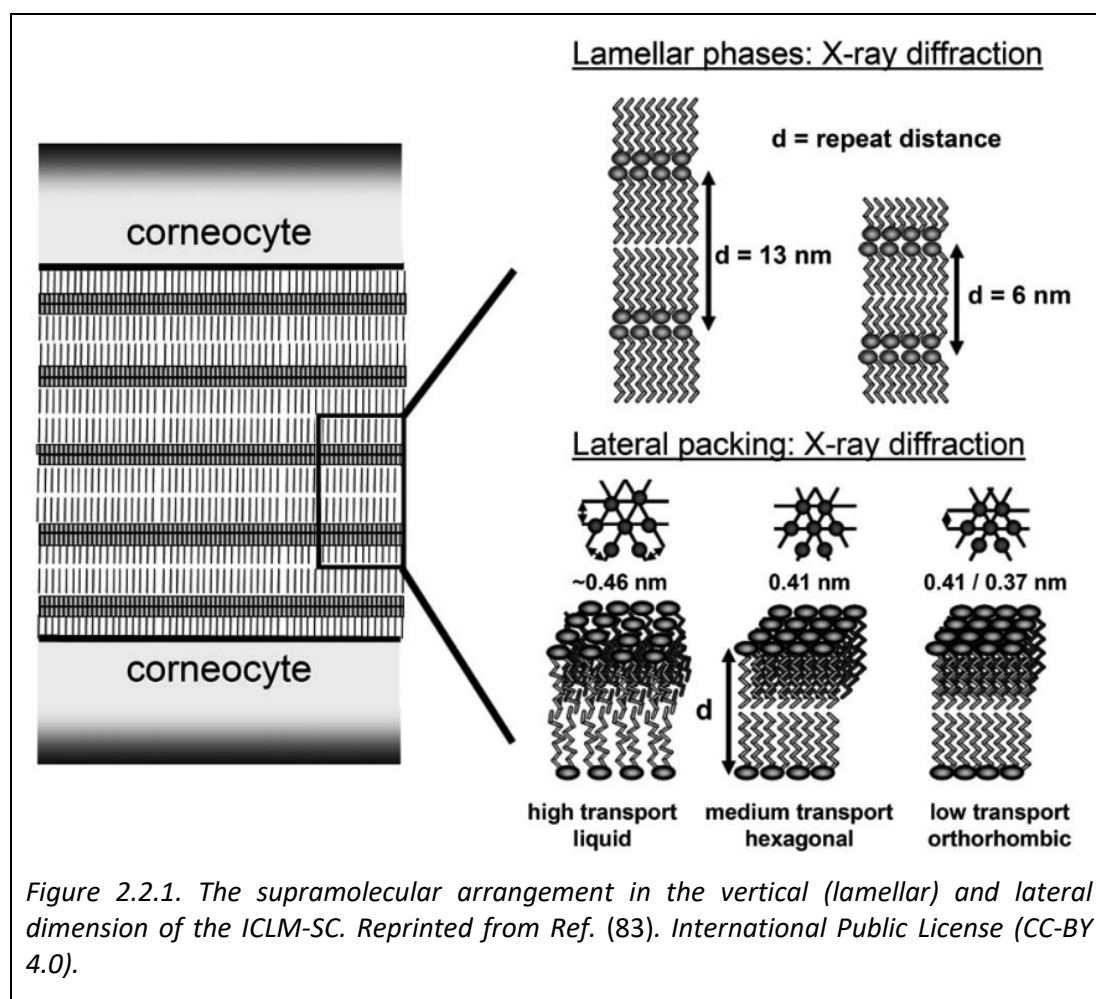
Using SAXS on human abdomen skin, Bouwstra et al. reported the characteristic short and long periodicity phases (SPP and LPP) as given by repeat distances of 13.4 and 6.4nm, respectively (131). A schematic diagram of the repeat distance of the unit cell that is measured in SAXS experiments is provided in Figure 2.2.2. In addition, by testing a range of rehydration conditions, they showed that increased water content produced only the SPP, indicating that higher hydration affects the structural arrangement of the ICLM-SC. They also concluded that water is a very potent penetration enhancer. Furthermore, two thermal transitions were associated with reversible phase transitions at 37° and 70°C. The nature of these transitions was

hypothesised to be caused by the melting of the lipid tails, changes in lamellar structure or changes in lateral packing (orthorhombic to hexagonal). Ultimately at 75°C both SPP and LPP disappear. These findings highlight the structural stability of the ICLM of the SC, which starts to show structural alterations above 60% water content (by weight) and above 67°C (131).

Figure 2.2.2. Representation of a unit cell (left) and the lamellar structure with repeat distance 'd', which can be retrieved from SAXS experiments. Adapted from Ref. (131).
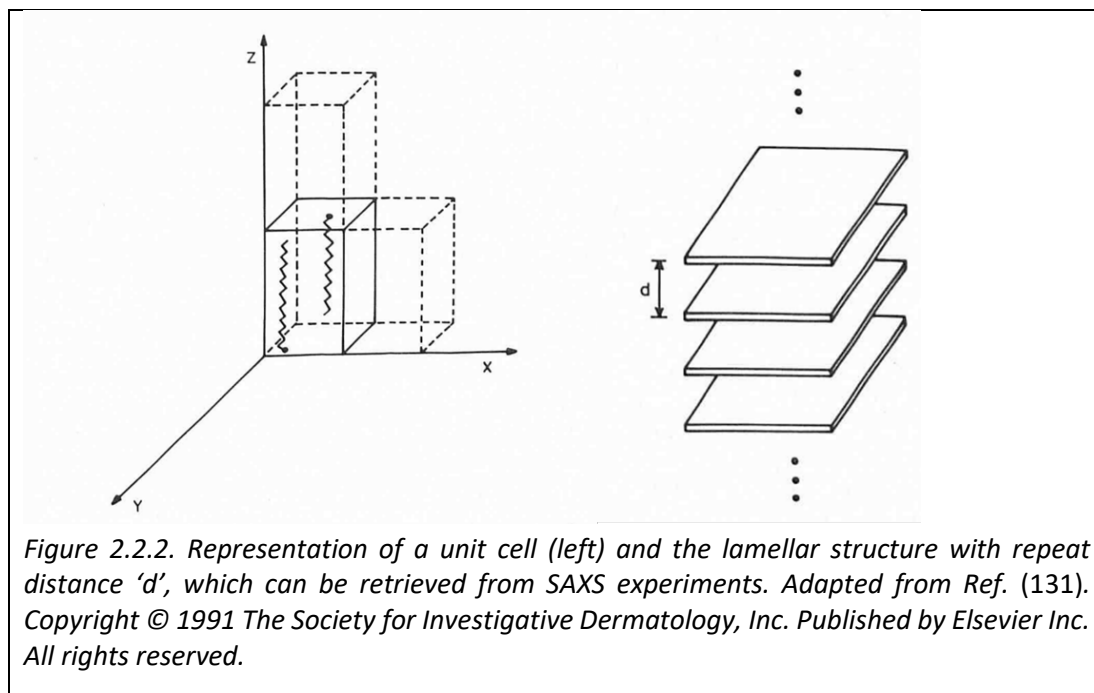
Abraham and Downing (30) tried to recreate the SPP and LPP using model membranes. The dynamics of the model membranes was probed using NMR spectroscopy and their structure was studied using electron microscopy (EM). They used a mixture of CER species purified from pig SC, deuterated cholesterol sulphate, and palmitic acid (C16:0). One of the molar ratios investigated resembles the 2:2:1 molar ratio, containing 30 mol% of CER, 38% CHOL, 19% palmitic acid and 5% cholesterol sulphate, and it "was taken as a close approximation to the *in-situ* lipid composition of SC". In that work, CER species were purified using thin layer chromatography, and since some are difficult to resolve because they elute at the same time, it is possible that CER subclass diversity may have been underestimated. Nonetheless, all mixtures containing CERs were in the rigid gel phase with increased CHOL content increasing fluidity. The phase transition from orthorhombic to hexagonal was observed above 60°C. This is close to the transition temperature of 67°C reported for human abdomen skin by Bouwstra et al. (131), considering that the former was measured for model bilayers with reduced complexity and the latter was measured for *ex vivo* tissue. However, their findings were predominantly associated with the SPP because only a weak LPP was observed. The LPP resembled the pattern observed with human SC at 80°C, i.e. after two thermal transitions. The weak

presence of the LPP could be attributed to the lack of fully native CER diversity and the preparation of the samples, as the sharp peaks for the head groups were observed only when the model membranes were kept above their gel-liquid crystalline transition temperature and then cooled down.

A subsequent study by Bouwstra et al. (82) using SAXS and WAXS compared the barrier function of reconstructed epidermis (*in vitro* cell culture of adult human keratinocytes) with that of native skin. The former exhibited less abundant lamella than native skin, with the presence of crystalline anhydrous CHOL indicating phase separation of CHOL. Finally, for lateral organization, orthorhombic packing was observed to disappear between 30° and 45°C, whereas for lamellar organization disordering occurred between 25° and 45°C. The phase transitions were observed at lower temperatures, indicating an unstable structural arrangement compared to native skin.

The SC has a pH gradient going from pH 7.0 at the interface with the stratum granulosum (layer beneath SC) to pH 5-6 at the surface. Given the ionizable carboxyl groups of FFA, changes in local pH could affect the properties of the lipid bilayers. Considering this, a study by Bouwstra et al. investigated the changes in structural arrangement of the ICLM-SC observed upon changes in pH and molar ratio of its components (31). Model bilayers were built using six CER subclasses (purified from pig skin), a FFA mixture (containing C16 to C26), and CHOL (with or without cholesterol sulphate). The resulting three mixtures were: i) a binary CHOL:CER equimolar mixture; ii) a ternary CER:CHOL:FFA equimolar mixture; iii) a quaternary mixture containing cholesterol sulphate (10 % mol) with an overall molar ratio of 1:1:1:0.3. The three types of mixtures showed lamellar arrangement displaying the SPP and LPP at both pH tested (5 and 7.4). However, the intensity of the SPP and LPP peaks, the presence of phase-separated cholesterol, and the lateral arrangement showed differences across all mixtures. The binary equimolar mixture exhibited only the hexagonal phase at both pH, being an indication of the role of FFAs in stabilizing the orthogonal lateral packing. The ternary mixture exhibited phase-separated cholesterol, alterations to the lamellar arrangement and coexisting hexagonal and orthorhombic phases, being an indication of the role of the molar ratio in reproducing the lamellar organization. Finally, the mixture containing cholesterol sulphate induced the fluid phase without crystalline CHOL, indicating the role of cholesterol sulphate in destabilizing the hexagonal lateral arrangement and subsequently fluidizing the mixture. Although minor, some differences were observed between pH 6 and 7.4 for the ternary and quaternary mixtures: both exhibited less pronounced SPP peaks at higher pH, being an indication of less defined structure. The apparent pK_a of FFAs in the SC lipid mixtures is 6.0, which means that at pH 7.4 a large fraction is ionized. The authors rationalized these differences in terms of the ionization of the FFAs and how it affects their ability to participate in the hydrogen-bonding network

31

that governs the barrier properties of bilayers containing CERs (16). A subsequent study investigated the effects of pH and temperature (36) on the SC bilayers, using CERs extracted from human skin and differential scanning calorimetry (DSC), fluorescence spectroscopy and confocal microscopy. At skin physiological temperatures (28°C– 32°C), with a radial resolution limit of 300 nm, a single gel phase at pH 7, coexistence of different gel phases between pH 5 and 6, and no fluid phase at any pH were observed. This suggests that the pH gradient in the SC may control the physical properties of the ICLM, regulating membrane lateral structure and stability, with the possibility of coexistence of structural arrangements along said gradient.

Murine, pig, and human skin have similar trans-epidermal water loss (TEWL), a measure that relates to the integrity of the barrier function of the skin (132). However, murine SC features only the LPP and is thinner than its pig or human counterparts. This suggests that LPP alone can perform the barrier function of the skin (31). CER1 or CER EOS (the omega-esterified linoleic acid on the fatty acid tail) is required for the formation of a LPP in i*n vitro* studies using model bilayers built from ternary mixtures with molar ratios of 2:2:1 and 1:1:1 (CER:CHOL:FFA) (133). Figure 2.2.3. shows two molecular models indicating that the presence of CER EOS promotes the formation of the LPP (29). *In vivo* studies using pig and human skin also confirmed the important role of CER1 in the formation of LPP and reported the contribution of CER EOH (6-hydroxy 4-sphingenine with omega esterified linoleic acid on the fatty acid tail) (20).

Figure 2.2.3. The role of CER1 in the formation of LPP. Electron density of the SPP (left) and LPP (right) with their corresponding suggested molecular arrangements. Adapted from Ref. (29). *Copyright © 1969, Elsevier (CC-BY)*
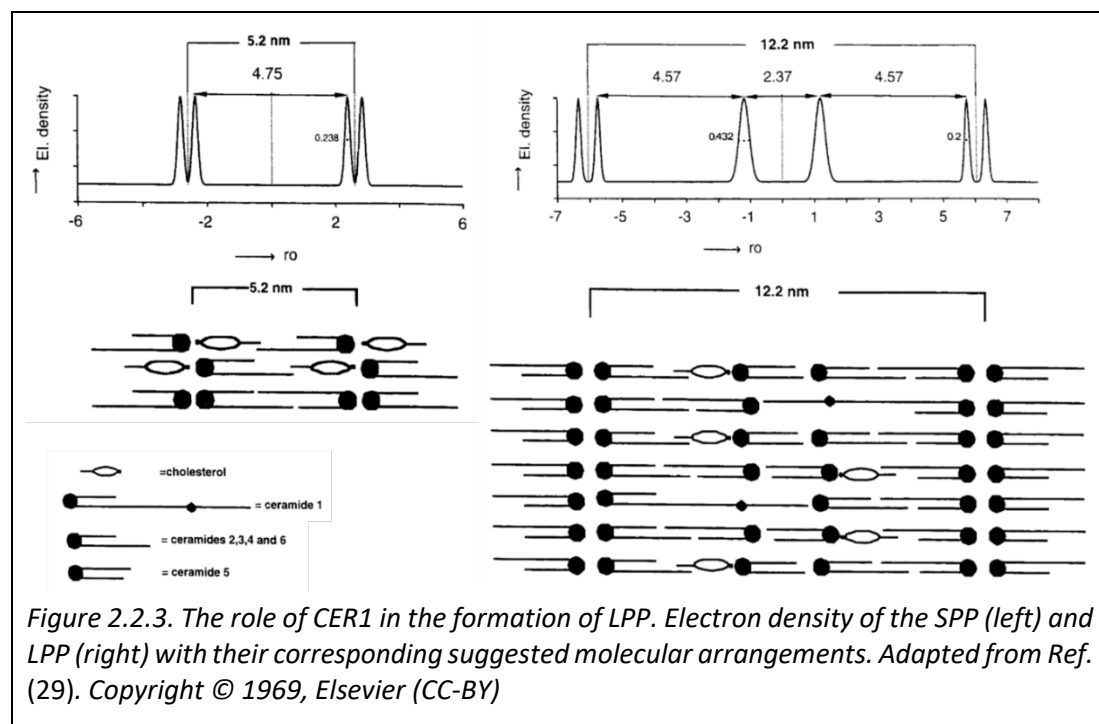
The ability of CERs to be in a hairpin or a splayed conformation is at the centre of the debate around supramolecular structure. The hairpin conformation is energetically favourable considering the V shape of the crystallized form (29), and it is the native conformation of the precursors of ceramides: "glucosylceramides and sphingomyelins, would most likely prefer the hairpin conformation due to their large and hydrophilic polar head groups. Thus, the hydrolysis of these precursors would release CERs in the hairpin conformation" (134). These precursors are found inside keratinocytes forming unilamellar liposomes that are later extruded to the ICLM (135). The splayed conformation has been suggested to appear naturally during the formation of the ICLM-SC (135). Ceramides could undergo a conformational transition from hairpin to splayed conformation during the formation of the ICLM-SC, which could promote the acyls chains of sphingosine and fatty acid moieties to be in separate lamella. This transition was first suggested by Downing and collaborators (136).

Aside from the preferred conformation of CERs, other aspects that differentiate the models of the ICLM-SC are the coexistence of the SPP/ LPP phases and the lateral packing arrangements. The fact that the ICLM has gradients of hydration, pH and composition suggests that along the depth of the SC there might be regions (depths) at which one of the models would be more realistic the others.

2.2.1 The domain mosaic model

The domain mosaic model explains the coexistence of phases in the lateral dimension as separate phases forming domains (like rafts). This model was proposed by Forslind in 1994 and was inspired by concepts from materials science, with the aim of explaining the mechanical features of the skin and its barrier function. The model suggests that the lateral dimension of the lamella is inhomogeneous with irregular boundaries between domains. The boundaries are composed of short chain lipids (C<20) which tend to be in the fluid phase, and the bulk of the ICLM corresponds to domains composed of the more abundant long chain lipids which tend to be in the gel-like state (137) (Figure 2.2.4, top). Garidel et al. presented evidence to support the domain mosaic model as the microstructure that explains the properties of the ICLM-SC (138). Their model systems (equimolar ternary lipid mixtures) showed coexistence of hexagonal and orthorhombic lateral packing as well as coexistence of gel-like domains and liquid crystalline domains. The proposed microstructure is shown in Figure 2.2.4 (bottom) and features liquid-crystalline boundaries that separate grains of gel-like domains. The authors propose this is likely to appear predominantly in the outer half of the SC due to the desquamation process. Other evidence supporting the domain mosaic model was related to reports of lipid mixtures with components of the ICLM in which cholesterol undergoes phase

separation, and whereby cholesterol leaves the mixture and forms domains of pure cholesterol (31, 82).
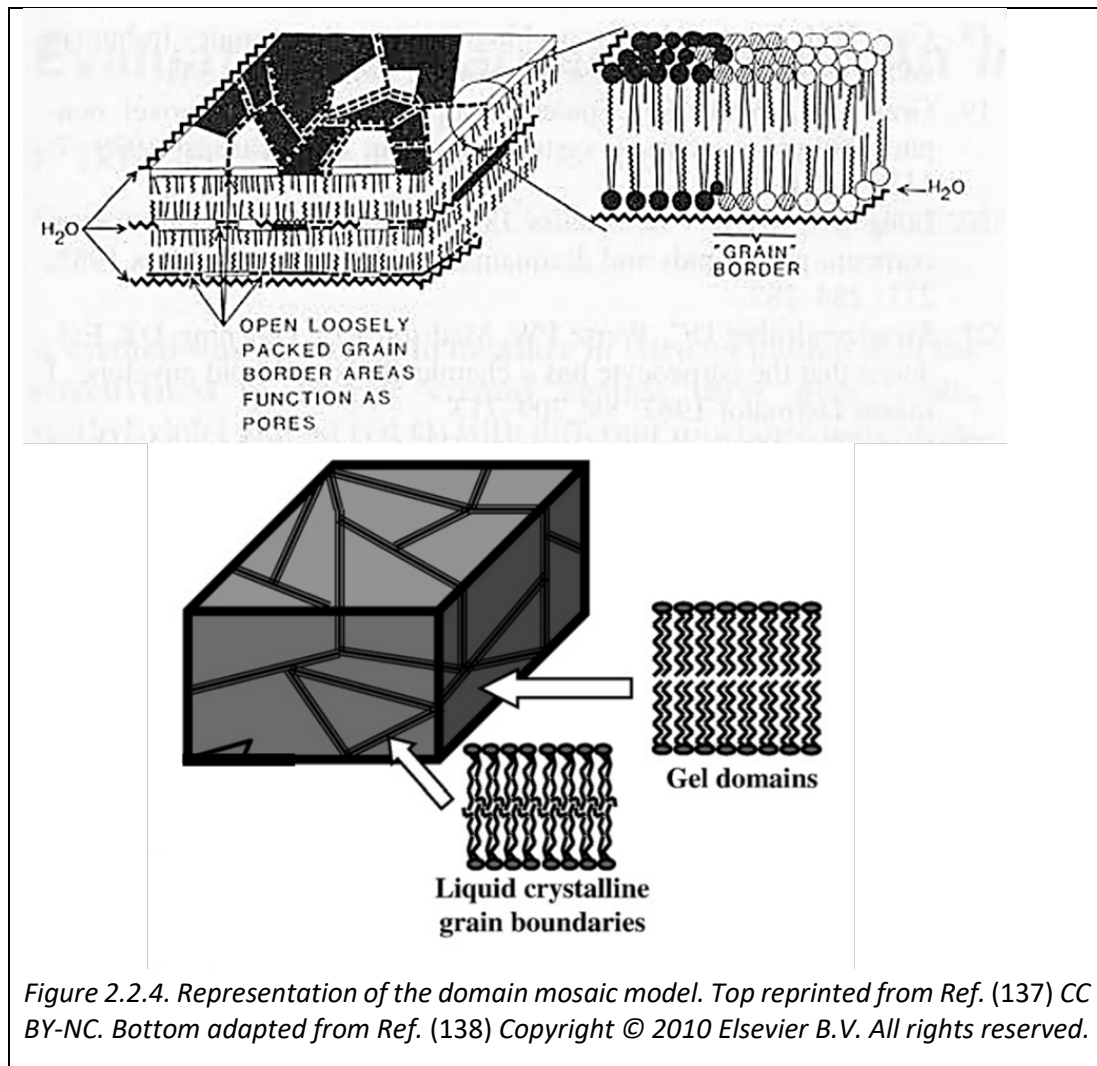
Figure 2.2.4. Representation of the domain mosaic model. Top reprinted from Ref. (137) *CC BY-NC. Bottom adapted from Ref.* (138) *Copyright © 2010 Elsevier B.V. All rights reserved.*

2.2.2 The single phase model

The single-phase model assumes homogeneity along the lateral dimension and relies on the miscibility of each lipid in the mixture, which seems to be change as a function of the ratio of its components. The rationale for the single gel phase model is that "from a functional point of view, the stratum corneum intercellular lipid matrix should be as homogeneous as possible, that is without abrupt phase transitions and with little phase separation. This can be achieved only by heterogeneous lipid compositions which broaden phase transition zones, stabilize gel phases and ensure the lamellae remain intact (no pores of other structures formed)" (139). The stability of the gel phase increases with the length of the acyl chains (above 20 carbons), heterogeneity in chain length distribution (also known as polydispersity), and high relative amounts of cholesterol, rendering the gel phase less viscous (more plastic).

This gives rise to the close packing of hydrocarbon chains with rotational disorder in the lateral arrangement, which causes the plasticity that translates into the mechanical resistance of the skin (139).

Figure 2.2.5. The SPP (5.36nm repeat distance) and its characteristic interdigitation region can be achieved with CERs in the splayed (top) or hairpin conformation. Adapted from Ref. (140). Copyright © 2011 Biophysical Society. Published by Elsevier Inc. All rights reserved.
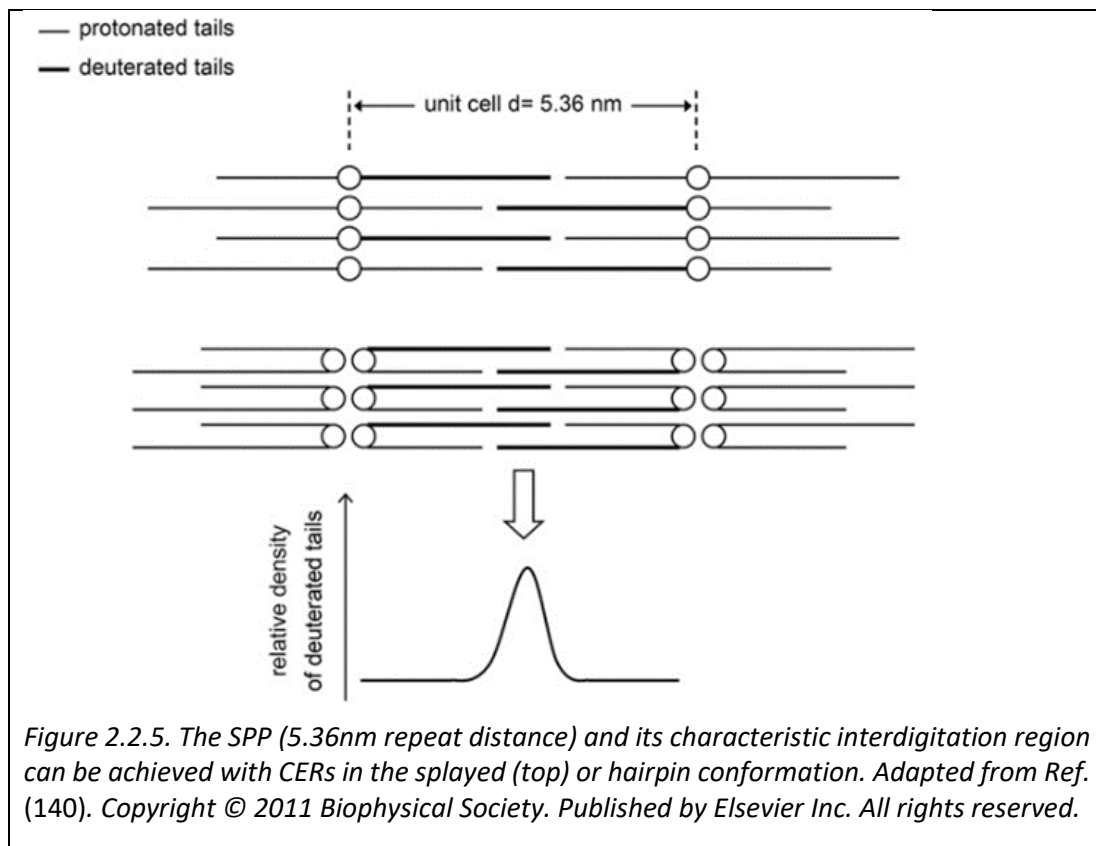
Two key players of the single gel phase model are the conformations of ceramides and the content of water. The coexistence of hairpin and splayed conformations is plausible in the single gel phase model of SC. In addition, a more recent study using neutron diffraction (140) observed that interdigitation of CER lipid tails in a symmetric SPP unit cell (bottom) is possible with both fully splayed (top) and hairpin (middle) conformations of ceramides (Figure 2.2.5).

2.2.3 The sandwich model

This model was proposed to explain the requirement of CER EOS (formerly known as CER1) in the formation of the LPP with its characteristic 'broad-narrow-broad' sequence of electron density regions, along with presence of a liquid phase. Instead of addressing the lateral dimension, this model explains the coexistence of phases in the stacking axis of the lamellae. It consists of a narrow lipid layer in the fluid phase and two broad layers with a crystalline structure on each side. These three layers are held together by the cohesive action of the extra-long lipid tails of the omega esterified CER, which protrude from the thick outer layers into the thinner central

layer (141), as can be observed in Figure 2.2.6. Results from neutron diffraction studies of equimolar ternary mixtures support this three-layer arrangement (142).

Figure 2.2.6. Schematic of the sandwich model. Reprinted from Ref (141). *Copyright ©*
2002, Kluwer Academic Publishers.
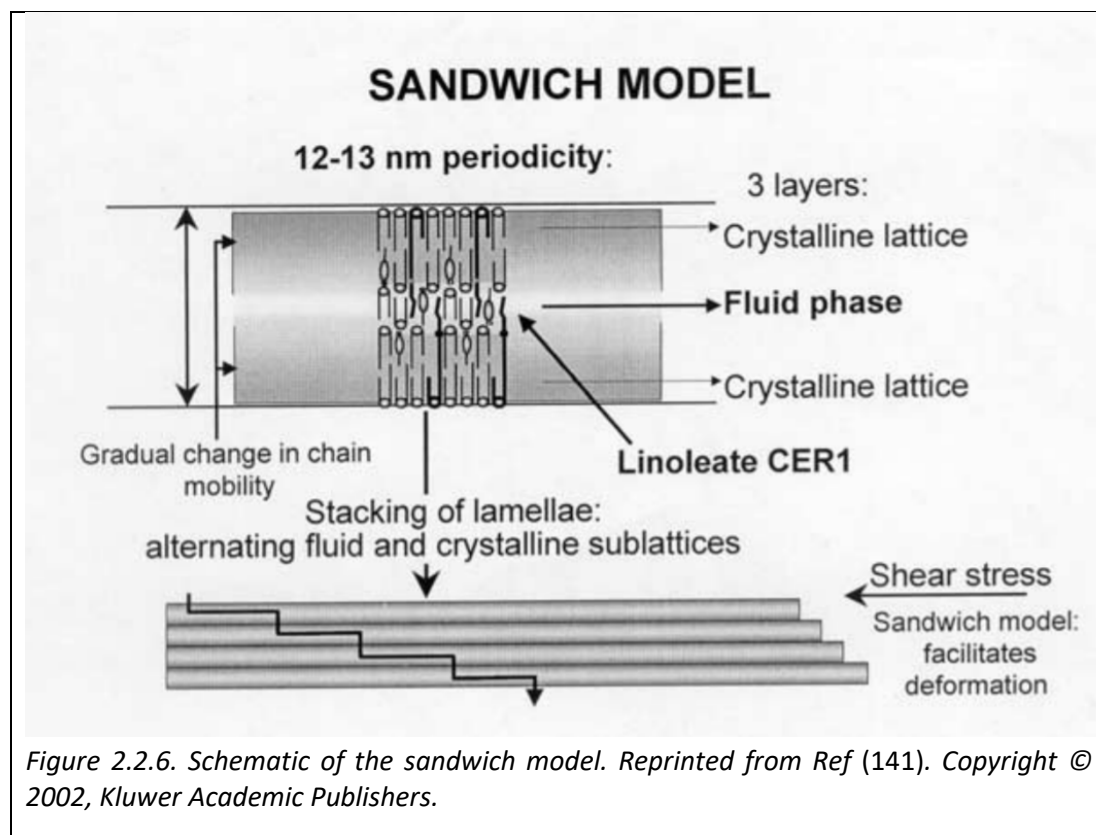
2.2.4 The splayed CER model

In 2012, Norlen and collaborators presented evidence in support of a splayed-chain conformation of ceramides in the ICLM-SC. This was based on cryoelectron microscopy of the vitreous section (CEMOVIS) of human skin and the pattern of intensity of the bands observed between corneocytes. In this model, cholesterol is primarily associated (segregated) to interact with the short tail of CER (the sphingosine moiety). This novel arrangement "rationalizes the skin's low permeability toward water and toward hydrophilic and lipophilic substances, as well as the skin barrier's robustness toward hydration and dehydration, environmental temperature and pressure changes, stretching, compression, bending, and shearing" (143).

In this model a rather unconventional repeating unit can be observed, where each of the two leaflets forming the bilayer has two sections according to the splayed CER: one closer to the centre with the short tail of CER (sphingosine moiety) and cholesterol, and the outer section with FFA and the acyl moiety of CER (longer tail). Interdigitation of lipid tails occurs not only between leaflets but also across bilayers, since they face each other with lipid tails and not with head groups, as conventionally considered.

36

Figure 2.2.7. Atomic model of a repeating unit (d) that matches the average density of the CEMOVIS micrograph (a). Adapted from Ref. (143). Copyright © 2012 The Society for Investigative Dermatology, Inc.
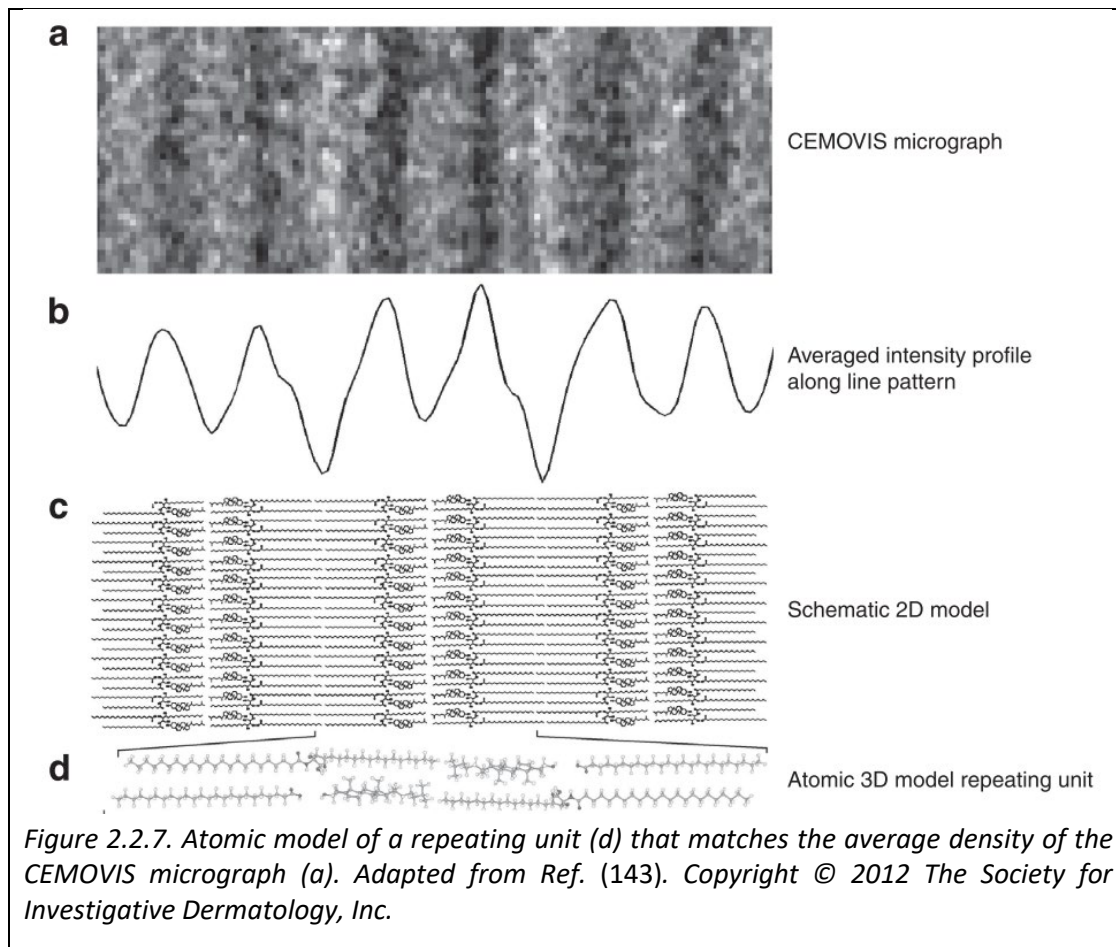
A subsequent study supports the segregation of FFA with the acyl chain of CER when CERs chains are splayed. Evidence that CerNS24 prefers an extended (splayed chain) conformation in which the fatty acid is associated with the very long CER chain explains the SPP of SC. Vavrova and collaborators revealed the effect of the lipid tail asymmetry of the CER chains (sphingosine or acyl tails) on the structural arrangement of lipid bilayers in relation to their conformation (134). Using deuterated CERs and Fourier-transform infrared spectroscopy (FITR), differences in lipid mixing, packing, and thermotropic phase behaviour of (lipid mixtures of) SC model bilayers featuring either symmetric (C16 acyl) or asymmetric (C24 acyl) CERs were observed. These differences were observed regardless of the diversity of the FFAs and CHOL fractions, and in a wide range of hydration levels (5-95% relative humidity), indicating that this is an intrinsic behaviour of CERs. In contrast, under the same conditions, the symmetric CER shorter (acyl CerNS16) do not mix well with FFAs and appears mostly phase separated. These findings indicate that CerNS16 prefers the hairpin conformation, which would favour its miscibility with CHOL (due to the same cross section area). "This conformation could also explain the observed higher sensitivity of CerNS16 than of CerNS24 membranes to hydration" (134).

37

2.3 MD simulation models of the ICLM-SC.

As mentioned above, ceramides show significant conformational flexibility. In a simulation of a pure CER bilayer, Notman et al. showed that CER NS 24:0 molecules (formerly known as ceramide 2) can adopt many conformations, some of which involve one of the lipid tails lying flat across the bilayer interface (144) as can be seen in Figure 2.3.1. Given the models of the supramolecular structure of the ICLM-SC that were described above, it is not surprising to observe a number of MD simulation models that arose in response. The differences between these models can be categorized into: the number of lipid classes that they include, the size of the simulation cell, the level of detail in the representation chosen for the molecules (all atom, united atom and coarse grained ffs), the conformation of ceramides, and the number of lipid bilayers that are addressed explicitly. This section summarizes the works that presented each model with a focus on their components and the properties that they reproduce.
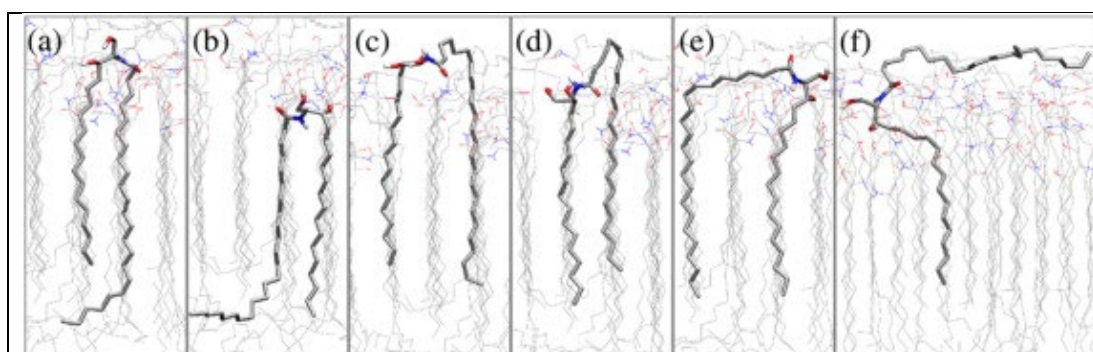
Figure 2.3.1. Six conformations of CER NS 24:0) as observed in MD simulations. Reprinted from Ref. (144). Copyright © 2007 The Biophysical Society. Published by Elsevier Inc. All rights reserved.

2.3.1 Single bilayer in hairpin conformation of CER

A number of studies have reported the development and validation of CER parameters in response to the lack of parameters for CERs in the traditional lipid ff descriptions (144–149). The scarcity of experimental characterization of the properties of pure CER bilayers, combined with early lipid profiling reports of the high content of CER NS in the ICLM-SC, are likely two reasons to explain the majority of early MD simulation works concentrating on the CER NS 16:0 and CER NS 18:0. The structural similarity between these CERs and sphingomyelin also suggested the CERs to be predominantly in the hairpin conformation.

A benchmark of a pure ceramide bilayer in full hydration was presented in 2006 by Pandit and Scott (145). To obtain GROMOS-compatible force field parameters for the CER NS (16:0) they considered 15 random conformations of the polar region of the molecule and calculated average charges using the quantum chemistry software GAUSSIAN. Their simulations were conducted in the liquid-crystalline phase by keeping the system above the main phase transition of CER NS (16:0) ≈93°C. They reported an APL of 55.1 ± 0.7 Å^2 and an increased intermolecular hydrogen-bonding capability when compared to sphingomyelin 18:0 (145). Although this CER is not the most abundant in the ICLM-SC, and the simulation was conducted away from physiological conditions (phase and temperature), this work presented the characteristic profiles of the tail order parameters and density of pure CER bilayers. Later, the parameters of CER NS and NP were presented in the AA CHARMM ff with refinements to reproduce their respective phase transitions (146). For the amide group of CERs the authors used the parameters from the peptide bond of the corresponding protein force field, and for the partial charges of the remaining explicit atoms in the polar headgroup they used *ab initio* quantum chemical calculations. Their simulated heating/cooling scans were also conducted at full hydration. The updated parameters for CER NS (16:0) proved to maintain structural agreement with experiment but were more accurate in reproducing the thermotropic phase transition, compared to the GROMOS-compatible ff, which were reported at 14°C and 54°C above experimental values, respectively (146).

The simulations of a pure CER NS 24:0 bilayer mentioned above (Figure 2.3.1) were conducted using the UA GROMOS-compatible ff. The parameters for the CER molecule were obtained from a structurally related sphingomyelin and the partial charges of the headgroup were taken from serine. Compared to CER NS 16:0, CER NS 24:0 features asymmetry in the length of its lipid tails. In the physiologically relevant gel phase, this confers a characteristic lateral arrangement in the centre of the bilayer that resembles the liquid-crystalline phase (instead of the dense packing associated with the gel-phase). Simulations were able to reproduce the hexagonal lateral arrangement observed in the gel-phase at temperatures below the phase transition (80 to 90°C), but not the orthorhombic lateral arrangement. The tilt angle of the lipid tails was reported at ≈17°, the APL was 0.374 nm^2, and the mass density and order parameters profiles indicated a dense and ordered region below the headgroups and a less-dense and less-ordered region closer to the midplane (144).

The APL, order parameters, tilt angle and bilayer thickness were recently reported for pure lipid bilayers composed of six other abundant CER subclasses, including CER NP (non-hydroxyl acyl chain with phytosphingosine moiety) the most abundant ceramide subclass (147) (see Figure 1.2.2). These simulations were conducted at 310 K (37°C), i.e. 5 degrees above the temperature of human skin. CER NP (24:0) yielded the lower APL (≈0.38 nm^2) and the largest bilayer thickness (≈5.1 nm) compared to

CER bilayers composed of the other CER subclasses (NDS, AP, AS, NH, and AH), whilst displaying comparable high order parameters (S ≈ 0.9) for both the lipid tail of the phytosphingosine moiety and the acyl chain. The tilt angle was reported separately for the two lipid tails of CERs, and CER NP was characterized by the lower tilt angles of ≈7.5° and ≈12.5° for the sphingosine chain and the acyl chain, respectively (147).

A coarse grain (CG) ff of CER NS 24:0 was presented in 2015 which reproduced experimental data on the phase transition (148). Parameters for the hydrocarbon beads were adopted from the standard Martini force field, whilst the parameters for headgroup beads were optimized to reproduce structural properties (APL, bilayer thickness, etc) of atomistic simulations. Noteworthy, these atomistic simulations were conducted using GROMOS-compatible (united atom) parameters which were derived independently from the simulations mentioned above. These atomistic simulations were conducted at low temperature (below T_m) and reported a tilt angle of lipid tails of 22°, bilayer thickness of 4.9 nm and APL of 0.46 nm^2. This APL is an overestimation when compared to prior experimental and simulation reports for the gel phase of CER NS 24:0. The resulting CG CER parameters performed well above T_m and reproduced the bilayer thickness in the gel phase, but were unable to reproduce the tilt angle of the lipid tails and overestimated the volume per lipid. Additionally, the CG CER was able to adopt the splayed conformation from a starting structure of a bilayer "with a geometry far from equilibrium", and remained splayed for the 5 µs of the simulation (148).

Taken together, the studies summarized above indicate that the gel and liquid crystalline phases of pure CER bilayers can be well differentiated with available force field descriptions. However the agreement with experimental T_m and the bilayer properties of CER NS 24:0 differ across force fields.

Interestingly, two studies reported binary mixtures of FFA and CHOL in the context of model bilayers of the SC (i.e. not including CERs). The first, was reported in 2001 by Höltje et al. In their work, the presence of CHOL in equimolar ratio to FFA (saturated C18 and C16) led to a "fluidizing effect" which was characterised by a decrease in order parameters (specially towards the bilayer centre) and a decrease in bilayer thickness, with concurrent increase in APL (from 0.22 to 0.29 Å^2) (150). The second study reported the development of CG parameters for FFA (C16:0) and CHOL which were able to reproduce the self-assembly into a binary (equimolar) bilayer, with an APL of 33.3 Å^2 (151). In addition, simulations of CHOL with longer FFA (C24:0) helped to unveil the experimental instability of these bilayers. It was observed that "the extra length in the fatty acid tails prevents the leaflets from being in close contact with each other, resulting in the formation of voids or pockets", which were quickly filled with water with subsequent 'unzipping' and bilayer disruption (151). This suggest that the abundant presence of CERs with long acyl chains in the ICLM-SC could help

support the integrity of the bilayer by alleviating the 'hydrophobic size mismatch' between these two molecules.

A subsequent study reported the self-assembly of a binary mixture of CER and FFA using CG representations (149). The development of the CG model reproduced well the structural properties and radial distribution functions (RDF) of the target equimolar bilayer (CER NS 24 - FFA 24:0), which was simulated using the CHARM36 AA force field. The equilibrated self-assembled CG bilayers featured a bilayer thickness of 60 Å and an APL of 40 Å^2 for CER NS 24 and 30 Å^2 for FFA 24:0 with high order parameters (S>0.9), with "lipid headgroups being offset in the bilayer normal direction, as observed in previous work". The methods used (isochoric expansion/compression cycles) were also able to generate the self-assembly of the binary mixture into lamellae, i.e., two adjacent bilayers in the normal direction with low lipid headgroup hydration in the interlayer space. Interestingly, extended (angle > 90°) and hairpin configurations of CER were found, suggesting that a mixture of configurations is favourable for CERs of the middle layers (149).

In 2009, Das et al. reported the first systematic study of the interplay between the three major lipid classes found in the ICLM-SC (129). The most abundant lipid subclass of CER according to the lipid profiling reports available at the time (Farwanah et al. (18)) was CER NS 24:0 with a sphingosine moiety of 18 carbons. Note that later, CER NP was updated as the most abundant by Masukawa et al. (2009) (22) and Van Smeden et al. (2013) (25). The lipids were described with a UA ff in which only polar hydrogens were explicit. They used the CER NS 24:0 parameters presented by Notman et al. (144), and the CHOL and FFA parameters of Höltje et al. (151), both of which were described above. The five ternary mixtures studied included the 1:1:1 (equimolar) and the 2:2:1 CER:CHOL:FFA molar ratio, where all FFA were in the unionised form. These mixtures were built from an equilibrated anhydrous multilayer of pure CER in the hairpin configuration, and FFA and CHOL were introduced later by transforming random CER molecules of one bilayer. The results focused on simulations conducted using a group-based cut-off scheme for electrostatic forces because they showed agreement with the more accurate and computationally expensive particle mesh Ewald (PME) calculation. Additionally, the results focused on simulations conducted at a temperature of 340 K (66°C) because the authors were "more confident of the equilibration at 340 K than at skin temperature T ≈300 K" (129).

Bilayer thickness, mass density, order parameter and interdigitation, were some of the structural properties used to compare the ternary mixtures. The findings indicated that "the effect of FFA is to increase the bilayer thickness and reduce the density by a small amount" (129), with a concurrent increase in order parameters. In contrast, in the presence of CHOL, the order of the lipid tails was reduced due to their

tendency to fill the space around CHOL (i.e. to be less aligned with the normal axis). This means that CHOL also "reduces the bilayer thickness and increases the density at the tail region" (129) by increasing the overlap of CER tails across leaflets (partial interdigitation). In turn, partial interdigitation "is expected to increase the interleaflet friction and couple the dynamics of the two leaflets". The 2:2:1 model was characterized by the smaller bilayer thickness (4.89 nm) and the highest interdigitation measure of all the ternary mixtures studied. For simplicity, bilayer thickness was defined by the decay of the water density instead of the density of the headgroups. Regardless of the molar ratio and temperature, all bilayers were observed to be in "a soft glassy state" which is characteristic of the gel phase (129).

A subsequent study conducted by Faller and collaborators investigated an equimolar ternary mixture at 300 and 340 K (152) using the same description of the lipids as Das et al. (129). The structural properties analysed correspond to the previous study, except for bilayer thickness. The bilayer thickness was defined as "the full width of the density profile at half of the maximum density in the membrane" (152). At the lower temperature, the reported bilayer thickness was ≈5.2 nm and the interfacial density was 1060 kg/m^3. Changes observed at the higher temperature included a decreased bilayer thickness of ≈5.02 nm and a reduced interfacial density of 1045 kg/m^3. Additionally, a moderate increase in interdigitation across leaflets was also reported at the increased temperature. These results suggested that the APL will increase and order parameters of lipid tails will decrease upon increase in temperature from 300 to 340 K (152). This suggest caution when employing ff parameters from simulations conducted at non-physiological temperatures. Despite the use of a different definition of bilayer thickness in the earlier study, the values at the higher temperature for the equimolar ratio bilayer (5.17 nm at 340K) (129) seem to have been overestimated.

Del Regno and Notman reported a systematic comparison of bilayer properties between the ternary 1:1:1 and 2:2:1 molar ratios (153). In their work, simulations were conducted at skin temperature (305 K), using the UA GROMOS ff description for the lipids and the SPC model of water. Their results for mass density profiles, order parameters, APL and tilt angle are summarized in Figure 2.3.2 for individual lipids at both molar ratios (1:1:1 left and 2:2:1 right column). The main differences observed in the mass density profiles (top panel) are the increased interdigitation of CER tails at the bilayer midplane and the associated reduction in bilayer thickness of the 2:2:1 model compared to the equimolar bilayer. The order parameters are presented in the middle panel, for the sphingosine tail and acyl chain of CER NS 24:0 (black), and for the FFA 24:0 (blue). Results were reported at two lipid-water ratios, i.e. hydration levels: (1:30) Full hydration shown in empty symbols and (1:2) low hydration shown in full symbols. These profiles are almost identical, with the exception of the fully hydrated equimolar bilayer (FH 1:1:1), which appears to be slightly more ordered

than the 2:2:1 at both hydration levels. Lastly, the table in the bottom panel shows that individual lipids take more space in the lateral dimension in the 2:2:1 model compared to the 1:1:1 model, which could be traced to the higher tilted angle of the lipids. This leads to higher average APL (33.54 $Å^2$) and reduced bilayer thickness (4.55 nm) in the 2:2:1 model (153).

Property		Composition (CER[NS]24:CHOL:FFA24)	
		1:1:1	2:2:1
Area per lipid /$Å^2$	CER[NS]24	32.43(44)	35.01(32)
	CHOL	31.19(39)	34.40(34)
	FFA24	27.47(42)	28.88(54)
	Average	30.37(2)	33.54(3)
Tilt angle /°	CER	12.37(86)	14.28(88)
	CHOL	7.46(71)	8.30(52)
	FFA24	11.60(79)	13.25(1.13)
	CER[NS]24 headgroup	94.90(3.60)	93.82(3.10)
Bilayer thickness /nm		4.76(3)	4.55(2)

Figure 2.3.2. Comparison of mass density profiles (top), order parameters (middle), APL and tilt angles (bottom) of CER:CHOL:FFA lipid bilayers at molar ratios 1:1:1 (left column) and 2:2:1 (right column). Reproduced from Ref. (153) with permission from the Royal Society of Chemistry.

A MARTINI-compatible CG ff representation of a ternary bilayer in the 2:2:1 molar ratio was presented by Quiao and collaborators in 2016 (154). The bilayer was assembled in the hairpin configuration of CER, and simulations were conducted at 310 K (37°C). Upon equilibration, the CERs displayed the V-shaped configuration, the APL was 0.36 nm^2 and bilayer thickness was ≈4.32nm (154). In this study, the bilayer

thickness was defined as the distance between the maximum density peak (on the mass density profile) of the hydrophilic beads.

Recently, Podewitz and Cournia presented an updated systematic study of the interplay between the three major lipid components of the SC. They conducted CG simulations of lipid bilayers featuring 23 different composition ratios at two temperatures. Structural and dynamical properties were measured to determine the phase behaviour of the mixtures (155). Noteworthy, they reported a new CG CER ff which "is in excellent agreement with experimental results in terms of APL, bilayer thickness, and transition temperature, and also for lipid order parameters and lateral self-diffusion, which were not part of the benchmark" (155). This MARTINI-compatible CG ff representation of CER (24:0) is presented in Figure 2.3.3, along with the phase diagrams of the mixtures at temperatures above and below the reported T_m of the equimolar mixture (337 K).
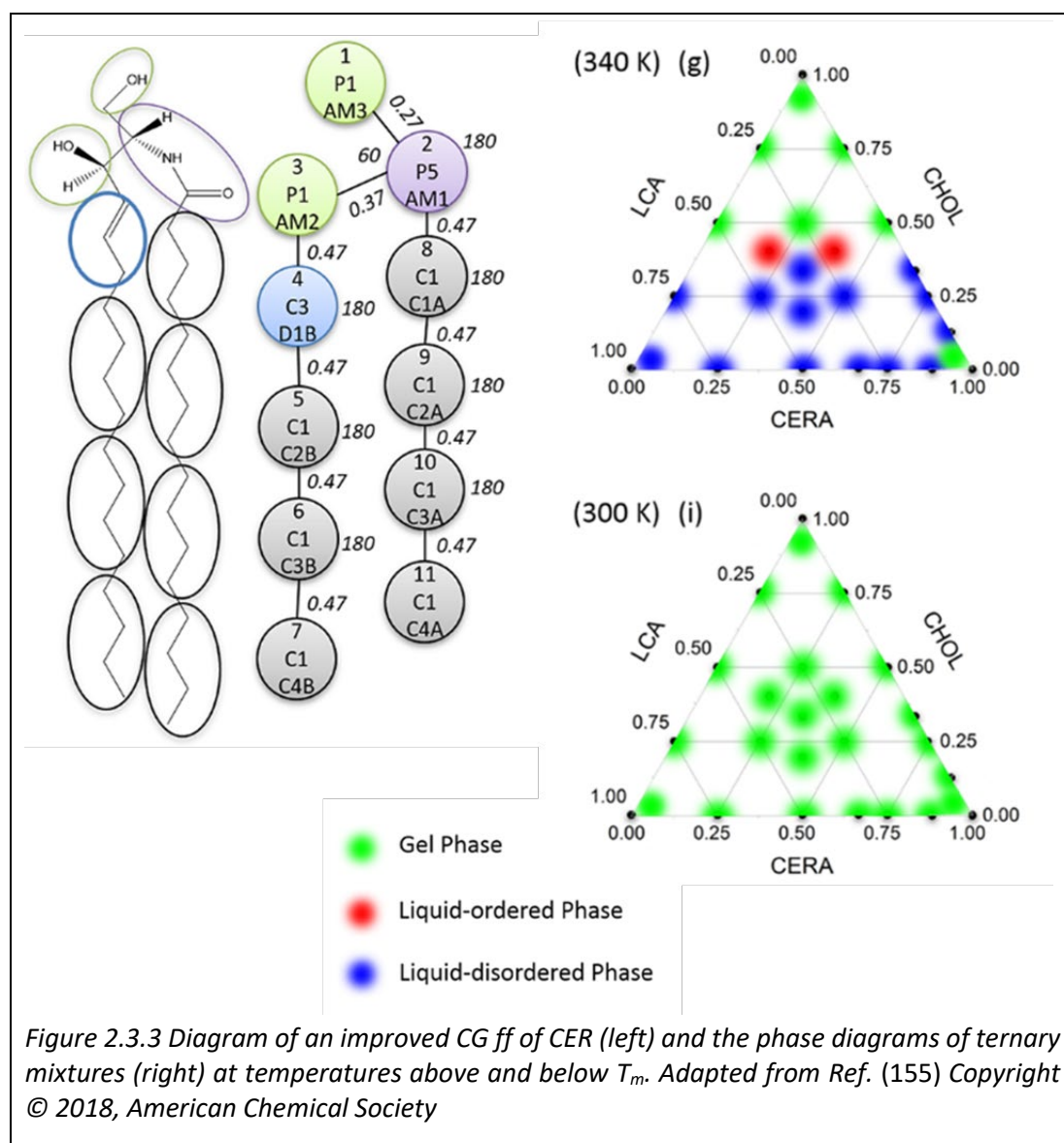
Figure 2.3.3 Diagram of an improved CG ff of CER (left) and the phase diagrams of ternary mixtures (right) at temperatures above and below T_m. Adapted from Ref. (155) Copyright © 2018, American Chemical Society

The phase diagrams show that the interplay between their CER ff and the 2007 CHOL MARTINI ff appropriately reproduces the gel phase at all molar ratios below the T_m, and are in agreement with the different phases observed at $T > T_m$. Other findings of this study include i) that higher content of CER the increases the average APL of the other lipids in the mixture (measured from the Voronoi tessellation) and increases the interdigitation across leaflets, ii) that at $T > T_m$, increased CHOL content causes a reduction in order parameters of FFA and CER, and iii) that bilayer thickness of pure CER bilayers is the maximum of all systems tested, and it remains almost constant for mixtures of up to 60 mol %, when the bilayer thickness starts to decrease.

Lastly, Wang and Klauda, recently demonstrated that the CHARM36 ff for lipids (with updates for sphingolipids) appropriately reproduces structural properties of CER bilayers (pure and in ternary mixtures) (156). A subsequent study showed that the increase in CER concentration triggers CER conformations that are more compact (leading to a reduced APL) whilst retaining the order parameter of the acyl chains. The same study measured the effect of FFA protonation on the structural properties of ternary bilayers and concluded that "while protonated FFA does induce significant changes in certain membrane properties, these are strongest in FFA-specific properties, and the effects on other lipids or the overall bilayer tend to be more muted" (157).

Overall, the increase in computational power and efficiency of algorithms has enabled researchers to test more complex mixtures and the effects of several key parameters like molar ratio on the structural properties of the resulting bilayers. With the development and improvement of the ffs described here, more subtle changes of structural properties have been measured. However, the lack of definite experimental data for the structure of the SPP of the ICLM-SC, combined with the lack of systematic studies of phase behaviour at several compositions, means that it is still difficult to make a direct comparison of MD simulation estimates with experimental measurements.

2.3.2 Double and multilayered systems

Changes in hydration content (water molecules per lipid) can affect the structural properties of bilayers (APL, bilayer thickness, compressibility, order parameters, etc) and the phase behaviour of the lipids. Considering the low-water content of the lamellae of the ICLM-SC, simulating fully hydrated models might lead to wrong estimations. Thus, it is pivotal to test the effects of fully hydrated SC models by characterizing bilayer properties and phase behaviour at low hydration. One way to achieve this is by simulating two bilayers separated by a thin water layer, thus creating a simulation cell containing adjacent bilayers.

Simulations conducted by Das et. al. predicted the formation of hydrogen-bonds between lipids belonging to adjacent bilayers, which caused the strong coupling of the opposing leaflets. In turn, the midplane of each bilayer ('the hydrocarbon tail-tail interface') easily allowed the sliding of leaflets (34). These inter-layer H-bonds were rationalised as the cause of the two-order of magnitude decrease in lateral diffusion of the lipids, which was recently reported by Del Regno and Notman (153). In their work, "a greater variation in bilayer thickness (of up to 1.4nm)" was observed in the double bilayer system compared to the single fully hydrated system (153). The permeability coefficient of a water molecule was computed for the translocation across the two midplanes of adjacent bilayers and the predictions were in the order of 10^{-15} to 10^{-14} nm/ps, depending on the path of the water crossing the inter-layer space through a 'water-pool' region or a 'dry' region, respectively (153). These values are in the same order of magnitude as the permeation of water across model bilayers in hairpin conformation, as will be discussed below (section 2.4.2.2). Additionally, the high rotational diffusion of CHOL (i.e. fast flip-flop motion) observed in multilayered systems has been rationalised as an important property conferring the "adaptability to curvature and other geometrical features" of the SC (34, 153, 158).

Simulating multiple layers also enables the investigation of the preferred configurations adopted by the extra-long tail of CER EOS. Four stacked bilayers in the hairpin conformation of CERs were simulated at 305 K by Vogel et al. (130). Their findings indicate the ability of the ω-esterified lipid chain (linoleate) to penetrate into the adjacent bilayer, as well as to fold (at the ester bond) into the same bilayer, indicating that the formation of the LPP (with fully splayed CER conformation) could not be corroborated (130).

Two multilayer systems resembling the sandwich model (presented in Figure 2.2.6) have been reported. The first system is the model reported in the work of Das and Olmsted, which was simulated with the GROMOS UA ff and included three CER subclasses and explicitly included the tail length polydispersity of CERs and FFA (159). In this work "none of the CER EOS molecules were found to simultaneously occupy both bilayers", with the folding of the long acyl chain occurring at the ester bond or at the unsaturation of the linoleate tail (159).

The second is the model of Wang and Klauda, which was simulated with the AA CHARM36 ff (160). Pure CER EOS bilayers were characterized by higher order parameters of the acyl chain of CER EOS compared to the corresponding acyls chains of CER NS and CER NP. However, beyond the ester bond, the order parameters of the ω-esterified linoleate were significantly lower. "This work required a microsecond of simulation to begin seeing transition into the interior-disordered state", which is the characteristic feature of the sandwich model, and several microseconds were required to observe water molecules translocating into the central region (160).

Overall, both supramolecular arrangements (the multilayer stacking and interior-disordered sandwich model) are at least metastable in the microsecond timescale of simulations, with the possibility of both contributing to the lamellar structure of the ICLM-SC (160).

2.3.3 Single bilayer in the splayed conformation of CER

Very recently, a new SC model was developed to account for the low water content of the ICLM-SC. The model was built to resemble the LPP unit cell described in Figure 2.2.7, with a composition that mimics the diversity of CER subclasses and polydispersity of the lipid tail lengths of CERs and FFAs. Parameters of the model such as molar ratio of the three major lipid classes, specific location of the CHOL fraction, content of CER EOS and hydration (number of water molecules per lipid) were iteratively optimised to reproduce the banding patterns of the ICLM-SC, as resolved by CEMOVIS. The resulting model features all CER molecules in the splayed conformation, i.e. with an angle between the sphingosine and alkyl lipid tails ≈180° (Figure 2.3.4). This model has each leaflet exhibiting two hydrophobic regions that are separated by a thin hydrophilic region where the head groups of the lipids and a few water molecules are located. The interdigitation occurs both at the inner end of the leaflet (with the opposite leaflet of the same bilayer) and at the outer end of the leaflet (with the neighbouring bilayer along the lamella stacking axis).

The resulting composition is detailed in Table 2.1. Briefly, the CER fraction includes the two most abundant CER subclasses CER NS and CER NP, the latter with six acyl chain lengths. Similarly, the FFA fraction includes the six most abundant tail lengths in their relative proportions. Additionally, the three lipid classes of the ILCM-SC are in a relative equimolar fraction, with 75% of the CHOL content co-localized with the sphingosine tail of CERs, an overall 5 mol % of CER EOS, and 0.3 water molecules per lipid.

Table 2.1 Composition of the optimized SC molecular model with CER in splayed conformation.

CER EOS		CER NS		CER NP		FFA		CHOL	WATER
				C20	4	C20	4		
				C22	8	C22	8		
				C24	16	C24	30		
C30	12	C24	16	C26	24	C26	24	88	90
				C28	8	C28	8		
				C30	2	C30	14		
				62		**88**			
Total Num. CER = 90									
Total Num. lipids 266									

Figure 2.3.4. Structural model of the SC at low hydration. Panel (a) and (b) show the optimised splayed model of the SC, featuring CER and FFA tail polydispersity, and the presence of CER EOS. Reprinted from Ref. (161). © 2018 The Author(s). Published by Elsevier Inc. (CC-BY-NC-ND)
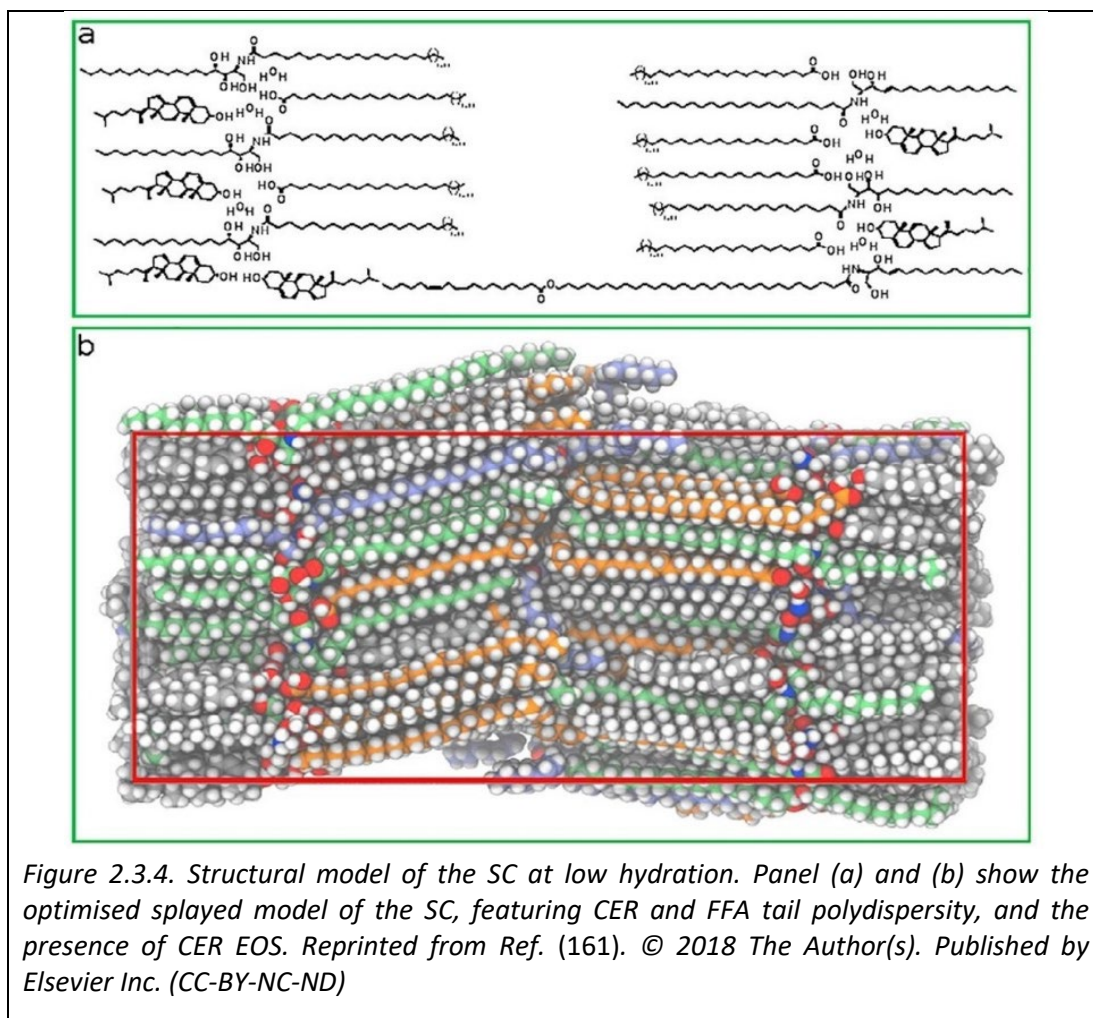
2.4 Permeation and diffusion across the ICLM-SC.

2.4.1 Experimental studies

Any compound that reaches the viable layers of the skin has to translocate across the stacked bilayers of the ICLM-SC. Given that the ICLM-SC is a continuous medium that surrounds corneocytes, this means that compounds not only translocate in the vertical direction (into deeper layers) but also have to diffuse sideways (lateral diffusion). Trans-bilayer translocation (permeation) and lateral diffusion are different processes that occur at significantly different rates.

In 1978, Moore and collaborators postulated that the mechanism of transdermal permeation (i.e., in the vertical direction) of small molecules was "dependent on the hydrogen-bonds in the desolvation of the solute during this penetration process and by the overall 'viscosity' of the stratum corneum" for the more polar molecules.

Whereas for the non-polar molecules, the barrier of penetration would be located in the "aqueous boundary layers" (162). This mechanism was postulated based on measured transdermal permeability across human skin and partition coefficients (octanol/water) of 19 phenolic compounds and short chain alcohols.

Lateral diffusion in model bilayers was reported in the work of Langer and collaborators for SC model bilayers and for phospholipid bilayers (DMPC with and without CHOL) (163). Lipophilic fluorescent probes were conjugated to lipids and their lateral diffusion was measured with image-based fluorescence recovery after photobleaching (video-FRAP). The structures of the probe-conjugated lipids, their MW and lateral diffusion coefficients in the SC model bilayer are summarized in Figure 2.4.1. A clear dependence of the lateral diffusion coefficients on MW was observed, with the increase in viscosity of the bilayer (SC>DPMC+CHOL>DMPC) reducing the diffusivity of each molecule, but also amplifying the differences between the largest and the lowest diffusivity values (163).

	MW	D [10^{-8} cm^2/s]
BOD	262	1.22
NBD-dicot	405	0.712
NBD-Chol	761	0.385
BOD-Chol	797	0.125

Figure 2.4.1. Lateral diffusivity of probe-conjugated lipids in a SC model bilayer measured by video FRAP. Adapted from Ref (163). Copyright © 1996 The Biophysical Society. Published by Elsevier Inc. All rights reserved.
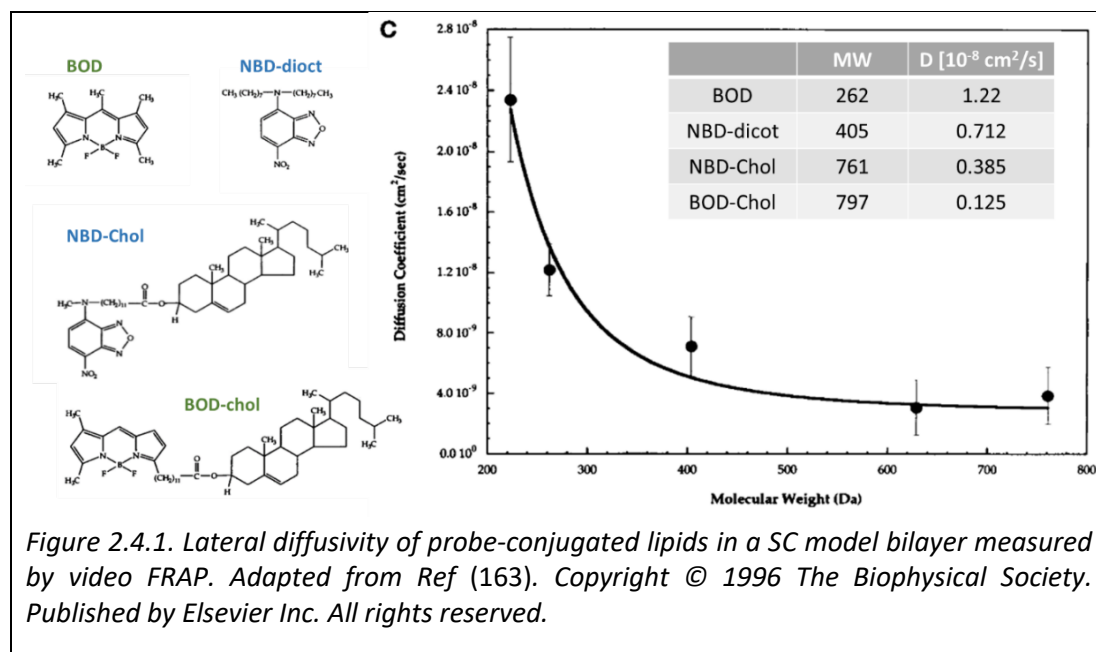
2.4.1.1   Amino acids and short peptides

The work of Chen and collaborators demonstrated that for the transdermal permeability of amino acids and dipeptides across skin "the effect of lipophilicity is a more dominant factor than the molecular weight" (164). They reached this conclusion after measuring the partition and permeability coefficients of eight amino acids (A, G, L, K F, P W, V) and three dipeptides (AL, AF, AW) (Figure 2.4.2). The partition coefficient (ln K) was measured in a two-phase aqueous system, which correlated well with the lipophilicity data for the dipeptides. The transdermal permeability was measured across porcine skin in a diffusion cell at 32°C.
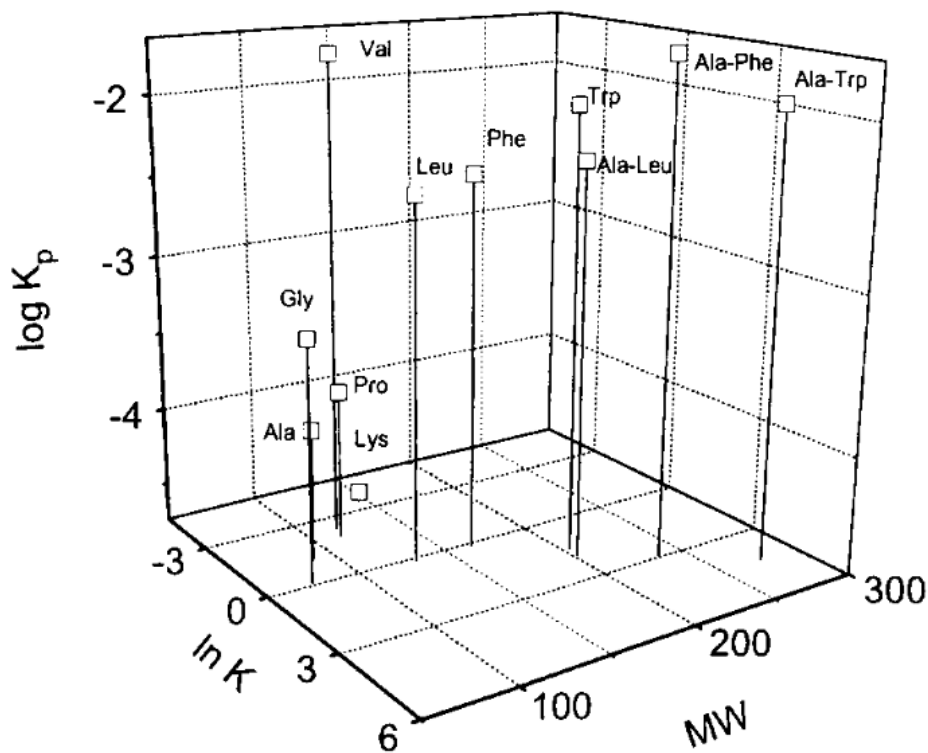
Figure 2.4.2 Permeability (Log K_p) in the space of MW and partition coefficient (ln K) for amino acids and dipeptides across porcine skin. Reprinted from (164). Copyright © 1996 Published by Elsevier B.V.

As observed in Figure 2.4.2, the molecules with MW < 200 (except V) yielded lower permeability than those with higher MW. However, it appears that lipophilicity alone does not predict the ranking in permeability of the four molecules with MW > 200 (namely W, AL, AF, AW) because the dipeptide with the highest lipophilicity (AW) displays lower permeability than the dipeptides ranked second and third in lipophilicity (AF and AL, respectively). Furthermore, for the same group, W and AL have similar MW and similar lipophilicity, yet different permeability.

In a subsequent study, the partition coefficient into SC lipid vesicles and associated binding/partition enthalpy were measured for the same set of molecules. In this instance the partition coefficients between the lipid vesicles and acetate buffer were determined" (86) and the binding/partition enthalpy was measured by isothermal titration calorimetry (ITC (86), which also allowed the derivation of the Gibbs free energy (ΔG) and the entropy of binding/partition. The partition coefficients were not found to correlate with the transdermal permeability (86). This finding further challenges the use of partition coefficients as a reliable representation of the partition into the ICLM-SC and evidently as predictors of transdermal permeability.

50

As mentioned in the Introduction chapter, the AAPV tetrapeptide is an inhibitor of the HNE with potential for the treatment of inflammation-mediated skin conditions in topical applications. Trans-epidermal penetration was measured for two chemically modified versions of the AAPV tetrapeptide (57). The first version with capped termini featured a methylated peptide bond in the amino end and an amidated cap in the carboxyl end. The second version featured a Laa of eight total carbons (C8) (i.e., six carbons in the side chain) and the same amidated cap in the carboxyl terminus. Note that their nomenclature indicates the total number of carbons in the moiety (C8) as opposed to the number of carbons of the side chain. The two epimers of the chiral carbon in the Laa moiety were tested independently (57). Epidermal tissue (from human skin) was mounted on a Franz-type diffusion cell and exposed to the derivatives in a propylene glycol solution during 24 h at 32°C. A higher percentage of dose penetration was observed for the D-Laa compared to the L-Laa (2.53 and 1.47%, respectively) with no penetration of the capped tetrapeptide (57).

Using the same experimental procedure, a subsequent study measured the transdermal permeability and flux of these epimers and two additional (short chain) Laas (56). Upon contact with the skin, the parent tetrapeptide underwent substantial degradation with ≈30% of the initial concentration being recovered after 24h. By contrast, all the Laa conjugates demonstrated significant stability, with the racemic mixture (D, L) of C8-Laa conjugated tetrapeptide being the most stable. Similarly, Laa conjugation "substantially enhanced AAPV permeation for all chain lengths" without significantly changing the inhibitory activity against HNE (56). The additional Laa conjugates featured a shorter (C6) and longer (C10) Laa moiety. The transdermal permeability of the C8 Laa in the racemic mixture was superior to the other two Laa conjugates, indicating a U-shaped response in permeation with respect to the increase in lipophilicity of the Laa moiety. These findings suggest that "there is an optimal lipophilicity (length of Laa chain) of the derivatives for improving their transdermal delivery" (56). Furthermore, the permeability of the pure D (C8) Laa epimer was nearly two orders of magnitude larger than the L (C8) Laa epimer (56).

Another study compared the stability, inhibitory activity and penetration of acyl derivatives of the tetrapeptide across human skin. In that study, the Laa conjugation was compared to another chemical modification increasing the lipophilicity without generating epimers. A short (C7) acyl chain was chemically linked at either terminus of the tetrapeptide and both acyl-conjugated derivatives (N and C-termini) yielded ≈3.8% of dose penetration, with increased (*in vitro*) inhibitory activity and increased stability against degradation (165). From this percentage of dose penetration, the acylated (C7) derivatives are expected to have a larger permeability coefficient compared to the previous C8 Laa measurements (57), although explicit permeability coefficients were not reported. Figure 2.4.3 displays the structure of the C7 acyl

derivative at the N-terminus (middle) with the parent tetrapeptide (top) and the C8 Laa-conjugated derivative (bottom).

Figure 2.4.3. Structures of uncapped AAPV tetrapeptide and two of its derivatives. Adapted from Ref (165). *(CC-BY-NC 3.0) Copyright © 2016 Rocco et al.*
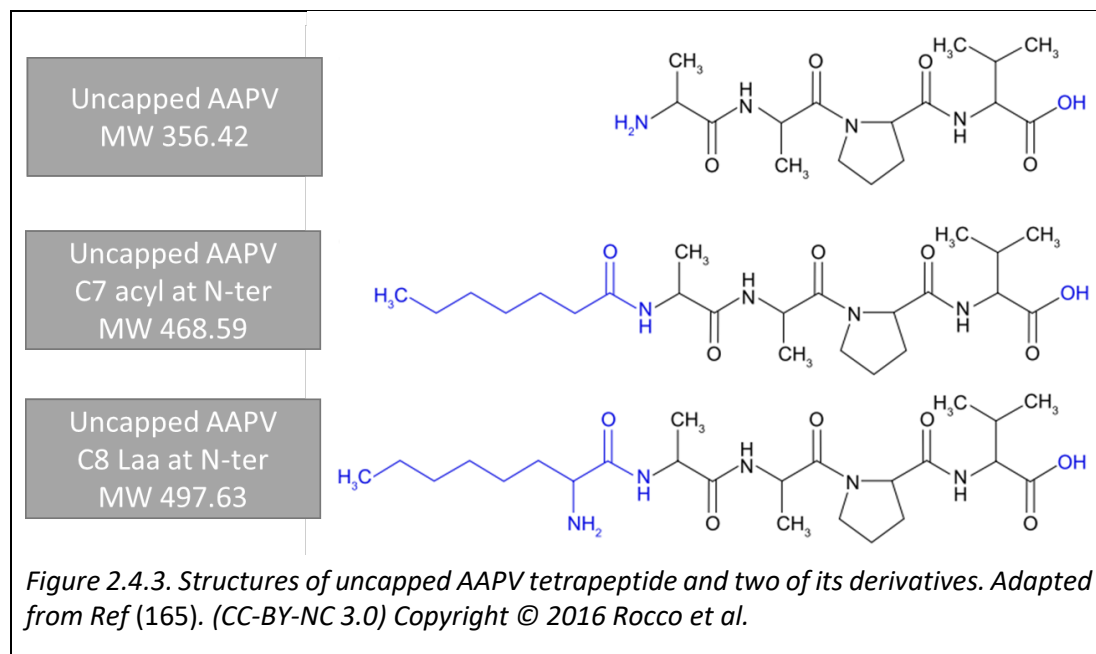
The superior dose penetration percentage of the C7 acyl derivative compared to the C8 Laa derivative could be rationalized by considering the two functional groups in the latter, i.e. the amino group and the methyl group at the end of the side chain of the Laa. The amino group confers additional polar surface area and hydrogen-bonding capabilities, whereas the methyl group confers additional non-polar surface area. It could be said that that the 6.2% increase in MW, along with the change in the ratio between polar and non-polar surface area of the derivative, represents nearly a 50% reduction in dose penetration for the modified tetrapeptide.

2.4.2 MD simulation studies

2.4.2.1   Background and seminal works

The description of permeation across lipid bilayers has evolved in the last several decades. In early studies of permeation the membrane was considered as a homogenous oil slab and permeation data was often correlated to water/oil partition coefficients (referred to as the Meyer-Overton rule) (166). Despite being intuitive and widespread, this model is known to underestimate boundary effects. Subsequent models use the *homogeneous* solubility-diffusion model, in which three successive steps are considered: (i) binding of the molecule to the water-lipid interface and subsequent insertion into the lipid core of the membrane, (ii) passive diffusion through the membrane core, and (iii) unbinding of the molecule at the water-lipid

interface on the other side of the membrane. While this model treats the water-lipid interface explicitly, the membrane core is still considered to be homogenous.

In fact, the bilayer interior shows distinct regions that exert different resistance to a permeant. Pioneering studies highlighted the inhomogeneous nature of the bilayer interior in the prediction of one-dimensional diffusion coefficients of solutes. Estimates at different positions across a phospholipid bilayer suggested the presence of two distinctive regions where the diffusion coefficient (of solutes such as benzene and the drug nifedipine) was either slow or fast (118, 167, 168). This led to the development of the *inhomogeneous* solubility-diffusion model, which is based on a model that divides the lipid bilayer into four distinctive regions (Figure 2.4.4), each posing a distinct resistance to permeation: (1) the low head group density, (2) the high head group density, (3) the high tail density, and (4) the low tail density region (120).

Figure 2.4.4. The four-region model for a phospholipid bilayer in full hydration. Numbers correspond to the regions described in the main text. Reprinted from Ref. (91). © 2020 Wiley-VCH Verlag GmbH & Co. KGaA, Weinheim.
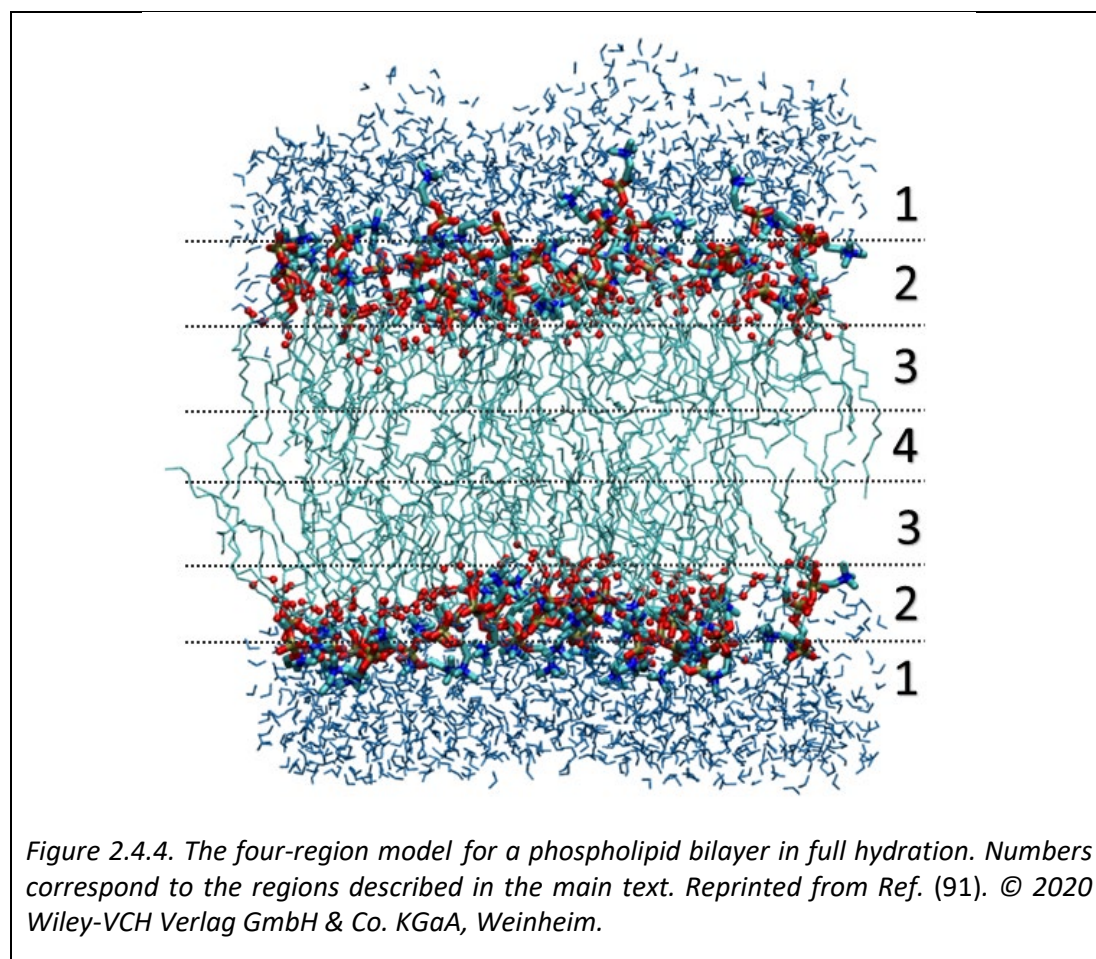
Taking into consideration the evidence towards distinctive regions, the seminal work by Marrink and Berendsen (120, 121) was one of the first studies to use MD simulation to calculate the permeability of small molecules across a lipid bilayer. They performed a series of short simulations where a small molecule (water, molecular

oxygen or ammonia) was inserted and constrained at different positions along the bilayer normal, in a fashion referred to as the *z*-constraint algorithm. The free energy profile (or potential of mean force (PMF)) was later retrieved from these constrained simulations. Their theoretical framework for the *inhomogeneous solubility-diffusion model* of permeation was used to calculate permeation from said free energy profile and the position dependent diffusion coefficient as presented in the Introduction chapter for Equation 1.3. The widespread four-region model described in Figure 2.4.4 was derived in their work, and together with their theoretical framework lies at the core of most MD permeation studies to this date. Permeation across a phospholipid bilayer is influenced by the physicochemical properties of the permeant molecule, such as its MW, shape, hydrophobicity/lipophilicity and net charge (169). For molecules with MW smaller than 50 it has been shown that permeation is mostly dependent on the size of the permeant molecule. For larger molecules, permeation is more likely a function of volume and shape (if corrected for hydrophobicity) (121). Hydrophobicity and net charge affect permeation because they dictate the energy barrier experienced by the permeant when moving across the different areas of the membrane. If the molecule is too hydrophobic, it will become trapped in the lipid core reducing its overall permeability (170). Similarly, permeability is reduced if the molecule bears hydrophilic or charged functional groups, as the preferential interactions with the polar head groups at the water-lipid interface will result in a large energy barrier to penetration beyond the interfacial region (171).

2.4.2.2 MD simulations of diffusion and permeation across SC models

Noro and collaborators conducted a pioneering study where the permeation of water across a model bilayer ICLM-SC was reported. In their work, the lipid bilayer was constructed as a ternary mixture composed of CER, CHOL, and FAA in a 2:2:1 molar ratio, water was represented with the single point charge (SPC) model, and the simulations were conducted using the UA GROMOS ff. Permeability of water across the ICLM-SC is a characteristically slow process, which occurs three to five orders of magnitude slower than across plasma membranes (i.e. phospholipid bilayers) (172). Thus, to capture statistically relevant estimates, 15 water molecules were constrained at 0.2 nm intervals (following the z-constraint method) across the bilayer and their position-dependent diffusivity and free energy were estimated. The average crossing time of a water molecule across the SC model bilayer was predicted to be 0.69 ms at 300 K and 0.02 ms at 350 K. These times underscore the need for MD enhanced sampling methods (such as the z-constraint method) to provide realistic estimates, as these are several orders of magnitude larger than ordinary simulation times.

The Kubo relation was used to estimate the diffusion coefficient from the integrated autocorrelation time (IACT) of the force experienced by the constrained water

molecule. The diffusion coefficient was found to be highly anisotropic given that "once the water molecule is inside the bilayer, it faces little resistance in moving along the z direction, but the motion in the x-y plane is severely restricted" (172). This was an indication that a simple absorption-diffusion description would not be applicable, but instead the *inhomogeneous solubility-diffusion model* of permeation would be required for a proper description of the permeation process. The calculated one-dimensional diffusivity profiles in the normal direction (D_z) at 300 K (red) and 350 K (blue) are presented in Figure 2.4.5 (top left). The mass density profile in Figure 2.4.5 (bottom left) presents the partial densities of individual components of the simulation cell in the negative COM distance of the horizontal axis, with the bilayer midplane located at 0 nm and the bilayer surface at ≈-2.8 nm. It can be seen that once the water molecules are inside the bilayer, the effect of temperature on D_z is negligible because the diffusivity is reduced by nearly one order magnitude, with a recovery at the bilayer midplane. Similar trends are observed for the (x-y plane) lateral diffusivity ($D_\perp$) at both temperatures (Figure 2.4.5, top left), with an initial reduction of $D_\perp$ of nearly two orders of magnitude and recovery at the bilayer midplane, reaching $D_z \approx D_\perp$. This indicates that the hydrophobic core of the bilayer presents two district resistance regions: one with higher resistance and anisotropy below the head groups, and one with lower resistance and lower anisotropy closer to the midplane.

Figure 2.4.5 Diffusivity profiles (left) and free energy profile for the permeation of water across the 2:2:1 CER CHOL FFA model of the SC from MD simulations. Reproduced from Ref (172) *with permission from the Royal Society of Chemistry.*
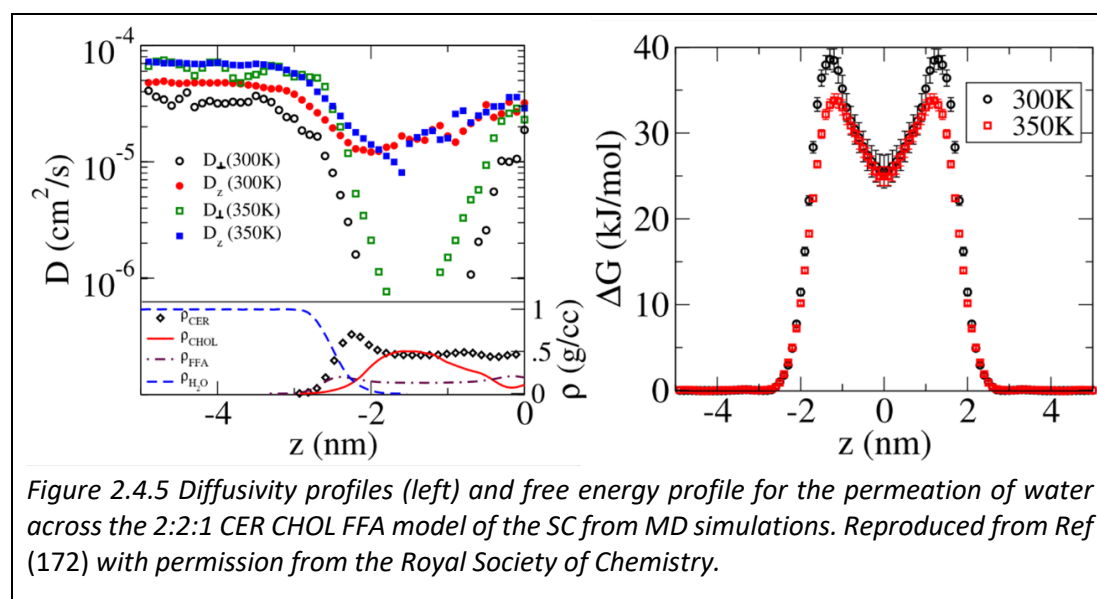
The free energy profiles were also reported at both temperatures (Figure 2.4.5, right). The increase in temperature appears as a reduction of ≈5 kJ/mol in the height of the barrier to insertion, which is located below the headgroups of CER and CHOL. Said barrier was found to be "much higher than in typical fluid phospholipid bilayers at the same temperature" (172). Lastly, the permeability coefficients of water increased with an increase in temperature. At 300 K, P_{water} = 3.7x10^{-9} cm/s (equivalent to 3.7

x10 $^{-14}$ nm/ps) which "is about 30 times smaller than existing experimental results on mammalian skin sections" (172), whereas at 350 P_{water} = 1.3 x10^{-7} cm/s (equivalent to 1.3 x10^{-12} nm/ps). The two-order of magnitude increase in the permeability following the increment in temperature is not surprising considering that 350 K is above the phase transition reported for the ICLM-SC (as discussed in section 2.2). These results support the gel state of SC bilayers as a key factor contributing to the barrier properties of the skin.

Using the Z constraint method, Gupta and collaborators conducted simulations of the permeation of water and other eleven small molecules across a ternary (equimolar) model of the SC, at 310 K (37°C) (173). The reported PMF of water is shown in the top left corner of Figure 2.4.6, and is in agreement with the findings discussed above for Figure 2.4.5 (right). However, the reported permeability coefficient of water was higher than any of the values reported by Noro and collaborators (see Table 2.2), and "is almost 2 orders of magnitude higher than experimental values" (173).

Table 2.2 Permeability coefficients of water from MD simulations across SC models featuring ternary mixtures at full hydration.

P_{water} (nm/ps)	Temp. K (°C)	CER:CHOL:FFA ratio	Ref.
3.70 x 10^{-14}	300 (27)	2:2:1	(172)
1.30 x 10^{-12}	350 (77)	2:2:1	(172)
1.30 x 10^{-13}	350 (77)	1:1:1	(172)
7.08 x 10^{-10}	310 (37)	1:1:1	(173)
3.30 x 10^{-15}	310 (37)	1:1:1	(153)

Upon comparison to available experimental data for water, DMSO, ethanol and urea, their analysis showed that "the permeability of hydrophilic permeants mostly depends upon the PMF", despite not being able to reproduce the experimental ranking. The PMFs of all the small hydrophilic molecules resembled the shape of the PMF of water (Figure 2.4.6), with differences in energy barrier heights and displaying energy minima in the headgroup region of CER and FFA. By contrast, for the hydrophobic molecules, the calculated permeabilities reproduced the experimental ranking but were higher than the respective experimental values. A common feature is the shape of the PMF, where the free energy barrier is located in the headgroup region, and a free energy minimum is located inside the bilayer. From their observations it was "deduced that the permeability of a hydrophobic compound depends upon both PMF and D(z)" (173). Overall the shape of the PMFs explains the ability of the model bilayer to pose resistance to both hydrophilic and hydrophobic molecules of up to MW 110.
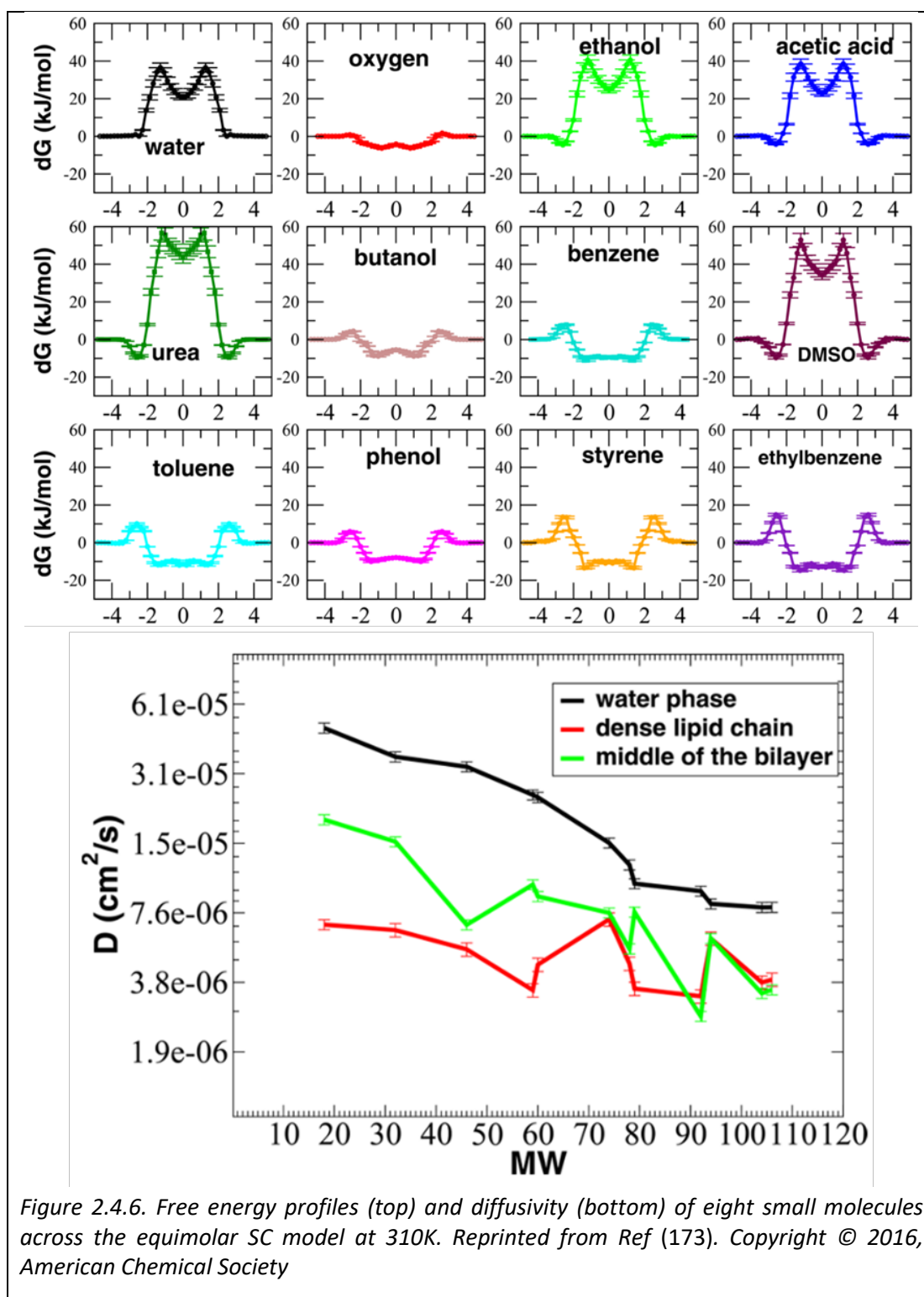
Figure 2.4.6. Free energy profiles (top) and diffusivity (bottom) of eight small molecules across the equimolar SC model at 310K. Reprinted from Ref (173). Copyright © 2016, American Chemical Society

Lastly, the bottom panel of Figure 2.4.6 provides the one-dimensional diffusivity values of each of the eight small molecules as a function of their MW in the water phase (black), showing the expected downwards trend with increase in MW. The figure compares this clear trend with what is observed in the two characteristic regions of hydrophobic core, namely the 'dense lipid chain' (red) and the 'middle of

the bilayer' (green). The anisotropic environment of the bilayer interior distinctively reduces the diffusivity in the COM distance coordinate, with the region with the highest density presenting the lowest diffusivity values and the region with the lowest density presenting intermediate diffusivity values. The plot also indicates that the dampening of diffusivity in these regions appears to be smaller for the molecules with larger MW. In other words, the diffusivity is reduced to a greater extent for the smaller molecules upon entry to the 'dense lipid chain' region. The PMF, diffusivity profile and permeability coefficient of water across an equimolar ternary bilayer at full hydration and at 305 K were recently reported by Del Regno and Notman (153). Both the PMF and the diffusivity profile are in qualitative agreement with the earlier predictions discussed above; however, the height of the free energy barrier is lower ($\approx$27 kJ/mol) and the permeability coefficient (3.3 x 10^{-15} nm/ps) is the smallest reported for water in this context (Table 2.2). Considering the very similar structural parameters of the equimolar and the 2:2:1 bilayers (Figure 2.3.2), a very similar value of the permeability of water across the 2:2:1 model bilayer would be expected.

The permeability of water, solvents and drug molecules was estimated across the splayed model of the ICLM-SC (section 2.3.3) (174). In this work, the permeant molecules were pulled by a *stiff-spring* constant along the translocation path (i.e. the COM distance along the z axis) in the reverse and forward directions. Consequently, the free energy profiles and diffusion coefficients were estimated from the fluctuation-dissipation theoretical framework. The PMFs had to be calibrated by calculating the binding free energy of the permeant at the insertion distance from a thermodynamic cycle (174). Note that for the works described above, this step was unnecessary given the presence of a bulk water region in which the reference free energy is commonly assumed to be zero. The PMF and diffusivity of water are presented in Figure 2.4.7. As depicted in the top panel, the model bilayer is symmetrical around the midplane (z = 0 nm), where the long acyl chains of CER and FFA of opposing leaflets can interdigitate. The headgroups of the lipids and the water molecules are located $\approx$3 nm away from the midplane, and the short chains of CER (sphingosine moiety) and most of the CHOL are located in the furthest ends of the z axis, where interdigitation across stacked bilayers can occur. High resolution over a long distance ($\approx$10 nm along the z axis) characterizes both the PMF and diffusivity profiles. It is noteworthy that the diffusivity values estimated for this system are on average one order of magnitude lower than in the works described above. This could be attributed to either the unique characteristics of the model or to the method employed to estimate D(z), i.e. by relating it to the dissipative work of the molecule as it is pulled. By contrast, the PMF displays qualitative agreement with previous works discussed, i.e. a free energy barrier of similar height ($\approx$35 or 30 kJ/mol) for the insertion from the headgroup region into either of the hydrophobic regions, with a favourable drop in free energy as it reaches the interdigitation planes. Lastly, the

58

permeability of water was reported as 8.78 x 10^{-14} nm/ps (at 303 K), which is in the same order of magnitude as the value calculated across the 2:2:1 molar ratio bilayer of reduced complexity (see Table 2.2).
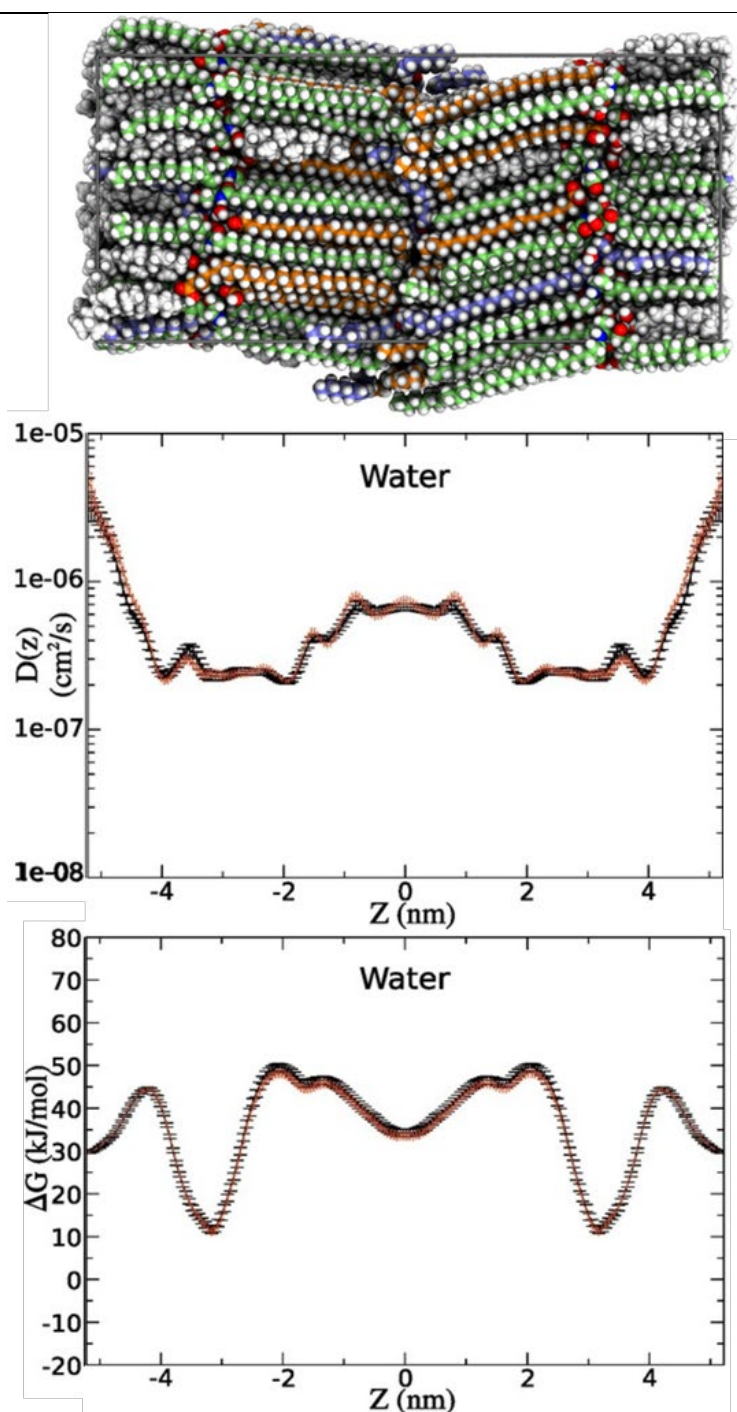
Figure 2.4.7 Diffusivity profile (middle) and free energy of permeation (bottom) of a water molecule across the splayed model of the SC (top). Adapted from Ref (174) (CC BY-NC-ND 4.0)

3 Validation of the enhanced sampling method REST3 for the simulation of the permeation of peptides across the stratum corneum

3.1 Introduction.

The permeation of small molecules across lipid bilayers is a slow process. The average crossing time of a water molecule across a SC model bilayer was estimated to be 0.69 ms from MD simulations featuring CERs in the hairpin configuration (172). The combined simulation time reported in that work was 750 ns, which is nearly 10^3 times less than the reported average crossing time. Nonetheless, such estimation was possible because the MD simulations of the permeation of water employed the z-constraint method, a form of enhanced sampling that enables the *reconstruction* of the translocation path and the sampling of relevant molecular events at each position along said path. This millisecond timescale demonstrates the slow rate at which water permeates across model bilayers of the SC and it is still beyond what is commonly (and reasonably) achievable with current computer resources (i.e. more than a decade later!). The permeability of water typifies the requirement of enhanced sampling methods for the study of small molecule – membrane interactions (SMMIs) occurring between the ICLM-SC and any exogenous molecule permeating into the viable layers of the skin (e.g. a drug candidate). Since the drug candidate molecules of interest for transdermal drug delivery applications are larger and more complex than a water molecule, their average crossing time is expected to be substantially larger than 0.69 ms. Hence, this requires conducting MD simulations with methods optimised to effectively sample a larger space of relevant molecular interactions and configurations at each position along the translocation path.

Replica exchange with solute tempering (REST) is one of several enhanced sampling methods that have been developed for biomolecular simulations (126). The rationale of the method is to enhance the sampling of the degrees of freedom (DOFs) that are related to the solute only (e.g. configurations of the molecule), whilst keeping the

DOFs of the solvent unperturbed. This is important because the number of solvent molecules is usually very large. Enhanced sampling is achieved by *tempering* the solute, i.e. by artificially increasing its temperature until the transitions between *all* the relevant configurations are observed more frequently. Thus, REST is more efficient than previous replica exchange methods that increase the temperature of all components of the simulation cell.

REST2 presents a more efficient approach to the sampling of configurations of the solute by introducing scaling factors (175, 176). This alternative method was originally developed to optimize protein folding simulations, where the main sampling difficulties arise from the high energy barriers associated with the rotation of some of the dihedral angles in the backbone of the protein. In REST2, the solute-solute interaction terms of the potential energy function are artificially *tempered* by applying scaling factors to dihedral angle terms and non-bonded interactions. This enables the computational effort to be directed at the relevant DOFs of the solute (i.e. the protein), whilst all the other DOFs of the system are unperturbed (175, 176).

Recently, REST3 was developed to address limitations in the sampling of a solute due to the *long-lived* interactions between a small molecule and a lipid bilayer. REST3 employs scaling factors to selectively *temper* the non-bonded interactions between the solute (i.e. the permeant) and the other components of the simulation cell (i.e. the lipid bilayer and the solvent). The rationale is that this *tempering* enables the permeant molecule to *escape* the *long-lived* interactions that hamper the sampling of relevant configurations. It is important to note that separate scaling of the solute-solvent and solute-bilayer interactions is not possible in the original REST2 formulation. In practice, in REST3 the interactions between the solvent molecules (usually water and any ions present) and the lipid molecules (making up the bilayer) remain unperturbed. Additionally, the solute-solute interactions are also unperturbed. REST3 is thus ideally suited to study SMMIs because it enables the interactions that maintain the integrity of the lipid bilayer (i.e. lipid-lipid and lipid-water interactions) to remain unperturbed.

Very slow transition rates are often observed between the statistically relevant configurations of the permeant as it interacts with a bilayer. The slow transition rates are rationalized by considering *long-lived* interactions that kinetically *trap* the permeant into a more favourable configuration (175). From the theory of statistical mechanics (i.e. the partition function) it is well known that sampling *all* relevant configurations (i.e. not just the more favourable ones) is a requirement to obtain reliable estimates of thermodynamical and mechanical properties from MD simulations. Furthermore, the reaction coordinates (RCs) that describe the transition path between these relevant configurations are commonly unknown *a priori*. This scenario can render the conventional US method inadequate for sampling purposes.

However, in combination with US, the REST3 enhanced sampling can address the sampling of relevant configurations and interactions along the permeation pathway. The appendix "Derivation of REST3" contains a detailed derivation of the approach and information on the implementation of the algorithm.

As presented in the Literature Review (section 2.4.1.1), Chen and collaborators reported the experimental permeability coefficient of eight amino acids and three dipeptides across porcine skin at 32°C (305 K) (164). In a subsequent study they reported the thermodynamic parameters for the binding of the same 11 molecules to large unilamellar vesicles (LUV) made of a lipid mixture mimicking the molar ratio of the ICLM-SC. The binding/partition enthalpy (ΔH) was obtained with ITC, from which the Gibbs free energy (ΔG) and the entropy were derived. The ITC experiments were conducted at 25°C (298 K) by injecting the amino acid / dipeptide solution into a micro-reaction system containing the LUV solution (LUV average size of 130 nm), and monitoring the heat released (86). The Ala-Trp dipeptide is one of such dipeptides for which these experimental values are available. It was chosen as a test case because its properties (MW, lipophilicity and permeability) are representative of the other peptides that were studied as reported in this thesis.

This chapter presents the application of the US-REST3 enhanced sampling approach to the estimation of the permeability coefficient and free energy of insertion of an Ala-Trp dipeptide across a ternary lipid bilayer representing the ICLM-SC. The US-REST3 enhanced sampling method works in combination with conventional US, allowing the use of the in-built tools available in the GROMACS simulation package.

The working hypothesis is that US-REST3 is an efficient enhanced sampling approach that can facilitate the sampling of the interactions of the Ala-Trp dipeptide with a model lipid bilayer of the SC and ultimately provide predictions that match the available experimental values of the insertion and permeation of Ala-Trp. The specific aims of this work were i) to optimize the simulation parameters of US-REST3 to characterise the permeation of a dipeptide across a model lipid bilayer of the SC, and ii) to compare its performance against conventional US (the gold-standard enhanced sampling method) for reproducing experimental values and efficiency in the use of computational resources.

3.2 Methods.

3.2.1 HPC resources and software

The simulations and part of the analysis were conducted using the high-performance facilities at the Pawsey Supercomputing Centre, i.e. Magnus (Cray XC40) and Zeus

(HPE cluster). All conventional umbrella sampling (US) simulations were performed using GROMACS 4.6.7 (177) whereas all the US-REST3 simulations were performed using an in-house version of GROMACS 4.6.7.

3.2.2 Simulation system

To represent the bilayers found in the intercellular lipid matrix of the SC, a ternary bilayer composed of ceramide (CER), cholesterol (CHOL) and free fatty acid (FFA) in a 2:2:1 molar ratio (CER:CHOL:FFA) was used. This molar ratio is regularly used to represent the complex lipid composition of human SC (129, 153, 172, 178). The bilayer was constructed with 160 lipids distributed in symmetrical leaflets and solvated with 6000 water molecules (Table 3.1). This corresponds to excess full hydration conditions with 37.5 water molecules per lipid. Despite the characteristic low water content of the ICLM-SC, the pioneering work of Das et. al. was conducted at full hydration. In that work, the excess water was considered to be "required to stabilise the bilayer structure, and can be viewed as a replacement of the layering field imposed by the flat corneocytes" (129). In addition, despite the moderate structural changes predicted for bilayers at low hydration (in multilayer systems, section 2.3.2), the reported permeability coefficients of water are in the same order of magnitude as those predicted for full hydration (section 2.4.2.2).

Table 3.1. Description of the contents of the simulation system.

RESNAME	Atoms	Num	Common name(s) and description
CR224	49	64	Ceramide NS (24:0), formerly known as ceramide 2. Non-hydroxyl free fatty acid (C24:0) and sphingosine backbone (C18)
FA24	27	64	Lignoceric acid, tetracosanoic acid (C24:0) Saturated free fatty acid of 24-carbon hydrocarbon tail.
CHOL	29	32	Cholesterol Parameters of Höeltje and Brandt 1998 (150)
SOL	3	6000	SPC water

Topology files and a starting configuration for each lipid species were obtained from the work of Das and Olmsted, and Hoopes et al. (152, 159). The simulation system was assembled using Packmol (179), and the output configuration was energy minimised using the steepest descents algorithm in GROMACS, allowing 10^5 steps of size 0.001 nm and a maximum force of 250 kJ/mol∗nm).

3.2.3 Equilibration of the bilayer

All simulations were performed using rectangular periodic boundary conditions (with the longer dimension corresponding to the z-axis and the normal to the bilayer plane) and a time step of 2 fs. The centre-of-mass (COM) motion was removed linearly at every step and applied to the groups that constitute the simulation system (i.e. lipids and water). The LINCS algorithm (180) was used to constrain the lengths of all bonds. Non-bonded interactions were evaluated using a single-range cut-off scheme, whereby interactions within a 1.4 nm cut-off were calculated at every step, and the pair list was updated every five steps. To account for electrostatic interactions beyond the cut-off, a reaction field (181) was applied with a relative dielectric constant (ε_r) of 62. This was done for consistency with the interaction scheme used in the development of the GROMOS 54A7 force field (110, 182), which was used here to model the lipids and permeant molecule. Both GROMOS 54a7 parameters and the GROMOS-compatible lipid force field have been shown to reproduce the structure and dynamics of a wide range of phospholipid bilayers (106, 182), and have been used to represent the lipids of the ICLM-SC in conjunction with the SPC model of water (183), as discussed in section 2.3.

A series of NPT simulations was run during which the area per lipid (APL) was monitored as a proxy for bilayer stability. The temperature was kept at 305 K (32°C, the physiological temperature of the skin) using the Berendsen thermostat (184) with coupling constant τ_T = 0.5. The pressure was controlled with the Berendsen barostat for all equilibration simulations. The barostat coupling constant (τ_p) was sequentially decreased from 0.5 to 0.2 to 0.1 ps in intervals of 100 ns, thus increasing the frequency of action of the barostat every 100 ns. The simulation with the lowest τ_p ran for 700 ns until the APL was stable for at least 300 ns.

APL was defined as the area of the cross section of the simulation cell, divided by the number of lipids in one leaflet. Considering that each lipid species occupies a distinct area, this is effectively an average APL of the three lipid species. The dimensions of the box were obtained using the *g_energy* module in GROMACS and selecting the X and Y dimensions of the simulation cell (L_x and L_y, respectively). The output was processed to obtain the average APL [nm^2] as indicated by Equation 3.1.

$$\langle APL \rangle = \frac{(L_x) * (L_y)}{80 \; lipids}$$

Equation 3.1

The bilayer was further equilibrated using the Nose-Hoover thermostat (185) and the semi-isotropic Parrinello-Rahman barostat (186) for over 1 μs and the APL was monitored as described above. These barostat and thermostat were used for all the remainder of this work. To confirm that the bilayer was in a gel-like state, the mass

density profile [kg/m^3] of the system was computed using the *g_density* module in GROMACS and selecting each lipid species, water, and the lipids as groups. Furthermore, the APL of each lipid species was computed using the VMD plug-in for Voronoi tessellation (187), by selecting the oxygen atoms of each lipid. The APL was compared to previously reported data of pure bilayers; however, this did not provide any additional information in the context of the equilibration of the bilayer.

3.2.4 Insertion of the dipeptide in the simulation cell

The last trajectory frame of the above NPT equilibration simulation was used as a starting configuration for the manual insertion of the permeant molecule (uncharged with uncapped termini in all cases) in the bulk water region.

Figure 3.2.1 Representation of the simulation system showing the ternary lipid bilayer in the centre of the simulation cell surrounded by water. This bilayer represents the SC featuring a 2:2:1 molar ratio for CER (blue), CHOL (orange) and FFA (green), respectively. Three landmark COM distances between the Ala-Trp dipeptide and the bilayer are marked for reference. The right-hand side panel shows the definition of vectors and torsion used to describe the orientation and conformations of the Ala-Trp.

To avoid steric clashes with the solvent, all water molecules within 0.3 nm of the small permeant molecule were removed. This was performed using VMD 1.9.2 (188),

manually editing the resulting number of atoms, and re-numbering all residues in the structure file using the *editconf* module in GROMACS. The resulting structure file is represented in Figure 3.2.1.

3.2.5 Pull simulation

The system was subjected to a pull simulation to produce the starting configurations for the US windows with the Ala-Trp dipeptide at several insertion depths. The reaction coordinate selected to represent the translocation path of the dipeptide across the bilayer was the z-axis component of the distance between the COM of the bilayer and the COM of the permeant molecule, and this is henceforth referred to as the COM distance. The pull simulation covers the translocation path from the bulk water (COM distance > 4.0 nm) to the centre of the bilayer (COM distance = 0.0 nm). This was achieved using the following options in the molecular dynamics parameter (MDP) file (Table 3.2). This file contains the instructions to run the simulation (e.g. the barostat and thermostat mentioned above) and is one of the inputs for the *grompp* module in GROMACS.

Table 3.2. Options for the pull simulation that are included in the MDP file

MDP option	Choice	Description
pull	constant-force	Pull the peptide towards the centre of the bilayer
pull_dim	N N Y	Y/N for each dimension (x, y, z), only pulling along the z axis
pull_geometry	distance	Distance vector between group0 and group1
pull_ngroups	1	Pull only one group towards the COM of group0
pull_group0	Lipids	Lipid bilayer as an additional group created in the index file
pull_group1	Protein	Refers to the Ala-Trp dipeptide
pull_k1	120	Force constant acting to pull the COM of group1
pull_nstxout	500	Frequency of output of positions of the groups
pull_nstfout	500	Frequency of output of forces acting on group1

The pull simulation trajectory was visualized using VMD 1.9.2 (188) to make sure that no significant disruption to the membrane was caused by pulling the peptide into the bilayer. Starting structures for some of the US windows were obtained using the *trjconv* module in GROMACS and said pull simulation trajectory as input. This module produces a structure file from a frame of a trajectory file as indicated by the user. To select a frame one can search the *pullx.xvg* file to find a time frame in which the COM of the dipeptide was near the intended reference COM distance of the US window of

interest. The *pullx.xvg* file is produced by the *mdrun* module as the simulation is run (by indicating the *-px* option), and contains a time series of the z-coordinates of the COM of groups indicated in the MDP file (i.e. lipids and Ala-Trp dipeptide). The starting configurations for the US windows that complete the translocation path were obtained from the neighbouring windows. As before, this was done using the *trjconv* module, in this case using trajectories of US windows as input (as opposed to the pull simulation). This was systematically done by searching in their corresponding *pullx.xvg* files for the latest frame of the trajectory which displayed the nearest COM distance of the dipeptide to the desired US window reference. Conventional US

Neighbouring US windows were spaced at intervals of either 0.2 or 0.1 nm to achieve sufficient coverage of the reaction coordinate. All US windows used a harmonic position restraint with a force constant of 500 kJ mol^{-1} nm^{-2} acting on the COM of the permeant molecule. Preliminary analyses were conducted for simulation times of at least 100 ns per US window, yielding a combined simulation time of ≈3.3 μs. Additional simulation times were used for each US window in an attempt to appropriately compare performance (in terms of computational effort) with the enhanced sampling obtained with US-REST3 (Section 3.2.9 Simulation times, and Table 3.7)

3.2.6 Selective replica exchange with solute tempering (REST3)

For the REST3 simulations the exchange attempt frequency was set to 0.1 ps, following Sindhikara et al. (189), and replica exchange acceptance percentages between 20-30% were considered to be optimal.

Table 3.3 shows the additional section of the topology file required for the implementation of REST3. The two headings [scale_vdw] and [scale_q] require lower triangular matrices with the values of scaling factors that will be applied to the non-bonded interactions (van der Waals and electrostatic, respectively). In these matrices, the number of rows and columns and their order, matches the list of components outlined in the section [system] of said topology file. For example, the first row of the matrix, featuring a value of 1.0, indicates that CR224 will have full non-bonded interaction forces with itself. This is done similarly for the remaining lipid-lipid and lipid-water interactions, as indicated by the following rows of the matrix. In contrast, the first value of the last row indicates that the non-bonded interactions between CR224 and the dipeptide are multiplied by the AAA scaling factor. This means that every replica (in every US window) had a unique topology file in which AAA was replaced by the corresponding scaling factor.

Table 3.3. Topology file sections indicating scaling factors (AAA) for non-bonded interactions between pairs of components of the simulation cell.

```
[ scale_vdw ]
1.0
1.0 1.0
1.0 1.0 1.0
1.0 1.0 1.0 1.0
AAA AAA AAA AAA 1.0

[ scale_q ]
1.0
1.0 1.0
1.0 1.0 1.0
1.0 1.0 1.0 1.0
AAA AAA AAA AAA 1.0
```

Table 3.4 shows the parameters in the MDP file that are required for the REST3 implementation. LAMBDA (init-lambda-state) can take one of two values (1 or 0.999) depending on whether the replica is even or odd numbered in the replica scheme.

Table 3.4. Free energy parameters included in the MDP file.

```
; Free energy variables
free-energy          = yes
couple-moltype       = system
couple-lambda0       = vdw-q
couple-lambda1       = vdw-q
couple-intramol      = yes
init-lambda          = -1
init-lambda-state    = LAMBDA
delta-lambda         = 0
nstdhdl             = 50
fep-lambdas          = 0.00 0.00 0.00 0.00 0.00 0.00 0.00 0.00 0.00 0.00 0.00
mass-lambdas         = 0.00 0.00 0.00 0.00 0.00 0.00 0.00 0.00 0.00 0.00 0.00
coul-lambdas         = 0.00 0.00 0.00 0.00 0.00 0.00 0.00 0.00 0.00 0.00 0.00
vdw-lambdas          = 0.00 0.00 0.00 0.00 0.00 0.00 0.00 0.00 0.00 0.00 0.00
bonded-lambdas       = 0.00 0.00 0.00 0.00 0.00 0.00 0.00 0.00 0.00 0.00 0.00
restraint-lambdas    = 0.00 0.00 0.00 0.00 0.00 0.00 0.00 0.00 0.00 0.00 0.00
temperature-lambdas  = 0.00 0.00 0.00 0.00 0.00 0.00 0.00 0.00 0.00 0.00 0.00
calc-lambda-neighbors = 1
init-lambda-weights  =
dhdl-print-energy    = no
sc-alpha             = 0
sc-power             = 1
sc-r-power           = 6
```

sc-sigma	= 0.3
sc-coul	= no
separate-dhdl-file	= yes
dhdl-derivatives	= yes
dh_hist_size	= 0
dh_hist_spacing	= 0.1

3.2.6.1 Choice of scaling factor and replica ladder

The first parameter to be optimized was the scaling factor applied to the non-bonded interactions that is required in order to achieve sampling enhancement. The underlying premise is that a region posing higher resistance to the movement of the permeant will require more effort to increase the sampling of the configurational space of the dipeptide. Therefore, the non-bonded interactions need to be more "tempered", in this case by using a smaller scaling factor. Sampling enhancement is regarded as the exploration of new regions of configurational space as defined by the angle histograms of the orientation and the conformation angles. This enhancement was assessed as changes in the profiles of the three (orientational and conformational) angles that were defined for the Ala-Trp dipeptide (top panel in Figure 3.2.1), which will be explained in section 3.2.8. For each angle at three selected US windows (COM distances of 2.8, 1.3 and 0.0 nm), the enhancement of sampling was assessed by comparing to the corresponding angle distribution obtained from the converged US simulation as a reference.

The second parameter to be optimized was the exchange probability. This required consideration of two other variables apart from the interaction scaling factor: the number of replicas needed to arrive at such scaling factor from the ground replica, and the spacing between replicas. The combination of scaling factors with the spacing and number of replicas is regarded as a replica scheme. For each US window, a replica scheme was chosen to ensure adequate exchange probabilities.

3.2.6.2 Starting configurations

Configurations were obtained from the last frame of each conventional US simulation (100 ns long).

3.2.7 Configurational space of the Ala-Trp dipeptide

The two vectors and one tortional angle shown in the top panel in Figure 3.2.1 were used to define the sampling of orientational and conformational space of the Ala-Trp dipeptide. The orientation was defined using two orthogonal vectors. The first orientation vector is defined from the C_α of Ala to the C_α of Trp, as seen in (A) in the same figure. The second orientation vector is defined as the normal vector to the peptide bond plane, which in turn is defined by its three heavy atoms (N-C=O), as

seen in (B) in the same figure. The angle between each of these two vectors and the z-axis was used to measure the orientation of the peptide. The conformation of the dipeptide was defined by the relative orientation of the side chains and was measured by the dihedral angle between the two C_α and the two C_β, as seen in (C) in the same figure. This angle determines if the side chains are in *cis* conformation at $0°$, in *trans* conformation ($180°$) or any other intermediate conformation. The three angles were measured (in degrees) using the *gmx_gangle* module in GROMACS 5. This module requires an index file with the groups containing the atoms that describe the vectors of interest.

The following are the selections used to create said index file using the *make_ndx* module. The groups required to measure the three angles are indicated in Table 3.5. For example, the syntax needed to select the carbon alpha of residue 1 is: r 1 & a CA.

Table 3.5. Definition of index groups for the two orientation vectors and the conformation angle.

Group	Atoms	Description
"Calpha"	2	r1 & a CA | r2 & a CA
"PepBond"	3	r1 & a C O | r2 & a N
"Dihedral"	4	r1 & a CA CB | r2 & a CA CB

Table 3.6 lists the options used to measure each of the three angles using the module *gmx gangle* in GROMACS.

Table 3.6. Computation options used for each angle measured using the gmx gangle module (GROMACS 5)

Angle	-g1	-g2
"Calpha"	vector	Z
"PepBond"	plane	Z
"Dihedral"	dihedral	

3.2.7.1   Normalization of orientation angles

The probability profiles (histograms) of orientation angles were normalized to account for the bias that favours equatorial angles measured in 3D, when projected in 2D. This is achieved by dividing the probability by the sine of the angle in radians. The effect of this normalization is easily noticeable when the peptide is free to rotate, whereby the probability distribution changes from a bell shape in the raw data to a flat shape after normalization.

3.2.8 Simulation times

Table 3.7 indicates total simulation time in ns (including equilibration) allowed for each US window and for both enhanced sampling methods. For the US-REST3 approach, the table details the number of replicas used, and the combined simulation time. The latter is calculated as the simulation time per replica multiplied by the number of replicas. Note that the simulation time per replica also corresponds to the simulation time of the ground replica (no scaling of non-bonded interactions), which is used for all analyses of REST3 simulations.

The last row of the table presents a summation of each column, indicating comparable simulation times (i.e. computational effort) across methods. The total simulation time of the permeation of the Ala-Trp dipeptide with conventional US is 25.88 µs, which was achieved with varying simulation times per window in 28 windows. For US-REST3, the summation of the total simulation time is 24.58 µs, which was achieved by simulating 215 replicas in 23 windows. However, the simulation time that was used for the estimation of permeability (and free energy) with US-REST3 corresponds to the summation of the last column, i.e. the simulation times of the ground replicas only (2.64 µs). In terms of wall-time required to achieve these values, the US-REST3 approach required 48 h of run time with a performance of the code of about 50 ns/day. In contrast, the wall-time required to complete the conventional US windows was longer for all windows, even with a performance of the code twice as fast (above 100 ns/day). For example, the longest conventional US times are 1.2 µs per window, which required more than 240 h of run time. The last consideration in comparing the methods is the wait time between runs. This is due to the policy of shared HPC facilities, which allows for 24 h jobs only. The wait time was difficult to predict and account for since it depended on the decisions made by the scheduler (SLURM). However, in the example above there were 10 events of wait time for the conventional US simulations compared to only one for the US-REST3 simulation.

Table 3.7. Simulation times per US window are given in ns for both enhanced sampling methods for every COM distance.

Conventional US	∑REST3	COM distance	N replicas	per replica
600	600	0.0	5	120
600	600	0.2	5	120
600	600	0.4	5	120
600	600	0.6	5	120
1100		0.7		
1100	1000	0.8	10	100
	1100	0.9	11	100

Conventional US	∑REST3	COM distance	N replicas	per replica
1100	1200	1.0	10	120
	1320	1.1	11	120
960	960	1.2	8	120
960		1.3		
960	960	1.4	8	120
	1320	1.5	11	120
1100	1320	1.6	11	120
1100	1320	1.8	11	120
1100		1.9		
1100	1320	2.0	11	120
1100	1320	2.2	11	120
1100	1320	2.4	11	120
1100	1320	2.6	11	120
1200	1200	2.8	10	120
1200	1200	3.0	10	120
1000	1000	3.2	10	100
1000	1000	3.4	10	100
1000		3.5		
	1000	3.6	10	100
1000		3.7		
1000	1000	3.8	10	100
1000		3.9		
1000		4.1		
100		4.3		
100		4.5		
		4.8		
25880	**24580**		**215**	**2640**

3.2.9 Free energy profile

The free energy profile of the interaction between the permeant molecule and the bilayer, also known as potential of mean force (PMF), was obtained using the weighted histogram analysis method (WHAM) with the *g_wham* module in GROMACS (190). This was performed by assigning weights according to the integrated autocorrelation times (IACT) of each window, by specifying the *-ac* option. The reference value of zero for the free energy was set at a COM distance of 4.0 nm, which corresponds to the bulk water region, by specifying the *-zprof0* option. This reference was chosen based on the stable, flat shape of the PMF for distances larger than 3.9 nm. The temperature was set to 305 K (with the option *-temp*). The standard deviation of the free energy was calculated with the in-built bootstrap function (*-bs*

200). The first 20 ns of each conventional US simulation were discarded as equilibration. The first 10 ns of each US-REST3 simulation were discarded as equilibration. The free energy profile was deemed to have converged when consecutive PMFs (i.e. in increments of simulation time) were within a standard deviation of each other. A second criteria to assess convergence was the comparison of the PMFs obtained with the first and second halves of the simulation trajectory (after equilibration).

3.2.10   Diffusion coefficient

D(z) estimates were obtained following Hummer's derivation, which relates the position autocorrelation function to the friction (and thus its diffusivity) experienced by a solute under a US harmonic restraint (48). The integrated autocorrelation time (IACT or τ) of the position of the COM of the permeant molecule for each US window was retrieved from the *g_wham* output file (with the option *-oiact*). This feature of the *g_wham* module calculates the correlation function (R) as defined in Equation 3.2 for each of the US windows along the reaction coordinate (COM distance or ξ). For robustness in the calculation of the IACT of each US window ($τ_i$) with Equation 3.3, and in consideration of the typically noisy correlation functions produced from US simulations, the decay threshold is predefined to 0.05 (190). Finally, the one-dimensional diffusion coefficient for a given US window is calculated as indicated by Equation 3.4:

$$R_i(\Delta t) = \frac{\langle(\xi_i(t) - \langle\xi_i\rangle)\,(\xi_i(t + \Delta t) - \langle\xi_i\rangle)\rangle}{\sigma_{\xi_i}^2} \qquad \text{Equation 3.2}$$

$$\tau_i = \sum_{\Delta t=1}^{\infty} R_i(\Delta t) \qquad \text{Equation 3.3}$$

$$D(z) = \frac{var(z)}{\tau_i} \qquad \text{Equation 3.4}$$

The variance in Equation 3.4 was calculated from the time series of COM positions in the *z*-coordinate (using the *pullx.xvg* file) following the procedure outlined by Carpenter et al. (122).

3.2.11   Permeability coefficient

The equation for the one-dimensional permeability of small molecules across lipid bilayers has been derived from the theoretical framework for steady-state mass transport (24), in which the permeability, *P*, is defined as Equation 1.3 (in section

1.5.2 Permeability coefficients from MD) and is given in [nm/ps], where T is the absolute temperature, ΔG is given by the free energy profile (or PMF) in [kJ/mol] and $D(z)$ is the one-dimensional position-dependent diffusion coefficient defined in Equation 3.4, which is given in[cm^2/s].

3.3 Results and discussion.

3.3.1 Equilibration of the bilayer

The mass density profile [kg/m^3] of the simulation system was calculated along the longer dimension of the simulation cell as a time average over the 1.2 μs equilibration simulation in the NPT ensemble. The shape of the mass density profile of the lipids is consistent with the distinctive gel-state profile of bilayers containing ceramides, and with ternary mixtures of the same components (129, 152). The centre of the bilayer provides a plane of symmetry and is located at z = 0, corresponding to a COM distance of 0.0 nm. The simulation cell extends up to 5.4 nm away from the centre plane in both directions, but only the positive z-axis from 0 to 4.0 nm is shown for clarity.

There are four regions of the simulation cell that can be identified in the mass density profile shown in Figure 3.3.1 (top panel). The hydrophilic region commences where the density profile of water becomes flat, and reaches bulk water density. The bulk water region is found within the hydrophilic region, approximately from 1 nm away from the bilayer interface to the boundaries of the simulation cell (≈3.8 to 5.4 nm). The interface is the region where the mass density profile for water and lipids intersect, which contains the head groups of CER and FFA and extends up to 2.8 nm away from the bilayer centre, whereas the hydroxyl group of CHOL is located slightly below the interface. The high-density region of the hydrophobic core is located below the head groups and is identified as the lipid mass density (black) is higher than the bulk water density. The planar rigid portion of CHOL (orange) is located in this region. Finally, the low-density region of the hydrophobic core is found near the bilayer centre from 0 to ≈0.8 nm. This region contains the so-called interdigitating region, in which lipid tails of opposite leaflets can interact with each other, as seen by the modest increment in the CER mass density profile (blue) from 0 to 0.2 nm COM distance.

The bottom panel in Figure 3.3.1 shows the time evolution of the representative APL [Å^2] of each lipid species, calculated with the Voronoi tessellation plug-in for VMD. As expected, CER covers a larger area than CHOL and FFA.
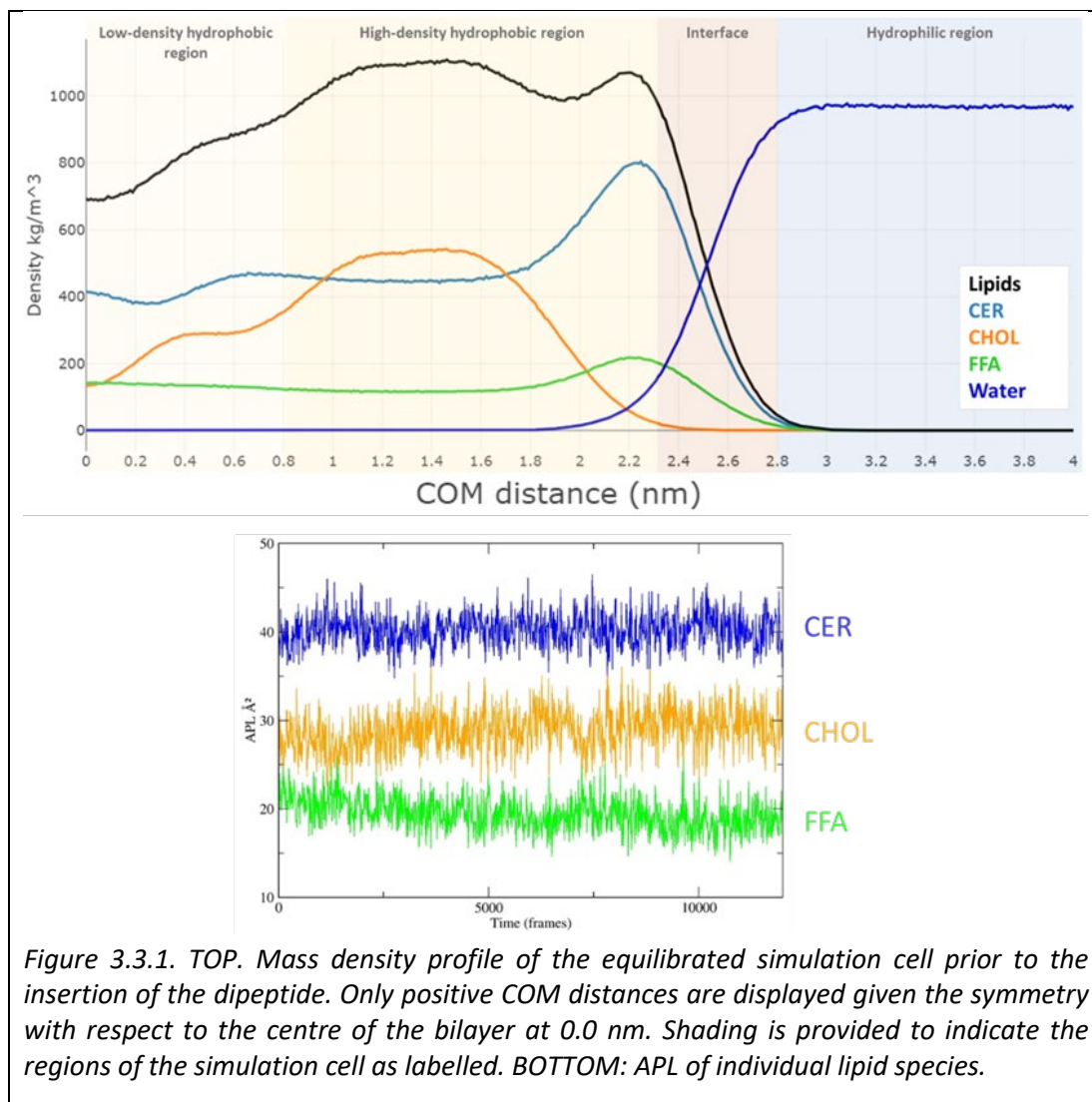
Figure 3.3.1. TOP. Mass density profile of the equilibrated simulation cell prior to the insertion of the dipeptide. Only positive COM distances are displayed given the symmetry with respect to the centre of the bilayer at 0.0 nm. Shading is provided to indicate the regions of the simulation cell as labelled. BOTTOM: APL of individual lipid species.

3.3.2 Sampling of configurational space with conventional US simulations

This analysis was conducted for 100 ns of conventional US trajectories to characterize the behaviour of the dipeptide at four representative regions of the simulation cell, represented by US windows at 4.8 nm (blue), at the interface at 2.8 nm (orange), the midway into the hydrophobic core at 1.3 nm (green), and in the bilayer centre at 0.0 nm (red). The top panel of Figure 3.3.2 shows the distributions of the angle between the C_α to C_α vector (indicated by the green arrow) and the z-axis, whereas the bottom panel shows the distributions of the angle between the vector normal to the peptide bond plane (dotted area) and the z-axis. For both orientation angles, at a COM distance of 4.8 nm, the dipeptide is considered to be free of the effects of the bilayer and, thus, can explore all orientations.

Similarly, the dipeptide is almost completely free to rotate at the bilayer centre (i.e. at a COM distance of 0.0 nm). Not surprisingly, for both orientation angles, when the dipeptide is inserted into the high-density region of the hydrophobic core (US COM distance of 1.3 nm, green), the angle histograms show the most biased distributions with the highest probability peaks. This indicates that this region poses the highest resistance to the free rotation of the dipeptide. The histograms for a US COM distance of 2.8 nm (orange) show moderate restrictions for C_α to C_α angle (top panel), and are intermediate between free rotation in the bulk and the restrictive environment of the high-density region.

Figure 3.3.2. Histograms of the distribution of the sampling of two orientation angles defined for the Ala-Trp dipeptide at four representative US windows (COM distances of 0.0, 1.3, 2.8 and 4.8 nm) during 100 ns long simulations.
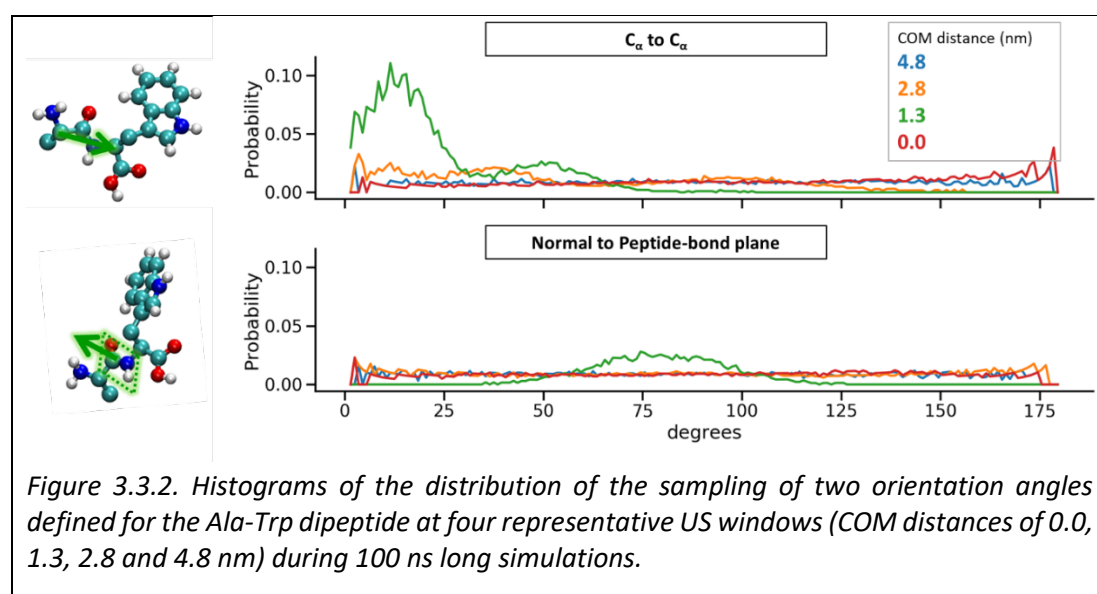
The same analysis was conducted to assess the conformational sampling of the dipeptide in the four regions of the bilayer, and the corresponding dihedral angle distributions are shown Figure 3.3.3. This figure also includes detailed schematics to define the dihedral angles as a proxy for the conformation of the dipeptide. In the bulk water region at a COM distance of 4.8 nm (blue), the dihedral angle histogram shows a bimodal distribution with modes at -120° and 110°, revealing what can be considered as the equilibrium distribution in an aqueous environment. The angle distribution at the interface (at a COM distance of 2.8 nm, orange) shows remarkable similarity to the aqueous environment despite being in close proximity to the head groups of the lipids. In contrast, when the dipeptide is embedded in the high-density region, the dihedral angle distribution becomes narrow with a sharp peak (at a COM distance of 1.3 nm, green). Lastly, a bimodal distribution with inverted modes at 110° and -120° is observed when the dipeptide reaches the bilayer centre (at a COM distance of 0.0 nm, red). This can be interpreted as the equilibrium distribution in a hydrophobic environment.

Figure 3.3.3.Dihedral angle histograms of the Ala-Trp dipeptide at four representative US windows (COM distances of 0.0, 1.3, 2.8 and 4.8 nm) with schematic representation of the dihedral angle and three most visited angles.
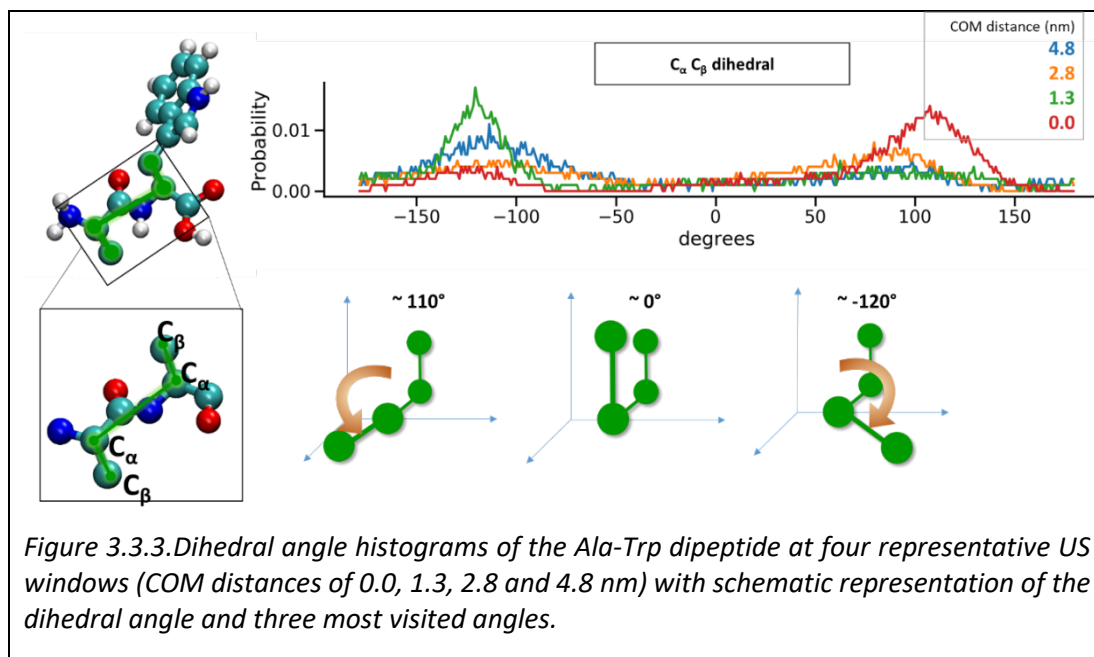
This preliminary analysis confirmed that the regions of the bilayer pose different resistance to the sampling of orientations and conformations of the dipeptide. The region with the highest resistance is the dense-hydrophobic region (represented by US at a COM distance of 1.3 nm), as indicated by the more biased probability distributions in all three angles.

3.3.3 Choice of replica ladder schemes

The first tests were conducted at the three regions where the dipeptide is in direct contact with the bilayer. Three scaling factors (0.5, 0.2 and 0.1) were tested for their ability to change the shape of the angle distributions obtained with the conventional US simulations described above. The effect of downscaling the interactions between the dipeptide and the other components of the system is revealed by changes in the shape of the angle distribution histograms, which indicate changes in the sampling of orientations: the broader and flatter the distribution the more rotational sampling is achieved.

The distributions of the two orientation angles are shown in Figure 3.3.4, where the left column is the C_α angle, and the right column is the normal vector to the peptide bond. It is evident that none of the scaling factors were able to affect the angle distributions at the bilayer centre (bottom row). This supports the premise that the peptide can rotate freely in the interdigitating region of the bilayer. Scaling factors of 0.1 (blue), 0.2 (orange) and 0.5 (green) are equally successful for both orientation angles at the bilayer surface at a COM distance of 2.8 nm (top row), suggesting that the same maximum enhancement effect is reached. However, the enhancement of

78

sampling is not as significant when the dipeptide is in the high-density region of the bilayer at a COM distance of 1.3 nm (middle row), as indicated by the C_α angle histograms.

Figure 3.3.4. Comparison of histograms of the orientation angle distributions obtained from simulations where non-bonded interactions were downscaled at three COM distances (0.0, 1.3 and 2.8 nm). Three scaling factors of the non-bonded interactions are 0.1 (blue), 0.2 (orange), and 0.5 (green).
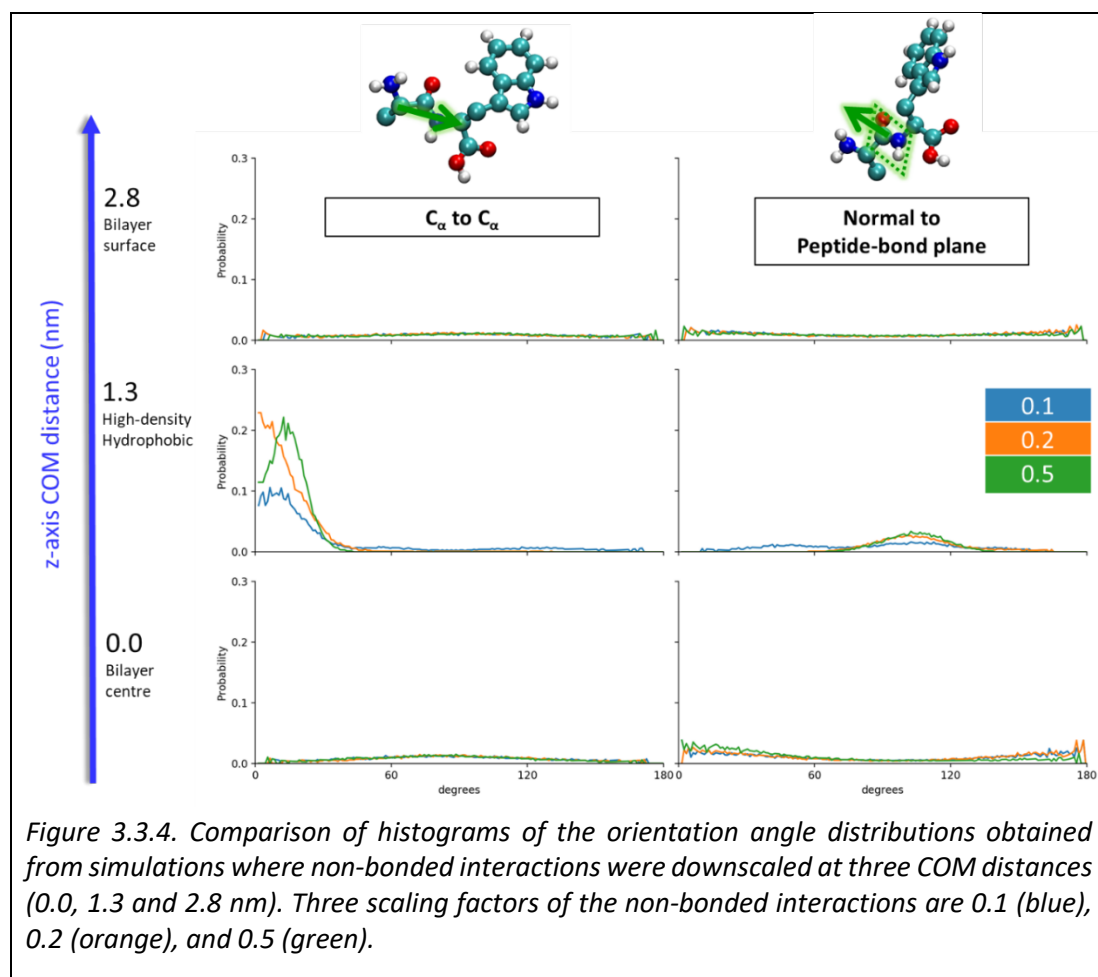
Although the three scaling factors tested yield biased distributions, it is clear that the bias obtained with a scaling factor of 0.1 is more modest and enables the sampling of more orientations for both angles. These results highlight the higher resistance that this region poses to the movement of the dipeptide. Additionally, the clear differences between the regions of the bilayer suggest differences in the scaling factors required to enhance sampling of orientations in each region.

The sampling of conformations described by the dihedral angle were analysed with the same scaling factors and at the same COM distances. As can be observed in the bottom panel of Figure 3.3.5, the downscaling of interactions between the dipeptide and the other molecular species in the simulation cell does not change the shape of the equilibrium distributions of angles in the hydrophobic environment at the centre of the bilayer. Instead it modestly accentuates the preference for a dihedral angle value of 110 ° at the expense of the second angle mode (-120 °). For the dense-

hydrophobic region (i.e. a COM distance of 1. 3nm), the downscaling of interactions enables the sampling of a "closed-book" conformation, characterised by a dihedral angle of 0°, which could be considered a transition state between the modes of the two equilibrium states defined previously. The "closed book" conformation of the dipeptide is likely to represent a compact conformation of the dipeptide, which allows a reduction in drag resistance in this region. With a downscaling factor of 0.1 (blue) the conformations visited have similar probability for the three modes, whereas with a downscaling factor of 0.2 (orange) the "closed book" conformation is more likely than the other two modes. At this distance with a downscaling of 0.5 (blue) the dipeptide does not visit the characteristic modes of the two equilibrium states, but instead is restricted to sample only the transition state given by "the closed book" conformation. Lastly, the dihedral angle distributions observed at the bilayer surface are very similar to the equilibrium in the hydrophobic environment of the low-density hydrophobic region (i.e. at a COM distance of 0.0 nm, bottom panel).
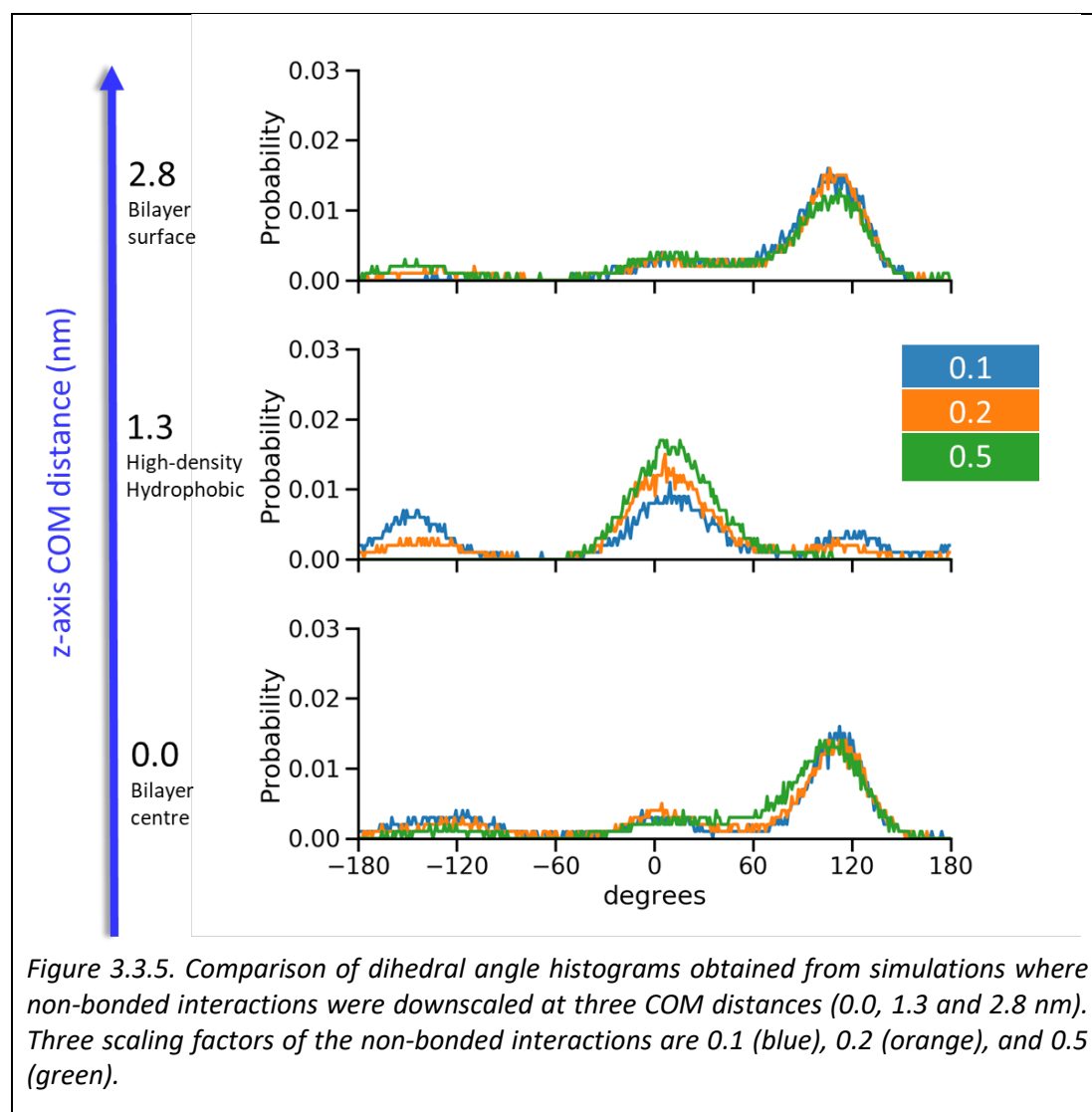
Figure 3.3.5. Comparison of dihedral angle histograms obtained from simulations where non-bonded interactions were downscaled at three COM distances (0.0, 1.3 and 2.8 nm). Three scaling factors of the non-bonded interactions are 0.1 (blue), 0.2 (orange), and 0.5 (green).

This suggests that the downscaling of interactions at the interface causes a shift from the equilibrium distribution in a hydrophilic environment to an equilibrium distribution in a hydrophobic environment with all downscaling factors tested.

Based on these findings, the next parameters that needed to be optimized were the number of replicas and the increments in scaling factor that would ensure the enhancement of sampling of orientations and conformations with an adequate exchange probability, as well as with an efficient use of computational resources. Figure 3.3.6 shows schematics representing the four replica schemes that were selected and applied to the different regions of the bilayer, in consideration of the three conditions mentioned previously. The label 'r05eq' refers to a scheme with five replicas that are equidistant (eq) in the spacing of their scaling factors from 1.0 (no downscaling, ground replica) to 0.5 (50% strength of all non-bonded interactions). The r05eq replica scheme was only applied to US windows in the low-density hydrophobic region. The three remaining replica schemes cover scaling factors from 1.0 to 0.1 and were applied to the other regions of the simulation cell. The label 'r08ue' corresponds to a replica scheme that features uneven spacing of scaling factors between replicas. This scheme was created in response to the high exchange probability observed between replicas with higher scaling values, and features eight replicas in consideration of the computational resources needed. The label 'r10eq' refers to a replica scheme with ten replicas whose scaling factors are spaced in equidistant increments. Lastly, the label 'r11eq' corresponds to a replica scheme featuring 11 replicas with uneven spacing in the scaling factors: larger spacing towards middle values and shorter spacing towards the edges of the replica ladder. This scheme was applied to most US windows located in the dense hydrophobic region.

The bottom panel in Figure 3.3.6 shows the exchange probability values obtained for these replica schemes when applied to each US window. The x-axis is the exchange number between neighbouring replicas such that a value of 1 corresponds to the exchange between replicas 0 and 1. Given that replicas 0 and 1 in different replica schemes have different scaling factors, the x-axis indicates the replica number for clarity. Each series line in the depth axis corresponds to an US window (covering the insertion depth) that was allocated either the r05eq, r08ue, r10eq or r11eq replica scheme.
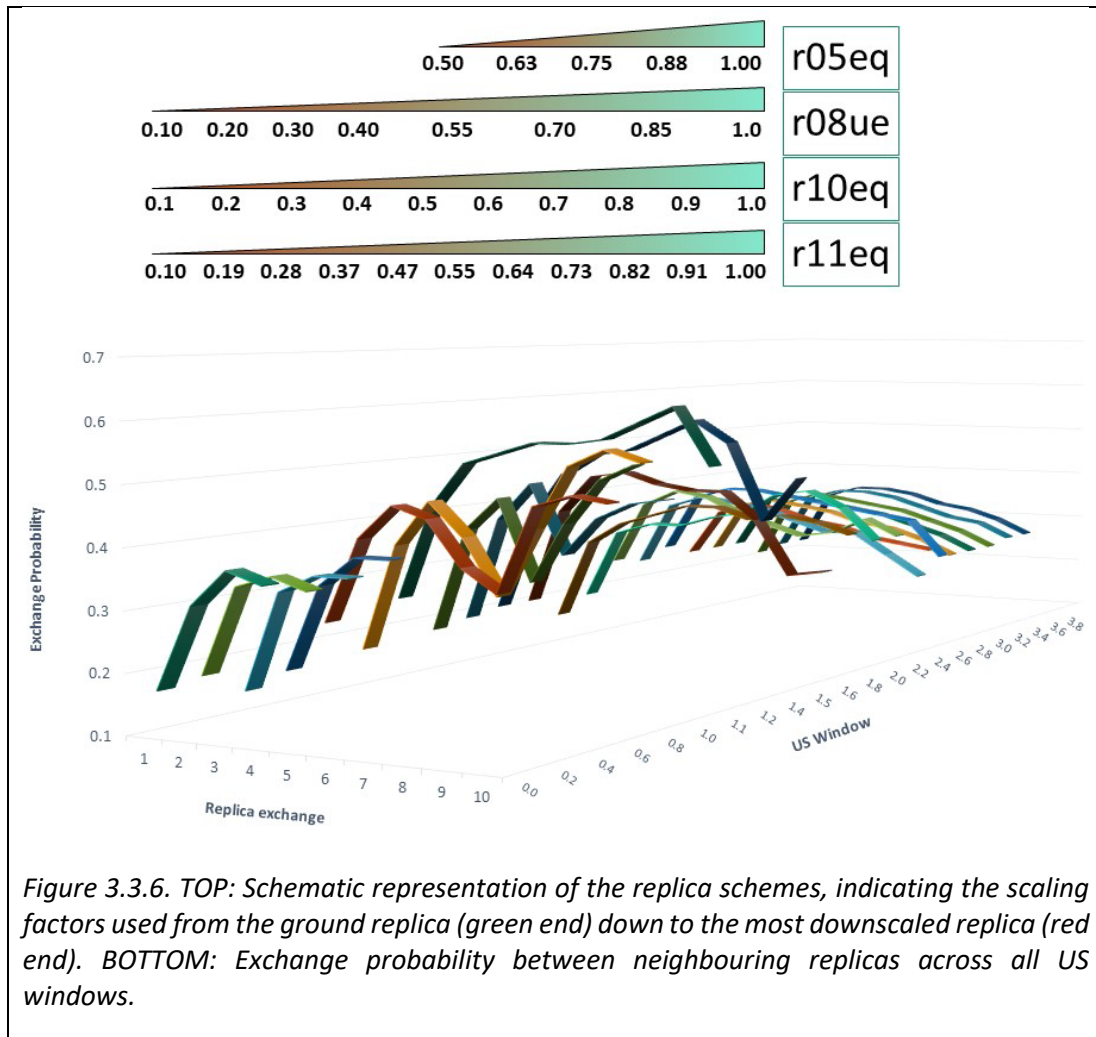
Figure 3.3.6. TOP: Schematic representation of the replica schemes, indicating the scaling factors used from the ground replica (green end) down to the most downscaled replica (red end). BOTTOM: Exchange probability between neighbouring replicas across all US windows.

The lowest exchange probabilities were observed in the lower end of the scaling factor ladder, between replicas with scaling factors of 0.1 and either 0.19 or 0.2 (depending on the replica scheme). In contrast, the high exchange probability observed for the rest of the replica ladder is nearly always above 30% regardless of the spacing between neighbouring replicas. Given the high exchange probability, there is room for further improvement in the use of computational resources, which could be achieved with further changes to the spacing of replicas in the middle and high end of the replica ladder. However, the apparent non-linear response of the exchange probability to the spacing of the replicas throughout the COM distances would make this a time-consuming task. Hence, no further schemes were tested.

3.3.4 Sampling of configurational space with US-REST3

Figure 3.3.7 shows a comparison of the performance of the conventional US and the US-REST3 simulations in the sampling of orientations and conformations of the dipeptide at selected insertion depths. The performance of US-REST3 is expected to be less successful in enhancing the sampling of configurations than the test simulations of interaction downscaling described in the previous section. This is because those configurations that are easily sampled at the lower end of the replica ladders have to meet the exchange criteria to *trickle up* into the ground replica (where all non-bonded interactions are 100% of their strength and in which the angle distributions are assessed). As discussed earlier, for the two orientation angles the sampling can be considered uniform (i.e. freely rotating) when all orientations have a similar probability. This is the case for all US windows located beyond a COM distance of 3.8 nm (i.e. in the bulk water region).

In Figure 3.3.7 the left and middle columns correspond to the C_α angle and normal-to-peptide bond angles, respectively, and the right column corresponds to the dihedral angle. The first row of plots shows the sampling of angles obtained with conventional US in the window at a COM distance of 3.9 nm, indicating the free rotation of orientations and the hydrophilic equilibrium shape of the dihedral angle histogram. The following rows in Figure 3.3.7 show the performance of US-REST (blue) compared to conventional US (orange). At the bilayer interface at a COM distance of 2.6 nm (second row), US-REST shows substantial improvement in the sampling of both orientation angles, as indicated by the broader distributions with lower probabilities. As revealed by the mass density profile in Figure 3.3.1, at this COM distance the dipeptide can interact with water and with the polar head groups in CER and FFA. The strong nature of these interactions likely causes the strong bias in the orientations observed with conventional US. At the same distance, the distribution of dihedral angles indicates that US-REST3 enables the dipeptide to retain the conformations of the hydrophilic equilibrium, whereas conventional US yields a shape that resembles the hydrophobic equilibrium.

In Figure 3.3.7, the high-density hydrophobic region is represented by a COM distance of 1.6 nm (third row). In this region, US-REST3 moderately improves the sampling of the C_α angle, as indicated by the larger range of angles transiently visited. In contrast, the sampling of the other orientation angle appears as biased as the conventional US is, but with opposite skewness. The behaviour of the dihedral angle with both sampling methods does not resemble any of the patterns described so far. The conventional US samples the three modes described previously with a preference for -110°, whereas US-REST3 preferentially samples the mode at 120°. A novel

conformation of almost fully "open book" with dihedral angle nearly 180° is also visited with US-REST3. Lastly, and in agreement with the previously discussed results, US-REST3 does not affect the sampling of orientations and conformations of the dipeptide at the bilayer centre (bottom row).

Figure 3.3.7. Comparison of the configurational sampling achieved with conventional US (orange) and US-REST3 (blue) at four distinct regions of the simulation cell (COM distance of 0.0, 1.6, 2.6 and 3.9 nm), as indicated by the z-axis (dark blue arrow) and the orientation and conformation angles indicated at the top of each column.
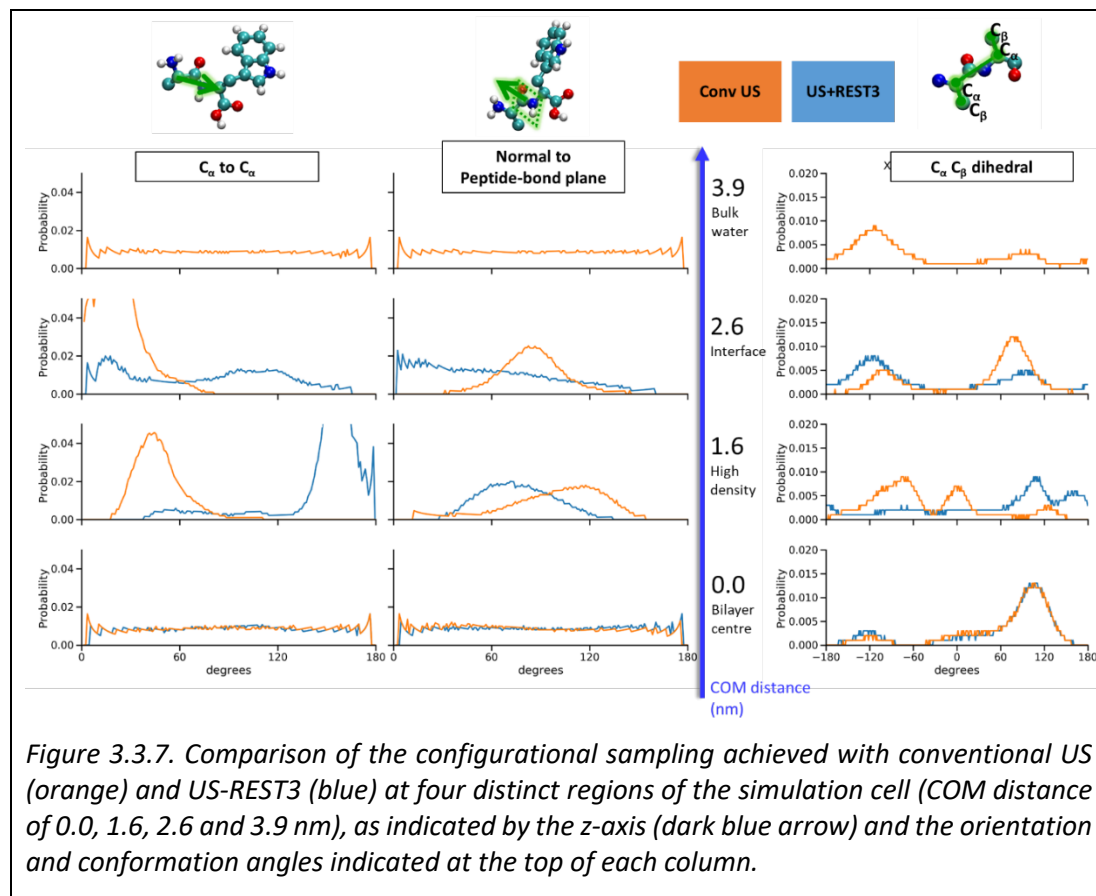
Figure 3.3.8 presents the sampling achieved in the high-density hydrophobic region, and follows the conventions explained for Figure 3.3.7 but with larger ranges of probability in the y-axis for the orientation angles. This highlights the more biased angle distributions that were observed in this region, with COM distances spanning from 1.0 nm (bottom row) to 2.0 nm (top row). It is remarkable that the C_α angle exhibits very high probability peaks compared to the orientation angle of the normal to the peptide bond. This suggests that rotational sampling of the dipeptide is restricted in the former more that in the latter. In other words, when crossing the high density-hydrophobic region of the bilayer, the dipeptide experiences more restrictions to flip from its amino to carboxyl ends (or vice versa) than to rotate around the backbone axis. The lesser resistance to rotation could be due to the hydrophobic nature of the sidechains, which may pack effectively among the lipid tails of CER and FFA and interact with the rings of CHOL.

Figure 3.3.8. Comparison of the configurational sampling achieved with conventional US (orange) and US-REST3 (blue) in the high-density hydrophobic region of the bilayer. COM distances are shown in the z-axis (dark blue arrow) and angles are indicated at the top of each column.
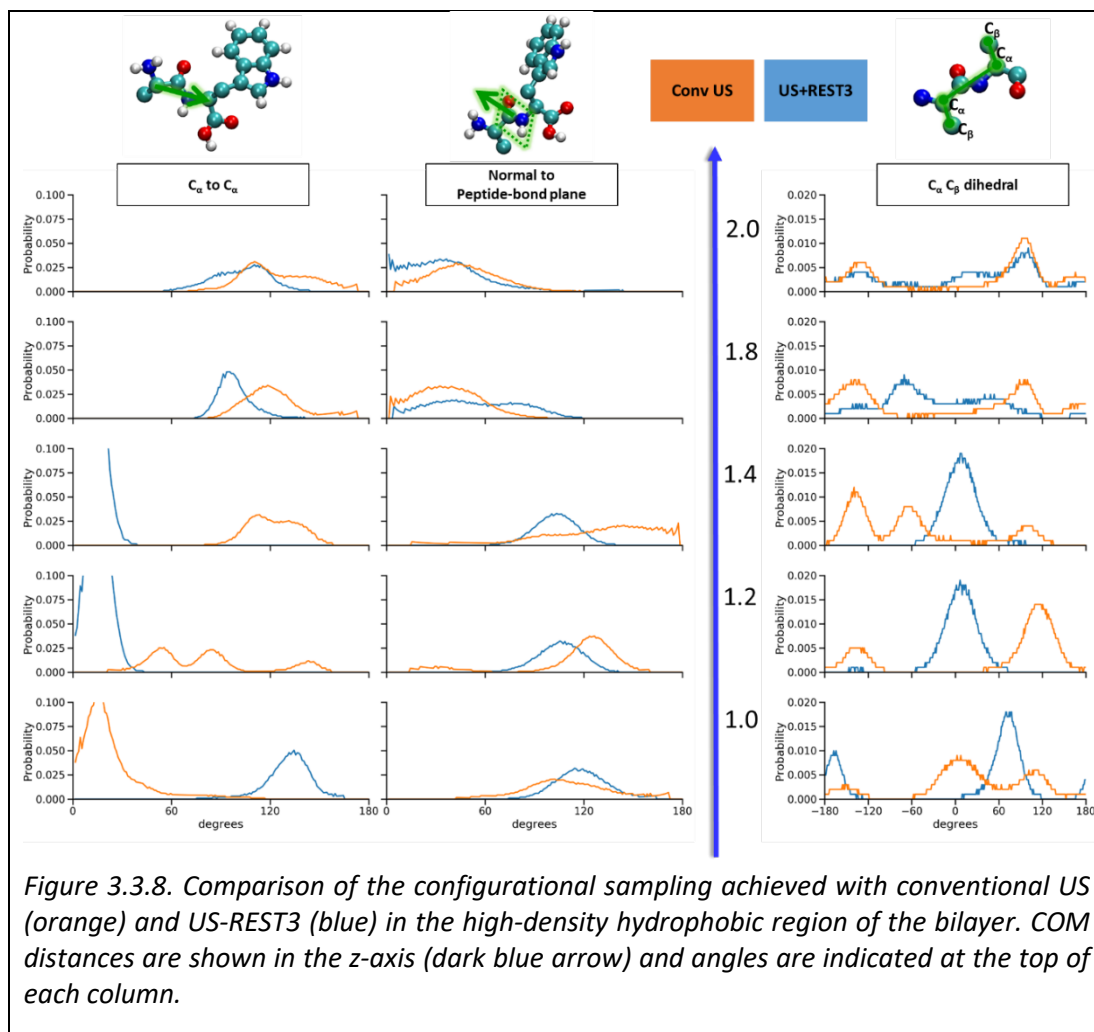
When the dipeptide is located at COM distances of 1.4 and 1.2 nm, it can be seen that US-REST (blue) produces C_α angle histograms that display higher peaks compared to conventional US (orange). These peaks are consistent with those described in Figure 3.3.4 at a COM distance of 1.3 nm with downscaling factors 0.5 and 0.2. At these COM distances, even with the downscaling of interactions acting with US-REST3 and a sufficient exchange probability, the dipeptide still experiences restrictions to flip (amino to carboxyl ends). In contrast, conventional US exhibits broader distributions of the same angle, with lower probabilities (less biased). At the same COM distances, US-REST3 samples the orientation angle normal to the peptide bond (middle column) with a distribution centred at around ≈110°, and a dihedral angle indicating high probability of angles around 0°, in which the side chains are faced almost to the same side, as depicted in Figure 3.3.3. These observations suggest that the dipeptide is preferentially oriented with the backbone almost in line with the vertical axis (≈15°) and an orthogonal dimension that is almost perpendicular to the same axis. This configuration seems to be dominated solely by the "closed book" conformation of the side chains. Hence, it appears that US-REST3 enables the dipeptide to *"escape"* more efficiently the configuration initially imposed by the insertion into the

membrane (from the pull simulation) and reach a more compact (and presumably more favourable) configuration.

In general, for all other regions of the simulation cell (hydrophilic, interface and low-density hydrophobic), US-REST3 yields broader sampling of orientation and conformation angles (not shown). However, despite the comparable (expensive) computational efforts invested for both enhanced sampling methods, they do not reach agreement in the sampling of configurations in this region of the bilayer. This suggests a *very* slow rate at which transitions between configurations occur, in comparison with lower density regions. In fact, most COM distances in the high-density hydrophobic region show dramatic changes in the sampling observed in each half of the conventional US trajectory, despite being run for 1.1 or 0.96 µs. This is evidenced in Figure 3.3.9, where angle histograms are plotted as the sampling achieved with each half of the simulation (and the entire trajectory) at five selected COM distances.

Figure 3.3.9. Sampling of orientations and conformations of the Ala-Trp dipeptide with conventional US simulations, at selected COM distances in the high-density hydrophobic region. Each subplot displays angle distributions corresponding to first half, second half and the entire simulation. Color-codes and simulation times are presented in the inset table.
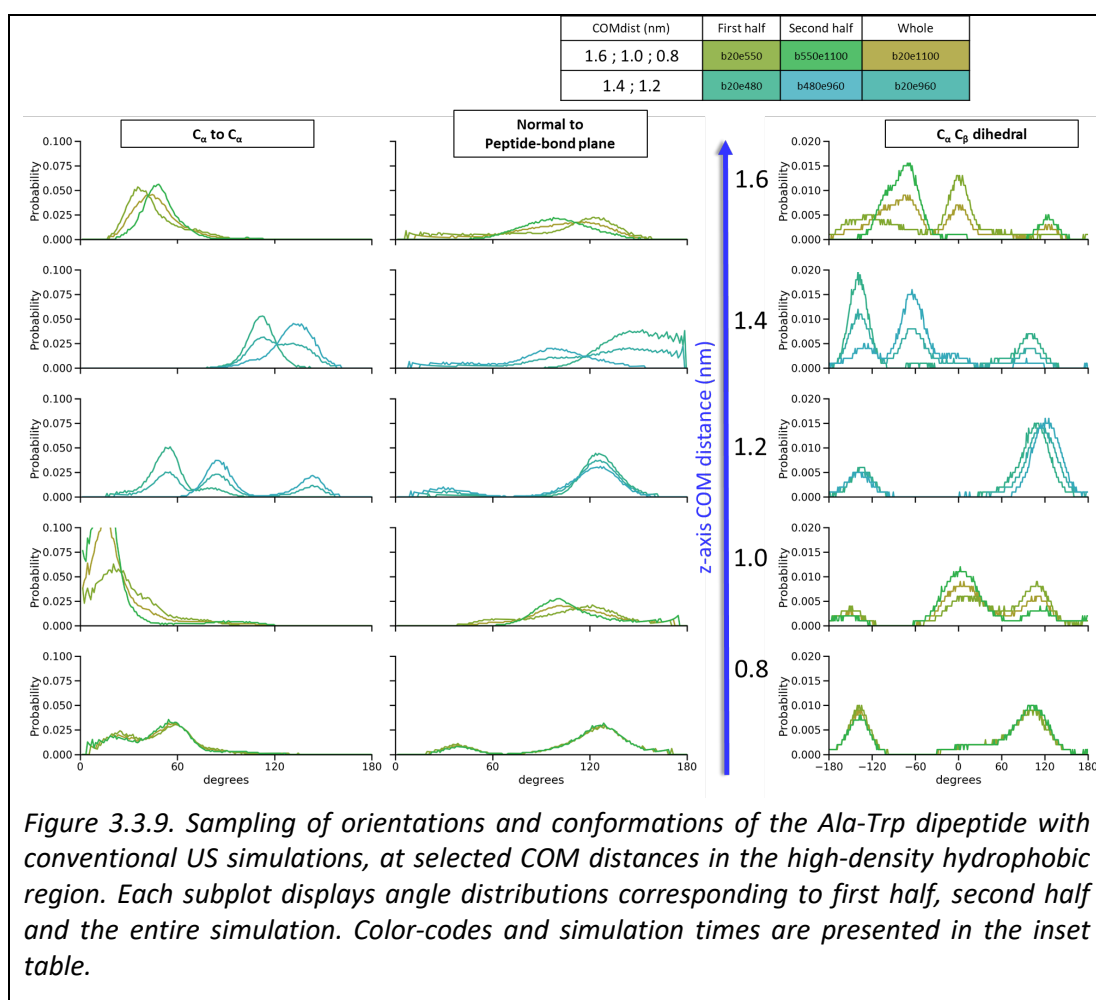
As a means of comparison, Figure 3.3.9 includes a COM distance of 0.8 nm, at which the sampling of all angles has converged as it exhibits the least change between the

two halves of the simulation. Note that the range in the vertical axis for the orientation angles (left and centre columns) and for the conformation angle (right column) is smaller than the range in Figure 3.3.8: this is done so that the changes are clearer.

3.3.5 Free energy

Assessment of convergence was ultimately based on the free energy profile (i.e. the PMF) and in consideration that, upon convergence, PMFs produced with increments in simulation time, or by comparing the two halves of the simulation, should be almost identical within the standard deviation. Prior tests were run to determine the amount of equilibration time required for conventional US and US-REST3, i.e. the time discarded at the beginning of the simulation. This equilibration time is thus not considered for the calculation of the free energy profile. Conventional US simulation required 20 ns for equilibration whereas US-REST3 simulation required only 10 ns (per replica, results not shown). Hence the starting times of the analysis are b20 and b10, respectively. Figure 3.3.10 shows the application of the convergence criteria to the PMFs obtained with each sampling method.

Upon comparison of the PMFs for the two halves of the US-REST3 simulation (Figure 3.3.10, bottom), it can be seen that the PMF has converged in less than 100 ns of production run (per US window) almost throughout the entire range of COM distances. Notably, the PMF from conventional US in a comparable production time (per US window), shown in grey, indicates that the dipeptide has the same affinity for the surface as for the bilayer interior, with free energy minima of ≈-42 kJ/mol. This prediction is problematic considering the very different environments that these regions entail and the interactions that the dipeptide could engage in. However, the PMFs obtained with increased simulation time with conventional US (Figure 3.3.10, top) show that the first major changes to the shape of the PMF occur after 600 ns of simulation (pink). These changes are observed in comparison to the PMF obtained with a 80 ns production run (per US window) (grey), and include a lower energy minimum at the interface, a lower energy maximum in the free energy barrier, and a more favourable ΔG of insertion at the bilayer centre (ΔG_i).

Further simulation time was added for all the regions of the bilayer except the low-density hydrophobic region, as indicated in Table 3.7 . With these increments in simulation time, the PMFs reach a shape that resembles the converged US-REST3 at 800 ns (ice blue) and remains for the rest of the simulation time (1000 ns, turquoise).
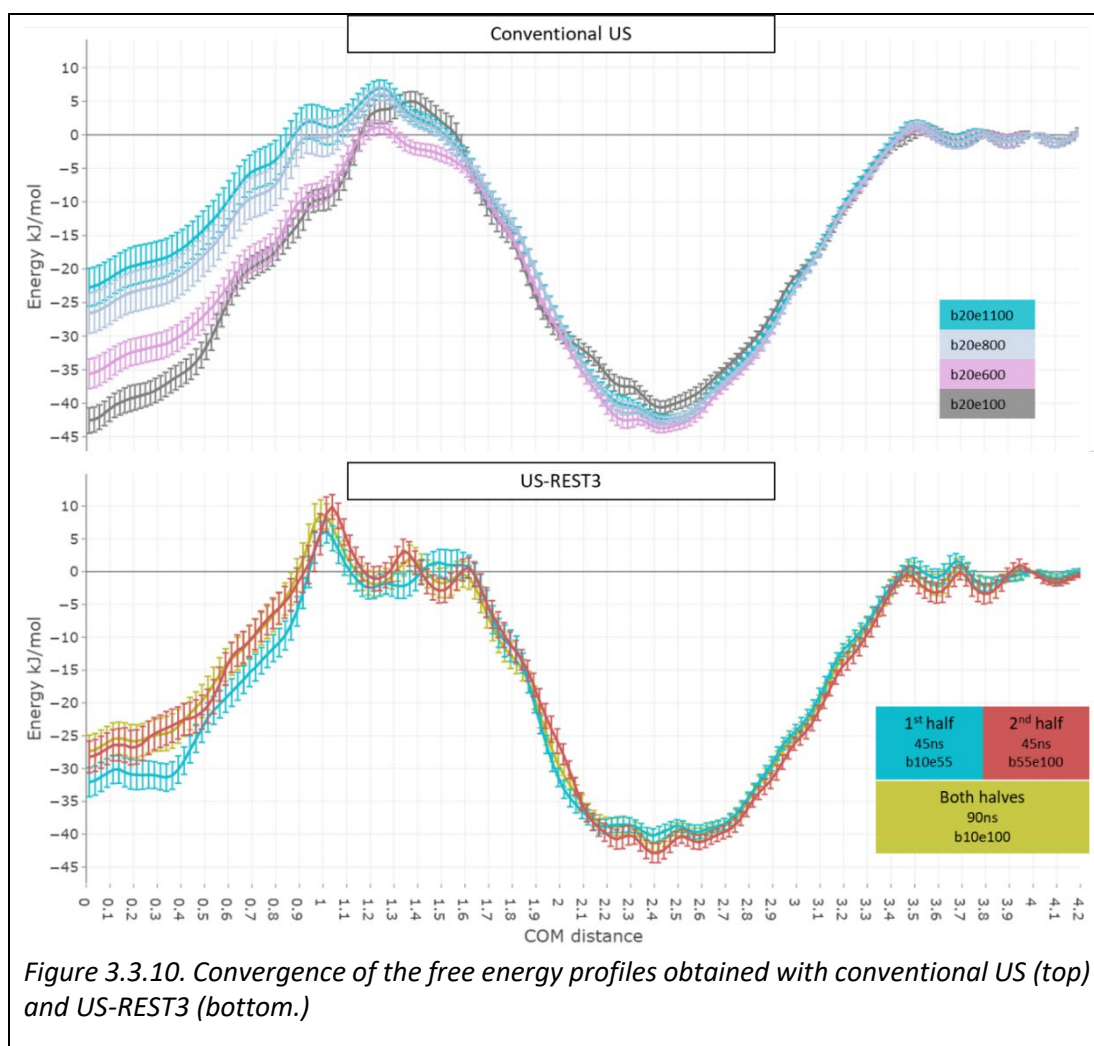
Figure 3.3.10. Convergence of the free energy profiles obtained with conventional US (top) and US-REST3 (bottom.)

Based on the shape of the PMFs produced with the longest simulation times for each method, it can be seen that both sampling methods yield free energy profiles that agree with each other. This indicates that thermodynamic (free energy) and conformational properties need not converge at similar speeds. The similarities in the shape of the converged PMF from both methods include the favourable interaction at the interface with a free energy minimum ≈-40 kJ/mol, the free energy barrier located in the high-density hydrophobic region ranging from 5 to 10 kJ/mol, and a ΔG_i ≈-25 kJ/mol (Table 3.8). In particular, the PMF obtained with conventional US shows a broad barrier with a maximum of ≈5 kJ/mol at a COM distance of about 1.2 nm compared to the PMF with US-REST, which has a narrow peak with a maximum of ≈10 kJ/mol located at a COM distance of 1.0 nm.

These observations suggest that conventional US eventually samples a transient transition of the system between at least two energy states: one in which the free energy at the bilayer centre is similar to the free energy at the bilayer surface, and one in which it is less favourable than the bilayer surface with $\Delta\Delta G$ ≈15 kJ/mol. The first state is represented by the PMFs obtained from conventional US production runs

ranging from 80 to 480 ns. The second state is represented by the converged PMF obtained from US-REST3 and which is transiently achieved by the conventional US production run of 900 ns. The changes in the shape of the histograms (Figure 3.3.11) that are located in the region of the free energy maxima are evidence of this transient sampling. With increments in simulation time, histograms covering the region of COM distances from 0.6 to 2.1 nm exhibit changes in their relative height and skewness. This indicates that in the region of high-density and high order of the lipid tails, the location of the COM of the Ala-Trp dipeptide is shifted from the reference of the harmonic potential (applied to each window), and that it remains shifted for several hundred nanoseconds. In fact, the slow changes in the sampling of orientations and conformations also suggest that some of these conventional US runs have not converged.

Given the time scales in the top and bottom panels of Figure 3.3.10, and the comparable computational effort, it can be concluded that US-REST3 is a remarkably fast converging method compared to conventional US, and that the differences in resolution of the free energy profile are minor.

Figure 3.3.11. Overlap of histograms produced with conventional US, and with increments in simulation time.
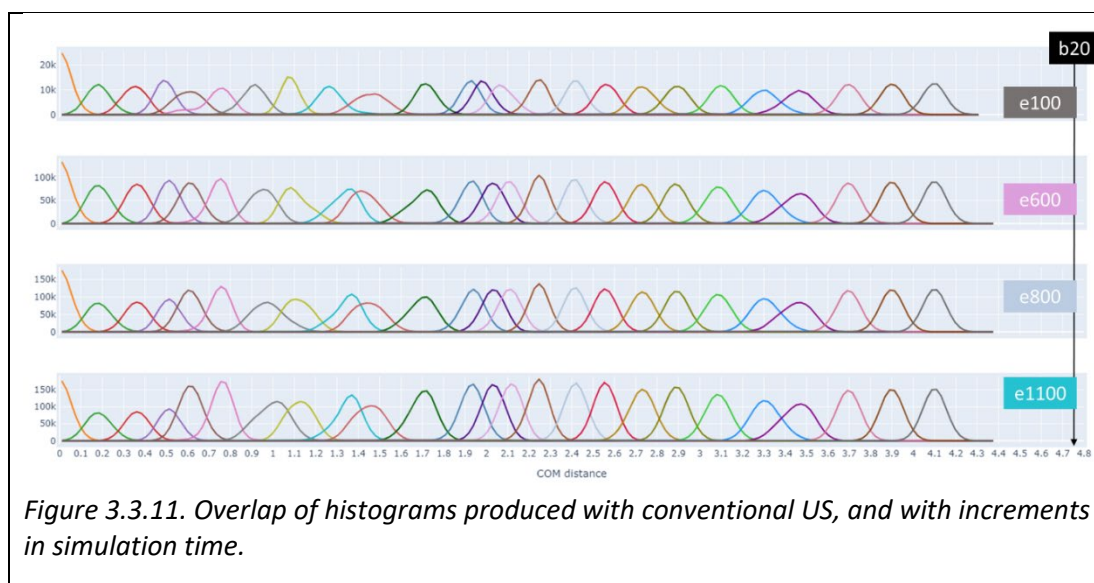
Table 3.8. presents the comparison of free energy of insertion of the dipeptide into the model bilayer using the two enhanced sampling methods, and compares them to the experimental value reported by Lin et al. (86). It can be seen that the conventional US approach yields closer agreement with the experimental value that what is predicted with the US-REST3 enhancing sampling method. However, it must be noted that the latter value was obtained with a fraction of the computational effort and with less waiting time. This suggests that the free energy values obtained with the fast-converging US-REST3 method can be representative of experimental values obtained using model bilayers. The improved sampling obtained with US-REST3

described above suggests that the better agreement with experiment obtained with conventional US could be simply fortuitous.

Table 3.8. Comparison of free energy of insertion of the dipeptide.

Method	ΔG_i (kJ/mol)
Experimental. Ref (86)	-21.7
Conventional US	-22.7 ± 2.8
US-REST3	-27.5 ± 2.5

The LUVs used for these free energy experiments featured seven lipid species, representing the three major lipid classes in a molar ratio CER:CHOL:FFA of 2.7: 1.7: 1. The details of the conversion are presented in Table 3.9. As previously described, the simulations described here used a 2:2:1 molar ratio with one lipid species representing each lipid class. Therefore, the difference between experimental and predicted free energy could be attributed to minor changes in the properties of the bilayer, which arise from the more diverse lipid composition, the molar ratio and the temperature at which experiments were conducted (25°C).

Table 3.9. Molar ratio of the large unilamellar vesicles (LUVs) used for experimental free energy measurements.

Reported by Liao and collaborators (86)			MW (g/mol)	MW %	Moles	Mole ratio
	Lipid species	Weight %	Ratio			
	Ceramide 3 (NP)	55	3	582	33.00	0.05670	2.65
	Ceramide 4		2	369.6	22.00	0.05952	
	Cholesterol	25		386.7		0.06465	1.72
	Cholesterol sulphate	5		466.7		0.01071	
C16	Palmitic acid	15	1	256.43	3.75	0.01462	1
C24	Lignoceric acid		2	368.63	7.50	0.02035	
C28	Octacosanoic acid		1	424.7	3.75	0.00883	

3.3.6 Diffusivity profiles

The position-dependent diffusion coefficient for each US-window was calculated for both conventional US and US-REST3 simulations. The resulting diffusivity profiles are shown in Figure 3.3.12 (top). These profiles converge in the bulk water region and show similarity at the bilayer centre where the diffusivity is slightly lower than in bulk water. Despite the noisy nature of the profiles and the differences observed between them in the dense-hydrophobic region and at the interface, both profiles are in agreement with results reported by Paloncyova et al. (191), which are also presented Figure 3.3.12 (bottom).
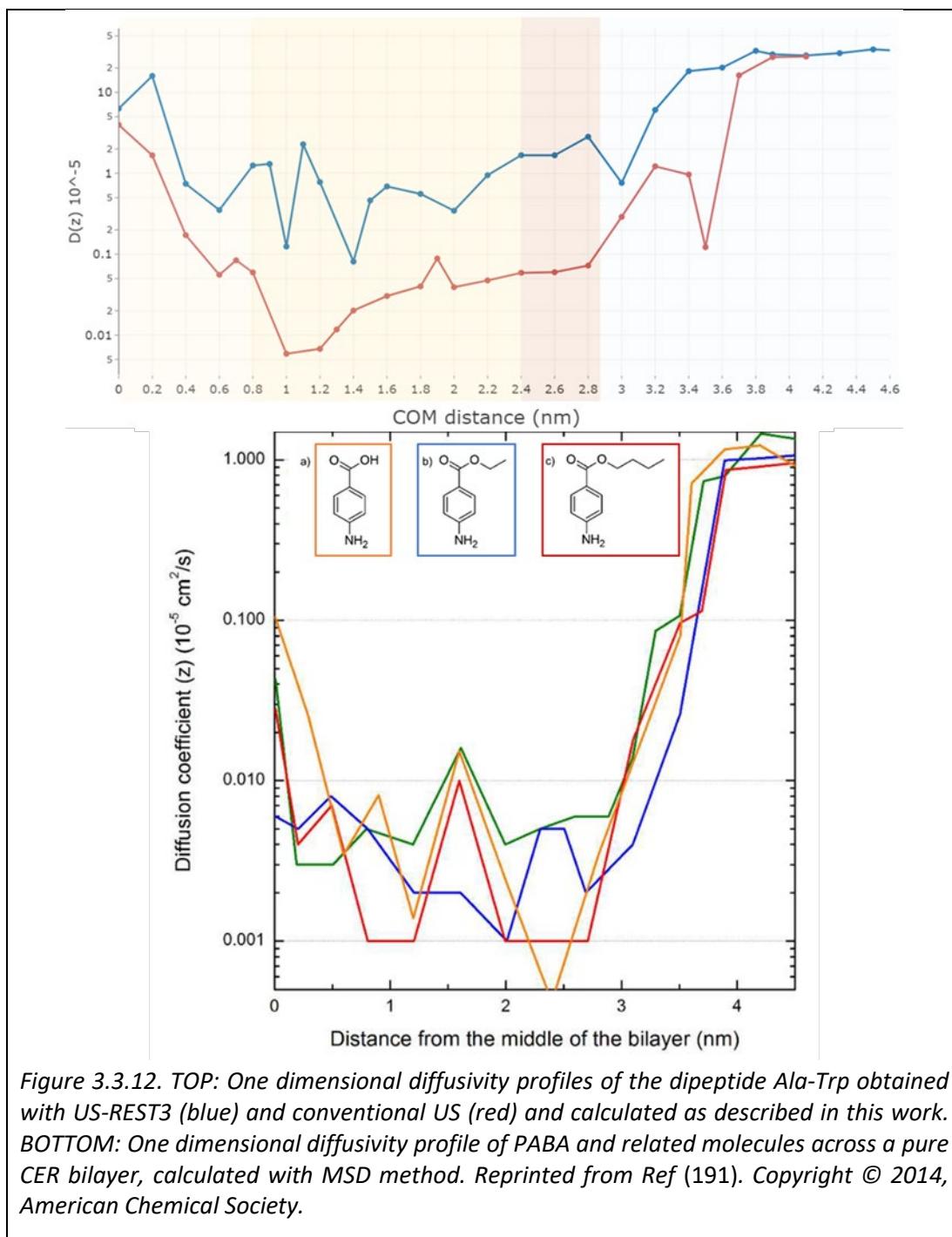
Figure 3.3.12. TOP: One dimensional diffusivity profiles of the dipeptide Ala-Trp obtained with US-REST3 (blue) and conventional US (red) and calculated as described in this work. BOTTOM: One dimensional diffusivity profile of PABA and related molecules across a pure CER bilayer, calculated with MSD method. Reprinted from Ref (191). Copyright © 2014, American Chemical Society.

In their study of the translocation of para-amino benzoic acid (PABA) and two of its esters across a pure CER bilayer in the gel phase, these authors calculated diffusion coefficients using the mean square displacement (MSD) method. They reported a drop in diffusivity of four orders of magnitude from bulk water to the dense hydrophobic region, and about one order of magnitude to the bilayer centre. Further comparison between the top and bottom panels of Figure 3.3.12 is likely misguided as the bilayers, the small permeant molecules, the temperature and simulation control settings (barostat and thermostat) are all different. As discussed in previous

sections, the conformational properties of the dipeptide appear not converged when the dipeptide crosses the high-density hydrophobic region, even for μs long simulations (per US window) with conventional US. In view of the lack of experimental values of diffusivity to compare with, it would be risky to comment on the accuracy and the differences between the estimates produced with both methods. These findings suggest, nonetheless, that the overall shape of the diffusivity profiles is reasonable, but future work is needed to further study the convergence and accuracy of methods to calculate diffusion coefficients in slow-relaxing environments, and to assess their impact on the calculation of permeability coefficients.

3.3.7 Permeability coefficients

Following Equation 1.3, the permeability coefficient of the dipeptide can be estimated from MD simulations by calculating the free energy and the diffusivity profiles. Table 3.10 shows the values obtained with conventional US and with US-REST3. It is clear that the conventional US simulation approach estimates a slower permeability of the dipeptide than the US-REST3 approach, by one order of magnitude. Table 3.10 also provides the experimental value for the transdermal permeability across porcine skin at 32°C (164). In fact, US-REST3 method yields a much closer estimate.

Table 3.10. Comparison of permeability coefficients

Method	Permeability [nm/ps]	Temperature [°C]
Experimental (porcine skin) (164)	1.39×10^{-7}	32
Conventional US	1.95×10^{-8}	32
US-REST3	1.70×10^{-7}	32

3.4 Conclusions.

The model bilayer of the ICLM-SC reproduced the behaviour reported by other studies using the same lipid molar ratio and using similar simulation parameters. The bilayer shows distinctive density regions that are conceptualised from the *inhomogeneous diffusion solubility-model* to pose distinct resistance to the movement of small permeant molecules.

The findings discussed in this chapter prove that microsecond-long conventional US simulations (per US window) are required for a reliable estimation of the PMF of permeation across a SC model lipid bilayer. This is based on the convergence to an

accurate free energy profile (PMF) and comparison against experimental ΔG of interaction with LUVs. It is likely that microsecond-long conventional US simulations are required for the characterisation of other SMMIs involving bilayers in the gel-state and small peptide-like biomolecules. However, these timescales are unusual in the field of SMMIs. This fact highlights the importance of convergence assessment of free energy profiles of SMMIs in the context of SC model bilayers.

In contrast, with the US-REST3 enhanced sampling approach a simulation timescale of 100 ns (per US window) yielded a PMF in agreement with the one obtained from converged conventional US estimate and reached sufficient agreement with the experimental ΔG of interaction with LUVs. These findings show that US-REST3 simulations converged much faster to reasonably reliable estimates. This could be achieved after optimization of replica ladder schemes that were designed to ensure sufficient exchange for efficient use of computational resources, and which were assigned more or less to the distinct regions of the simulations cell. It is important to note that the exchange probability appears to be a function of the spacing between replicas, the maximum scaling or tempering factor used and the COM distance. The replica schemes applied in this work resulted in exchange probability profiles displaying regions above the ideal 20-30% exchange probability. This suggests that the procedure followed for optimization leaves room for further improvement. The knowledge obtained in the optimization procedure can be transferred to the interaction of other short peptides and small biomolecules with the same SC model lipid bilayer. Hence the replica schemes used here could be used for SMMIs of the same bilayer at similar COM distances with confidence for obtaining sufficient exchange probabilities.

The angle histogram plots served as a proxy for the extent of sampling across well-defined states (orientations and conformations) of the permeant at different insertion depths. With this information it was possible to establish a link between the high-density region and the highest restriction to the sampling of roto-translation of the dipeptide. Considering that the high-density region showed poor convergence in the sampling of angles with conventional US (as indicated by the comparison of the first and second halves of the simulation), the findings reported here indicate that the sampling of configurations with US-REST3 contributes to improving the accuracy and speed of convergence of the free energy profile. However, the orientation and conformation angles defined here are not transferrable to the study of other SMMIs.

The accuracy of the one-dimensional diffusion coefficient of the permeant in environments more restrictive than bulk water could be affected by the sampling impairment associated with interactions with lipid membranes, in particular with the high-density region of the SC model used in this work.

The extent of this effect is likely to be distinct for each method of calculating the diffusion coefficient, i.e. with the assumptions made to derive the diffusivity from MD simulations. This effect could be studied by comparing estimates from different methods against experimental diffusion values upon interaction with the bilayer. With the approach used in this work, the larger error of diffusion estimates is found in the high-density region, where the estimates from the two sampling methods differ the most. The inherent exchange of configurations in US-REST3 could suggest an overestimation of the diffusion coefficient with this method. However, the fact that estimates are in agreement in bulk water and in the less restrictive region at the bilayer centre, suggest that this overestimation could have a noticeable effect only in certain ranges of the RC.

Overall, it can be concluded that US-REST3 provides enhanced sampling of orientations and conformations of the dipeptide in restrictive regions of the SC model bilayer, and that said enhanced sampling contributed to the fast convergence of the PMF. It can be expected that the replica schemes used are transferrable to the study of permeation of other short peptides and peptide-like molecules, which will provide reliable PMFs with an efficient use of computational resources and reduced wall-times compared to conventional US simulations.

4 Lipidation of bioactive peptides: Effect of lipid-tail length on transdermal permeability.

4.1 Introduction.

Experimental evidence demonstrates that for the tetrapeptide Ala-Ala-Pro-Val (AAPV), a chemical modification with a lipoamino acid (Laa) enables the permeability of the parent molecule (Chapter 2, section 2.4.1.1). Briefly, a U-shaped relationship was observed between the number of carbons in the Laa moiety (C6, C8, C10) and the transdermal permeability of the derivative as measured across human skin in a Franz diffusion cell assay. In other words, it was found that permeation reaches a maximum at a specific tail length (C8), such that if tail length is further increased, the permeability decreases (56). In this work, two Laa derivatives with either 4 or 8 carbons in the lipid side chain (C4 and C8, respectively) were characterised for their ability to enhance the predicted transdermal permeability of three parent molecules with lower MW than the tetrapeptide AAPV. The analysis is focused on the free energy of interaction and the features that distinguish the derivatives from the parent molecule and how these affect their predicted permeability.

4.1.1 Choice of molecules

Molecules with skin activity and evidence of transdermal permeability were selected as parent molecules to be modified with the Laa moiety and study their interaction with a 2:2:1 model of the SC. With the aims of reaching insight of the permeation mechanism and establishing generalizations on the physicochemical properties of drug candidates that permeate across the skin, three small molecules were chosen. These molecules range in MW, number of rotatable bonds and number of hydrogen bonding groups. The choice was partly guided by the availability of experimental permeability data of the parent molecule, allowing comparison of permeability estimates to experimental values. The three molecules are i) the peptide-like drug 5-aminolevulinic acid (5-ALA, 5-amino-4-oxopentanoic acid), ii) Dipeptide 2 (Val-Trp)

and iii) the cosmeceutical agent melanostatin, a tripeptide with sequence Pro-Leu-Gly-NH$_2$. The effect of lipid conjugation on the transdermal permeability of the parent molecules was investigated with a focus on their molecular interactions with the model lipid bilayer.

4.1.1.1 Aminolevulinic acid

5-ALA is a naturally occurring delta amino acid (MW 131.1) which is used as a prodrug to treat some forms of skin cancer. The treatment involves the application of 5-ALA to the skin and its absorption prior to photodynamic therapy (PDT). When 5-ALA reaches the cytoplasm of nucleated cells, it is enzymatically converted to protoporphyrin-IX (PpIX), an endogenous photosensitiser and the precursor of heme (192). During PDT, light activation triggers a reaction between molecular oxygen and PpIX (193), producing cytotoxic reactive oxygen species, mainly singlet oxygen free radicals which are deleterious to the cell (194). PTD features low systemic toxicity given the superficial penetration of 5-ALA into the skin and the higher accumulation of PpIX by malignant cells compared to the surrounding healthy tissue (195). The main drawback of PTD is the high photosensitisation (i.e. sunburn-like side effects) of the patient's skin that lasts for several days (196). Several clinical practices have been developed to overcome the low transdermal permeability of 5-ALA. Some of these enhance the penetration of the active molecule by altering the skin (peeling, laser therapy, microdermabrasion) prior to its application, while others optimize the formulation of vehicles to help its penetration into the skin (192).

First generation derivatives of 5-ALA include a series of alkyl esters of the main carboxylic acid group. These were generated with the aims of reducing the long lag-phase ($\approx$20 h) of absorption and improving the poor skin intake of 5-ALA, which is characterized by a permeability across the human SC of 10^{-13} nm/ps (196). The permeability of 5-ALA and its ester derivatives across cell membranes was indirectly measured in a fluorescence-based assay using the T-cell lymphoma cell line Jurka. These cells were incubated with a series of ester prodrugs of 5-ALA and given time to incorporate and subsequently enzymatically convert the prodrugs into PpIX (Figure 4.1.1) (193). Assuming that the rate of conversion to PpIX is similar across all of the ester derivatives, the measured fluorescence values suggest that faster translocation rates across the cell membrane are achieved for derivatives with increasing number of carbons in the ester moiety, with the pentyl ester yielding the fastest rate. After this, a decreasing trend in translocation rate is observed for the hexyl- and octyl-ester. The reasoning for this U-shaped behaviour was proposed to be the excess hydrophobicity (i.e. the larger number of carbons), causing the trapping of the compounds with long alkyl chains in the hydrophobic environment of the cell membrane bilayer. Nonetheless, all esters, except the methyl-ester, exhibited significantly higher fluorescence, indicating an improvement in permeability over the 5-ALA parent molecule (193).

Figure 4.1.1. Fluorescence of PpIX induced by 5-ALA and its alkyl ester derivatives with structures as indicated by the number of carbons in the ester moiety, and incubation times as indicted in the inset. Adapted from (193) © The American Society of Photobiology
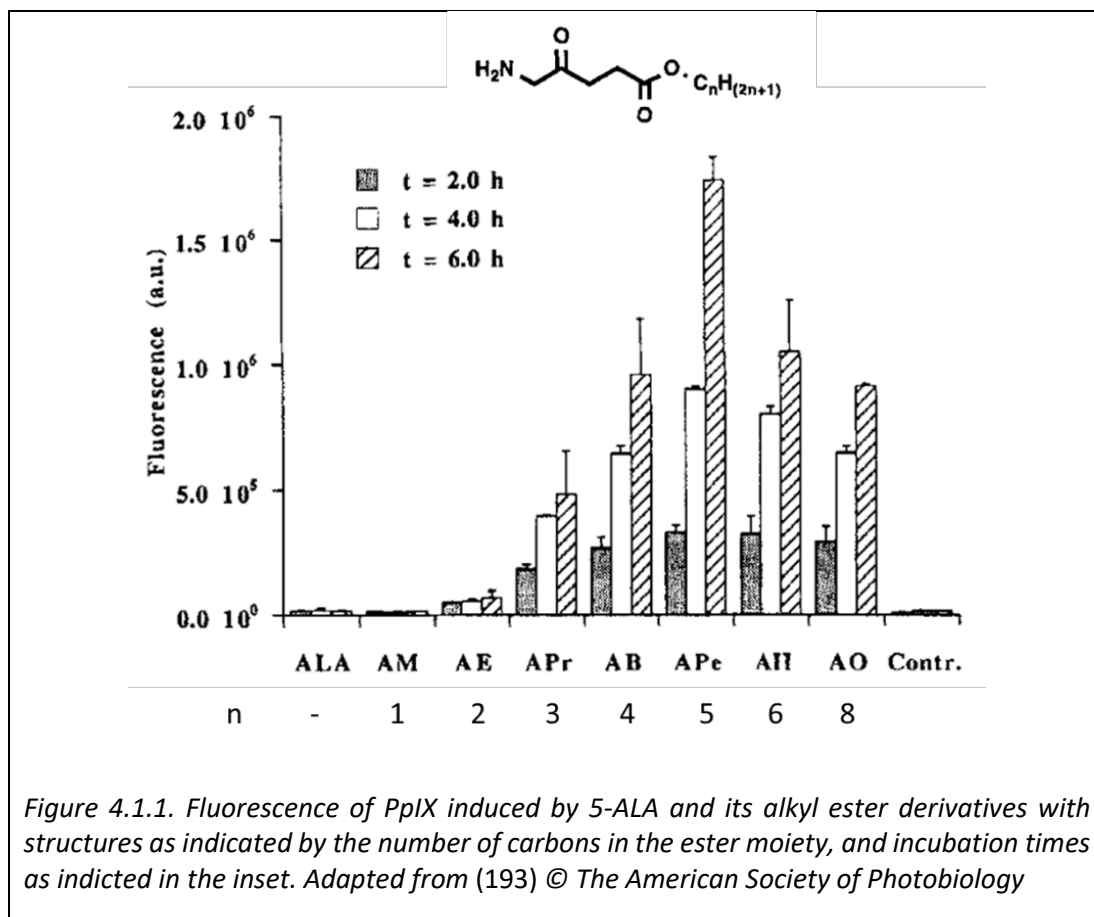
Aside from 5-ALA (commercialised as Levulan), two of these esters are currently available in the market for dermal applications: the methyl ester (Metvix® and Metvixia) is now approved for the treatment of actinic keratosis (192) and basal cell carcinoma, and the hexyl ester (Hex-vix®) has been approved for fluorescence-based diagnosis of bladder cancer (194, 197). Although Metvix showed improved transmembrane permeability and selectivity, its use for PDT is still associated with pain and a long lag-phase (198). As reported by Jhanker, the transdermal permeability of the methyl-ester derivative of 5-ALA (in several formulations including the brand Metvix) is also in the order of 10^{-13} nm/ps, as measured in the passive permeation across excised piglet skin mounted in a Franz-cell diffusion assay (198). The piglet skin used in that work had a SC layer that was three times thinner and more loosely structured than previously reported for human skin, indicating that the permeability values are expected to be lower when extrapolated to case of human skin (198).

MD simulations conducted by Eriksson and collaborators investigated the permeability of 5-ALA and some of its first-generation derivatives across a phospholipid bilayer in the fluid phase (DPPC at 323K). Their simulations predicted that all prodrugs preferentially locate in the head group region and that the free

97

energy barrier to permeation is located at the centre of the bilayer (199, 200) (Figure 4.1.2, top). Compared to the free energy profile of the parent neutral 5-ALA molecule (light green), the height of the energy barrier was predicted to reduce substantially for the methyl-ester (blue) and substantially increase for the ethyl ester (black). This suggests a higher permeability of the methyl-ester compared to the other derivatives and the parent 5-ALA molecule. Additionally, it reveals a non-linear relationship between the number of carbons in the ester moiety and transmembrane permeability. The disagreement between these predictions and the fluorescence-based measurements presented in Figure 4.1.1 highlights the indirect nature of the experimental permeability test and suggests the role of other factors on the activity of 5-ALA derivatives and their transmembrane permeability. At the same time, it raises questions about the validity of using pure DPPC bilayers to model complex cell membranes.

Figure 4.1.2. Free energy profiles of the permeation of 5-ALA and first-generation ester derivatives (top) or second-generation oxime derivatives (bottom) across a DPPC lipid bilayer. Structures are provided in coloured boxes that match the plots. Top adapted from Ref. (200) Copyright © 2009 Elsevier B.V. All rights reserved. Bottom adapted from Ref. (194) Copyright © 2016, Springer-Verlag Berlin Heidelberg.

Second-generation 5-ALA derivatives include a series of oximes on the central carbonyl group. These derivatives are more efficient for the accumulation of PpIX and are thought to have improved transmembrane permeability due to their increased lipophilicity (194). However, subsequent work conducted by Eriksson and

collaborators (194) revealed that their activity could not be explained by higher permeability across the cell membrane (Figure 4.1.2, bottom). Their predictions suggested that the transmembrane permeability of the oxime derivatives is comparable to the parent 5-ALA and yet lower than the methyl-ester. The transdermal permeability of these compounds is yet another factor that could hinder their activity; however, there is no clear understanding of the molecular mechanism that enables their translocation across the ICLM-SC and if their permeability across a simple phospholipid bilayer is a good predictor of their transdermal permeability.

4.1.1.2   Dipeptide-2

Dipeptide 2 is a bioactive peptide with sequence Val-Trp (VW) and MW 300.3, which has been marketed by Sederma in skin care products. Despite the lack of clinical studies addressed to assess its skin activity (39, 201), the dipeptide Val-Trp has potent activity as an angiotensin converting enzyme (ACE) inhibitor and reduces blood pressure when delivered orally (39).

4.1.1.3   Melanostatin

Melanostatin is a naturally occurring antibiotic oligopeptide, and is a product of the degradation of the oxytocin hormone (202). Its sequence is Pro-Leu-Gly-NH2 (PLG) and its MW is 284.3 (203). It acts as an inhibitor of the release of the melanocyte-stimulating hormone, for which it receives the name of melanocyte inhibition factor 1 (MFI-1); however, this is not its main or consistent function (204). Its cosmeceutical applications include lightening of skin tone and as anti-ageing agent for its inhibitory activity on collagenase (an enzyme that digests skin collagen) (198). Melanostatin also acts as a dopamine agonist response enhancer, making it a candidate for the treatment of neurodegenerative diseases such as Parkinson's disease (205), although further studies are required to assess its clinical efficacy, especially given its likely degradation upon absorption and low permeability across the blood brain barrier (206). Anti-depressant activity in humans has also been suggested (207).

A study conducted using fluorescein-tagged PLG (MW ≈800) studied the distribution across a layer of (*ex-vivo*) human skin. Despite the physical bypassing of the SC through pre-treatment with microneedles, the observed fold increase in the translocation of the peptide was observed to be low compared to other peptides with similar MW, and with other delivery enhancement methods (42). This suggests that factors besides the permeation across the SC could be affecting the delivery to the viable layers of the skin. Transdermal permeability measurements across intact piglet skin were reported to be in the order of 10^{-14} nm/ps, with a lag time of 4.26 hours (198), illustrating the slow permeation of PLG across skin with an intact barrier function.

4.2 Methods.

All MD simulations were conducted in the same manner as described in Chapter 4. Briefly, a symmetrical bilayer consisting of three components (CER, CHOL, FFA in a 2:2:1 ratio) with a total of 160 of lipids was equilibrated in a rectangular simulation cell. The permeant molecule was manually inserted in the bulk water region (i.e., away from the influence of the bilayer) using VMD. To cover its translocation pathway, a pull simulation was conducted to obtain the starting configurations at several COM distances. An umbrella sampling (US) harmonic restraint (500 kJ mol^{-1} nm^{-2}) was applied to the centre of mass (COM) of the permeant molecule at a series of distances from the COM of the bilayer. These US windows were spaced every 0.2 or 0.1 nm, depending on the quality of the histogram overlap. For each US window, the REST3 enhanced sampling method was applied to scale down the non-bonded (electrostatics and van der Waals) interactions of the permeant molecules with the other components of the simulation cell. One of the replica schemes previously described (Figure 3.3.6) was allocated to each US window and the exchange probability was monitored to ensure sufficient exchanges between neighbouring replicas. All simulations were run for at least 100 ns. The 10 ns at the start of each one of the replica simulations were discarded as equilibration, leaving a production run of 90 ns per (ground) replica and per window. The US windows located away from the bilayer (in the bulk water region) were simulated with conventional US to reduce the computational effort. Table 4.1 presents the aggregated number of US windows, replicas, and simulation time for the translocation of each permeant molecule.

Table 4.1. Aggregated number of US windows, replicas, and simulation time.

| | | 5amino-4oxopentanoic acid | Dipeptide 2 | Melanostatin |
		5-ALA	**Val-Trp**	**Pro-Leu-Gly**
Parent	**US windows**	21	21	24
	Replicas	200	200	221
	Simulation time (us)	18	18	19.89
C4LAa	**US windows**	21	21	21
	Replicas	200	200	179
	Simulation time (us)	18	18	16.11
C8Laa	**US windows**	21	22	26
	Replicas	200	210	252
	Simulation time (us)	18	18.9	27.72

4.2.1 Molecular topologies

Topologies for the permeant molecules were obtained from the Automated Topology Builder (ATB) (208). This server enables the user to submit a structure in text format and retrieve a topology file and structure file with optimised geometry compatible with Gromos 54a7, the UA ff used in this work. The ATB combines a knowledge-based approach and quantum mechanics (QM) calculations to generate non-bonded and bonded parameters as well as charges for new molecules. Table 4.2 provides the identifier of each molecule in the ATB public repository, which can be used to access the files. The table includes their chemical formula, number of united atoms in the output topology and the type of QM calculation that originated the output files. Note that parent molecules Dipeptide2 and Melanostatin do not have ATB identifiers because they are composed of amino acids, which are considered standard residues within the Gromos 54a7 ff.

Table 4.2. Naming of the parent molecules and their Laa conjugates included in this study.

		5-aminolevulinic acid (5-ALA)	Dipeptide 2	Melanostatin
		5-amino-4-oxopentanoic acid	Val-Trp	Pro-Leu-Gly
Parent molecule	**Formula**	$C_5H_9NO_3$	$C_{16}H_{21}N_3O_3$	$C_{13}H_{24}N_4O_3$
	United atoms	12	32	24
	ATBresname	OEIP	NA	
	ATB ID	44335		
	Calculation	QM2		
C4Laa	**Formula**	$C_{11}H_{20}N_2O_4$	$C_{22}H_{32}N_4O_4$	$C_{19}H_{34}N_4O_5$
	United atoms	22	44	36
	ATBresname	6TT0	L63B	WAT5
	ATB ID	458883	458882	458877
	Calculation	QM2	QM0	QM0
C8Laa	**Formula**	$C_{15}H_{28}N_2O_4$	$C_{26}H_{40}N_4O_4$	$C_{23}H_{42}N_4O_5$
	United atoms	26	48	40
	ATBresname	094C	LGE4	OON3
	ATB ID	458809	458808	458807
	Calculation	QM1	QM0	QM0

4.2.2 Convergence of free energy profiles

The free energy profiles or potentials of mean force (PMFs) were obtained using the weighted histogram analysis method (WHAM) as implemented in the *g_wham* module in GROMACS (190). This was performed by assigning weights according to the integrated autocorrelation times (IACT) of each window, by specifying the *-ac* option. A reference value of zero for the free energy was set at a COM distance of 4.0 nm (i.e. in the bulk water region), by specifying the *-zprof0* option. The temperature was set to 305 K (with the option *-temp*) to match the temperature of the simulations. The standard deviation of the free energy was calculated with the in-built bootstrap function (*-bs 200*). The convergence of the free energy profile was deemed to have been attained when consecutive PMFs (in increments of 10 ns) were within a standard deviation of each other.

4.2.3 Estimation of diffusivity profiles

Calculations were conducted as described in Chapter 3. According to Equation 3.4, for the one-dimensional diffusion coefficient at each US window, two values are required: the variance and the integrated autocorrelation time IACT (τ) of the series of positions (COM distances). The former was calculated in Python using the variance function included in the NumPy library, following the procedure outlined by Carpenter et al. (122). The latter is automatically reported as an output file by the *g_wham* module in GROMACS when the user specifies the *-ac* option.

4.2.4 Permeability coefficient

Following Equation 1.3, the permeability across the model lipid bilayer can be calculated by integrating the ratio between the free energy profile and the diffusivity profile. To estimate the transdermal permeability, we assume an average of 10 layers of corneocytes as the depth of the human *stratum corneum*. Because each corneocyte is embedded in the ICLM, it can be assumed to be surrounded by 10 bilayers. Consequently, the prediction of the actual skin permeability of each peptide will be computed as Equation 4.1 (178):

$$1/P = 1/P_1 + 1/P_2 + \cdots + 1/P_{100} \qquad \textit{Equation 4.1}$$

In the remainder of this work only the transdermal permeability *P* is considered, its values are computed as indicated in the equation above.

4.3 Results and discussion.

4.3.1 Aminolevulinic acid

The structures of the neutral form of 5-ALA and the two Laa derivatives (lipid conjugates) studied in this work are shown in Figure 4.3.1, along with the naming convention and colour code used in this section. 5-ALA has a MW of 131.1 and features four rotatable bonds, two hydrogen-bond donors and four hydrogen-bond acceptors, with a polar surface area of 80.4 $Å^2$ (209). It is important to note that the addition of the Laa moiety not only increases the MW and hydrophobicity of the derivatives, but also increases the number of rotatable bonds, the number of polar groups (and polar surface area) and, thus changing the hydrogen-bonding capabilities compared to the parent molecule.

Figure 4.3.1. Chemical structure of 5-aminolevulinic acid (5-ALA) and two lipoamino acid (Laa) conjugated forms.
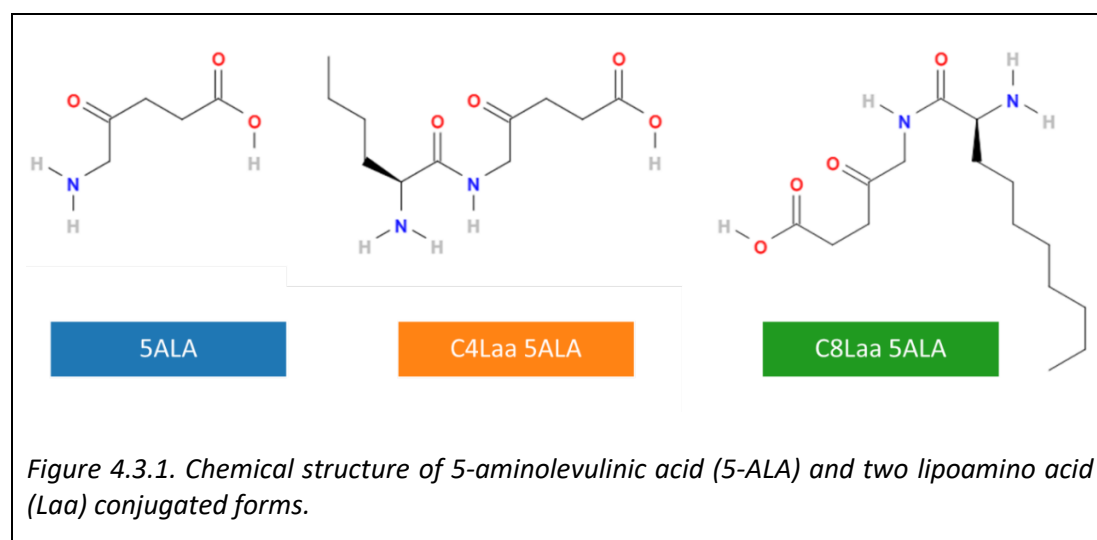
The converged predicted free energy profiles for the permeation of the three molecules are shown in Figure 4.3.2 (top). The shape of the free energy profile (PMF) of the parent 5-ALA molecule (blue) agrees qualitatively with the translocation of a small polar molecule, as was observed by Eriksson and collaborators (Figure 4.1.2). In their work, the crossing of uncharged 5-ALA across a fluid-state DPPC bilayer was characterised by a free energy maximum of ≈5 kJ/mol at the bilayer centre and a minimum value ≈-25 kJ/mol in the vicinity of the head group region. Our predictions with a model SC show a favourable minimum in the free energy (≈-20 kJ/mol) for the interactions below the bilayer interface, in the vicinity of the polar head groups of the lipids. Upon insertion into the hydrophobic interior of the bilayer, the free energy reaches a broad maximum (i.e. a free energy barrier of ≈20 kJ/mol) in the low-density hydrophobic region, indicating the occurrence of the most unfavourable interactions. The free energy profile of the C4Laa 5-ALA derivative (orange) features a free energy

profile with a similar shape, but with more pronounced minimum and maximum values of -30 and 50 kJ/mol, respectively. The increased affinity for the bilayer interface can be explained by the additional hydrogen-bonding capability of the Laa moiety. This likely also explains the increase in the free energy barrier located in the hydrophobic centre of the bilayer. Despite having the same polar surface area increase, the C8Laa 5-ALA derivative (green) has the most favourable free energy of interaction of these molecules at the interface. This may be explained by the ability of the longer hydrophobic chain to insert into the hydrophobic core of the bilayer at the same time as the polar backbone of the peptide forms hydrogen bonds with the lipid head groups at the bilayer interface, resulting in a more favourable ensemble of molecular configurations than those of the C4Laa derivative. In this case, the longer hydrophobic tail appears to confer advantageous favourable non-polar interactions. Similar increase in hydrophobic interactions could explain why C8 Laa 5-ALA features the lowest free energy barrier (≈10 kJ/mol), which appears as a maximum in the free energy in the high-density hydrophobic region of the bilayer (at a COM distance of 1.0 nm). The translocation of this derivative into the low-density hydrophobic region of the bilayer is characterised by a local minimum with a favourable free energy of ≈ -10 kJ/mol.

Direct comparison of our predictions to experimental data (193) (discussed in Figure 4.1.1) is discouraged for two reasons. In the first place, those experiments indirectly reflect the permeability across a (single) cell membrane made of a complex mixture of phospholipids, under the assumption that the enzymatic conversion occurs at the same rate for all derivatives. In contrast, our predictions represent the permeability across the lamella of ICLM-SC. Secondly, because of the two different approaches to chemically modify the parent molecule. Briefly, the experimental data reported (193) was obtained for molecules synthesized by a attaching a short carboxylic acid to the 5-ALA via an ester bond in its carboxylic end, whereas our derivatives bear a Laa attached to the amino end. This means that a 5-ALA molecule modified, for example, with butyric acid via an ester bond will increase its hydrophobicity without addition of hydrophilic groups, unlike the case of the C4Laa derivative (amino and acid). The predictions reported here suggest that the modification with a C4Laa shifts the balance of hydrophobic/hydrophilic regions of the molecule to very unfavourable interactions with hydrophobic regions of the lamellae in the ICLM-SC.
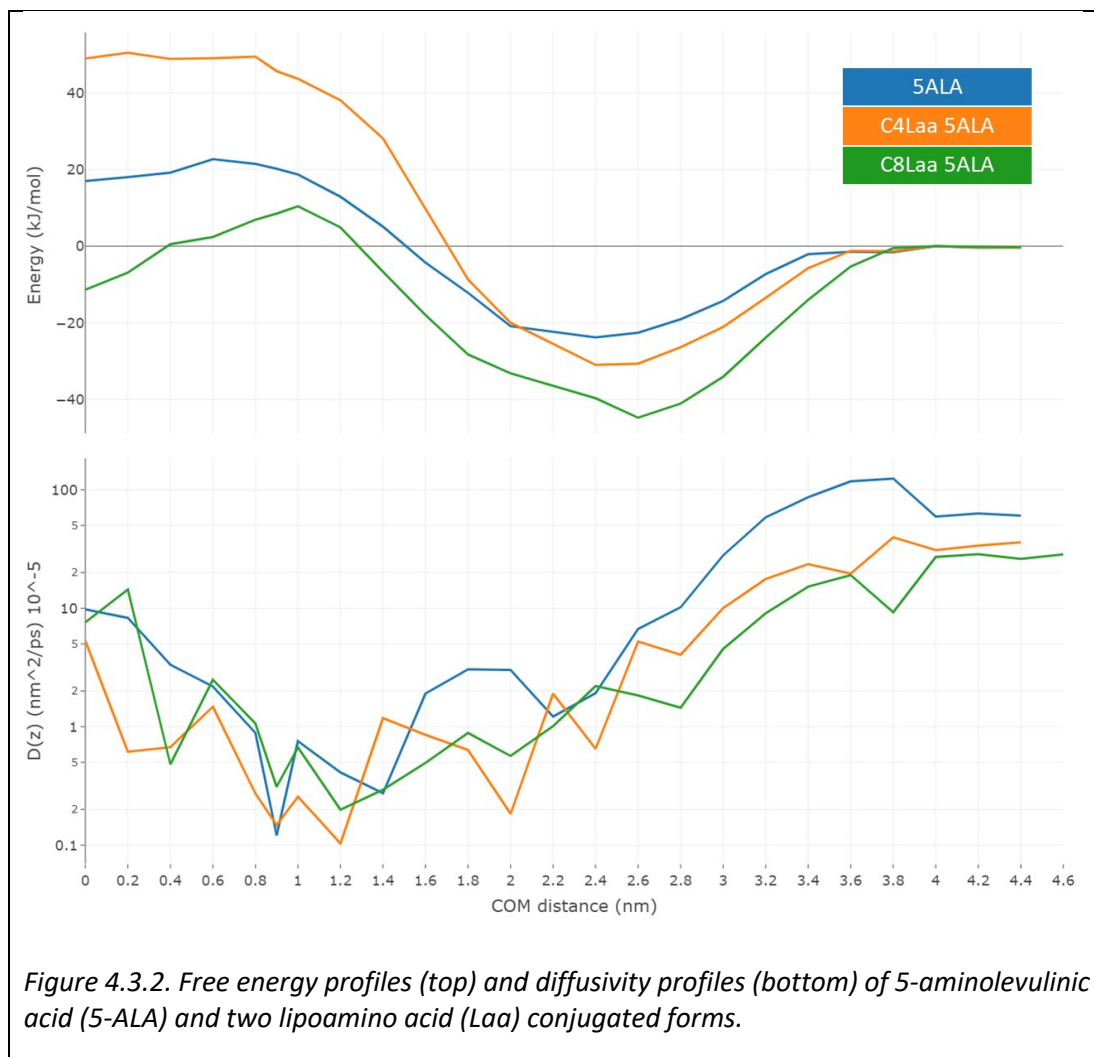
Figure 4.3.2. Free energy profiles (top) and diffusivity profiles (bottom) of 5-aminolevulinic acid (5-ALA) and two lipoamino acid (Laa) conjugated forms.

The estimated one-dimensional diffusivity profiles for the three molecules are also displayed in Figure 4.3.2 (bottom). In the bulk water region, where the molecules are far away enough from the influence of the bilayer (at COM distances larger than 4.0 nm), the diffusion coefficient appears to follow a decreasing trend with increasing MW, as expected. The diffusivity of the three molecules decreases by three orders of magnitude as they insert into the high-density hydrophobic core, and moderately recovers when they translocate to the low-density hydrophobic region, where they reach very similar diffusivity values. This behaviour agrees with what was discussed for the Ala-Trp dipeptide in section 3.3.6 of Chapter 3. Briefly, a three order magnitude decrease in diffusion was calculated for the Ala-Trp dipeptide at the dense-hydrophobic region (compared to bulk water) in the US-REST3 simulations. It is interesting to note that the diffusivity of the derivatives in the hydrophobic interior of the bilayer does not seem to be affected by the differences in MW, number of polar groups or rotatable bonds, suggesting that the changes in density across the lipid bilayer play the most important role in determining the overall trend in the rate of diffusion of these molecules. Therefore, the predicted differences in the

permeability estimates of these molecules are determined by their distinctive free energy profiles, as discussed above.

Table 4.3 presents a summary of the permeability values reported in the literature for 5-ALA and some of its derivatives. Regardless of the skin sample and the type of diffusion cell assay, the experimental transdermal permeabilities of both 5-ALA and methyl 5-ALA are in the order of 10^{-13} nm/ps. In contrast, the transmembrane permeability predicted for 5-ALA (and most derivatives tested by Erdtman et al.) across a pure DPPC bilayer is in the order of 10^{-4} nm/ps (194). This striking difference is explained by the marked differences in membrane properties expected between a pure phospholipid bilayer and the CER-containing lamella of the ICLM-SC. The former is associated with the fluid state, with low order and low density in the hydrophobic core, with lower thickness than CER-containing bilayers. It is thus expected that the permeation of a small molecule across a phospholipid bilayer will occur at a faster rate than across a CER-containing bilayer. In addition, the series of CER-containing bilayers forming the ICLM-SC in skin samples could amplify the impact of these structural differences.

Table 4.3. Permeability values for 5-ALA and its derivatives.

Year	Molecule	Sample and method	P (nm/ps)	Ref.
1996	5-ALA	Human upper thigh skin using a horizontal-type diffusion cell	2.25×10^{-13} (average)	(196)
2009	Neutral 5-ALA Methyl 5-ALA Ethyl 5-ALA	MD simulation across pure phospholipid (DPPC) bilayer	1.89×10^{-4} 5.28×10^{-4} 7.45×10^{-8}	(200)
2011	(HCl) 5-ALA	Human abdomen skin using a Franz-type diffusion cell	2.36×10^{-13}	(210)
2016	Oxime derivatives	MD simulation across a pure phospholipid (DPPC) bilayer	1.93×10^{-4} (average)	(194)
2018	Methyl ALA	Piglet skin using a Franz-type diffusion cell Solution Gel	4.17×10^{-13} 7.50×10^{-13}	(198)
2021	5-ALA C4Laa 5-ALA C8Laa 5-ALA	MD simulation across a model SC lipid bilayer (this work)	9.8×10^{-12} 1.04×10^{-16} 1.53×10^{-9}	NA

Table 4.3 also lists the predicted transdermal permeability of the neutral 5-ALA calculated in this work. Our permeability rate is one order of magnitude larger than experimentally determined values, which is likely due to the assumptions made in

the calculation, including the lack of lipid class diversity and polydispersity featured by our ICLM-SC model. Additionally, our permeability estimate is one-dimensional and accounts only for the rate of translocation in the normal direction, assuming a series of identical lipid bilayers posing the same resistance. In experiments, the small molecule also translocates on the bilayer plane (lateral diffusion) which is expected to occur at a different rate. This lateral component of the diffusion is likely to affect the predicted transdermal permeability estimates. A marked decrease of permeability coefficient was predicted for the C4Laa 5-ALA , this could be attributed to the significant increase in MW and the addition of polar groups by the modification with the C4 Laa. In contrast, a marked increase in the transdermal permeability of three orders of magnitude is predicted for the C8 Laa 5-ALA. In this case, the increase in MW and the addition of polar groups given by the Laa conjugation, seem to be counterbalanced by the four extra aliphatic carbons in the sidechain of the Laa (C8 vs C4).

4.3.2 Dipeptide-2

The structure of the uncapped, uncharged Val-Trp (VW) dipeptide and the two Laa derivatives studied are shown in Figure 4.3.3, along with the naming convention and the colour code used throughout this section. The MW of Val-Trp is 300.3, it has six rotatable bonds and a polar surface area of 108 Å^2, with four hydrogen-bond acceptors and four donors (211).

Figure 4.3.3. Chemical structure of Dipeptide2 (Val-Trp) and two lipoamino acid (Laa) conjugated forms.
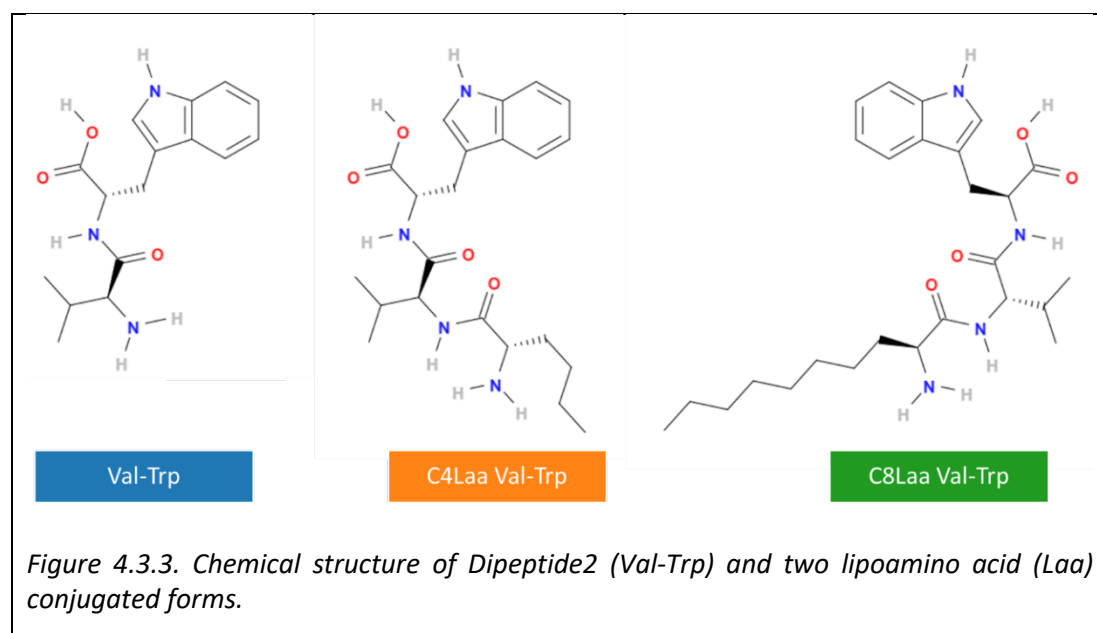
The converged predicted PMF of the permeation of the dipeptide Val-Trp is shown in blue in Figure 4.3.4 (top). This profile shows various similarities to what was described

for the dipeptide Ala-Trp in Chapter 3 (Figure 3.3.10), which is expected considering their structural similarity. In this case, the amphiphilic nature of the Val-Trp dipeptide explains the global minimum in free energy observed below the bilayer interface, with a favourable free energy of ≈-55 kJ/mol. At a COM distance of 2.4 nm, the backbone of the peptide can interact with the polar groups of the lipid headgroups and with any surrounding water molecules, whilst its hydrophobic sidechains can interact with the hydrocarbon chains of the lipids. Upon further insertion, the Val-Trp reaches the global free energy maximum located at a COM distance of 1.0 nm (i.e., in the high-density hydrophobic region) with a barrier of ≈10 kJ/mol. In contrast to the PMF calculated for the dipeptide Ala-Trp (Figure 3.3.10), when the dipeptide Val-Trp translocates into the low-density hydrophobic region, the predicted free energy decreases modestly, reaching a local free energy minimum of ≈0 kJ/mol. The C4Laa Val-Trp (Figure 4.3.4, orange) exhibits a very similar free energy profile despite the increase in MW and complexity of the Laa moiety. The lipid conjugation modestly reduces the favourable interactions at the bilayer interface by ≈5 kJ/mol. However, the C4Laa Val-Trp shows a decrease of ≈ 10 kJ/mol in the barrier height, which now has the same relative free energy as the bulk water region (i.e. 0 kJ/mol), and a more favourable local free energy minimum at the bilayer centre compared to the parent Val-Trp peptide. The increase in lipid tail length in the C8Laa moiety (green) substantially reduces the free energy barrier associated with the crossing at the high-density region and favours insertion at the bilayer centre by ≈-40 kJ/mol, whilst keeping similar favourable values at the bilayer interface. The free energy of interaction at the bilayer interface is mostly unperturbed despite the addition of C4 and C8 Laa moieties, which could indicate that the interactions are dominated by the parent molecule.

Figure 4.3.4 (bottom) shows the diffusivity profiles of the Val-Trp and lipid-conjugated derivatives. The one-dimensional diffusion coefficient of each molecule stabilizes at COM distances larger than 4 nm, indicating that the molecules are in bulk water, i.e. far away enough from the effect of the bilayer. The ranking of the diffusivity of the peptides in this region corresponds to the expected downward trend with increasing MW. However, in the other regions of the simulation cell, the diffusivity of the lipid-conjugated derivatives of Val-Trp is indistinguishable from that of the parent molecule. Notably, the diffusivity of the three molecules is predicted to be very similar at the bilayer centre in the low-density hydrophobic region, with an overall order of magnitude reduction in diffusion coefficient compared to bulk water.

Figure 4.3.4. Free energy profiles (top) and diffusivity profiles (bottom) of Dipeptide2 (Val-Trp) and two lipoamino acid (Laa) conjugated forms.
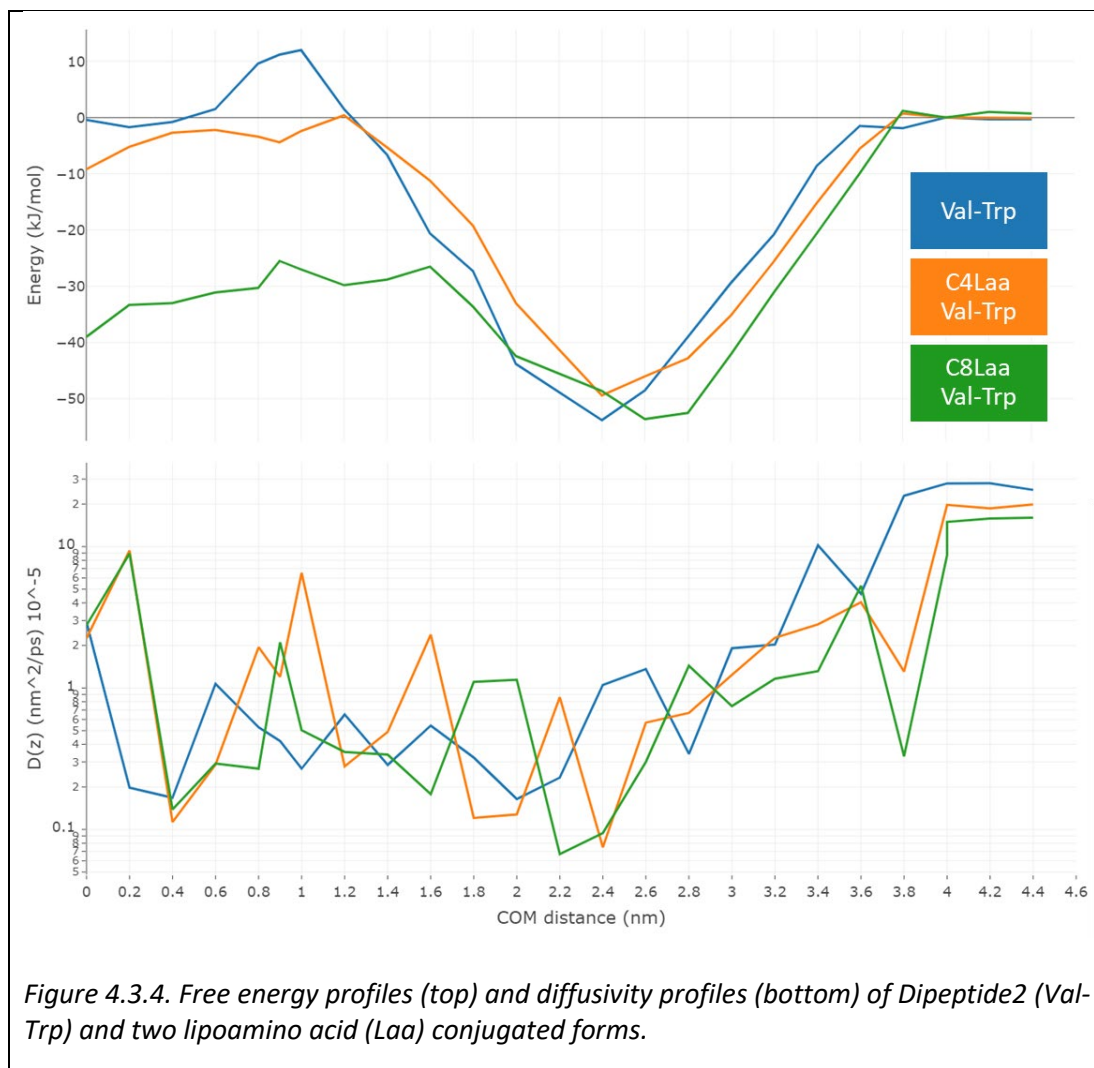
Table 4.4 reports the predicted permeability coefficients of the Val-Trp peptide and its Laa conjugates. The predicted permeability coefficient of the Val-Trp peptide is three orders of magnitude slower compared to the Ala-Trp (Table 3.10). A reduction in permeability coefficient with increase in MW is expected. Additionally, the figures reported in Table 4.4 predict that the permeability coefficients of the Laa conjugates are faster than that of the parent molecule (Dipeptide 2), with the C4Laa conjugate showing one order of magnitude improvement and the C8Laa conjugate showing two order of magnitude improvement. These findings agree with the experimental measurements of the AAPV tetrapeptide, where the permeability of the Laa conjugates increased with increasing number of carbons in the sidechain. Our findings suggest that for Dipeptide 2, lipid conjugation (by addition of the C8Laa moiety) could improve its transdermal delivery.

Table 4.4. Predicted permeability coefficients of Dipeptide 2 (Val-Trp) and two Laa conjugated forms.

Molecule	Permeability (nm/ps)
Val-Trp	6.3×10^{-10}
C4Laa Val-Trp	2.18×10^{-9}
C8Laa Val-Trp	3.71×10^{-8}

4.3.3 Melanostatin

Melanostatin has seven rotatable bonds and features four hydrogen-bond acceptors and four donors. These hydrogen-bonding groups are distributed along the peptide backbone and represent a polar surface area of 111.3 Å^2 (203). Figure 4.3.5 shows the structure of the uncapped, uncharged peptides that were studied. The tripeptide Pro-Leu-Gly (PLG) and two Laa derivatives are shown with the naming convention and colour code used in this section.

Figure 4.3.5. Chemical structure of Melanostatin (Pro-Leu-Gly) and two lipoamino acid (Laa) conjugated forms.
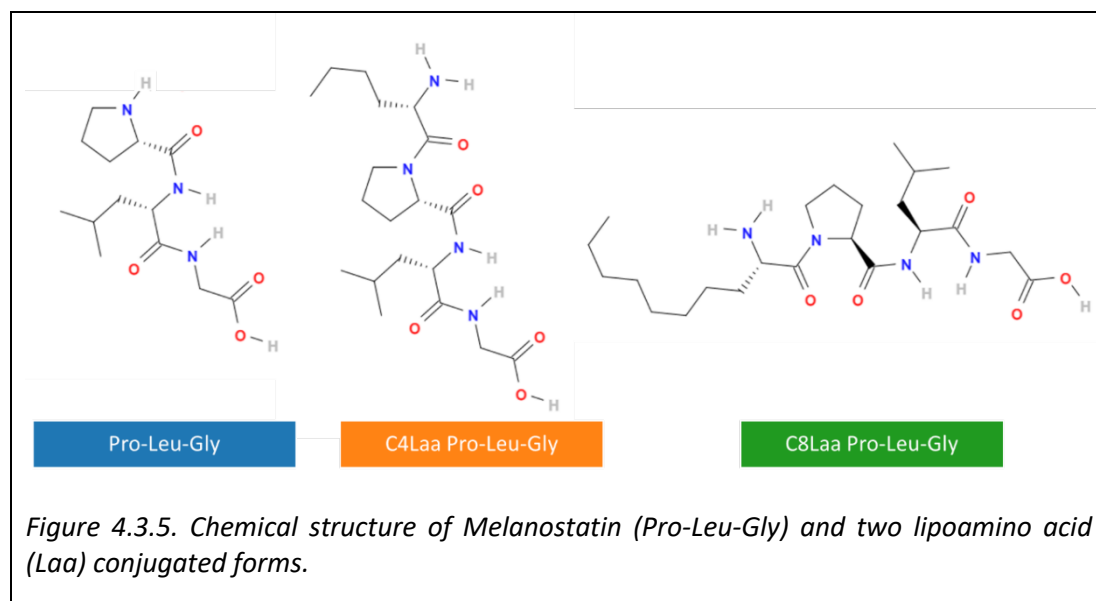
The converged predicted PMFs of these molecules are shown in Figure 4.3.6 (top). For PLG (blue), the interaction near the bilayer interface and the insertion into the bilayer are predicted to be favourable ($\approx$-55 kJ/mol and $\approx$-28 kJ/mol, respectively). However, the shape of the PMF shows a free energy barrier near the boundary between the high- and the low-density hydrophobic regions of the bilayer (at a COM distance of 0.8 nm). The shape of the PMFs for the two Laa conjugated peptides indicates the presence of broader free barriers in the same region, and global minima slightly closer to the interface of the bilayer. For C4Laa PLG (orange), the interaction near the bilayer interface and insertion are predicted to be slightly less favourable than for the parent PLG ($\approx$-50 kJ/mol and $\approx$-20 kJ/mol, respectively), but the free

energy barriers are very similar in magnitude. This is similar behaviour to what was discussed for the 5-ALA derivatives (Figure 4.3.2), in which the C4Laa conjugate was predicted to have an overall less favourable free energy of insertion than the parent molecule. In this case, it appears that conjugation with a C4Laa shifts the free energy profile to less favourable values at most distances when the peptide is in contact with the lipids. Notably, for the C8Laa PLG, the interaction near the bilayer interface and insertion are predicted to be more favourable than the parent PLG (≈-65 kJ/mol and -40 kJ/mol, respectively). One common feature of these three free energy profiles is that the free energy barrier is below or very close to zero, suggesting that the insertion into the dense-hydrophobic region is a favourable process, or at least does not involve a free energy penalty.
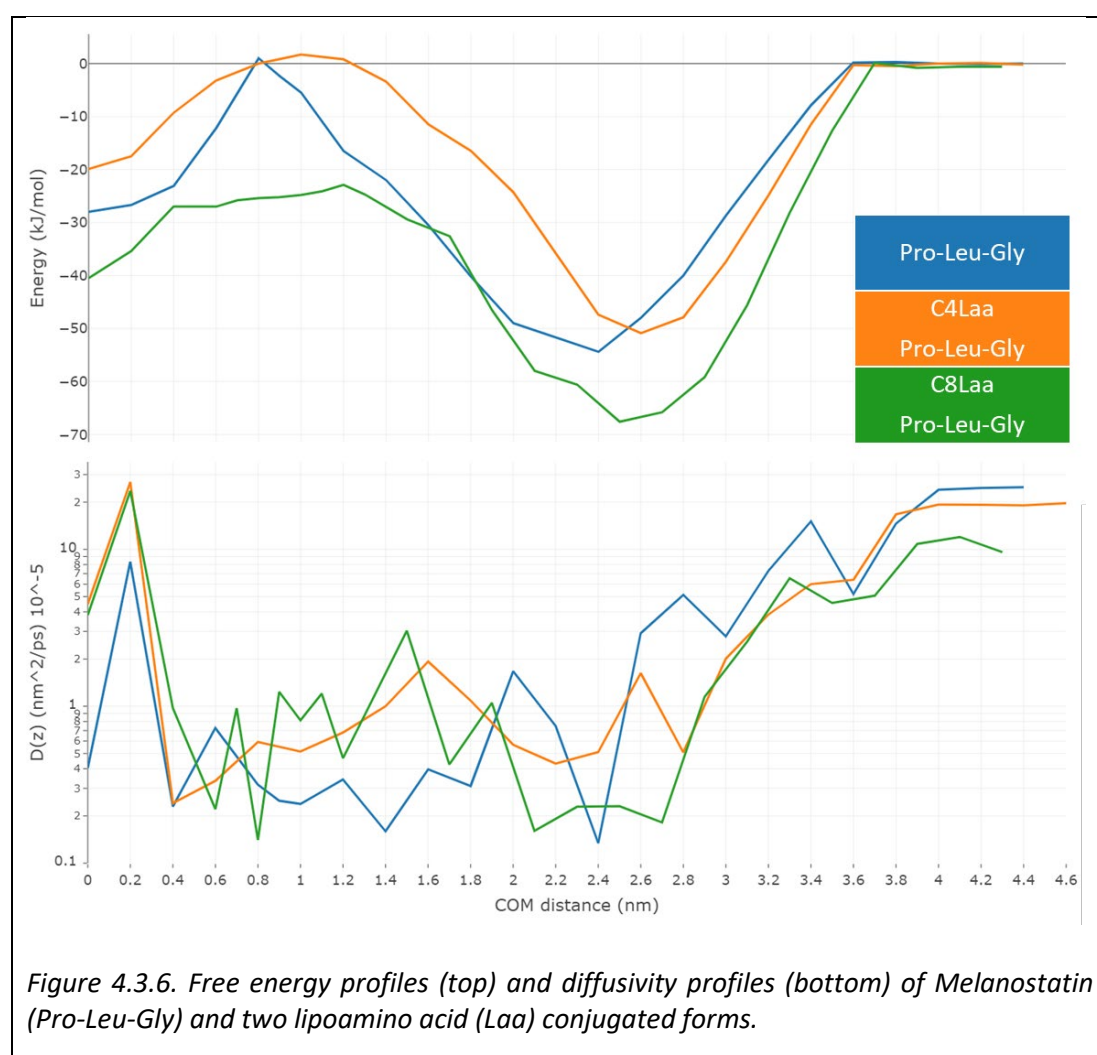
Figure 4.3.6. Free energy profiles (top) and diffusivity profiles (bottom) of Melanostatin (Pro-Leu-Gly) and two lipoamino acid (Laa) conjugated forms.

The diffusivity profiles displayed in Figure 4.3.6 (bottom) show that the diffusion coefficient in bulk water is again sensitive to the increase in MW, as expected. The diffusivity of the three molecules decreases by two orders of magnitude as they insert into the high-density hydrophobic core. The diffusivity of the Laa conjugated forms

of PLG oscillates around higher values in the high-density hydrophobic region (at COM distances of 0.8 – 1.8 nm) and is one order of magnitude larger at the bilayer centre, compared to the parent PLG. These differences will affect the predicted permeability coefficients of the Laa conjugated peptides.

Table 4.5 lists the predicted transdermal permeability coefficient of melanostatin (PLG) as well as the experimental value obtained using stillborn piglet skin with the capped from of the tripeptide at the C terminus (198). In addition to the expected overestimation of the predicted values, which was discussed in previous sections, the striking difference in orders of magnitude between these values could be partly explained by the capping -NH_2 group at the C-terminus. Given its hydrogen bonding capability, it is likely that this additional polar group makes the free energy of interaction at the bilayer interface more favourable. However, at the same time, the presence of the same moiety could significantly increase the energy barrier to translocation into the hydrophobic core of the bilayer, making the free energy of insertion less favourable at the bilayer centre. Assuming that the diffusivity of the capped and uncapped tripeptides is similar, these changes to the free energy profile could be partly responsible for the differences observed.

Table 4.5. Permeability of PLG and its lipoamino acid conjugates

Molecule	Permeability (nm/ps)
PLG-NH$_2$(198)	5.56 x10^{-14}
PLG	6.3 x10^{-8}
C4Laa PLG	2.76 x10^{-8}
C8Laa PLG	6.5 x10^{-7}

In a similar fashion to what was predicted for the 5-ALA derivatives, these predictions of permeability (Table 4.5) indicate that the addition of the C4Laa negatively affects the transdermal permeability of the PLG tripeptide. In the case of melanostatin (PLG), the reduction in permeability is more modest. By contrast, the C8Laa moiety is predicted to improve transdermal permeability by one order of magnitude. These predictions suggest that the chemical modification of PLG with a C8Laa moiety in the amino terminus could enhance its delivery across the skin.

4.4 Conclusions.

Any chemical modifications of a parent molecule will result in changes in the ratio of hydrophobic/ hydrophilic surface area for any parent molecule compared to the resulting derivative. In particular, the conjugation with a Laa moiety results in an

increase in hydrophilic surface area and hydrogen-bonding capabilities with the addition of another peptide bond in the backbone of the peptide. This increase will remain constant regardless of the length of the lipid tail in the side chain of the Laa (either C4 or C8). In contrast, the length of the lipid tail linearly determines the increase in hydrophobic surface area of the derivative molecule.

The addition of a C4 Laa moiety represents an increase in both hydrophobic and hydrophilic surface area for any parent molecule. According to the predictions of this work, the addition of C4Laa greatly reduces the permeability of 5-ALA, improves the permeability of Val-Trp and modestly reduces the permeability of PLG. The larger changes experienced by the 5-ALA in comparison to the two other parent molecules suggest that the MW of the parent molecule has an effect on the outcome of permeability upon conjugation with C4 Laa. In other words, these results suggest that, upon addition of the C4 Laa, the change in the ratio of hydrophilic/hydrophobic surface area (compared to the parent molecule) will be larger for the smaller parent molecules and more moderate for the larger ones. This indicates that in addition to MW, the ratio of hydrophilic/hydrophobic surface area is another molecular descriptor playing an important role in the permeation process.

In comparison to the C4 Laa, the addition of a C8 Laa moiety increases the hydrophobic surface area whilst keeping the hydrophilic surface area constant. The predictions in this work suggest that this modification triggers a substantial improvement in permeability for 5-ALA ($\approx 10^2$), a moderate increase in permeability for Val-Trp dipeptide ($< 10^1$) and increased permeability for PLG ($\approx 10^1$). Despite the increase in MW that this modification implies, the additional hydrophobic area conferred by the C8 Laa moiety (compared to the C4 Laa) improves the permeability of all the parent molecules studied, having the larger effect with the parent molecule with the lowest MW.

Altogether, the findings reported in this chapter suggest that for the range of MW considered, a subtle balance between the hydrophobic and hydrophilic regions determines the enhancement of the predicted transdermal permeability by Laa conjugation of short peptides and peptide-like molecules. It could be suggested that a molecular descriptor that represents a MW-normalized ratio between polar and non-polar surface area could be explored as a predictor of transdermal permeability of Laa-conjugated forms of active molecules.

Lastly, to capture the U-shaped effect on permeation reported by the experimental data in the work of Namjoshi et al. (56), it would be necessary to test at least three lengths of the aliphatic side chain of the Laa. Future works involving MD simulations could be conducted with two additional (lengths of the) Laa to appropriately resolve said U-shaped effect. In this prospective study, the selection of the two additional

Laas would have to be carefully tuned considering the different nomenclature given to the Laa in experimental works. In particular, the work of Caccetta et al. (57) depicts a C8 Laa-conjugated tetrapeptide with six carbons in the side chain, whereas the work of Namjoshi et al. (56) depicts it with eight (section 2.4.1.1 Amino acids and short peptides). This mismatch would potentially shift the U-shaped profile, including the optimal side-chain length, by two carbons with respect to the simulations.

5 Influence of the stereochemistry of the Laa moiety on transdermal permeability

5.1 Introduction.

5.1.1 Concepts in chirality

Chirality originates from the ability of a carbon atom to form four covalent bonds with four different substituents. A molecule that has only one chiral carbon can be one of two isomers according to the geometric arrangement of said substituents. These two isomers are mirror images of each other, which means that they are not superimposable. The two isomers are called *enantiomers* and share the same physical and chemical properties (e.g. boiling and melting points, density, solubility, reactivity, etc.). However, enantiomers differ in their optical activity, causing the plane of circularly polarized light to rotate in either a left (-) or right (+) -handed manner. This effect can be measured using a polarimeter or by optical rotary dispersion and circular dichroism. Based on their optical activity, enantiomers can be classified into either laevorotary (l-isomer) or dextrorotary (d-isomer). A racemic mixture (racemate) with sign (±) or (d, l) is a (50-50) mixture of the d- and l- enantiomers that, as a consequence, does not exhibit optical activity. Because of their optical activity, enantiomers are often called optical isomers. Note that the direction of the rotation of circularly polarized light is not determined by the 3-dimensional (3D) arrangement of the substituents.

An independent nomenclature of enantiomers is based on the absolute configuration of their substituents in 3D space, following the Cahn-Ingold-Prelog (CIP) convention. In this nomenclature, enantiomers are classified as either S or R, for the left- and right-handed 3D absolute configurations, respectively. The spatial arrangement of a chiral compound is experimentally determined by NMR and/or X-ray diffraction crystallography. Given the existence of two independent classification systems, a

complete description will include both, and thus an enantiomer can be designated as R(+), R(-), S(+) or S(-).

Diastereoisomers are a type of stereoisomers that have more than one chiral carbon. Unlike enantiomers, the physical and chemical properties of diastereoisomers can differ and, consequently, their chemical characterization is easier in comparison to enantiomers. When two diastereoisomers differ in their 3D configuration in only one chiral carbon atom, they are called *epimers*.

Homochirality is a feature in molecular biology in which the building blocks of macromolecules and other biomolecules all have the same chirality. One well-described case is that all amino acids are L amino acids (except Cysteine and glycine). Macromolecules like nucleic acids and proteins have chirality too. Some authors have suggested that there exists a guiding principle that explains the relationship between the homochirality of the building blocks of life and the higher-level structural organization of macromolecules, and that the homochirality of the building blocks originates the supramolecular chirality (212, 213). One of the reasons to rationalize the evolution of homochirality arises from the more favourable intermolecular interactions that occur given a particular 3D configuration. This is the basis of chiral-chiral recognition or discrimination, which is presented in more detail further below. Furthermore, the homochirality of biomolecules raises questions, not least with respect to the mechanism that explains the phenomenon, but also with respect to its implications for drug action and delivery.

5.1.2 Chiral lipids

Some lipids like phospholipids, sphingolipids and cholesterol, have chiral carbon atoms and, consequently, can exhibit stereoselective interactions with other chiral molecules (60). Just like amino acids and nucleosides, chiral lipids feature homochirality too, and isomers that are exclusively found in living organisms are often referred to as natural, endogenous, or native lipids. The location of the chiral carbon atom in phospholipids is in the glycerol backbone of their hydrophilic head groups (Figure 5.1.1). Similarly, sphingolipids (e.g. sphingosine in Figure 5.1.2) have two chiral carbons in the sphingosine moiety of the head group. This means that these chiral centres can play a role in membrane hydration, chiral lipid-lipid interactions and chiral lipid-solute interactions (e.g., the initial surface binding of a chiral permeant) (214). Ceramides are a product of the action of ceramide synthases on sphingomyelin (214), and share their two chiral carbons, more specifically at the C-2 and C-3 positions of the sphingosine moiety. This generates four diastereoisomers of sphingosine: (D-erythro: DE), (L-erythro: LE), (D-threo: DT), and (L-threo: LT) as shown in Figure 5.1.2. The homochirality of ceramides and sphingomyelin is reflected in the fact that only DE-erythro is endogenous (215).

116

Figure 5.1.1. Structure and chirality of common lipids. Top: phospholipids and sphingomyelin. Bottom: Cholesterol and epicholesterol (one non-biological epimer of cholesterol). Adapted from (62) *(CC BY 4.0)*
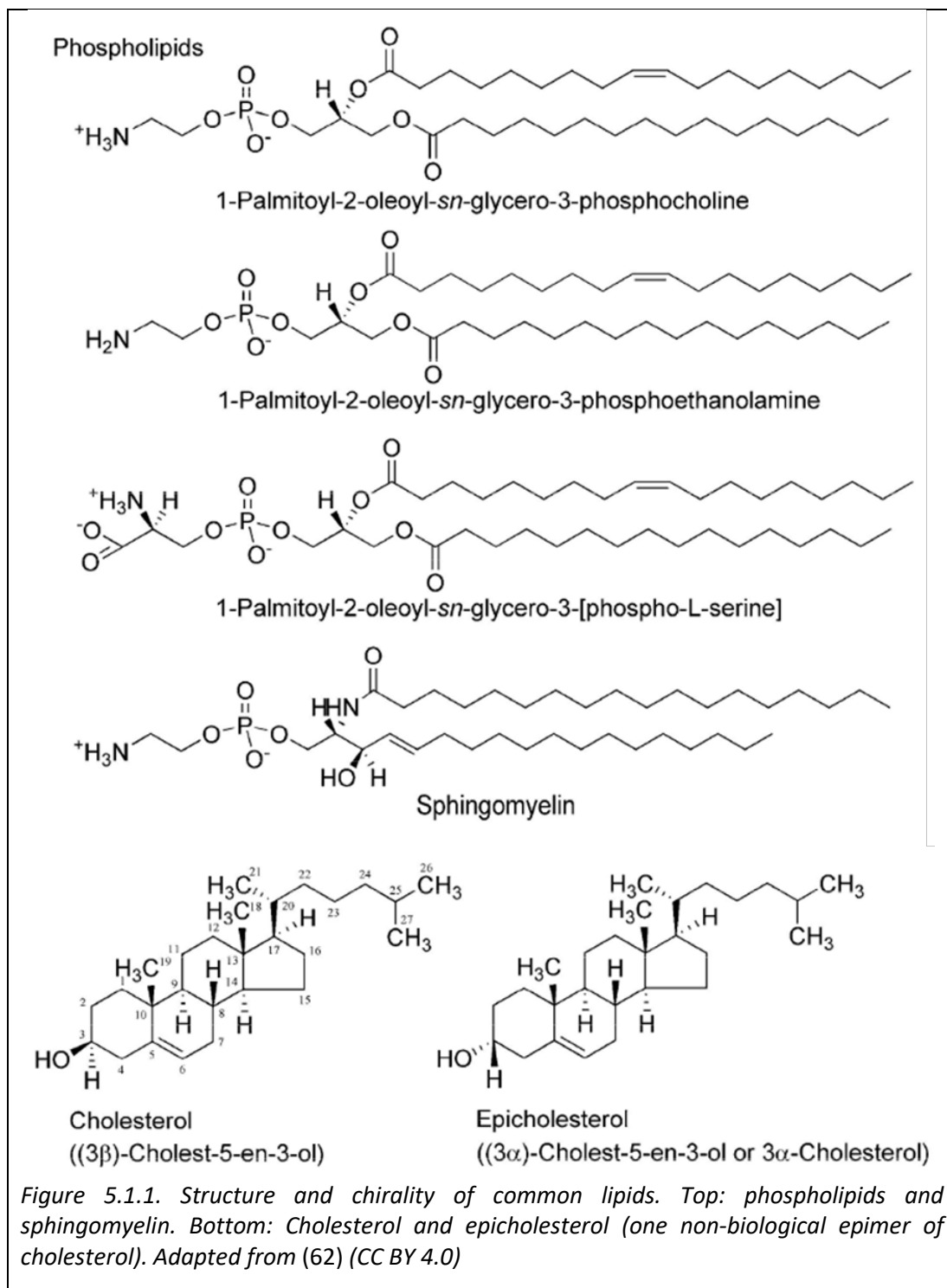
In contrast, cholesterol has eight chiral carbon atoms (C-3, C-8, C-9, C-10, C-13, C-14, C-17, and C-20), which are distributed throughout the molecule (Figure 5.1.1). Given the preferred orientation of cholesterol in lipid bilayers (i.e. with its hydroxyl in C3 oriented towards the interface), it can also play a role in interface interactions in the membrane, whilst the other chiral carbons interact with the acyl chains of other lipids (generally phospholipids and sphingolipids), contributing to lipid ordering.

117

Figure 5.1.2. Diastereoisomers of ceramides. Adapted from Ref. (215) © 2020 Wiley Periodicals, Inc.
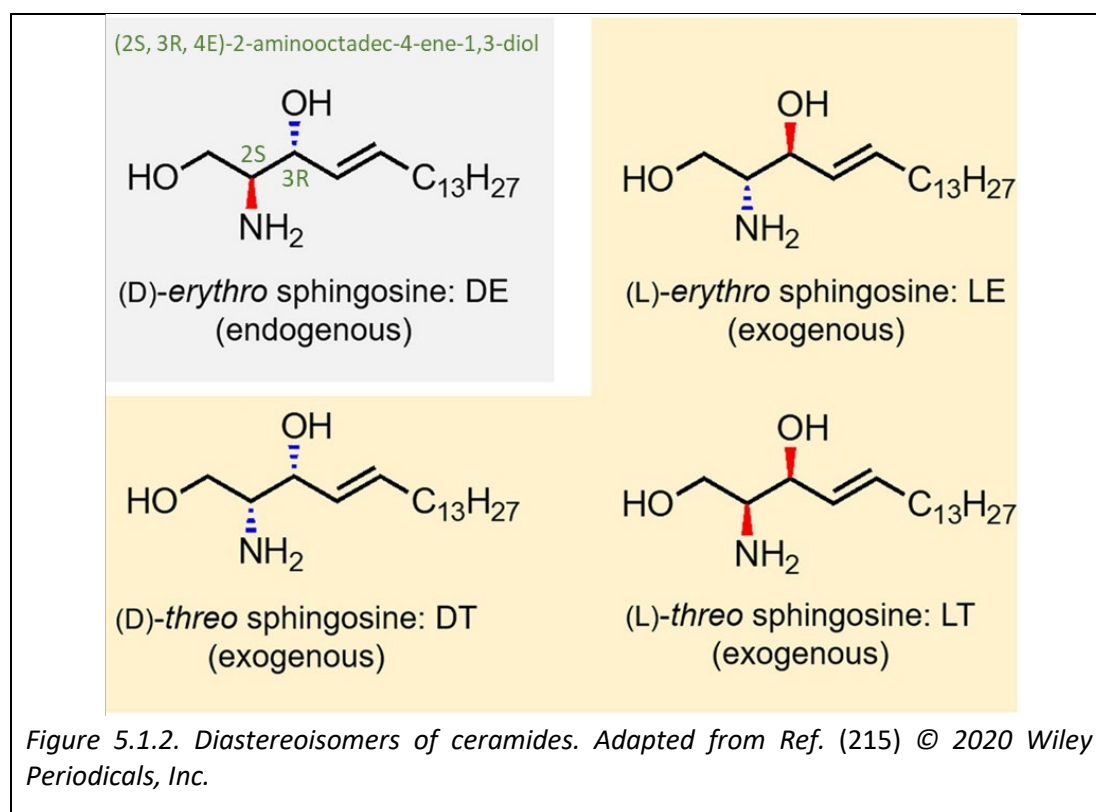
5.1.3 Chiral-chiral interaction of lipid bilayers

Lipid monolayers at the air-water interface are used as models to represent the biological barrier found in organs like the nose, eye, ear, and skin. This type of model membranes are called Langmuir monolayers, and are ideal models to study the molecular basis of the subtle phenomena of chiral discrimination, as reviewed by Nandi and Vollhardt (60). For example, in Langmuir monolayers, DPPC and DPPE are capable of self-recognition chiral discrimination, in what is called "homochiral interactions". This occurs because of the stronger interaction that takes place with the same type of isomers and can lead to the spontaneous formation of phase-separated domains driven by a favourable change in the free energy of the mixture (60). Homochiral interactions have implications for the evolution of prebiotic chemistry. For example, the enrichment of prebiotic lipid bilayers with one isomer could be linked to the homochirality of lipid bilayers in living organisms (61).

Furthermore, there is evidence that bilayers have different properties when they are formed with non-native lipids. For example, sphingomyelin bilayers containing the non-native L-threo isomer exhibit less tight lateral packing and a lower phase transition temperature, compared with an enantiopure native (D-erythro) bilayer. This effect can be traced back to the optimal hydrogen-bonding at the interface that occurs across native sphingomyelin molecules (214). Similarly, the hydrogen-bond network at the interface of phospholipid bilayers containing epicholesterol (the

118

epimer of cholesterol in the C3 chiral carbon, Figure 5.1.1) changes with respect to the native cholesterol. This is because epicholesterol sits closer to the interface (62). These changes in the hydrogen-bond network have implications for the interactions between the lipid bilayer and small molecules.

5.1.4 Chiral interactions determine the activity of drugs

The chirality of drug molecules can determine their activity. A common example is the 100-fold difference in potency of ibuprofen enantiomers (S>R). In fact, the term "chiral switch" in the pharmaceutical industry refers to the development of a single enantiomer from a chiral drug that has been developed (or even marketed) as a racemate or a mixture of diastereoisomers (216). The rationale for the interest in the chiral switches of chiral drugs is evident when there is higher activity of one stereoisomer. The interaction of chiral drugs with their chiral macromolecular targets causes differences in the pharmacological properties (e.g., activity, potency, toxicity, bioavailability, metabolism, and excretion rate) (216). Accounting for the interactions of chiral molecules within the organism is so crucial when designing chiral drugs that in the early 2000s the FDA issued guidelines to market enantiomerically pure drugs (217). Since then, 15 approved chiral switches were approved by 2011, and all new drugs approved in 2015 were enantiomerically pure (with known absolute configuration) (218). Furthermore, this also explains the current interest in developing new drugs as pure stereoisomers, characterizing the pharmacological and pharmacokinetic profiles of individual stereoisomers, and purifying stereoisomers from a mixture (219). The latter is referred to as chiral resolution (217), and involves the development of experimental and predictive methods to assign the absolute configuration of an isomer. This interest is not surprising considering that nearly 50% of all drugs commercially available have chiral properties.

Figure 5.1.3 (top) lists the possible outcomes of the activity of chiral drugs in the body. Two branches show the case of one isomer (S or R) having higher therapeutic effect (the eutomer), which gives rise to another two options: that the other isomer (the distomer) has reduced activity, or that it is responsible for toxicity or side effects. The third branch is when the isomers have comparable activity, which could be the case if the interaction with their target is not stereoselective. The superior activity of the eutomer can be explained by the chiral recognition between a chiral binding site and the chiral drug, which is referred to as stereoselectivity (Figure 5.1.3, bottom). In addition to the potentially chiral interaction with their target, most drugs must negotiate lipid bilayers before they reach their target. The interaction of chiral drugs with lipid molecules is thus another possible source of stereoselectivity (60, 66), in particular for peptides with therapeutic activity (63, 65). There is evidence that

homochiral lipid bilayers can promote the selection of chiral molecules due to interactions at the interface (61), leading to some chiral molecules having faster uptake rates into protocells (64), in particular L amino acids (65).

Figure 5.1.3. Top: The branching of outcomes of the activity of chiral drugs with examples of commercially available drugs for each case. Reprinted from Ref (212) *(CC BY 4.0). Bottom: Stereoselectivity of a chiral drug interacting with a chiral binding site.*
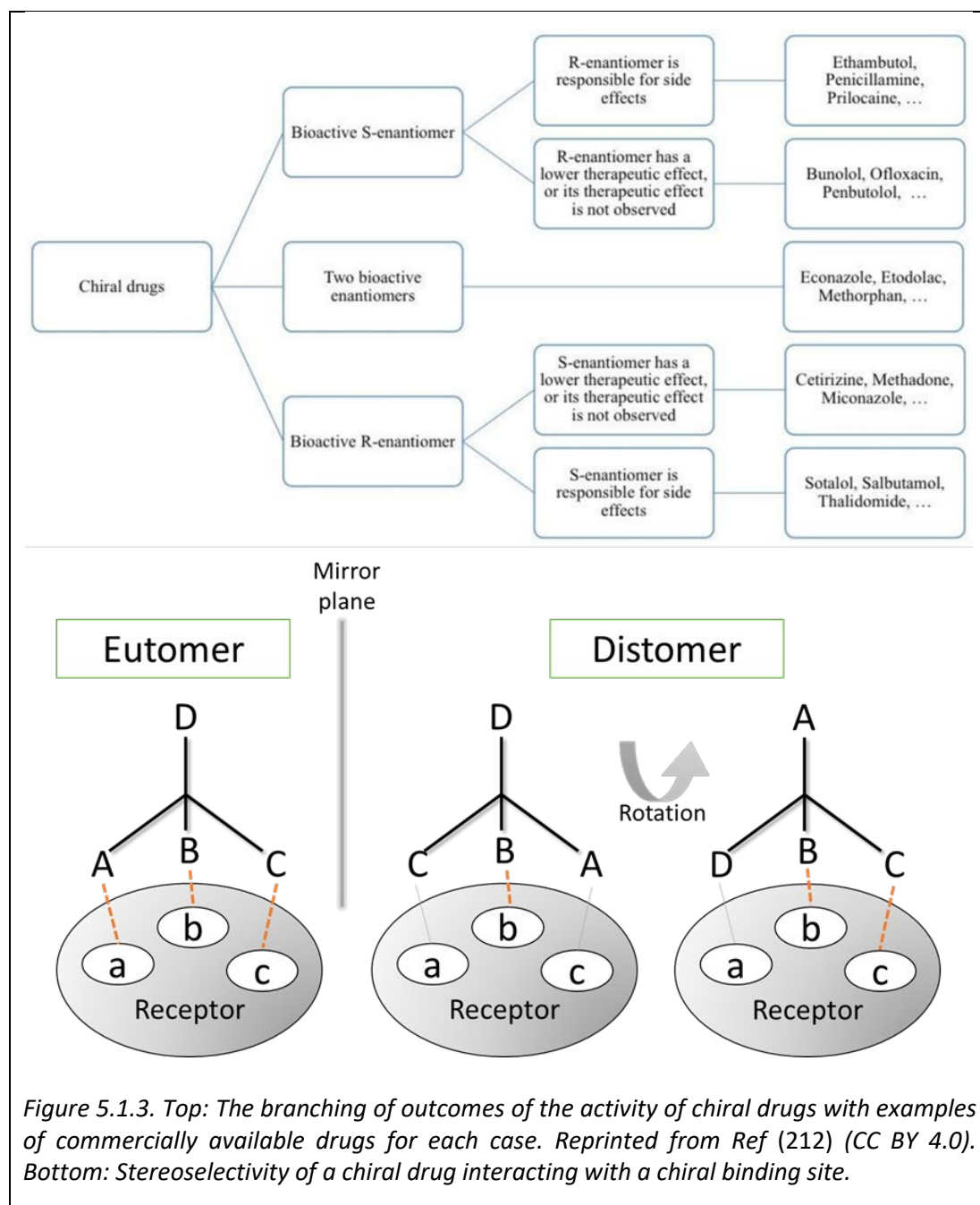
Unfortunately, the lack of metrics and models to predict the eutomer (and distomer) from theoretical studies evidences the lack of understanding of the basic principles that give rise to the differences in biological activity between stereoisomers. Most of the theoretical work has been devoted to the understanding and prediction of the optical properties of enantiomers in solution and their interactions with solvent molecules (213, 220, 221). For example, there is evidence that the local configuration

of solvent molecules around a chiral solute can be used to predict the rotatory strength (from the circular dichroism spectra) of the stereoisomer (70), and that chiral discrimination could be explained by subtle changes in the geometry of hydrogen-bonding interactions of isomers with their surroundings (69, 71). In fact, a chiral solute can induce the formation of a chiral shell (of solvent molecules), even if the solvent molecules are not chiral. This solvent shell can be responsible for the optical properties (chiroptical response) of the isomer (72, 222).

The global aim of predictive models, however, should be to rank the activity of a pool of stereoisomers on the basis of their chiral properties by estimating the outcome of their binding to macromolecular targets and their interactions with lipid bilayers. In 2011, Zunino et al. conducted a pioneering systematic study to measure the effects of monoterpenes on large unilamellar vesicles and correlate them with molecular descriptors. Monoterpenes are lipophilic bioactive molecules with chiral properties and, in their interactions with lipid bilayers, exhibit stereo-selective preferential locations of insertion depending on their molecular structure, which generates distinct changes in bilayer properties like curvature and area per lipid. Despite their systematic experiments using five pairs of optical isomers and 31 molecular descriptors, Zunino et al. could not elucidate the principal components of their bilayer activity that could generate a quantitative structure-activity relationship (QSAR) model. Instead, they provided a rationalization of the membrane effects of curvature and lateral expansion (223). Almost a decade later, in a recent review on membrane activity of non-steroidal anti-inflammatory drugs, the authors highlighted the paucity of stereospecific studies of their activity on lipid membranes (224).

Umakoshi and collaborators (2016) conducted an experimental study with the aim of optimising a formulation of liposomes that maximises the stereoselective uptake of ibuprofen (IBU). Their findings indicate that liposomes made of four pure phospholipids (DPPC, DMPC, DOPC, and DLPC) have almost no selectivity in their uptake of the S/R isomers, despite their range in fluidity and phase (solid ordered, liquid ordered, and liquid disordered). However, the higher fluidity of pure DLPC liposomes was deemed to be responsible for their higher uptake compared with the other pure liposomes. In contrast, a ternary lipid formulation including DOPC, sphingomyelin (bearing the sphingosine moiety) and cholesterol at a 4:4:2 ratio, improved the uptake and stereoselectivity of the liposomes. The higher uptake was associated with the nanophase-separated nature of this ternary mixtures (i.e., the liquid-ordered and the liquid-disordered phases are separated into small domains) because of discontinuity at the boundary edge between phases. The increased stereoselectivity of this mixture was associated with the effect of the chiral carbons present in sphingomyelin and cholesterol (225). Despite the interesting association of the stereoselectivity and uptake of IBU to the bilayer properties of these liposomes, the experimental methods used in this study could not provide the

resolution needed to assess the preferential interactions occurring between the lipids and each of the S/R isomers. In view of the composition of the skin, which features increased content of ceramides (also bearing the sphingosine moiety) and cholesterol, these findings are relevant in the context of the potential stereoselectivity of bilayers in the ICLM-SC.

5.1.5 Stereoselectivity of the skin

Rat skin (*ex vivo*) is stereoselective in the permeation of propranolol, where the S(-) enantiomer permeates four times more than the R(+) enantiomer. The stereoselectivity was demonstrated to be associated with the SC because when it was removed by tape stripping, the permeability values of enantiomers of drugs like IBU (67) and propranolol (226) were comparable. Notably, this stereoselectivity could only be reproduced using human skin in similar experiments in the presence of cellulose *TRIS* (3, 5-dimethyl-phenyl carbamate), which is also chiral (227, 228). This highlights the interspecies differences of the SC and further stresses the need for a reliable standardized transdermal permeability test that minimizes interspecies and inter-laboratory variability. This also shows the role that excipients could play in enhancing or preventing the permeation of a drug candidate across the SC (58). As was mentioned in the Introduction (section 1.3.2), changes in the formulation of an active molecule can increase its permeability. However, the link between the stereochemistry of the active compound and the permeability enhancers in the formulation (if present) remains elusive.

More recently, Kosina and Paloncyova et al. investigated the dermal intake of a set of nine bioactive diastereoisomers of silybin (SB) into human skin (68). They indicated that previous work on the ranking of the skin delivery of three SB diastereoisomers across mouse skin did not agree with their findings, most likely because of the more structured and impermeable *SC* and the thicker epidermis of human skin. The authors compared the experimental values of the octanol/water partition coefficient and transdermal permeability across human skin (*ex-vivo*) against predictions made by a range of computational tools. The structure of the two SB diastereoisomers that were tested in their enantiomerically pure form are shown in Figure 5.1.4 (top), along with their placement in the ranking of experimentally determined partition coefficients (bottom middle). This ranking includes other compounds purified from the same plant extract, with a focus on other bioactive diastereoisomers of SB. The experimental measurement of the partition coefficient was carried out following OECD guidelines for isocratic HPLC elution in gradient mode, instead of the more traditional shake flask method.

The experimental permeability across human skin was measured *ex-vivo* using a Franz-cell assay. However, permeability coefficients could not be calculated because

none of the bioactive compounds were detected in the acceptor compartment and, instead, were adsorbed into the skin. Hence, the authors used the skin intake metric defined as pmol of compound per gram of skin per 24 h. The relationship between these experimental values is shown Figure 5.1.4 (bottom left). Not surprisingly, the group of compounds with the highest partition coefficient also have the highest intake into the skin. The members of this group are diastereoisomers of SB (dehydroSB, isoSB, SB A, SB B). However, within this group, an increase in partition coefficient does not correlate with increased skin intake. This is evidence that an increased partition coefficient beyond a threshold is not favourable for skin intake (permeability in the general case).

Figure 5.1.4. TOP: structure of two diastereoisomers of silybin, which were tested as pure diastereoisomers. Bottom middle: the ranking of the experimentally determined lipophilicity of a set of compounds purified from Silybum extract, including the two shown above. Bottom LEFT: Relationship between the experimental partition coefficient and the intake to human skin (left) Bottom Right: relationship between the experimental intake to human skin and the predicted permeability. Adapted from Ref (68) *(CC BY 4.0).*

The performance of three *in-silico* tools (AlogP, Molinspiration, and COSMOtherm 15) was compared for the ability of their predicted partition coefficients to match the experimental ranking. The best performance was obtained with Molinspiration, which is based on topological descriptors (functional groups) of the permeant and a large set of experimental values (68). In an attempt to find closer agreement, the authors used the COSMOmic *in-silico* tool to estimate partition coefficients into

model lipid bilayers. Three model lipid bilayers were considered: a pure phospholipid bilayer (DOPC), a pure ceramide bilayer (CER), and a bilayer featuring a ternary (equimolar) mixture of ceramide, lignoceric acid and cholesterol (CLC) to represent the ICLM-SC. In this instance, the best correlation to experimental partition coefficients was obtained for the COSMOmic predictions for the DOPC bilayer (68). This not only reveals the close relationship between the water/octanol partition and the partition into a DOPC bilayer, but also highlights the failure of the experimental partition coefficient to represent the effects of the interactions occurring in the ICLM-SC.

The free energy profiles provided by COSMOmic were used for the estimation of permeability coefficients of the SB diastereoisomers across the three model bilayers. The results are shown in Figure 5.1.4 (bottom right). As expected, the permeability estimates for a DOPC bilayer are orders of magnitude higher than those for CER and CLC bilayers, which are thicker and in the gel state. The latter better resolves the differences in the low partition group (1 to 4). However, the resolution of the diastereoisomers belonging to the high partition group is not improved. In fact, the most hydrophilic compound (dehydroSB) has the highest predicted permeability across the CLC bilayer. Lastly, the COSMOmic free energy profiles for CER and CLC bilayers are very similar, resulting in similar permeability coefficients (68). This underpins the limitations of predictive models to resolve the interaction properties of structurally related compounds with *similar* lipid bilayers.

In addition to the chirality of ceramides, the chirality of cholesterol can also contribute to the stereoselectivity of the bilayers in the ICLM-SC. Despite ceramides playing a key role in conferring the bilayer properties of the ICLM-SC (and models like CLC), the presence of cholesterol and free fatty acids in the ICLM-SC shifts the bilayer properties to fulfil a healthy barrier function with appropriate fluidity, density and order parameters. Therefore, it is not expected that CER and CLC bilayers respond as similarly as predicted by COSMOmic.

The stereoselectivity that cholesterol can originate was demonstrated in the experimental work of Tsuchiya and Mizogami (62). They presented the distinct possible interactions that cholesterol and epicholesterol (Figure 5.1.1) can have with enantiomers of bupivacaine, as shown in Figure 5.1.5. The opposite chirality in the C3 of cholesterol causes a change in the location of cholesterol in the bilayers, which in turn changes the location of the interaction site of drugs and affects the ranking of the affinity of binding of the enantiomers (62).

Figure 5.1.5. Possible interactions of bupivacaine enantiomers with phospholipid bilayers containing either cholesterol or epicholesterol. Reprinted from (62) Copyright © 2017 by the authors (CC BY 4.0).
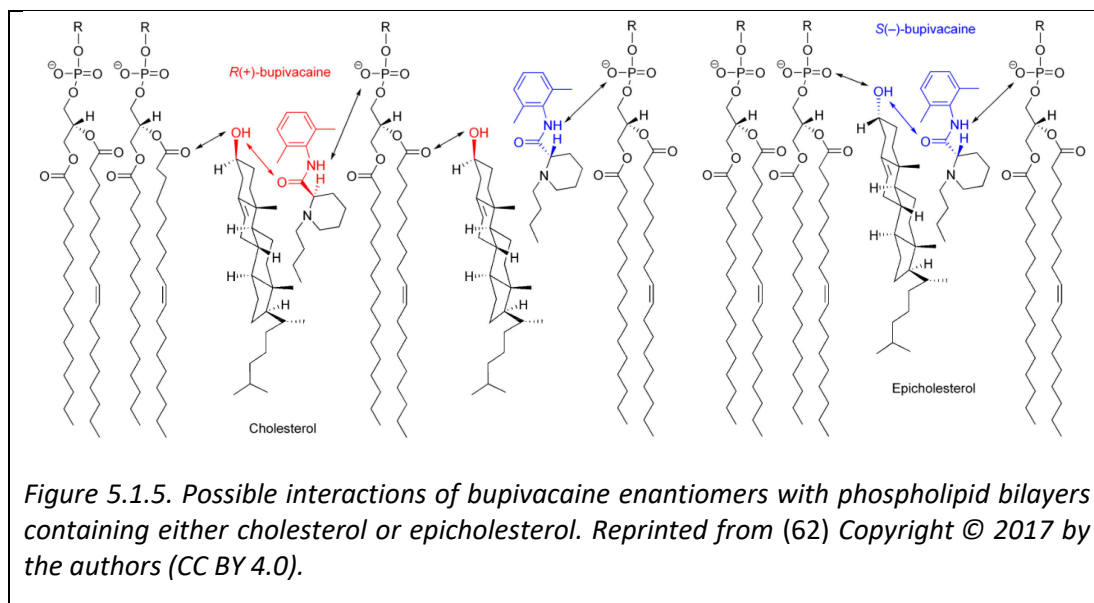
As previously discussed, the chemical modification of the tetrapeptide AAPV with a series of Laa moieties improved the transdermal permeability of the parent molecule across human skin in *ex vivo* experiments (56) (see Chapter 2 section 2.4.1.1). The addition of the Laa also improved the skin retention and stability whilst retaining the activity of the parent peptide. The Laa moiety is an alpha amino acid bearing an aliphatic chain (lipid tail) instead of a standard amino acid residue. Due to the chiral centre in the alpha carbon, any Laa can be either S or R stereoisomer. The skin retention increased linearly with the number of aliphatic carbons in the Laa moiety such that the higher retention was obtained with the C10Laa. However, the permeability was higher for the C8Laa conjugated tetrapeptide, indicating a negative effect of the additional carbons in the side chain of C10Laa. The permeability of the racemic mixture (L, D) and the pure epimers C8Laa (L) and (D) was reported. Results clearly indicate the effect of stereoselective factors favouring the permeability of one epimer over the other (D>L). The CIP convention categorizes all native amino acids (except for glycine and cysteine) as the S enantiomer. Because the Laa is an α amino acid the corresponding ranking in the CIP convention is R>S.

5.1.6 Molecular dynamics simulations can rationalize chiral phenomena.

MD simulation is a method ideally suited to study homochirality and chiral interactions in atomic resolution and from a free energy (of interaction) perspective (221). The differences between two isomers may be understood as the more common problem of calculating free energy differences between two well defined states, for example by generating a path from one stereo-configuration to the other (Figure 5.1.6) (229).

125

Figure 5.1.6. Transition pathway between one enantiomer to the other across intermediate stereo-configurations in the calculation of the free energy in chiral systems using MD simulations. Reprinted from (229) Copyright © 2020, American Chemical Society.
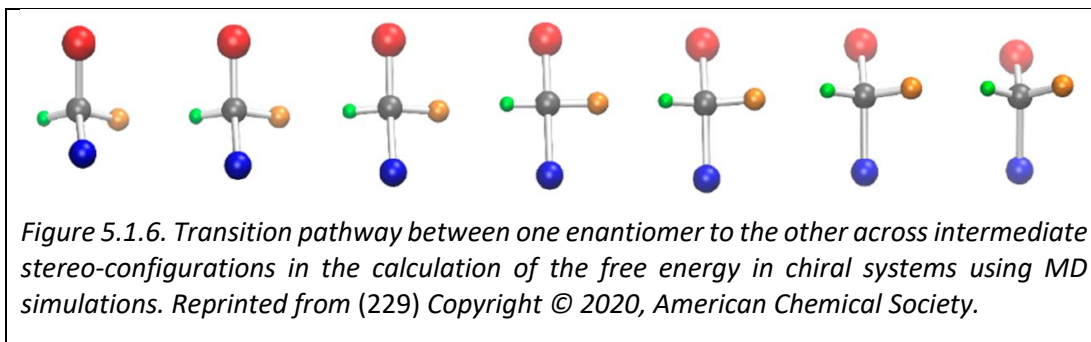
MD simulation is also well poised to study the molecular mechanisms that rationalize the phenomena observed in enantiopure bilayers. For example, using MD simulations of (chiral) glycerol monopalmitate (GMP) bilayers, Horta et al. showed how homochiral interactions vary in strength according to physicochemical conditions like the temperature and hydration of the system. In their work, a GMP racemic bilayer in the liquid phase underwent a transition to the gel phase, which was characterized by segregation of GMP enantiomers into separate lipid domains. This process occurred at low temperatures for full and half-hydration systems (61).

Lastly, MD simulations are an ideal method to gain understanding of the molecular basis of stereochemical discrimination in the interaction of small molecules with lipid bilayers. A number of key studies have demonstrated the relationship between the configurational preferences of chiral solutes with the observed chiral discrimination in their membrane activity (binding or permeation across lipid bilayers), establishing links to the observed differences in their activity/toxicity. The chiral solutes are small molecules such as naturally occurring monomeric sugars, drug molecules, and cyclic therapeutic peptides. Given the chirality of ceramides and cholesterol (CER and CHOL), the lipid bilayers of the ICLM-SC, have the ability to discriminate permeant molecules based on the chirality of the permeant. This stereoselective action is likely to occur near the chiral carbons of the lipids due to the preferential interactions that they may generate with the permeant.

An early study by Wei and Pohorille (2009) investigated the molecular interactions responsible for the ranking in experimental permeability coefficients of three (chiral) sugar monomers (aldopentoses) with implications for prebiotic chemistry: ribose and two of its diastereoisomers, arabinose and xylose. They calculated the free energy of transfer of the sugar monomers from water to the POPC, hydrophobic core and found that differences partly associated with the ability of the sugar monomers to adopt configurations that are rare in polar (aqueous) media. The more favourable configurations were reached by ribose and were characterized by intramolecular interactions between consecutive pairs of exocyclic hydroxyl groups of the

monomers in the pyranose form. These MD simulation findings were in agreement with the faster permeability of ribose relative to other aldopentoses (64).

Martini and Pickholz (2012) demonstrated the distinct changes that the enantiomers of the local anaesthetic bupivacaine (BVC) cause in the properties of a POPC bilayer when present in a 3:1 (POPC: BVC) ratio. The activity of both enantiomers as nerve blockers is similar, but their cardiotoxicity differs with R(+) > S(-). The electron density profiles indicated that the R(+) enantiomer of BVC sits below the head groups of POPC with a concomitant reduction in bilayer thickness and order parameters. In contrast, the S(-) enantiomer is distributed uniformly throughout the hydrophobic core of the bilayer and causes a very subtle decrease in order parameters and a subtle increase of the bilayer thickness. The increased cardiotoxicity of the R(+) enantiomer of BVC was rationalised by linking it to its damaging action on bilayer integrity, which in turn could affect the cardiac sodium currents and the activity of cardiac membrane receptors (73).

More recently, Riniker and collaborators (2019) tested the effect of a single amino acid modification on the permeability of a set of six cyclic decapeptides with therapeutic activity. Cyclic peptides with N-methylations to the backbone are preferred (over their linear counterparts) because of their rigidity and lower polarity. The more permeable undecapeptide cyclosporine A features anti-parallel β-strands and trans-annular H-bonds, resulting in a preferential *closed* conformation. The stability of the conformations available to the decapeptides was assessed in water, chloroform, and DMSO. Although these simulations did not include explicitly the interactions with lipids, the differential permeability of the peptides was addressed in an indirect way by testing the correlation between predicted and experimental permeability values obtained from parallel artificial membrane permeability assay (PAMPA) cell-based assays. The predicted values (from clogP and molecular polar surface area (3D-PSA)) did not show agreement with experiment; however, higher permeability was observed for the decapeptides that preferentially exhibit the closed conformation in water, which are the decapeptides with substitutions of D-proline. This highlights the poor performance of predictive models that are based on structural features and molecular descriptors of the permeant only (e.g. clogP and 3D-PSA), which cannot capture the conformational behaviour that dictates the differences in permeability between structurally similar permeants.

To our knowledge there are no other MD simulation studies reported addressing the stereoselectivity of the interaction of active molecules and the lipids found in the ICLM-SC. In this chapter the investigation of the molecular interactions that explain the differences in permeability of the epimers of the C8Laa conjugated tetrapeptide is reported. For this aim, MD simulations of the interaction of each epimer with the model lipid bilayer representing the ICLM-SC were conducted. These simulations

made use of the US-REST3 enhanced sampling method described in Chapter 3 (section 3.2.7).

5.2 Methods.

5.2.1 Topologies

Structures of the Laa modified tetrapeptides were obtained with the (open source) Avogadro software, by building a peptide using the available pre-set natural amino acids. The natural amino acid alanine was added to the peptide chain in place of the C8Laa. Using the manual drawing tool, the -CH$_3$ of the side chain was replaced with an aliphatic chain of eight carbons (C8). This resulted in the C8Laa conjugated tetrapeptide, in which all amino acids have the native chirality. Using the invert chirality tool in Avogadro the opposite stereoisomer of the C8Laa was obtained, resulting in the epimer of the C8Laa conjugated tetrapeptide. The structures of the two epimers were submitted to the Automated Topology Builder (ATB) (208) to obtain their topology and parameters compatible with the Gromos54a7 forcefield. The files can be retrieved from the ATB repository by using the identifiers presented in Table 5.1.

Table 5.1. Chemical formula and ATB identifiers of the epimers.

	Ala-Ala-Pro-Val	
	C8S Laa	C8R Laa
Formula	C26H47N5O6	
N. atoms (all atom)	48	
ATB resname	475H	0Z87
ATB ID	568858	567995
Calculation	QM0	

The structures of both epimers of the C8Laa conjugated tetrapeptides are presented in Figure 5.2.1. Their labels indicate the CIP convention indicating the left- and right-handed 3D absolute configurations, the common L and D notation, and the colour code that will be used throughout this chapter. The sticks-and-balls representation was rendered using VMD (188). Note that only polar hydrogens are shown explicitly in the structure, as per the UA Gromos54a7 ff. The orange circular arrows indicate the chiral centre where the epimers differ (in the amino end of the peptide) and the direction of rotation follows the ranking of substituents given by the CIP convention. Hereafter, the C8 Laa conjugated tetrapeptides will be referred by the chirality of their C8Laa moiety: (S) in blue and (R) in orange.

Figure 5.2.1. Sticks-and-balls representation of the structures of the two epimers of the C8Laa conjugated tetrapeptide in the Gromos54A7 UA ff.
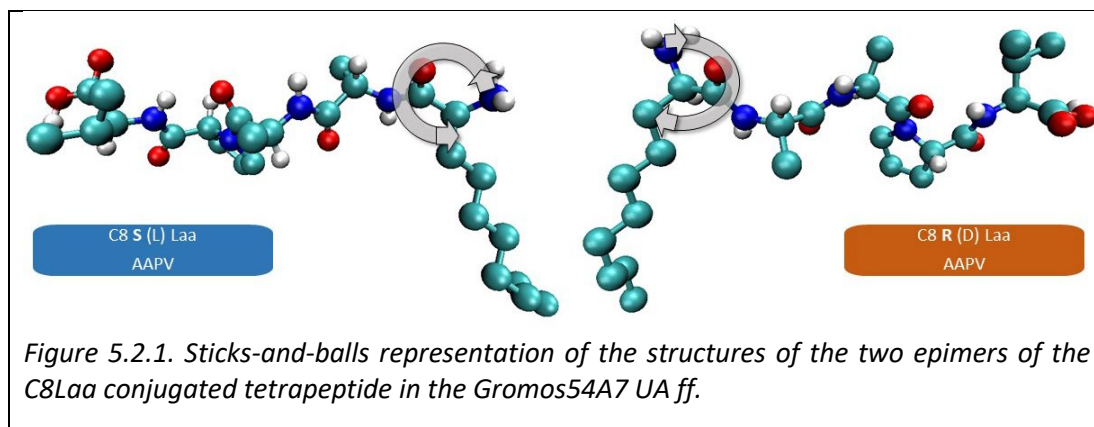
5.2.2 MD simulations

MD simulations were conducted as described previously. US windows were spaced every 0.2 nm in the reaction coordinate, covering COM distances from 0.0 to 4.6 nm. Conventional US simulation was used for the four US windows located in the bulk water region (to save computational effort). For the remaining twenty US windows, the REST3 enhanced sampling method was applied (Table 5.2). The first 10 ns of the US-REST3 simulations (per replica) were discarded as equilibration, giving a production time of 70 ns per US window in the ground replica. The aggregate time in the last column of Table 5.2 corresponds to the number of replicas running in parallel at each US window, as per the allocated replica scheme (Figure 3.3.6). Two replicate runs of each US-REST3 simulation were run from the same initial structure but with different initial velocities assigned. The total simulation time for the permeation of each epimer is nearly 30 µs and combining the two replicate runs the production time is 3.4 µs for the analysis of each epimer.

Table 5.2. List of US windows and simulation details.

COM distance (nm)	N. Replicas	Production time (ns)	Aggregate time (ns)
4.6	NA	80	80
4.4	NA	80	80
4.2	NA	80	80
4.0	NA	80	80
3.8	10	70	700
3.6	10	70	700
3.4	10	70	700
3.2	10	70	700
3.0	10	70	700
2.8	10	70	700
2.6	10	70	700
2.4	11	70	770
2.2	11	70	770

2.0	11	70	770
1.8	11	70	770
1.6	11	70	770
1.4	11	70	770
1.2	11	70	770
1.0	11	70	770
0.8	11	70	770
0.6	10	70	700
0.4	10	70	700
0.2	8	70	560
0.0	8	70	560
Total (per replicate)	**205**	**1720**	**14670**
Total (both replicates)		**3440**	**29340**

5.2.3 Free energy

The free energy profile for each replicate run was calculated as described in Chapter 3 (section 3.2.10). The average of the two free energy values is reported at every COM distance.

5.2.4 Diffusivity profile

The diffusion coefficient was calculated as described in Chapter 3 (section 3.2.11) for each replicate at each COM distance. The resulting diffusivity profiles are reported as an average of the two replicates.

5.2.5 Permeability

The permeability was calculated using the average free energy and average diffusivity profile across replicates, following Equation 1.3 (Chapter 1, section 1.5.2)

5.2.6 Enthalpy

The GROMACS module *g_energy* was used to retrieve the time average of the energy terms in the potential energy function by providing the energy file (.edr), which is automatically saved during the simulation (by the *mdrun* module). In particular, the average total enthalpy and the energy required to constrain the COM of the small permeant molecules were computed. The time average of the COM restraint energy was subtracted from the time average total enthalpy at each US window. The COM distance of 4.0 nm was used as a reference point to obtain the enthalpy change (ΔH) profile (Equation 1.1). The reference is in the bulk water region and is set to match

the reference set for the free energy profile (ΔG). Furthermore, knowing ΔG and ΔH allows estimation of the entropic contribution to the free energy by following Equation 5.2.

$$\Delta H = (\text{Enthalpy} - \text{COMrestraint})_{COM\ distance} \\ - (\text{Enthalpy} - \text{COMrestraint})_{4.0nm}$$

<div align="right">*Equation 5.1*</div>

$$\boldsymbol{\Delta G = \Delta H - (T\Delta S)}$$

<div align="right">*Equation 5.2*</div>

5.2.7 Hydrogen-bonds

The GROMACS module *g_hbond* was used to retrieve the number of hydrogen-bonds occurring between two (non-overlapping) atom groups as a time series. Given the five types of molecules present in the simulation cell, there are ten types of possible hydrogen-bonds across species and five possible hydrogen-bonds intra species as indicated in Table 5.3. Each of the 15 hydrogen-bond time series was retrieved for each US simulation into a file. The files were analysed with a custom Python script based on the open source Pandas library of functions to handle matrix-like data (data frame) (230). Briefly, for every US simulation the 15 files were imported into one data frame, from which operations could be readily executed. The functions in the Pandas library allow to efficiently perform operations such as the row wise addition of values. This was used to calculate the number of hydrogen-bonds between any of the lipid molecules and the other components of the simulation cell (water or permeant). A powerful feature of Pandas is the ability to calculate column wise averages, which was used to compute time averages of each type of hydrogen-bond. Time averages of each type of hydrogen-bond were plotted as function of the COM distance for each replicate run. All plots were produced with the (open source) Plotly graphing library for Python (231). The average of the replicates is reported with respect to the reference value, which was assumed to be at a 4.0 nm COM distance.

Table 5.3. Possible pair-wise interactions leading to the formation of hydrogen-bonds

	CER	CHOL	FFA	Water	Epimer
CER	CER-CER				
CHOL	CER-CHOL	CHOL-CHOL			
FFA	CER-FFA	CHOL-FFA	FFA-FFA		
Water	CER-Water	CHOL-Water	FFA-Water	Water-water	
Epimer	CER-epimer	CHOL-epimer	FFA-epimer	Water-epimer	Epimer-epimer

5.3 Results and discussion.

5.3.1 Free energy and diffusivity profiles

As demonstrated in previous chapters, the bulk water region of the simulation cell is characterized by a region of COM distance values where the free energy profile (PMF) does not change (and hence set to ΔG≈0). Figure 5.3.1 (top) indicates that for both epimers this region extends from 4.0 nm outwards. The interactions at the interface are equally favourable for both epimers, with a free energy of ≈-70 kJ/mol, and the PMFs start to diverge as the Laa-modified tetrapeptides translocate into the hydrophobic core of the bilayer. The C8 S Laa is characterized by a small barrier to penetration and a favourable free energy at the bilayer centre (≈-20 kJ/mol) whereas the C8 R Laa is characterized by a large barrier to penetration (>60 kJ/mol) that reaches a maximum at the bilayer centre. The PMFs of individual replicates are also displayed (Figure 5.3.1 top, insert).
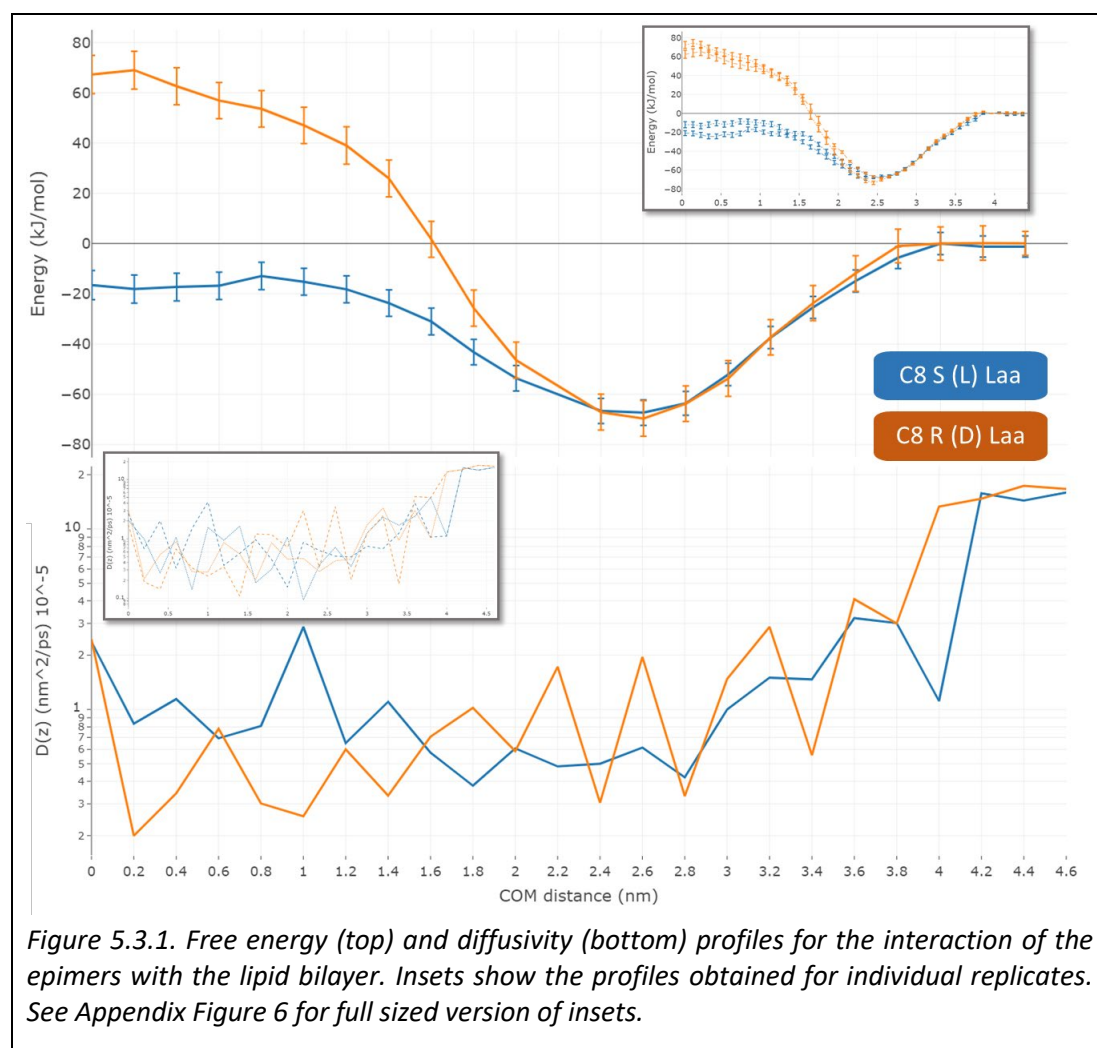
Figure 5.3.1. Free energy (top) and diffusivity (bottom) profiles for the interaction of the epimers with the lipid bilayer. Insets show the profiles obtained for individual replicates. See Appendix Figure 6 for full sized version of insets.

The predicted PMFs reveal that the molecular mechanism that determines the stereoselectivity appears to be independent of the binding to the bilayer interface. At the interface, the interactions are expected to be dominated by the polar head groups of lipids and it is also where the chiral centres of CER are located. Instead, stereoselectivity appears to be determined by the interactions taking place in the hydrophobic core of bilayer, where the barrier to penetration is located. It appears that the configuration in the C8 R Laa chiral centre prevents the modified tetrapeptide to engage in more favourable interactions than those made by the C8 S Laa. These interactions could be attributed to a combination of the intra-peptide interactions and the hydrophobic interactions occurring between the epimer and the hydrocarbon chains of CER and FFA or with the rings in CHOL. The chiral centre on CHOL C3 is roughly located at the boundary between the interface and the hydrophobic core of the bilayer. The remaining seven chiral centres in CHOL are distributed in its rings and are located in the high-density hydrophobic region. It is thus possible that these chiral centres could originate distinctive interactions with the permeant epimers in this region of the bilayer.

The predicted one-dimensional diffusivity profiles for each epimer are shown in Figure 5.3.1 (bottom). The diffusion coefficient of the two modified tetrapeptides is predicted to be the same in bulk water, as expected. Their diffusivity is, however, reduced by at least one order of magnitude upon contact with the lipid bilayer. The diffusion coefficient of the epimers reaches the same value at the bilayer centre, indicating that this region of the bilayer does not pose a differential resistance to their movement. However, the diffusivity of C8 S Laa appears to be on average higher at COM distances between 0.0 and 1.4 nm, which corresponds to the low-density hydrophobic region and part of the high-density hydrophobic region. Considering that the thickness of the leaflet is ≈2.8 nm, this suggests that for nearly half of the translocation pathway across the leaflet, C8 S Laa experiences less resistance to its movement in the normal direction. This superior diffusivity contributes to the differences observed in the permeability estimates discussed below.

The estimated enthalpic and entropic contributions to the free energy as a function of COM distance are shown in Figure 5.3.2. The absolute values of total enthalpy calculated by the module *g_energy* were in the order of $2x10^5$ kJ/mol (regardless of the COM distance, replicate and epimer), with a reported error in the order of 10^1 kJ/mol. This hinders a quantitative comparison of energy contributions because the order of magnitude of the error of the enthalpy profile corresponds to the same order of magnitude of the PMF. In other words, the fluctuation of the total enthalpy (raw data) as so large with respect to the ΔH values (processed data) that the values of ΔH (green) and entropic contributions (turquoise) do not appear to converge around zero in the bulk water region, as would be expected. Instead, the time averages at each US window vary greatly in the order of 10^1 kJ/mol range. This illustrates the

challenge in the estimation of entropy in this setting. Nonetheless, the qualitative differences observed in the enthalpy and entropy profiles could help identify the source of stereoselectivity.

The enthalpy profiles of the epimers (shown in green in Figure 5.3.2) reveal that the binding to the bilayer interface is predominantly an enthalpy-driven process. This result contrasts with experimental evidence of the entropy-driven binding/partitioning of the (non-lipidated) dipeptide Ala-Trp to SC lipid vesicles (86). The ΔH profiles of C8 S Laa (solid green line) and of C8 R Laa (dashed green line) show similar trends for the translocation from bulk water towards the bilayer interface. Upon insertion into the dense-hydrophobic region, the free energy barrier is associated with a large, unfavourable enthalpy change for both epimers, and the large differences in the ΔH profiles appear to explain the differences in the PMFs. For example, at a COM distance 1.0 nm (in the high-density hydrophobic region), where the free energy difference ($\Delta\Delta G$) between epimers (R-S) is is ≈60 kJ/mol, the enthalpic difference ($\Delta\Delta H$) is ≈120 kJ/mol. Upon further insertion towards the bilayer centre, the enthalpy profiles of both epimers drop towards less unfavourable values at a similar rate. However, given the different heights of their respective enthalpic barriers, their ΔH values at the bilayer centre are very different (C8 R ΔH ≈ 20 kJ/mol, and C8 S ΔH ≈ -80 kJ/mol), giving a $\Delta\Delta H$ ≈ 100 kJ/mol) with a largely favourable ΔH of insertion for C8 S Laa.

Figure 5.3.2. Enthalpic (green) and entropic (turquoise) contributions to the free energy profiles (grey) for the permeation of the epimers. Solid lines for C8 S Laa and dashed lines for C8 R Laa.
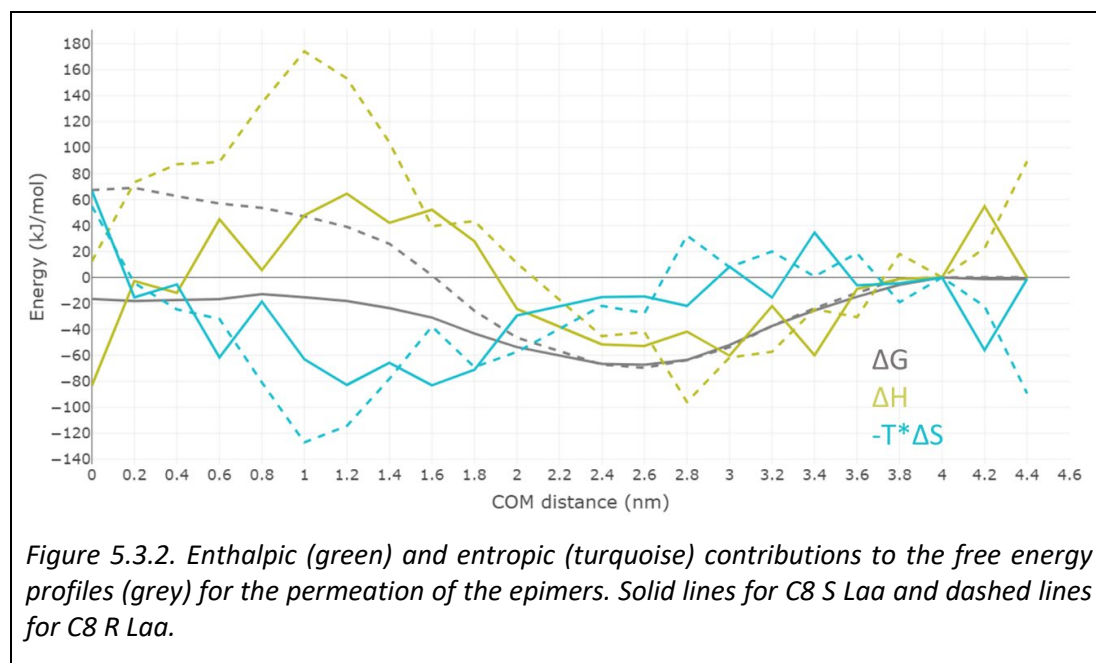
In contrast, the entropic contribution is fairly similar across the profiles of both epimers, with the largest difference between the epimers ($\Delta\Delta S$ ≈ 60 kJ/mol) observed at a COM distance 1.0 nm. This indicates qualitatively that at this COM distance, the

more negative TΔS contribution of C8 R Laa gives rise to a more unfavourable free energy barrier of the C8 R Laa compared to the C8 S Laa.

5.3.2 Transdermal permeability

Table 5.4 reports the predicted permeability values for the epimers of the C8Laa modified tetrapeptide and compares them to available experimental values (56). Experimental results are in the order of 10^{-11} to 10^{-12} nm/ps and the ranking in permeability is D epimer > D,L mixture > L epimer. In contrast, the predicted values span several orders of magnitude and the predicted value of the S (L) epimer is dramatically larger than the R (D) epimer. This arises as a consequence of the predicted lower free energy barrier and higher diffusivity of the former. At the time of writing of this thesis, this discrepancy in the ranking could not be resolved since the absolute configuration of the epimers in the experiments could not be confirmed. Nonetheless, the two MD simulation replicates were in excellent agreement and lend credibility to the predicted ranking.

Table 5.4. Transdermal permeability of the C8Laa epimers of the AAPV tetrapeptide.

	Permeability (nm/ps)	
Chirality	Experimental (56)	Predicted
C8 (D,L) Laa AAPV	9.17×10^{-12}	NA
C8 S (L) Laa AAPV	1.25×10^{-12}	2.47×10^{-7}
C8 R (D) Laa AAPV	5.28×10^{-11}	6.60×10^{-20}

5.3.3 Hydrogen-bonding analysis

The time (and replicate) average of the number of intramolecular and intermolecular hydrogen-bonds of each epimer were calculated for each US window and the results are displayed in Figure 5.3.3. The average number of hydrogen-bonds (of each type) at a COM distance 4.0 were used as a reference to normalize the plots, and hence the data is presented in terms of net gain or loss of hydrogen-bonds. The intramolecular (peptide-peptide) hydrogen-bonds (dotted lines) are infrequent for both epimers in bulk water but increase slightly when the epimers become embedded in the hydrophobic core of the lipid bilayer. The hydrogen-bonds between the epimers and water are expected to reach a maximum and plateau in bulk water as the peptides are fully solvated and surrounded by water only. The plot shows the net loss of hydrogen-bonding interactions between each epimer and water as it translocates into the bilayer centre (dashed lines). Full desolvation of the epimers involves a net loss of nearly eight hydrogen-bonds with water (in average). This appears to be a two-stage process that requires the full insertion of the peptides into the deeper region

135

of the hydrophobic core (COM distances from 0.0 to 0.6nm, the low-density region). In the first stage, both epimers gradually lose approximately three hydrogen-bonds with water whilst increasing their hydrogen-bonds with the lipids. This replacement of hydrogen-bonds occurs gradually as the COM of the epimer translocates from 4.0 to 2.0 nm but is not balanced as there is a loss of three hydrogen-bonds with water and a gain of two hydrogen-bonds with lipids. In the second stage, desolvation is completed (i.e. zero H-bonds with water) but the epimers lose hydrogen-bonds to water at different rates depending on the depth of insertion. The R epimer requires deeper insertion to lose all hydrogen-bonds with water and appears to gain approximately one additional hydrogen-bond with lipids in the crossing through the high-density hydrophobic core. In contrast, the S epimer keeps its desolvation rate fairly constant and reaches full desolvation at a shallower depth, whilst at the same time it gradually loses hydrogen-bonds with the lipids.

The intermolecular hydrogen-bonds between the epimer and the lipids are likely to occur in the vicinity of the headgroups. However, Figure 5.3.3 indicates that the number of these hydrogen-bonds does not decay at short COM distances (i.e. at deeper insertion). This suggests that the epimers retain some of their interactions with the hydrophilic groups of the lipids as they translocate into deeper regions of the hydrophobic core. This behaviour is more pronounced for the R epimer, which has more hydrogen-bonds with the lipids at COM distances <2.0 nm.
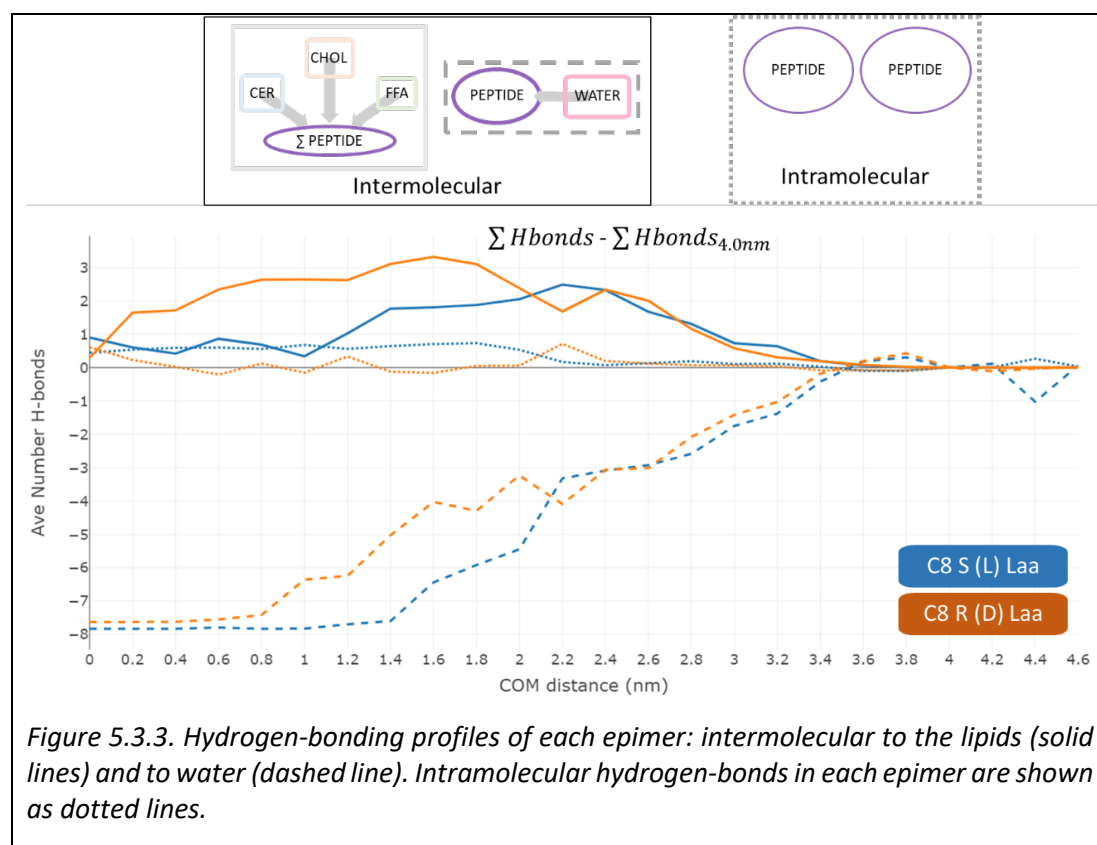
Figure 5.3.3. Hydrogen-bonding profiles of each epimer: intermolecular to the lipids (solid lines) and to water (dashed line). Intramolecular hydrogen-bonds in each epimer are shown as dotted lines.

Compared to the C8 S Laa, the C8 R Laa epimer presents a larger number of hydrogen-bonds with lipids (solid lines) and a larger number of hydrogen-bonds with water (i.e. a reduced loss of hydrogen-bonds with water (dashed lines)) at COM distances < 2.0 nm. This could be associated with the increased free energy barrier predicted for its translocation into the bilayer centre. The presence of these hydrogen-bonding groups into the high-density hydrophobic core of the bilayer is likely a reason for the highly unfavourable rise observed in the free energy profile of the C8 R Laa epimer.

Other types of hydrogen-bonds not directly involving the permeants but occurring in the simulation cell as the permeants translocate can also provide useful information. Two of these are the lipid-lipid hydrogen-bonds and the lipid-water hydrogen-bonds. Figure 5.3.4 presents the changes in these two types of hydrogen-bonds as measured in the simulation cell of each epimer. Similar to previous figures in this section, these values were obtained as time averages and replicate averages in each US window with respect to the values obtained at COM distance 4.0 nm. The lipid-lipid hydrogen-bonds could be interpreted as a proxy for the behaviour of the hydrogen-bond network between lipid head groups, which is associated with membrane integrity. Said hydrogen-bond network remains stable for the bilayers as the epimers approach and cross the interface, as indicated by both green lines hovering around zero. However the C8 R Laa epimer (dashed green line) deviates from zero and exhibits a loss of ≈ 4 lipid-lipid hydrogen bonds at the bilayer centre. In contrast, the C8 S Laa epimer remains closer to zero and exhibits approximately no loss in lipid-lipid hydrogen bonds at the bilayer centre. A likely explanation is that the translocation of the C8 R Laa epimer caused one of the lipid head groups to move "away" from the bilayer interface, preventing said lipid from participating in the hydrogen-bond network. In Figure 5.3.4, the blue lines indicate the change in lipid-water hydrogen bonds. When the epimers are away from the bilayer (i.e. in the bulk water region), the number of hydrogen bonds between the lipids and water reaches a dynamic equilibrium that is determined by the interaction between water molecules and the polar lipid headgroups. The presence of any other molecule at the interface is expected to competitively disrupt these interactions, which would be revealed as changes in the average number of lipid-water hydrogen bonds. Similarly, changes in the APL could affect the accessibility of water to the lipid headgroups. The data presented here indicate that when the C8 R Laa epimer is located in the bilayer centre, the lipids gained ≈5 hydrogen bonds with water compared to when the same epimer is in bulk water. In contrast, when the C8 S Laa epimer is located in the bilayer centre, the lipids lost ≈5 hydrogen bonds with water.

Figure 5.3.4 Hydrogen-bonding profiles of lipids to water (blue) and lipids to lipids (green) occurring in the simulation cell of each epimer Solid lines for C8 S Laa and dashed lines for C8 R Laa.
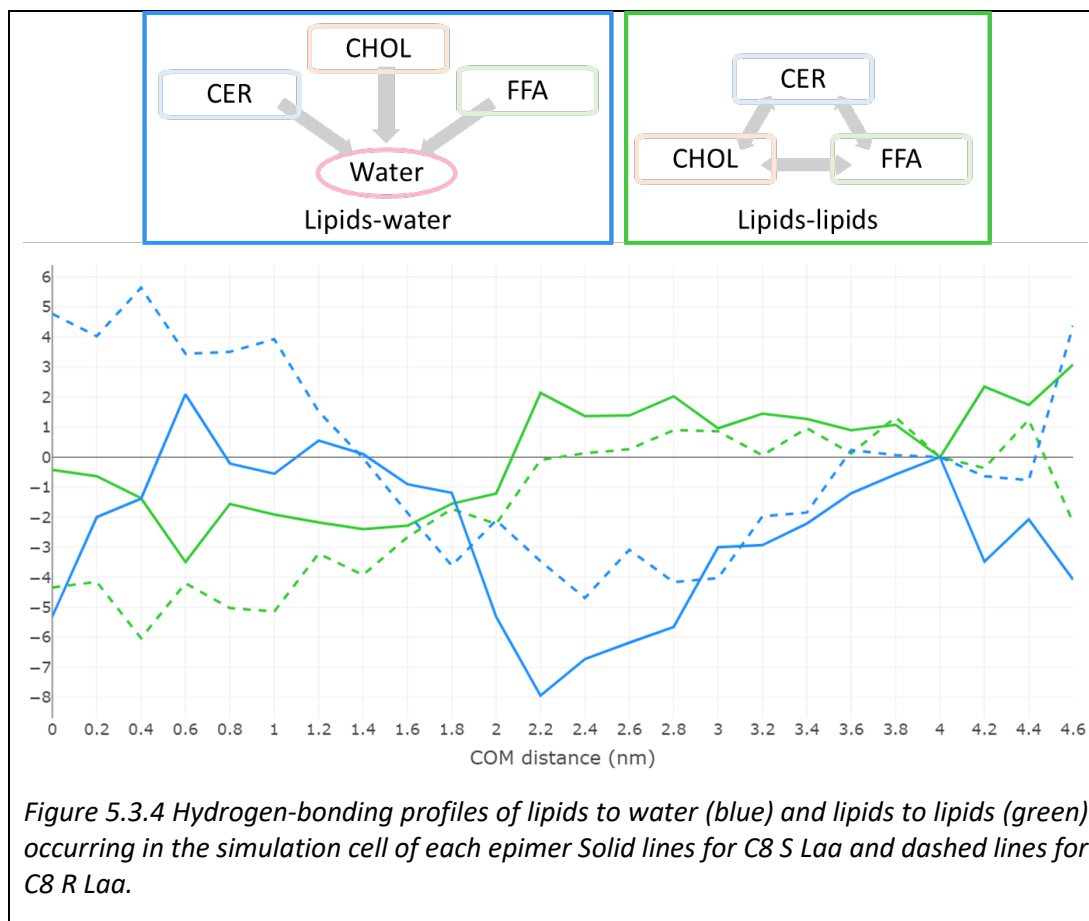
Overall in the simulation cell that contains the C8 S Laa epimer, the lipids did not lose substantial interactions with each other but lost interactions with water. By contrast, in the simulation cell containing the C8 R Laa epimer, the hydrogen-bond network between lipids lost nearly 4 hydrogen-bonds, which seem to be compensated by 5 hydrogen-bonds with water. The increased number of hydrogen-bonds with water when the C8 R Laa epimer is at the bilayer centre (at a COM distance of 0.0 nm) suggests an increase in accessibility of the lipid headgroups to water, compared to when the C8 R Laa epimer is in the bulk water region. This would be consistent with the notion that when a lipid headgroup is *buried* in the hydrophobic core of the bilayer it presents some *available area* at the plane of the interface for other lipid headgroups to distribute with increased APL, which in turn would make lipid headgroups more accessible to water.

5.4 Conclusions.

To our knowledge, this is the first work reporting MD simulations of the permeation of epimers across a model of the SC. The free energy profiles reported here were obtained using the fast-converging US-REST3 method, following the same approach

that was validated against the experimental transdermal permeability of the Ala-Trp dipeptide. This approach was able to distinguish two isomer molecules with different 3D configuration in only one of their five chiral carbon atoms, namely the S and R epimers of the Laa-conjugated Ala-Ala-Pro-Val tetrapeptide. This work underscores the suitability of MD simulations to elucidate molecular interactions that give rise to stereoselective outcomes. However, the predictions reported could not reproduce the ranking of experimental permeability of the Laa-conjugated tetrapeptide epimers (D>L, equivalent to R> S). One explanation for this disagreement is that other agents that were present in the experiments but not in the simulations (e.g. the chiral propylene glycol) could affect the stereo-specific interactions taking place between the Laa-conjugated tetrapeptides and cause the reversal of the transdermal permeability ranking. Given that efforts were made to confirm the 3D configuration of the MD model epimers at each step of the data workflow, an alternative explanation could be that the experimental data was erroneously recorded or reported for the epimers. It is acknowledged that by either replicating the experiments (with special attention to tracing the purification and labelling of the epimers) or by conducting additional MD simulations of other pairs of stereoisomers with reported stereoselective permeation, it would be possible to settle this apparent disagreement between experiment and simulation. However, said experiments and MD simulations, were outside the scope of this thesis.

Considering the unfeasibility of testing these scenarios, the focus of the analysis is on the very clear differences observed in the simulations, particularly, in the predicted PMFs of the epimers. In previous studies, the bilayer interface has been suggested as the locus of the stereo-specific molecular interactions giving rise to the experimental stereoselectivity of the Laa AAPV conjugates. However, the findings of this research do not show marked differences in this region. Instead, differences between the epimers are observed to occur in the hydrophobic core of the bilayer. In fact, the largest differences in free energy, number of hydrogen bonds involving the epimer, and the qualitative differences in enthalpy contributions appear to manifest predominantly in the hydrophobic interior of the bilayer at COM distances < 2.0 nm. Briefly, for the hydrogen bonds, the C8R epimer showed larger average number of hydrogen-bonds with lipids and with water at these distances compared to the C8S epimer, indicating a propensity to *retain* hydrogen-bonds at insertion depths at which the C8S epimer is de-solvated and has almost completely ceased to sustain hydrogen-bonds with lipids. The apparent locus of the differences in the hydrophobic core of the bilayer could suggest an active role of the chiral atoms of CHOL in selecting the epimers, as opposed to the notion of chiral carbons in the head groups of the lipids (CER and CHOL) being responsible for the stereoselectivity. In such case, it remains to be tested what particular atoms of the CHOL molecule originate the stereo-specific

interactions with the Laa-modified tetrapeptide and if said region is responsible for other stereoselective effects in the permeation of other chiral molecules.

6 Conclusions and future directions

The first objective of this PhD project was to establish the suitability of the enhanced sampling method US-REST3 for the accurate and efficient estimation of thermodynamical and kinetic properties of the interaction between a small biomolecule and a complex lipid bilayer. The second objective was to elucidate the mechanism of permeation of short peptides and peptide-like small molecules across a model of the SC by applying said enhanced sampling method.

The first objective was addressed in Chapter 3, where the performance of the recently developed selective replica with solute tempering (REST3) enhanced sampling method was compared to the gold-standard method, umbrella sampling (US). The availability of experimentally measured thermodynamics parameters of the interaction of the Ala-Trp dipeptide with large unilamellar vesicles in a SC-representative composition, enabled the comparison of the two enhanced sampling methods for their ability to reproduce experimental values, as well as in their use of computational resources and speed of convergence. Our results show that the US-REST3 approach was sufficiently close to the reported free energy of binding/partition and the predicted PMF rapidly reached the converged PMF calculated with US. Additionally, by monitoring the sampling of the orientation and conformation of the dipeptide at all distances in its translocation path, a link could be established between the superior sampling ability of US-REST3 and the rapid convergence of the PMF. Despite the significant use of computer resources (μs-long simulations), the PMF and sampling of configurations of the dipeptide were shown to still not have converged in some regions of the translocation path, in particular across the dense and ordered hydrophobic region. This suggests the strong association of the barrier function of the skin to the translocation across the dense-hydrophobic interior of the lamellae of the ICLM-SC and, it highlights the challenging nature of the estimation of thermodynamic properties from such systems. It may be possible in future to address this challenging region with a more targeted computational effort (i.e. a more efficient replica scheme), compared to the other regions of the simulation system which were characterized by faster convergence of properties. At the same time, future research may improve the replica schemes employed in this validation work in terms of use of computational resources whilst retaining the enhancement of sampling.

Similarly, it was possible to compare both enhanced sampling methods in their ability to reproduce the available permeability coefficient of the dipeptide across porcine skin, with the US-REST3 estimate being in better agreement with the experiment. The US-REST3 approach was shown to not affect the estimation of diffusion coefficients as calculated by relating the resistance experienced by the permeant to the ratio between the variance and the IACT of the position of the permeant. Lastly, for the Ala-Trp dipeptide, US-REST3 was shown to be able to provide a permeability coefficient estimate that is in closer agreement with the experimental value, compared with the estimate obtained with the US method.

Overall, the mechanism of permeation could be summarised in three stages, i) the binding of the dipeptide to the bilayer interface, which was driven by a favourable change in free energy, ii) the full insertion of the dipeptide into the dense-hydrophobic region of the bilayer core, which was characterized by a very steep free energy barrier, large restriction to the change in orientations and conformations, and very low one-dimensional diffusivity of the permeant, and iii) translocation into the low-density hydrophobic region, characterized by a favourable free energy change, free rotation and a shift in favourable conformation of the dipeptide as compared to that in bulk water.

Recent studies have reported artefacts in the calculation of diffusion coefficients from MD simulations which are inherent to the design simulation cell. It is thus likely that other approaches to the calculation of the diffusion coefficient of the permeant with better accuracy could show differences between the US and US-REST3 methods. Said differences could be better resolved when the permeant *experiences* a more dampening and anisotropic environment, i.e. in the dense-hydrophobic region. These differences could arise from the different nature of the MD trajectories, more explicitly: a continuous and long trajectory in US *versus* a trajectory with frequently exchanged configurations in US-REST3. Research aimed at testing the accuracy and convergence of methods to estimate diffusion coefficients in the context of solutes embedded in lipid bilayers will be a significant contribution to the field of SMMIs and a significant improvement in the estimation of permeability coefficients with MD simulation. This prospective work could ultimately provide a simple solution, such as the application of correction factors to different regions of the translocation path, if necessary.

The ability of US-REST3 to predict permeability coefficients and the elucidation of distinct molecular mechanisms of permeation across the SC model bilayer was then applied to explaining two interesting experimental findings. In chapter 4 the analysis was aimed at shedding light into the U-shaped response that increased hydrophobicity of lipid-conjugated peptide derivatives triggers in their transdermal permeability. Simulation of the permeation of one small peptide-like drug and two

short bioactive peptides, and two derivatives of each of these were conducted to address this aim. The derivatives were selected to reproduce the lipid-conjugation strategy of attaching modified lipoamino acids (Laa) of varying length to the N-termini of each peptide. Our results show that, for the range of MW tested (130 to 300) the addition of the shorter Laa did not significantly enhance the predicted permeability of any of the parent molecules, and instead it decreased the permeability of two derivatives compared with their respective parent molecules. However, the addition of the longer Laa increased the permeability of all the parent molecules by at least one order of magnitude. Consequently, C4 and C8 Laas (differing in only four aliphatic carbons) were shown to distinctively affect the balance of hydrophobic and hydrophilic interactions that the parent molecules exhibit with the model bilayer. However, because only two lipid tail lengths were tested (in the side chain of the Laa), the findings reported were not able to fully capture the U-shaped behaviour. To complete the trend, future research should aim to simulate the permeation of derivatives of at least one of the parent molecules modified with an intermediate-length (C6) and a larger-length (C10) Laa moiety. Having the corresponding experimental data of the permeability of four (C4, C6, C8, C10) Laa derivatives would also ultimately enable to test the hypothesis of a molecular descriptor representing the balance between polar and non-polar surface areas as a predictor of the transdermal permeability of small peptides and their lipid conjugates across the skin.

Lastly, in Chapter 5 an investigation of the stereoselectivity observed for the permeability of chiral permeants across the skin is reported. This involved the first MD simulations conducted of the permeation of epimers across a model of the SC. The predicted free energy profiles showed the largest differences in the hydrophobic core of the bilayer, indicating that the molecular mechanism behind the observed differences may not occur in the aqueous interface as previously suggested. Similarly, the analysis of hydrogen-bonding interactions suggests a mechanism whereby the loss of hydrogen bonds with water (in the desolvation-partition step) of each of the epimers occurs at different rates and with different outcomes for the hydrogen-bond network of the bilayer. Despite the clear differences in the free energy profile and the hydrogen-bonding profiles, it was not possible to reproduce the ranking of experimental permeabilities of the epimers (R > S). Better understanding of the different mechanisms of permeation of the epimers could be achieved in the future by further investigation into their interactions with cholesterol. Similarly, further exploration of other structural descriptors of the epimers, such as solvent accessible surface area, dihedral angle distributions, orientation angle distributions, etc. could provide a complete molecular mechanism of stereoselectivity for the C8 Laa epimers. Furthermore, an interesting avenue of investigation would be to predict the permeability of other chiral pairs across the model of the SC and to compare the

ranking of predicted transdermal permeability values against experimental data (obtained in the absence of other chiral compounds).

The research reported in this thesis demonstrates the valuable contribution of MD simulation to improving the mechanistic understanding of the permeation of small bioactive molecules across a model of the ICLM-SC with atomistic resolution. It is clear that use of an effective enhanced sampling method whose convergence and efficiency has been carefully tested is an important requirement. The above proposed future research will contribute to the estimation of permeability coefficients across complex gel-state bilayers using MD simulation, particularly for molecules with similar or very similar physicochemical properties.

References

1. Benson, H. (2005) Transdermal Drug Delivery: Penetration Enhancement Techniques. *Curr. Drug Deliv.* **2**, 23–33

2. Benson, H. A. E., and Namjoshi, S. (2008) Proteins and peptides: Strategies for delivery to and across the skin. *J. Pharm. Sci.* **97**, 3591–3610

3. Prausnitz, M. R., and Langer, R. (2009) Transdermal drug delivery. *Nat. Biotechnol.* **26**, 1261–1268

4. U.S. Food and Drug Administration (2017) FYs 2013 - 2017 GDUFA Science and Research Report: Transdermal Drug Products. [online] https://www.fda.gov/industry/generic-drug-user-fee-amendments/fys-2013-2017-gdufa-science-and-research-report-transdermal-drug-products (Accessed December 15, 2021)

5. Karande, P. S., Jain, A. K., and Mitragotri, S. (2005) Design principles of chemical permeation enhancers for transdermal drug delivery. in *AIChE Annual Meeting, Conference Proceedings*, p. 8372, [online] http://www.pnas.org/content/102/13/4688.full.pdf (Accessed May 17, 2017)

6. Alkilani, A. Z., McCrudden, M. T. C., and Donnelly, R. F. (2015) Transdermal drug delivery: Innovative pharmaceutical developments based on disruption of the barrier properties of the stratum corneum. *Pharmaceutics*. **7**, 438–470

7. Selzer, D., Neumann, D., and Schaefer, U. F. (2015) Mathematical models for dermal drug absorption. *Expert Opin. Drug Metab. Toxicol.* **11**, 1567–1583

8. van Smeden, J., and Bouwstra, J. A. (2016) Stratum Corneum Lipids: Their Role for the Skin Barrier Function in Healthy Subjects and Atopic Dermatitis Patients. *Curr. Probl. Dermatol.* **49**, 8–26

9. Olejnik, O., and Firestone, B. A. (2002) The structure and function of skin. in *Dermatological and Transdermal Formulations*, pp. 1–40, CRC Press, 10.1201/9780824743239-12

10. Bouwstra, J. A., and Ponec, M. (2006) The skin barrier in healthy and diseased state. *Biochim. Biophys. Acta - Biomembr.* **1758**, 2080–2095

11. Janssens, M., van Smeden, J., Gooris, G. S., Bras, W., Portale, G., Caspers, P. J., Vreeken, R. J., Hankemeier, T., Kezic, S., Wolterbeek, R., Lavrijsen, A. P., and Bouwstra, J. A. (2012) Increase in short-chain ceramides correlates with an altered lipid organization and decreased barrier function in atopic eczema patients. *J. Lipid Res.* **53**, 2755–2766

12. Wertz, P. W., and Downing, D. T. (1983) Ceramides of pig epidermis: structure

determination. *J. Lipid Res.* **24**, 759–765

13. Vavrova, K., Kovačik, A., and Opalka, L. (2017) Ceramides in the skin barrier. *Eur. Pharm. J.* **64**, 28–35

14. Motta, S., Monti, M., Sesana, S., Caputo, R., Carelli, S., and Ghidoni, R. (1993) Ceramide composition of the psoriatic scale. *BBA - Mol. Basis Dis.* **1182**, 147–151

15. Wertz, P. W. (1999) Lipids and barrier function of the skin. *Acta Dermato-Venereologica, Suppl.* 10.1080/000155500750042790

16. Moore, D. J., and Rerek, M. E. (1999) Insights into the molecular organization of lipids in the skin barrier from infrared spectroscopy studies of stratum corneum lipid models. *Acta Dermato-Venereologica, Suppl.* 10.1080/000155500750042817

17. Weerheim, A., and Ponec, M. (2001) Determination of stratum corneum lipid profile by tape stripping in combination with high-performance thin-layer chromatography. *Arch. Dermatol. Res.* **293**, 191–199

18. Farwanah, H., Wohlrab, J., Neubert, R. H. H., and Raith, K. (2005) Profiling of human stratum corneum ceramides by means of normal phase LC/APCI-MS. *Anal. Bioanal. Chem.* **383**, 632–637

19. T'kindt, R., Jorge, L., Dumont, E., Couturon, P., David, F., Sandra, P., and Sandra, K. (2012) Profiling and Characterizing Skin Ceramides Using Reversed-Phase Liquid Chromatography–Quadrupole Time-of-Flight Mass Spectrometry. *Anal. Chem*. **84**, 2021

20. Schreiner, V., Pfeiffer, S., Lanzendörfer, G., Wenck, H., Diembeck, W., Gooris, G. S., Proksch, E., and Bouwstra, J. (2000) Barrier Characteristics of Different Human Skin Types Investigated with X-Ray Diffraction, Lipid Analysis, and Electron Microscopy Imaging. *J. Invest. Dermatol.* **114**, 654–660

21. Masukawa, Y., Narita, H., Shimizu, E., Kondo, N., Sugai, Y., Oba, T., Homma, R., Ishikawa, J., Takagi, Y., Kitahara, T., Takema, Y., and Kita, K. (2008) Characterization of overall ceramide species in human stratum corneum. *J. Lipid Res.* **49**, 1466–1476

22. Masukawa, Y., Narita, H., Sato, H., Naoe, A., Kondo, N., Sugai, Y., Oba, T., Homma, R., Ishikawa, J., Takagi, Y., and Kitahara, T. (2009) Comprehensive quantification of ceramide species in human stratum corneum. *J. Lipid Res.* **50**, 1708–1719

23. Moore, D. J., and Rawlings, A. V. (2017) The chemistry, function and (patho)physiology of stratum corneum barrier ceramides. *Int. J. Cosmet. Sci.* **39**, 366–372

24. Yokose, U., Ishikawa, J., Morokuma, Y., Naoe, A., Inoue, Y., Yasuda, Y., Tsujimura, H., Fujimura, T., Murase, T., and Hatamochi, A. (2020) The ceramide [NP]/[NS] ratio in the stratum corneum is a potential marker for skin properties and epidermal differentiation. *BMC Dermatol.* **20**, 6

25. Van Smeden, J., Janssens, M., Gooris, G. S. S., and Bouwstra, J. A. A. (2014) The important role of stratum corneum lipids for the cutaneous barrier function. *Biochim. Biophys. Acta - Mol. Cell Biol. Lipids*. **1841**, 295–313

26. Norlén, L., Nicander, I., Lundh Rozell, B., Ollmar, S., and Forslind, B. (1999) Inter- and intra-individual differences in human stratum corneum lipid content related to physical parameters of skin barrier function in vivo. *J. Invest. Dermatol.* **112**, 72–77

27. Opálka, L., Kováčik, A., Maixner, J., and Vávrová, K. (2016) Omega-O-Acylceramides in Skin Lipid Membranes: Effects of Concentration, Sphingoid Base, and Model Complexity on Microstructure and Permeability. *Langmuir*. **32**, 12894–12904

28. Schmitt, T., Lange, S., Sonnenberger, S., Dobner, B., Demé, B., Langner, A., and Neubert, R. H. H. (2019) The long periodicity phase (LPP) controversy part I: The influence of a natural-like ratio of the CER[EOS] analogue [EOS]-br in a CER[NP]/[AP] based stratum corneum modelling system: A neutron diffraction study. *Biochim. Biophys. Acta - Biomembr.* **1861**, 306–315

29. Bouwstra, J. A., Gooris, G. S., Dubbelaar, F. E. R., Weerheim, A. M., Ijzerman, A. P., and Ponec, M. (1998) Role of ceramide 1 in the molecular organization of the stratum corneum lipids. *J. Lipid Res.* **39**, 186–96

30. Abraham, W., and Downing, D. T. (1992) Lamellar Structures Formed by Stratum Corneum Lipids in Vitro: A Deuterium Nuclear Magnetic Resonance (NMR) Study. *Pharm. Res. An Off. J. Am. Assoc. Pharm. Sci.* **9**, 1415–1421

31. Bouwstra, J. A. A., Gooris, G. S., Dubbelaar, F. E. R., Ponec, M., and Weerheim, A. M. (1998) pH, Cholesterol Sulfate, and Fatty Acids Affect the Stratum Corneum Lipid Organization. *J. Investig. Dermatology Symp. Proc.* **3**, 69–74

32. Norlén, L., Nicander, I., Lundsjö, A., Cronholm, T., and Forslind, B. (1998) A new HPLC-based method for the quantitative analysis of inner stratum corneum lipids with special reference to the free fatty acid fraction. *Arch. Dermatol. Res.* **290**, 508–516

33. Uchiyama, M., Oguri, M., Mojumdar, E. H., Gooris, G. S., and Bouwstra, J. A. (2016) Free fatty acids chain length distribution affects the permeability of skin lipid model membranes. *Biochim. Biophys. Acta - Biomembr.* **1858**, 2050–2059

34. Das, C., Noro, M. G., and Olmsted, P. D. (2014) Fast cholesterol flip-flop and lack of swelling in skin lipid multilayers. *Soft Matter*. **10**, 7346–7352

35. Mao-Qiang, M., Feingold, K. R., Thornfeldt, C. R., and Elias, P. M. (1996) Optimization of physiological lipid mixtures for barrier repair. *J. Invest. Dermatol.* **106**, 1096–1101

36. Plasencia, I., Norlén, L., and Bagatolli, L. A. (2007) Direct Visualization of Lipid Domains in Human Skin Stratum Corneum's Lipid Membranes: Effect of pH and Temperature. *Biophys. J.* **93**, 3142–3155

37. Benson, H. A. E., Grice, J. E., Mohammed, Y., Namjoshi, S., and Roberts, M. S. (2019) Topical and Transdermal Drug Delivery: From Simple Potions to Smart Technologies. *Curr. Drug Deliv.* **16**, 444–460

38. Vitorino, C., Sousa, J., and Pais, A. (2015) Overcoming the Skin Permeation Barrier: Challenges and Opportunities. *Curr. Pharm. Des.* **21**, 2698-2712(15)

39. Zhang, L., and Falla, T. J. Cosmeceuticals and peptides. *Clin. Dermatol.* **27**, 485–494

40. Namjoshi, S., Caccetta, R., and Benson, H. A. E. (2008) Skin peptides: Biological activity and therapeutic opportunities. *J. Pharm. Sci.* **97**, 2524–2542

41. Gupta, R., Dwadasi, B. S., Rai, B., and Mitragotri, S. (2019) Effect of Chemical Permeation Enhancers on Skin Permeability: In silico screening using Molecular Dynamics simulations. *Sci. Rep.* **9**, 1–11

42. Mohammed, Y. H., Yamada, M., Lin, L. L., Grice, J. E., Roberts, M. S., Raphael, A. P., Benson, H. A. E. E., and Prow, T. W. (2014) Microneedle enhanced delivery of cosmeceutically relevant peptides in human skin. *PLoS One*. **9**, e101956

43. Chaulagain, B., Jain, A., Tiwari, A., Verma, A., and Jain, S. K. (2018) Passive delivery of protein drugs through transdermal route. *Artif. Cells, Nanomedicine, Biotechnol.* **46**, 472–487

44. Schuetz, Y. B., Naik, A., Guy, R. H., and Kalia, Y. N. (2005) Emerging strategies for the transdermal delivery of peptide and protein drugs. *Expert Opin. Drug Deliv.* **2**, 533–548

45. El Maghraby, G. M., Barry, B. W., and Williams, A. C. (2008) Liposomes and skin: From drug delivery to model membranes. *Eur. J. Pharm. Sci.* **34**, 203–222

46. Williams, A. C., and Barry, B. W. (2012) Penetration enhancers. *Adv. Drug Deliv. Rev.* **64**, 128–137

47. Furuishi, T., Kato, Y., Fukami, T., Suzuki, T., Endo, T., Nagase, H., Ueda, H., and Tomono, K. (2013) Effect of terpenes on the skin permeation of lomerizine dihydrochloride. *J. Pharm. Pharm. Sci.* **16**, 551–563

48. Hadgraft, J., Peck, J., Williams, D. G., Pugh, W. J., and Allan, G. (1996) Mechanisms of action of skin penetration enhancers/retarders: Azone and analogues. *Int. J. Pharm.* **141**, 17–25

49. LEE, C. K., UCHIDA, T., KITAGAWA, K., YAGI, A., KIM, N., and GOTO, S. (1994) Relationship between Lipophilicity and Skin Permeability of Various Drugs from an Ethanol/Water/Lauric Acid System. *Biol. Pharm. Bull.* **17**, 1421–1424

50. Udata, C., Tirucherai, G., and Mitra, A. K. (1999) Synthesis, stereoselective enzymatic hydrolysis, and skin permeation of diastereomeric propranolol ester prodrugs. *J. Pharm. Sci.* **88**, 544–550

51. Ahmed, S., Imai, T., and Otagiri, M. (1996) Evaluation of stereoselective transdermal transport and concurrent cutaneous hydrolysis of several ester prodrugs of propranolol: Mechanism of stereoselective permeation. *Pharm. Res.* **13**, 1524–1529

52. Simerska, P., Moyle, P. M., and Toth, I. (2011) Modern lipid-, carbohydrate-, and peptide-based delivery systems for peptide, vaccine, and gene products. *Med. Res. Rev.* **31**, 520–547

53. SETOH, K., MURAKAMI, M., ARAKI, N., FUJITA, T., YAMAMOTO, A., and MURANISHI, S. (1995) Improvement of Transdermal Delivery of Tetragastrin by Lipophilic Modification with Fatty Acids. *J. Pharm. Pharmacol.* **47**, 808–811

54. Yamamoto, A., Setoh, K., Murakami, M., Shironoshita, M., Kobayashi, T., Fujimoto, K., Okada, N., Fujita, T., and Muranishi, S. (2003) Enhanced transdermal delivery of phenylalanyl-glycine by chemical modification with various fatty acids. *Int. J. Pharm.* **250**, 119–128

55. Toth, I., Christodoulou, M., Bankowsky, K., Flinn, N., Gibbons, W. A., Godeau, G., Moczar, E., and Hornebeck, W. (1995) Design of potent lipophilic-peptide inhibitors of human neutrophil elastase: In vitro and in vivo studies. *Int. J. Pharm.* **125**, 117–122

56. Namjoshi, S., Toth, I., Blanchfield, J. T., Trotter, N., Mancera, R. L., and Benson, H. A. E. (2014) Enhanced transdermal peptide delivery and stability by lipid conjugation: Epidermal permeation, stereoselectivity and mechanistic insights. *Pharm. Res.* **31**, 3304–3312

57. Caccetta, R., Blanchfield, J. T., Harrison, J., Toth, I., and Benson, H. A. E. (2006) Epidermal penetration of a therapeutic peptide by lipid conjugation; stereo-selective peptide availability of a topical diastereomeric lipopeptide. in *International Journal of Peptide Research and Therapeutics*, pp. 327–333, Springer Netherlands, **12**, 327–333

58. Afouna, M. I., Fincher, T. K., Khan, M. A., and Reddy, I. K. (2003) Percutaneous permeation of enantiomers and racemates of chiral drugs and prediction of their flux ratios using thermal data: A pharmaceutical perspective. *Chirality*. **15**, 456–465

59. Orsi, M., and Essex, J. W. (2010) Chapter 4 Passive Permeation Across Lipid Bilayers: a Literature Review. *Mol. Simulations Biomembr. From Biophys. to Funct.* 10.1039/9781849732154-00076

60. Nandi, N., and Vollhardt, D. (2008) Chiral discrimination and recognition in Langmuir monolayers. *Curr. Opin. Colloid Interface Sci.* **13**, 40–46

61. Horta, B. A. C., and Hünenberger, P. H. (2011) Enantiomeric segregation in the gel phase of lipid bilayers. *J. Am. Chem. Soc.* **133**, 8464–8466

62. Tsuchiya, H., and Mizogami, M. (2018) Discrimination of stereoisomers by their enantioselective interactions with chiral cholesterol-containing membranes. *Molecules*. **23**, 49

63. Henriques, S. T., Peacock, H., Benfield, A. H., Wang, C. K., and Craik, D. J. (2019) Is the Mirror Image a True Reflection? Intrinsic Membrane Chirality Modulates Peptide Binding. *J. Am. Chem. Soc.* **141**, 20460–20469

64. Wei, C., and Pohorille, A. (2009) Permeation of membranes by ribose and its diastereomers. *J. Am. Chem. Soc.* **131**, 10237–10245

65. Ishigami, T., Suga, K., and Umakoshi, H. (2015) Chiral Recognition of l -Amino Acids on Liposomes Prepared with l -Phospholipid. *ACS Appl. Mater. Interfaces*. **7**, 21065–21072

66. Tsuchiya, H., and Mizogami, M. (2012) The membrane interaction of drugs as one of mechanisms for their enantioselective effects. *Med. Hypotheses*. **79**, 65–67

67. Che, Q. E., Quan, P., Mu, M., Zhang, X., Zhao, H., Zhang, Y., You, S., Xiao, Y., and Fang, L. (2014) Enantioselective skin permeation of ibuprofen enantiomers: Mechanistic

insights from ATR-FTIR and CLSM studies based on synthetic enantiomers as naphthalimide fluorescent probes. *Expert Opin. Drug Deliv.* **11**, 1513–1523

68. Kosina, P., Paloncýová, M., Svobodová, A. R., Zálešák, B., Biedermann, D., Ulrichová, J., and Vostálová, J. (2019) Dermal delivery of selected polyphenols from silybum marianum. Theoretical and experimental study. *Molecules*. **24**, 61

69. Lukač, R., Clark, A. J., Khalid, S., Rodger, A., Snedden, A., and Mark Rodger, P. (2002) Chiral discrimination in mobile phases for HPLC. *J. Mol. Liq.* **98**, 413–425

70. Fidler, J., Rodger, A., and Rodger, P. M. (1994) Chiral Solvent Structure around Chiral Molecules: Experimental and Theoretical Study. *J. Am. Chem. Soc.* **116**, 7266–7273

71. Lukač, R., Clark, A. J., San-Miguel, M. A., Rodger, A., and Rodger, P. M. (2002) Predicting chiral discrimination in HPLC from computer simulations. in *Journal of Molecular Liquids*, pp. 261–272, Elsevier, **101**, 261–272

72. Neugebauer, J. (2007) Induced chirality in achiral media - How theory unravels mysterious solvent effects. *Angew. Chemie - Int. Ed.* **46**, 7738–7740

73. Martini, M. F., and Pickholz, M. (2012) Molecular dynamics study of uncharged bupivacaine enantiomers in phospholipid bilayers. *Int. J. Quantum Chem.* **112**, 3341–3345

74. Witek, J., Wang, S., Schroeder, B., Lingwood, R., Dounas, A., Roth, H.-J., Fouché, M., Blatter, M., Lemke, O., Keller, B., and Riniker, S. (2019) Rationalization of the Membrane Permeability Differences in a Series of Analogue Cyclic Decapeptides. *J. Chem. Inf. Model.* **59**, 294–308

75. Choe, C., Schleusener, J., Lademann, J., and Darvin, M. E. (2018) Human skin *in vivo* has a higher skin barrier function than porcine skin *ex vivo* - comprehensive Raman microscopic study of the stratum corneum. *J. Biophotonics*. 10.1002/jbio.201700355

76. Abd, E., Yousef, S. A., Pastore, M. N., Telaprolu, K., Mohammed, Y. H., Namjoshi, S., Grice, J. E., and Roberts, M. S. (2016) Skin models for the testing of transdermal drugs. *Clin. Pharmacol. Adv. Appl.* **8**, 163–176

77. Uche, L. E., Gooris, G. S., Bouwstra, J. A., and Beddoes, C. M. (2019) Barrier Capability of Skin Lipid Models: Effect of Ceramides and Free Fatty Acid Composition. *Langmuir*. **35**, 15376–15388

78. Shah, V. P., Flynn, G. L., Yacobi, A., Maibach, H. I., Bon, C., Fleischer, N. M., Franz, T. J., Kaplan, S. A., Kawamoto, J., Lesko, L. J., Marty, J. P., Pershing, L. K., Schaefer, H., Sequeira, J. A., Shrivastava, S. P., Wilkin, J., and Williams, R. L. (1998) 3-day AAPS/FDA Workshop on Bioequivalence of Topical Dermatological Dosage Forms - Methods of Evaluating Bioequivalence. in *Skin Pharmacology and Applied Skin Physiology*, pp. 117–124, Karger Publishers, **11**, 117–124

79. Escobar-Chávez, J. J., Quintanar-Guerrero, D., and Ganem-Quintanar, A. (2005) In vivo skin permeation of sodium naproxen formulated in pluronic F-127 gels: Effect of Azone® and Transcutol®. *Drug Dev. Ind. Pharm.* **31**, 447–454

80. Ng, S. F., Rouse, J. J., Sanderson, F. D., Meidan, V., and Eccleston, G. M. (2010)

Validation of a static Franz diffusion cell system for in vitro permeation studies. *AAPS PharmSciTech*. **11**, 1432–1441

81.   dos Santos, L., Rangel, J. L., Tippavajhala, V. K., da Silva, M. G. P., Mogilevych, B., and Martin, A. A. (2016) In vivo intra- and inter-individual variability study of human stratum corneum by confocal Raman spectroscopy. *Vib. Spectrosc.* **87**, 199–206

82.   Bouwstra, J. a, Gooris, G. S., Weerheim, A., Kempenaar, J., and Ponec, M. (1995) Characterization of stratum corneum structure in reconstructed epidermis by X-ray diffraction. *J. Lipid Res.* **36**, 496–504

83.   Bouwstra, J. A., and Gooris, G. S. (2010) The Lipid Organisation in Human Stratum Corneum and Model Systems. *Open Dermatol. J.* **4**, 10–13

84.   Garcia, M. T. J., de Vasconcellos, F. L. L., Raffier, C. P., Roberts, M. S., Grice, J. E., Benson, H. A. E., and Leite-Silva, V. R. (2018) Alternative Methods to Animal Studies for the Evaluation of Topical/ Transdermal Drug Delivery Systems. *Curr. Top. Med. Chem.* **18**, 287–299

85.   Abraham, W., and Downing, D. T. (1989) Preparation of Model Membranes for Skin Permeability Studies Using Stratum Corneum Lipids. *J. Invest. Dermatol.* **93**, 809–813

86.   Lin, R. Y., Chen, W. Y., and Liao, C. W. (1998) Entropy-driven binding/partition of amino acids/dipeptides to stratum corneum lipid vesicles. *J. Control. Release*. **50**, 51–59

87.   Čuříková, B. A., Procházková, K., Filková, B., Diblíková, P., Svoboda, J., Kováčik, A., Vávrová, K., and Zbytovská, J. (2017) Simplified stratum corneum model membranes for studying the effects of permeation enhancers. *Int. J. Pharm.* **534**, 287–296

88.   Školová, B., Januìššová, B., Zbytovská, J., Gooris, G., Bouwstra, J., Slepička, P., Berka, P., Roh, J., Palát, K., Hrabálek, A., and Vávrová, K. (2013) Ceramides in the skin lipid membranes: Length matters. *Langmuir*. **29**, 15624–15633

89.   Wen, J., Koo, S. M., Lape, N., Myoung Koo, S., and Lape, N. (2018) How Sensitive Are Transdermal Transport Predictions by Microscopic Stratum Corneum Models to Geometric and Transport Parameter Input? *J. Pharm. Sci.* **107**, 612–623

90.   Ghonaim, H. M., Periasamy, N., Noro, M. G., and Anwar, J. (2014) Towards a simplified model membrane of skin lipids: Preparation and characterisation of a ternary lipid mixture. *Int. J. Pharm. Pharm. Sci.* **6**, 148–152

91.   Martinotti, C., Ruiz-Perez, L., Deplazes, E., and Mancera, R. L. (2020) Molecular Dynamics Simulation of Small Molecules Interacting with Biological Membranes. *ChemPhysChem*. **21**, 1486–1514

92.   Selzer, D., Neumann, D., Neumann, H., Kostka, K. H., Lehr, C. M., and Schaefer, U. F. (2015) A strategy for in-silico prediction of skin absorption in man. *Eur. J. Pharm. Biopharm.* **95**, 68–76

93.   Tsakovska, I., Pajeva, I., Al Sharif, M., Alov, P., Fioravanzo, E., Kovarich, S., Worth, A. P., Richarz, A. N., Yang, C., Mostrag-Szlichtyng, A., and Cronin, M. T. D. (2017) Quantitative structure-skin permeability relationships. *Toxicology*. **387**, 27–42

94. Pugh, W. J., Degim, I. T., and Hadgraft, J. (2000) Epidermal permeability-penetrant structure relationships: 4, QSAR of permeant diffusion across human stratum corneum in terms of molecular weight, H-bonding and electronic charge. *Int. J. Pharm.* **197**, 203–211

95. ten Berge, W. (2009) A simple dermal absorption model: Derivation and application Wil ten Berge *. 10.1016/j.chemosphere.2009.02.043

96. Chen, C. P., Chen, C. C., Huang, C. W., and Chang, Y. C. (2018) Evaluating molecular properties involved in transport of small molecules in stratum corneum: A quantitative structure-activity relationship for skin permeability. *Molecules.* **23**, 1–17

97. Khajeh, A., and Modarress, H. (2014) Linear and nonlinear quantitative structure-property relationship modelling of skin permeability. *SAR QSAR Environ. Res.* **25**, 35–50

98. Ates, G., Steinmetz, F. P., Doktorova, T. Y., Madden, J. C., and Rogiers, V. (2016) Linking existing in vitro dermal absorption data to physicochemical properties: Contribution to the design of a weight-of-evidence approach for the safety evaluation of cosmetic ingredients with low dermal bioavailability. *Regul. Toxicol. Pharmacol.* **76**, 74–78

99. Bemporad, D., Essex, J. W., and Luttmann, C. (2004) Permeation of Small Molecules through a Lipid Bilayer: A Computer Simulation Study. *J. Phys. Chem.* **108**, 4875–4884

100. Van Gunsteren, W. F., Bakowies, D., Baron, R., Chandrasekhar, I., Christen, M., Daura, X., Gee, P., Geerke, D. P., Glättli, A., Hünenberger, P. H., Kastenholz, M. A., Oostenbrink, C., Schenk, M., Trzesniak, D., Van Der Vegt, N. F. A., and Yu, H. B. (2006) Biomolecular modeling: Goals, problems, perspectives. *Angew. Chemie - Int. Ed.* **45**, 4064–4092

101. Shinoda, W. (2016) Permeability across lipid membranes. *Biochim. Biophys. Acta - Biomembr.* **1858**, 2254–2265

102. Frenkel, D., and Smit, B. (2011) Free energy calculations. in *Understanding molecular simulation : from algorithms to applications.*, pp. 190–223, 10.1093/ejo/cjq172

103. Von Bülow, S., Bullerjahn, J. T., and Hummer, G. (2020) Systematic errors in diffusion coefficients from long-time molecular dynamics simulations at constant pressure. *J. Chem. Phys.* **153**, 021101

104. Vö, M., Rgen Kö, J., and Hummer, G. (2019) Finite-Size-Corrected Rotational Diffusion Coefficients of Membrane Proteins and Carbon Nanotubes from Molecular Dynamics Simulations. *J. Phys. Chem. B.* **123**, 12

105. Filipe, H. A. L., Moreno, M. J., Róg, T., Vattulainen, I., and Loura, L. M. S. (2014) How to tackle the issues in free energy simulations of long amphiphiles interacting with lipid membranes: Convergence and local membrane deformations. *J. Phys. Chem. B.* **118**, 3572–3581

106. Poger, D., Caron, B., and Mark, A. E. (2016) Validating lipid force fields against experimental data: Progress, challenges and perspectives. *Biochim. Biophys. Acta - Biomembr.* **1858**, 1556–1565

107. Lyubartsev, A. P., and Rabinovich, A. L. (2016) Force Field Development for Lipid Membrane Simulations. *Biochim. Biophys. Acta - Biomembr.* **1858**, 2483–2497

108. van Gunsteren, W. F., Daura, X., Hansen, N., Mark, A. E., Oostenbrink, C., Riniker, S., and Smith, L. J. (2018) Validation of Molecular Simulation: An Overview of Issues. *Angew. Chemie - Int. Ed.* **57**, 884–902

109. Paloncýová, M., Fabre, G., Devane, R. H., Trouillas, P., Berka, K., and Otyepka, M. (2014) Benchmarking of force fields for molecule-membrane interactions. *J. Chem. Theory Comput.* **10**, 4143–4151

110. Poger, D., Van Gunsteren, W. F., and Mark, A. E. (2010) A new force field for simulating phosphatidylcholine bilayers. *J. Comput. Chem.* **31**, 1117–1125

111. Lee, B. L., and Kuczera, K. (2017) Simulating the free energy of passive membrane permeation for small molecules. *Mol. Simul.* 10.1080/08927022.2017.1407029

112. Lee, C. T., Comer, J., Herndon, C., Leung, N., Pavlova, A., Swift, R. V., Tung, C., Rowley, C. N., Amaro, R. E., Chipot, C., Wang, Y., and Gumbart, J. C. (2016) Simulation-Based Approaches for Determining Membrane Permeability of Small Compounds. *J. Chem. Inf. Model.* **56**, 721–733

113. Pien, T., Trylska, J., Pieńko, T., and Trylska, J. (2019) Computational Methods Used to Explore Transport Events in Biological Systems. *J. Chem. Inf. Model.* **59**, 1772–1781

114. Lopes, D., Jakobtorweihen, S., Nunes, C., Sarmento, B., and Reis, S. (2017) Shedding light on the puzzle of drug-membrane interactions: Experimental techniques and molecular dynamics simulations. *Prog. Lipid Res.* **65**, 24–44

115. Kästner, J. (2011) Umbrella sampling. *Wiley Interdiscip. Rev. Comput. Mol. Sci.* **1**, 932–942

116. Kumar, S., Rosenberg, J. M., Bouzida, D., Swendsen, R. H., and Kollman, P. A. (1992) The weighted histogram analysis method for free-energy calculations on biomolecules. I. The method. *J. Comput. Chem.* **13**, 1011–1021

117. Ribeiro, R. P., Coimbra, J. T. S., Ramos, M. J., and Fernandes, P. A. (2017) Diffusion of the small, very polar, drug piracetam through a lipid bilayer: an MD simulation study. *Theor. Chem. Acc.* **136**, 1–10

118. Bassolino-Klimas, D., Alper, H. E., and Stouch, T. R. (1993) Solute diffusion in lipid bilayer membranes: An atomic level study by molecular dynamics simulation. *Biochemistry*. **32**, 12624–12637

119. Torin Huzil, J., Sivaloganathan, S., Kohandel, M., and Foldvari, M. (2011) Drug delivery through the skin: molecular simulations of barrier lipids to design more effective noninvasive dermal and transdermal delivery systems for small molecules, biologics, and cosmetics. *Wiley Interdiscip. Rev. Nanomedicine Nanobiotechnology*. **3**, n/a-n/a

120. Marrink, S.-J., and Berendsen, H. J. C. (1994) Simulation of Water Transport through a Lipid Membrane. *J. Phys. Chem.* **9898**, 4155–4168

121. Marrink, S. J., and Berendsen, H. J. C. (1996) Permeation Process of Small Molecules

across Lipid Membranes Studied by Molecular Dynamics Simulations. *J. Phys. Chem.* **100**, 16729–16738

122. Carpenter, T. S., Kirshner, D. A., Lau, E. Y., Wong, S. E., Nilmeier, J. P., and Lightstone, F. C. (2014) A Method to Predict Blood-Brain Barrier Permeability of Drug-Like Compounds Using Molecular Dynamics Simulations. *Biophys. J.* **107**, 630–641

123. Awoonor-Williams, E., and Rowley, C. N. (2016) Molecular simulation of nonfacilitated membrane permeation. *Biochim. Biophys. Acta - Biomembr.* **1858**, 1672–1687

124. Lee, B. L., Kuczera, K., Middaugh, C. R., and Jas, G. S. (2016) Permeation of the three aromatic dipeptides through lipid bilayers: Experimental and computational study. *J. Chem. Phys.* **144**, 245103

125. Parisio, G., Stocchero, M., and Ferrarini, A. (2013) Passive membrane permeability: Beyond the standard solubility-diffusion model. *J. Chem. Theory Comput.* **9**, 5236–5246

126. Liu, P., Kim, B., Friesner, R. A., and Berne, B. J. (2005) Replica exchange with solute tempering: a method for sampling biological systems in explicit water. *Proc. Natl. Acad. Sci. U. S. A.* **102**, 13749–54

127. Huang, X., Hagen, M., Kim, B., Friesner, R. A., Zhou, R., and Berne, B. J. (2007) Replica Exchange with Solute Tempering: Efficiency in Large Scale Systems. 10.1021/JP068826W

128. Boncheva, M. (2014) The physical chemistry of the stratum corneum lipids. *Int. J. Cosmet. Sci.* **36**, 505–515

129. Das, C., Noro, M. G., and Olmsted, P. D. (2009) Simulation Studies of Stratum Corneum Lipid Mixtures. *Biophys. J.* **97**, 1941–1951

130. Engelbrecht, T., Hauß, T., Sü, K., Vogel, A., Roark, M., Feller, S. E., Neubert, R. H. H., and Dobner, B. (2011) Characterisation of a new ceramide EOS species: Synthesis and investigation of the thermotropic phase behaviour and influence on the bilayer architecture of stratum corneum lipid model membranes. *Soft Matter*. **7**, 8998–9011

131. Bouwstra, J. A., Gooris, G. S., van der Spek, J. A., and Bras, W. (1991) Structural investigations of human stratum corneum by Small-Angle X-Ray Scattering. *J. Invest. Dermatol.* **97**, 1005–1012

132. Mojumdar, E. H., Madsen, L. B., Hansson, H., Taavoniku, I., Kristensen, K., Persson, C., Morén, A. K., Mokso, R., Schmidtchen, A., Ruzgas, T., and Engblom, J. (2021) Probing Skin Barrier Recovery on Molecular Level Following Acute Wounds: An In Vivo/Ex Vivo Study on Pigs. *Biomedicines*. **9**, 360

133. De Jager, M. W., Gooris, G. S., Ponec, M., and Bouwstra, J. A. (2005) Lipid mixtures prepared with well-defined synthetic ceramides closely mimic the unique stratum corneum lipid phase behavior. *J. Lipid Res.* **46**, 2649–2656

134. Školová, B., Hudská, K., Pullmannová, P., Kováčik, A., Palát, K., Roh, J., Fleddermann, J., Estrela-Lopis, I., and Vávrová, K. (2014) Different phase behavior and packing of ceramides with long (C16) and very long (C24) acyls in model membranes: Infrared

spectroscopy using deuterated lipids. *J. Phys. Chem. B*. **118**, 10460–10470

135. Norlén, L. (2001) Skin barrier formation: The membrane folding model. *J. Invest. Dermatol.* **117**, 823–829

136. Swartzendruber, D. C., Wertz, P. W., Kitko, D. J., Madison, K. C., and Downing, D. T. (1989) Molecular models of the Intercellular Lipid Lamellae in Mammalian Stratum Corneum. *J. Invest. Dermatol.* **92**, 251–257

137. Forslind, B. O. (1994) A domain mosaic model of the skin barrier. *Acta Derm. Venereol.* **74**, 1–6

138. Garidel, P., Fölting, B., Schaller, I., and Kerth, A. (2010) The microstructure of the stratum corneum lipid barrier: Mid-infrared spectroscopic studies of hydrated ceramide:palmitic acid:cholesterol model systems. *Biophys. Chem.* **150**, 144–156

139. Norlén, L. (2001) Skin barrier structure and function: the single gel phase model. *J. Invest. Dermatol.* **117**, 830–836

140. Groen, D., Gooris, G. S., Barlow, D. J., Lawrence, M. J., Van Mechelen, J. B., Demé, B., and Bouwstra, J. A. (2011) Disposition of ceramide in model lipid membranes determined by neutron diffraction. *Biophys. J.* **100**, 1481–1489

141. Bouwstra, J., Gooris, G., and Ponec, M. (2002) The lipid organisation of the skin barrier: Liquid and crystalline domains coexist in lamellar phases. in *Journal of Biological Physics*, pp. 211–223, **28**, 211–223

142. Mojumdar, E. H., Gooris, G. S., Barlow, D. J., Lawrence, M. J., Deme, B., and Bouwstra, J. A. (2015) Skin Lipids: Localization of Ceramide and Fatty Acid in the Unit Cell of the Long Periodicity Phase. *Biophys. J.* **108**, 2670–2679

143. Iwai, I., Han, H., den Hollander, L., Svensson, S., Öfverstedt, L.-G., Anwar, J., Brewer, J., Bloksgaard, M., Laloeuf, A., Nosek, D., Masich, S., Bagatolli, L. A., Skoglund, U., and Norlén, L. (2012) The Human Skin Barrier Is Organized as Stacked Bilayers of Fully Extended Ceramides with Cholesterol Molecules Associated with the Ceramide Sphingoid Moiety. *J. Invest. Dermatol.* **132**, 2215–25

144. Notman, R., den Otter, W. K., Noro, M. G., Briels, W. J., and Anwar, J. (2007) The Permeability Enhancing Mechanism of DMSO in Ceramide Bilayers Simulated by Molecular Dynamics. *Biophys. J.* **93**, 2056–2068

145. Pandit, S. A., and Scott, H. L. (2006) Molecular-dynamics simulation of a ceramide bilayer. *J. Chem. Phys.* **124**, 014708

146. Guo, S., Moore, T. C., Iacovella, C. R., Strickland, L. A., and Mccabe, C. (2013) Simulation Study of the Structure and Phase Behavior of Ceramide Bilayers and the Role of Lipid Headgroup Chemistry. *J. Chem. Theory Comput.* **9**, 5116–5126

147. Badhe, Y., Gupta, R., and Rai, B. (2019) Structural and barrier properties of the skin ceramide lipid bilayer: a molecular dynamics simulation study. *J. Mol. Model.* 10.1007/s00894-019-4008-5

148. Ofie, Z.̌, Sovová, S., Berka, K., Otyepka, M., Jureč, P., Sovová, Ž., Berka, K., Otyepka,

M., Jurečka, P., Ofie, Zˇ, Sovová, S., Berka, K., Otyepka, M., Jureč, P., Sovov??, ??ofie, Berka, K., Otyepka, M., and Jure??ka, P. (2015) Coarse-Grain Simulations of Skin Ceramide NS with Newly Derived Parameters Clarify Structure of Melted Phase. *J. Phys. Chem. B*. **119**, 3988–3998

149. Moore, T. C., Iacovella, C. R., Leonhard, A. C., Bunge, A. L., McCabe, C., and M C Cabe, C. (2018) Molecular dynamics simulations of stratum corneum lipid mixtures: A multiscale perspective. *Biochem. Biophys. Res. Commun.* 10.1016/j.bbrc.2017.09.040

150. Höltje, M., Förster, T., Brandt, B., Engels, T., Von Rybinski, W., and Höltje, H. D. (2001) Molecular dynamics simulations of stratum corneum lipid models: Fatty acids and cholesterol. *Biochim. Biophys. Acta - Biomembr.* **1511**, 156–167

151. Hadley, K. R., and McCabe, C. (2012) A simulation study of the self-assembly of coarse-grained skin lipids. *Soft Matter*. **8**, 4802–4814

152. Hoopes, M. I., Noro, M. G., Longo, M. L., and Faller, R. (2011) Bilayer structure and lipid dynamics in a model stratum corneum with oleic acid. *J. Phys. Chem. B*. **115**, 3164–3171

153. Del Regno, A., and Notman, R. (2018) Permeation pathways through lateral domains in model membranes of skin lipids. *Phys. Chem. Chem. Phys.* **20**, 2162–2174

154. Wan, G., Dai, X., Yin, Q., Shi, X., and Qiao, Y. (2015) Interaction of menthol with mixed-lipid bilayer of stratum corneum: A coarse-grained simulation study. *J. Mol. Graph. Model.* **60**, 98–107

155. Podewitz, M., Wang, Y., Gkeka, P., Von Grafenstein, S., Liedl, K. R., and Cournia, Z. (2018) Phase Diagram of a Stratum Corneum Lipid Mixture. *J. Phys. Chem. B*. **122**, 10505–10521

156. Wang, E., and Klauda, J. B. (2018) Simulations of Pure Ceramide and Ternary Lipid Mixtures as Simple Interior Stratum Corneum Models. *J. Phys. Chem. B*. **122**, 2757–2768

157. Wang, E., and Klauda, J. B. (2018) Models for the Stratum Corneum Lipid Matrix: Effects of Ceramide Concentration, Ceramide Hydroxylation, and Free Fatty Acid Protonation. *J. Phys. Chem. B*. **122**, 11996–12008

158. Schmitt, T., Gupta, R., Lange, S., Sonnenberger, S., Dobner, B., Hauß, T., Rai, B., and Neubert, R. H. H. (2018) Impact of the ceramide subspecies on the nanostructure of stratum corneum lipids using neutron scattering and molecular dynamics simulations. Part I: impact of CER[NS]. *Chem. Phys. Lipids*. **214**, 58–68

159. Das, C., and Olmsted, P. D. (2016) The physics of stratum corneum lipid membranes. *Philos. Trans. R. Soc. A Math. Phys. Eng. Sci.* **374**, 20150126

160. Wang, E., and Klauda, J. B. (2019) Structure and Permeability of Ceramide Bilayers and Multilayers. *J. Phys. Chem. B*. **123**, 2525–2535

161. Lundborg, M., Narangifard, A., Wennberg, C. L., Lindahl, E., Daneholt, B., and Norlén, L. (2018) Human skin barrier structure and function analyzed by cryo-EM and molecular dynamics simulation. *J. Struct. Biol.* **203**, 149–161

162. ROBERTS, M. S., ANDERSON, R. A., SWARBRICK, J., and MOORE, D. E. (1978) The percutaneous absorption of phenolic compounds: the mechanism of diffusion across the stratum corneum. *J. Pharm. Pharmacol.* **30**, 486–490

163. Johnson, M. E., Berk, D. A., Blankschtein, D., Golan, D. E., Jain, R. K., and Langer, R. S. (1996) Lateral diffusion of small compounds in human stratum corneum and model lipid bilayer systems. *Biophys. J.* **71**, 2656–2668

164. Lin, R. Y., Hsu, C. W., and Chen, W. Y. (1996) A method to predict the transdermal permeability of amino acids and dipeptides through porcine skin. *J. Control. Release*. **38**, 229–234

165. Rocco, D., Ross, J., Murray, P. E., and Caccetta, R. (2016) Acyl lipidation of a peptide: Effects on activity and epidermal permeability in vitro. *Drug Des. Devel. Ther.* **10**, 2203–2209

166. Orsi, M., Sanderson, W. E., and Essex, J. W. (2009) Permeability of small molecules through a lipid bilayer: A multiscale simulation study. *J. Phys. Chem. B*. **113**, 12019–12029

167. Bassolino-klimas, D., Alper, H. E., and Stouch, T. R. (1995) Mechanism of Solute Diffusion through Lipid Bilayer Membranes by Molecular Dynamics Simulation. *J. Am. Chem. SOC*. **117**, 4118–4129

168. Alper, H. E., and Stouch, T. R. (1995) Orientation and Diffusion of a Drug Analogue in Biomembranes: Molecular Dynamics Simulations. *J. Phys. Chem*. **99**, 5724–5731

169. Cocucci, E., Kim, J. Y., Bai, Y., and Pabla, N. (2017) Role of Passive Diffusion, Transporters, and Membrane Trafficking-Mediated Processes in Cellular Drug Transport. *Clin. Pharmacol. Ther.* **101**, 121–129

170. Ghaemi, Z., Alberga, D., Carloni, P., Laio, A., and Lattanzi, G. (2016) Permeability Coefficients of Lipophilic Compounds Estimated by Computer Simulations. *J. Chem. Theory Comput.* **12**, 4093–4099

171. Seydel, J. K., and Wiese, M. (2002) *Drug-Membrane Interactions* (Seydel, J. K., and Wiese, M. eds), Methods and Principles in Medicinal Chemistry, Wiley-VCH Verlag GmbH & Co. KGaA, Weinheim, FRG, 10.1002/3527600639

172. Das, C., Olmsted, P. D., and Noro, M. G. (2009) Water permeation through stratum corneum lipid bilayers from atomistic simulations. *Soft Matter*. **5**, 4549–4555

173. Gupta, R., Sridhar, D. B., and Rai, B. (2016) Molecular Dynamics Simulation Study of Permeation of Molecules through Skin Lipid Bilayer. *J. Phys. Chem. B*. **120**, 8987–8996

174. Lundborg, M., Wennberg, C. L., Narangifard, A., Lindahl, E., and Norlén, L. (2018) Predicting drug permeability through skin using molecular dynamics simulation. *J. Control. Release*. **283**, 269–279

175. Wang, L., Friesner, R. A., and Berne, B. J. (2011) Replica Exchange with Solute Scaling: A More Efficient Version of Replica Exchange with Solute Tempering (REST2). *J. Phys. Chem. B*. **115**, 9431–9438

176. Bussi, G. (2014) Hamiltonian replica exchange in GROMACS: a flexible implementation. *Mol. Phys.* **112**, 379–384

177. Van Der Spoel, D., Lindahl, E., Hess, B., Groenhof, G., Mark, A. E., and Berendsen, H. J. C. (2005) GROMACS: Fast, flexible, and free. *J. Comput. Chem.* **26**, 1701–1718

178. Notman, R., and Anwar, J. (2013) Breaching the skin barrier — Insights from molecular simulation of model membranes. *Adv. Drug Deliv. Rev.* **65**, 237–250

179. Martínez, L., Andrade, R., Birgin, E. G., and Martínez, J. M. (2009) PACKMOL: A package for building initial configurations for molecular dynamics simulations. *J. Comput. Chem.* **30**, 2157–2164

180. Berk Hess, Henk Bekker, Herman J. C. Berendsen, and Johannes G. E. M. Fraaije (1997) LINCS: A linear constraint solver for molecular simulations. *J. Comput. Chem.* **18**, 1463–1472

181. Tironi, I. G., Sperb, R., Smith, P. E., and Van Gunsteren, W. F. (1995) A generalized reaction field method for molecular dynamics simulations. *J. Chem. Phys.* **102**, 5451–5459

182. Poger, D., and Mark, A. E. (2010) On the validation of molecular dynamics simulations of saturated and cis-monounsaturated phosphatidylcholine lipid bilayers: A comparison with experiment. *J. Chem. Theory Comput.* **6**, 325–336

183. Berendsen, H. J. C., Postma, J. P. M., van Gunsteren, W. F., and Hermans, J. (1981) Interaction Models for Water in Relation to Protein Hydration, pp. 331–342, Springer, Dordrecht, 10.1007/978-94-015-7658-1_21

184. Berendsen, H. J. C., Postma, J. P. M., Van Gunsteren, W. F., DiNola, A., and Haak, J. R. (1984) Molecular dynamics with coupling to an external bath. *J. Chem. Phys.* **81**, 3684–3690

185. Hoover, W. G. (1985) Canonical dynamics: Equilibrium phase-space distributions. *Phys. Rev. A*. **31**, 1695–1697

186. Parrinello, M., and Rahman, A. (1981) Polymorphic transitions in single crystals: A new molecular dynamics method. *J. Appl. Phys.* **52**, 7182–7190

187. Guixà-González, R., Rodriguez-Espigares, I., Ramírez-Anguita, J. M., Carrió-Gaspar, P., Martinez-Seara, H., Giorgino, T., and Selent, J. (2014) MEMBPLUGIN: Studying membrane complexity in VMD. *Bioinformatics*. **30**, 1478–1480

188. Humphrey, W., Dalke, A., and Schulten, K. (1996) VMD: Visual molecular dynamics. *J. Mol. Graph.* **14**, 33–38

189. Sindhikara, D. J., Emerson, D. J., and Roitberg, A. E. (2010) Exchange often and properly in replica exchange molecular dynamics. *J. Chem. Theory Comput.* **6**, 2804–2808

190. Hub, J. S., De Groot, B. L., and Van Der Spoel, D. (2010) G-whams-a free Weighted Histogram Analysis implementation including robust error and autocorrelation estimates. *J. Chem. Theory Comput.* **6**, 3713–3720

191. Paloncyová, M., Devane, R. H., Murch, B. P., Berka, K., and Otyepka, M. (2014) Rationalization of reduced penetration of drugs through ceramide gel phase membrane. *Langmuir*. **30**, 13942–13948

192. Armoškait, V., Ramanauskien, K., and Briedis, V. (2011) Selection of the Optimal Pharmaceutical Form of 5-Aminolevulinic Acid and Its Application in the Treatment of Oncologic Diseases. *Medicina (B. Aires)*. **47**, 49–55

193. Kloek, J., Akkermans, W., and Beijersbergen Van Henegouwen, G. M. J. (1998) Derivatives of 5-Aminolevulinic Acid for Photodynamic Therapy: Enzymatic Conversion into Protoporphyrin. *Photochem. Photobiol.* **67**, 150–154

194. Eriksson, E. S. E., Erdtman, E., and Eriksson, L. A. (2016) Permeability of 5-aminolevulinic acid oxime derivatives in lipid membranes. *Theor. Chem. Acc.* **135**, 1–9

195. Van Hillegersberg, R., Van Den Berg, J. W. O., Kort, W. J., Terpstra, O. T., and Wilson, J. H. P. (1992) Selective accumulation of endogenously produced porphyrins in a liver metastasis model in rats. *Gastroenterology*. **103**, 647–651

196. Bretschko, E., Szeimies, R. M., Landthaler, M., and Lee, G. (1996) Topical 5-aminolevulinic acid for photodynamic therapy of basal cell carcinoma. Evaluation of stratum corneum permeability in vitro. *J. Control. Release*. **42**, 203–208

197. Tarstedt, M., Gillstedt, M., Wennberg Larkö, A.-M., and Paoli, J. (2016) Aminolevulinic acid and methyl aminolevulinate equally effective in topical photodynamic therapy for non-melanoma skin cancers. *J. Eur. Acad. Dermatology Venereol.* **30**, 420–423

198. Jhanker, Y. M. (2018) *Formulation Development and Optimization for Transdermal Delivery of Peptide and Peptide Like Drugs*. Ph.D. thesis, Curtin University

199. Erdtman, E., dos Santos, D. J. V. A., Löfgren, L., and Eriksson, L. A. (2008) Modelling the behavior of 5-aminolevulinic acid and its alkyl esters in a lipid bilayer. *Chem. Phys. Lett.* **463**, 178–182

200. Erdtman, E., dos Santos, D. J. V. A., Löfgren, L., and Eriksson, L. A. (2009) Erratum to "Modelling the behavior of 5-aminolevulinic acid and its alkyl esters in a lipid bilayer" [Chem. Phys. Lett. 463 (2008) 178]. *Chem. Phys. Lett.* **470**, 369

201. Ferreira, M. S., Almeida, I. F., Magalhães, M. C., and Sousa-Lobo, J. M. (2020) Trending anti-aging peptides. *Cosmetics*. **7**, 1–15

202. Ishihara, Y., Oka, M., Tsunakawa, M., Tomita, K., Hatori, M., Yamamoto, H., Kamei, H., Miyaki, T., Konishi, M., and Oki, T. (1991) Melanostatin, a new melanin synthesis inhibitor: Production, isolation, chemical properties, structure and biological activity. *J. Antibiot. (Tokyo)*. **44**, 25–32

203. Human Metabolome Database: Showing metabocard for Melanostatin (HMDB0005764) [online] https://hmdb.ca/metabolites/HMDB0005764 (Accessed June 3, 2021)

204. Pan, W., and Kastin, A. J. (2007) From MIF-1 to endomorphin: The Tyr-MIF-1 family of peptides. *Peptides*. **28**, 2411–2434

205. Saitton, S., Del Tredici, A. L., Mohell, N., Vollinga, R. C., Boström, D., Kihlberg, J., and Luthman, K. (2004) Design, synthesis and evaluation of a PLG tripeptidomimetic based on a pyridine scaffold. *J. Med. Chem.* **47**, 6595–6602

206. Fasciani, I., Petragnano, F., Aloisi, G., Marampon, F., Carli, M., Scarselli, M., Maggio, R., and Rossi, M. (2020) Allosteric modulators of g protein-coupled dopamine and serotonin receptors: A new class of atypical antipsychotics. *Pharmaceuticals*. **13**, 1–26

207. Brasnjevic, I., Steinbusch, H. W. M., Schmitz, C., and Martinez-Martinez, P. (2009) Delivery of peptide and protein drugs over the blood-brain barrier. *Prog. Neurobiol.* **87**, 212–251

208. Malde, A. K., Zuo, L., Breeze, M., Stroet, M., Poger, D., Nair, P. C., Oostenbrink, C., and Mark, A. E. (2011) An Automated force field Topology Builder (ATB) and repository: Version 1.0. *J. Chem. Theory Comput.* **7**, 4026–4037

209. Aminolevulinic acid

210. Krishnan, G. (2011) *Skin penetration enhancement techniques*. Ph.D. thesis, Curtin University

211. Showing metabocard for Valyltryptophan (HMDB0029138)

212. Malyshko, E. V, Semenova, E. V, Bagrova, O. E., Murtazina, A. R., and Tverdislov, V. A. (2021) Chiral Dualism as a Unifying Principle in Molecular Biophysics. *Biophysica*. **1**, 22–37

213. Xue, S., Xing, P., Zhang, J., Zeng, Y., and Zhao, Y. (2019) Diverse Role of Solvents in Controlling Supramolecular Chirality. *Chem. - A Eur. J.* **25**, 7426–7437

214. Hanashima, S., Yano, Y., and Murata, M. (2020) Enantiomers of phospholipids and cholesterol: A key to decipher lipid-lipid interplay in membrane. *Chirality*. **32**, 282–298

215. Koolath, S., Murai, Y., Suga, Y., Monde, K., and Yuta Murai, C. (2020) Chiral combinatorial preparation and biological evaluation of unique ceramides for inhibition of sphingomyelin synthase. *Chirality*. **32**, 308–313

216. Nguyen, L. A., He, H., and Pham-Huy, C. (2006) Chiral Drugs: An Overview. *Int. J. Biomed. Sci.*

217. Mane, S. (2016) Racemic drug resolution: A comprehensive guide. *Anal. Methods*. **8**, 7567–7586

218. Calcaterra, A., and D'Acquarica, I. (2018) The market of chiral drugs: Chiral switches versus de novo enantiomerically pure compounds. *J. Pharm. Biomed. Anal.* **147**, 323–340

219. Xie, R., Chu, L. Y., and Deng, J. G. (2008) Membranes and membrane processes for chiral resolution. *Chem. Soc. Rev.* **37**, 1243–1263

220. Mennucci, B., Cappelli, C., Cammi, R., and Tomasi, J. (2011) Modeling solvent effects

on chiroptical properties. *Chirality*. **23**, 717–729

221. Polavarapu, P. L. (2012) Molecular Structure Determination Using Chiroptical Spectroscopy: Where We May Go Wrong? *Chirality*. **24**, 909–920

222. Mukhopadhyay, P., Zuber, G., Wipf, P., and Beratan, D. N. (2007) Contribution of a Solute's Chiral Solvent Imprint to Optical Rotation. *Angew. Chemie Int. Ed.* **46**, 6450–6452

223. Zunino, M. P., Turina, A. V., Zygadlo, J. A., and Perillo, M. A. (2011) Stereoselective effects of monoterpenes on the microviscosity and curvature of model membranes assessed by DPH steady-state fluorescence anisotropy and light scattering analysis. *Chirality*. **23**, 867–877

224. Tsuchiya, H., and Mizogami, M. (2020) Membrane Interactivity of Non-steroidal Anti-inflammatory Drugs: A Literature Review. *J. Adv. Med. Med. Res.* **31**, 1–30

225. Okamoto, Y., Kishi, Y., Ishigami, T., Suga, K., and Umakoshi, H. (2016) Chiral Selective Adsorption of Ibuprofen on a Liposome Membrane. *J. Phys. Chem. B*. **120**, 2790–2795

226. Miyazaki, K., Kaiho, F., Inagaki, A., Dohi, M., Hazemoto, N., Haga, M., Hara, H., and Kato, Y. (1992) Enantiomeric difference in percutaneous penetration of propranolol through rat excised skin. *Chem. Pharm. Bull.* **40**, 1075–1076

227. Suedee, R., Brain, K. R., and Heard, C. M. (1999) Differential permeation of propranolol enantiomers across human skin in vitro from formulations containing an enantioselective excipient. *Chirality*. **11**, 680–683

228. Heard, C. M., and Brain, K. R. (1995) Does solute stereochemistry influence percutaneous penetration? *Chirality*. **7**, 305–309

229. Plazinska, A., and Plazinski, W. (2020) Chirality effects in biomolecular systems: Calculation of the relative free energies by Molecular Dynamics Simulations. *J. Chem. Inf. Model.* **60**, 5424–5436

230. Package overview — pandas 1.2.4 documentation [online] https://pandas.pydata.org/docs/getting_started/overview.html (Accessed June 17, 2021)

231. Plotly Python Graphing Library | Python | Plotly [online] https://plotly.com/python/ (Accessed June 17, 2021)

232. Terakawa, T., Kameda, T., and Takada, S. (2011) On easy implementation of a variant of the replica exchange with solute tempering in GROMACS. *J. Comput. Chem.* **32**, 1228–1234

Appendix

I. Supporting Figures

Appendix Figure 1. Simulations of downscaled non-bonded interactions without replica exchange of more than 80ns were required to "unlock" the sampling of dihedral angles of the Ala-Trp dipeptide while it is inserted in the dense hydrophobic core of the bilayer, at COM distance 1.3nm.
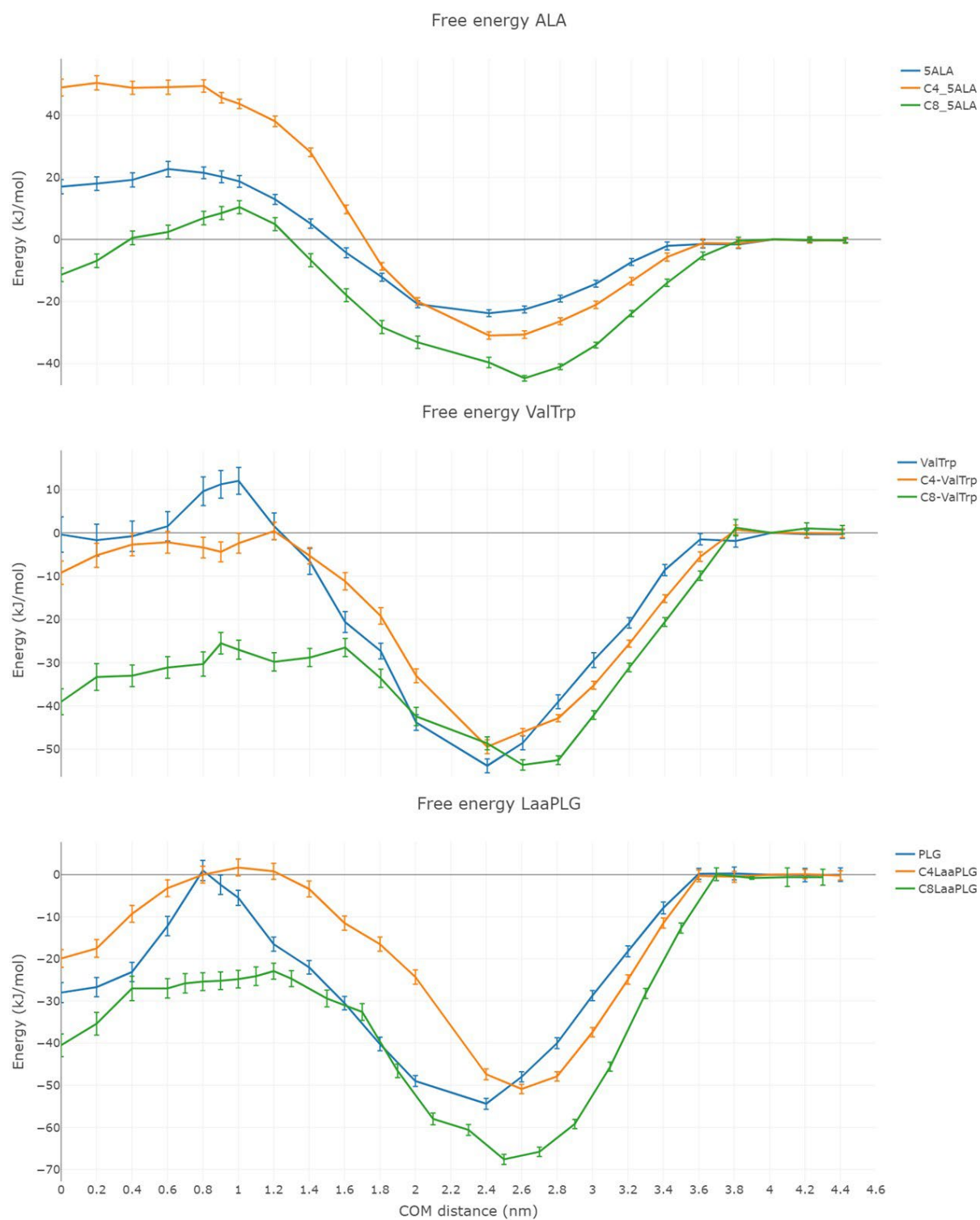
Appendix Figure 2. Free energy profiles of 5ALA (top), ValTrp (middle) and PLG (bottom) are compared with the free energy profiles of their respective C4 and C8 Laa derivatives. The free energy is shown with the standard deviation as calculated with the g_wham *module*
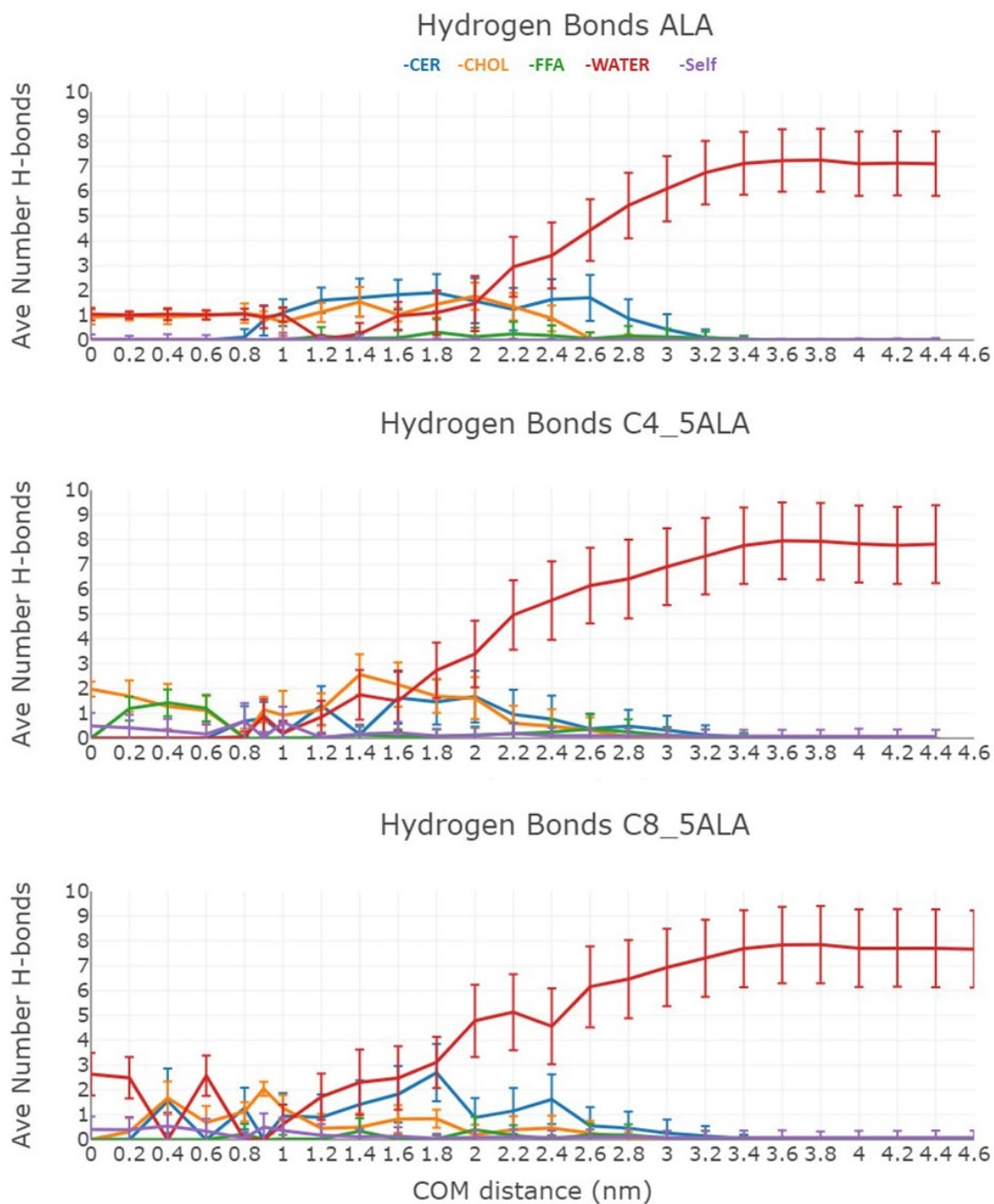
Appendix Figure 3. Average number of H-bonds of 5ALA (Top) and its C4 Laa (Middle) and C8 Laa (Bottom) derivatives. Error bars are standard deviation. Intermolecular H-bonds to each of the other types of molecules of the simulation box and intramolecular H-bonds are shown as a function of COM distance.
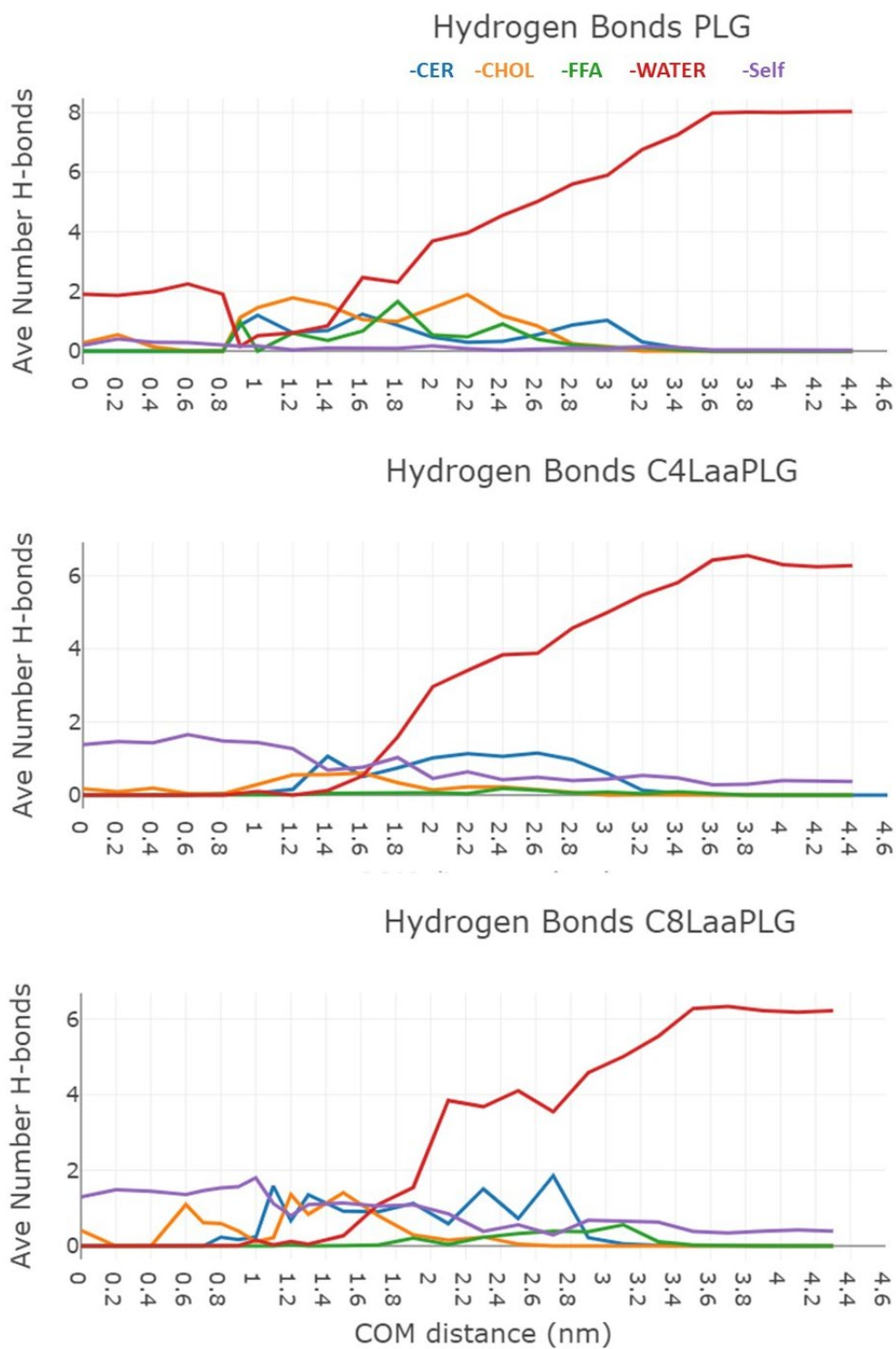
Appendix Figure 4. Average number of H-bonds of PLG (Top) and its C4 Laa (Middle) and C8 Laa (Bottom) derivatives. Intermolecular H-bonds to each of the other types of molecules of the simulation box and intramolecular H-bonds are shown as a function of COM distance.
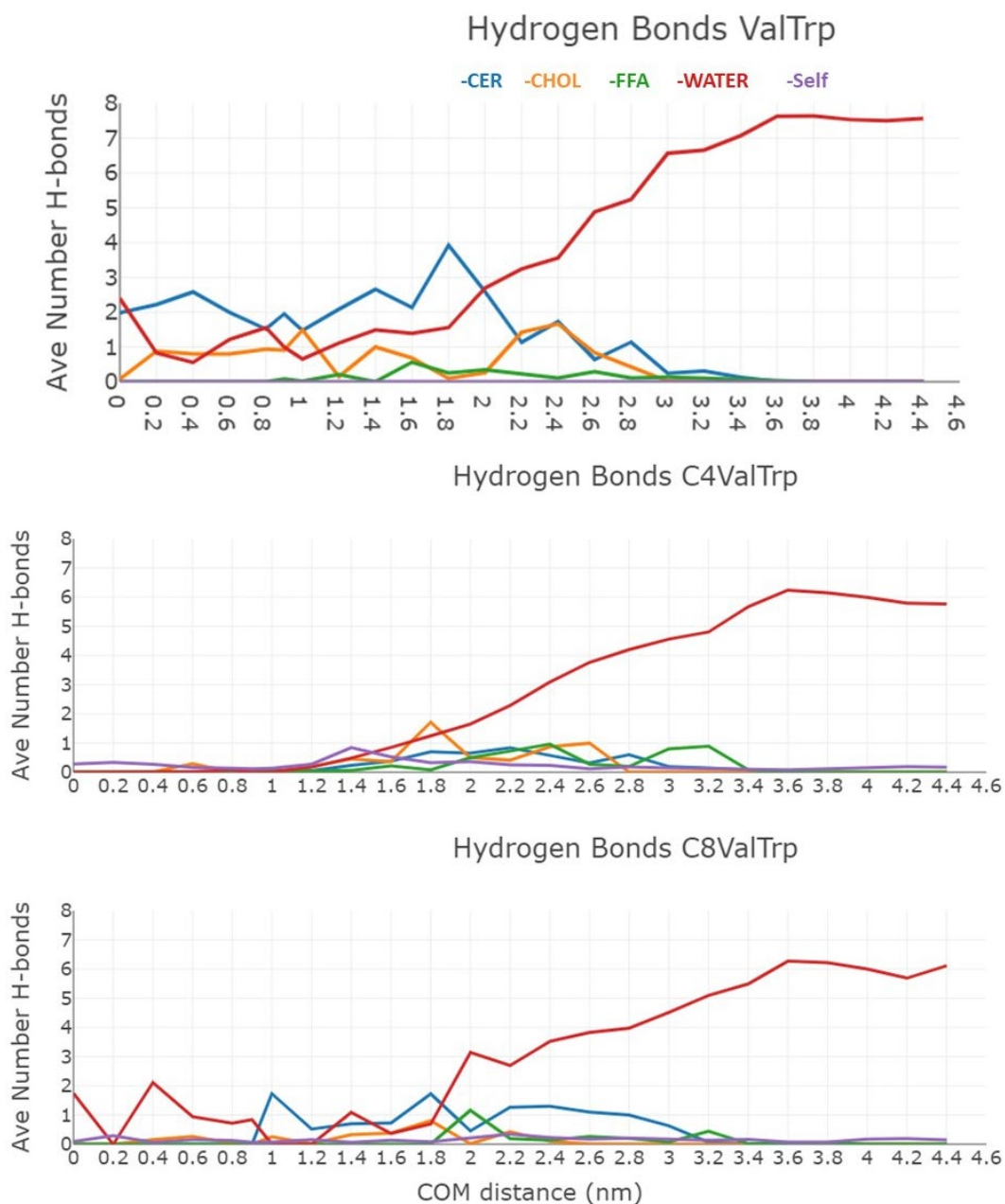
Appendix Figure 5. Average number of H-bonds of ValTrp (Top) and its C4 Laa (Middle) and C8 Laa (Bottom) derivatives. Intermolecular H-bonds to each of the other types of molecules of the simulation box and intramolecular H-bonds are shown as a function of COM distance.

.
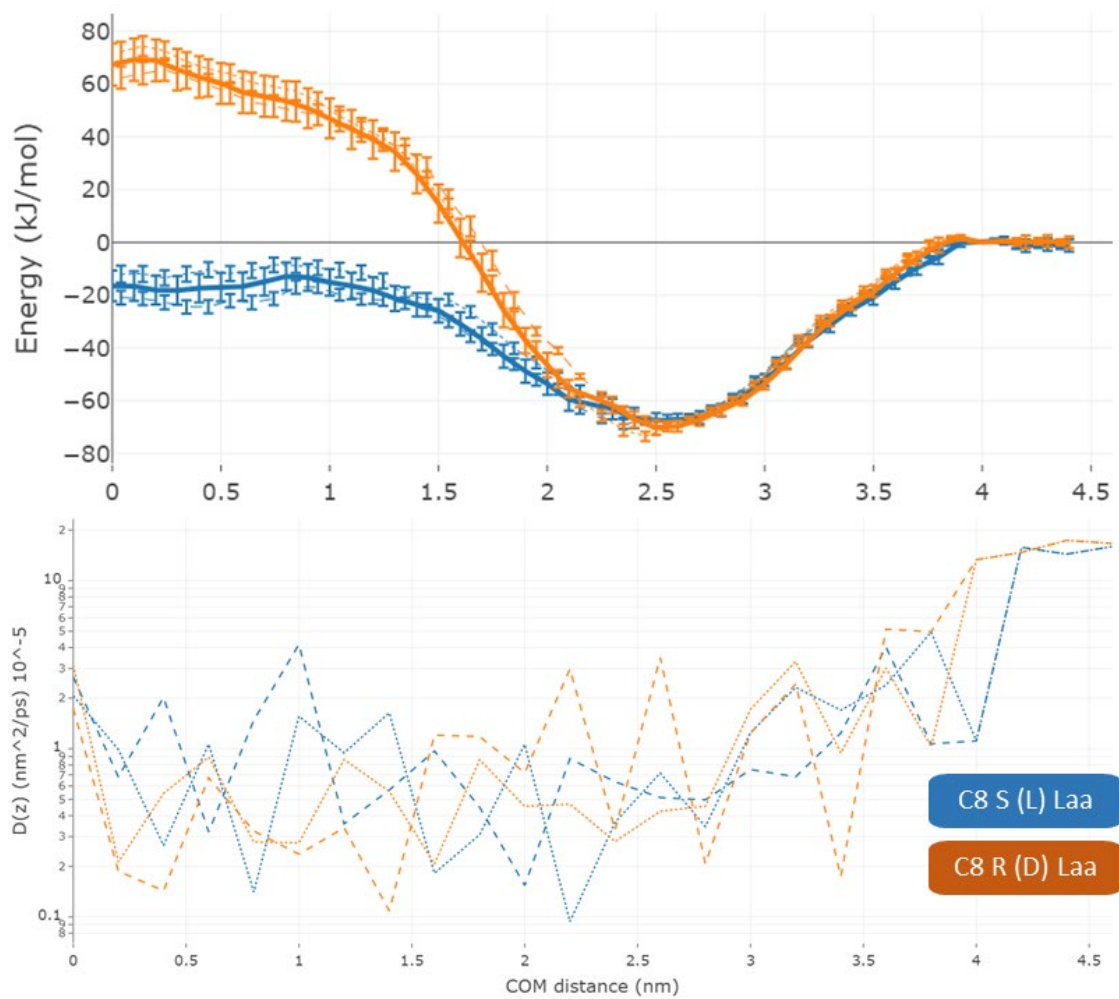
Appendix Figure 6. Insets to Figure 5.3.1. Free energy (top) and diffusivity (bottom) profiles for the interaction of the replicates run of each epimer with the lipid bilayer. Colour code as indicated.
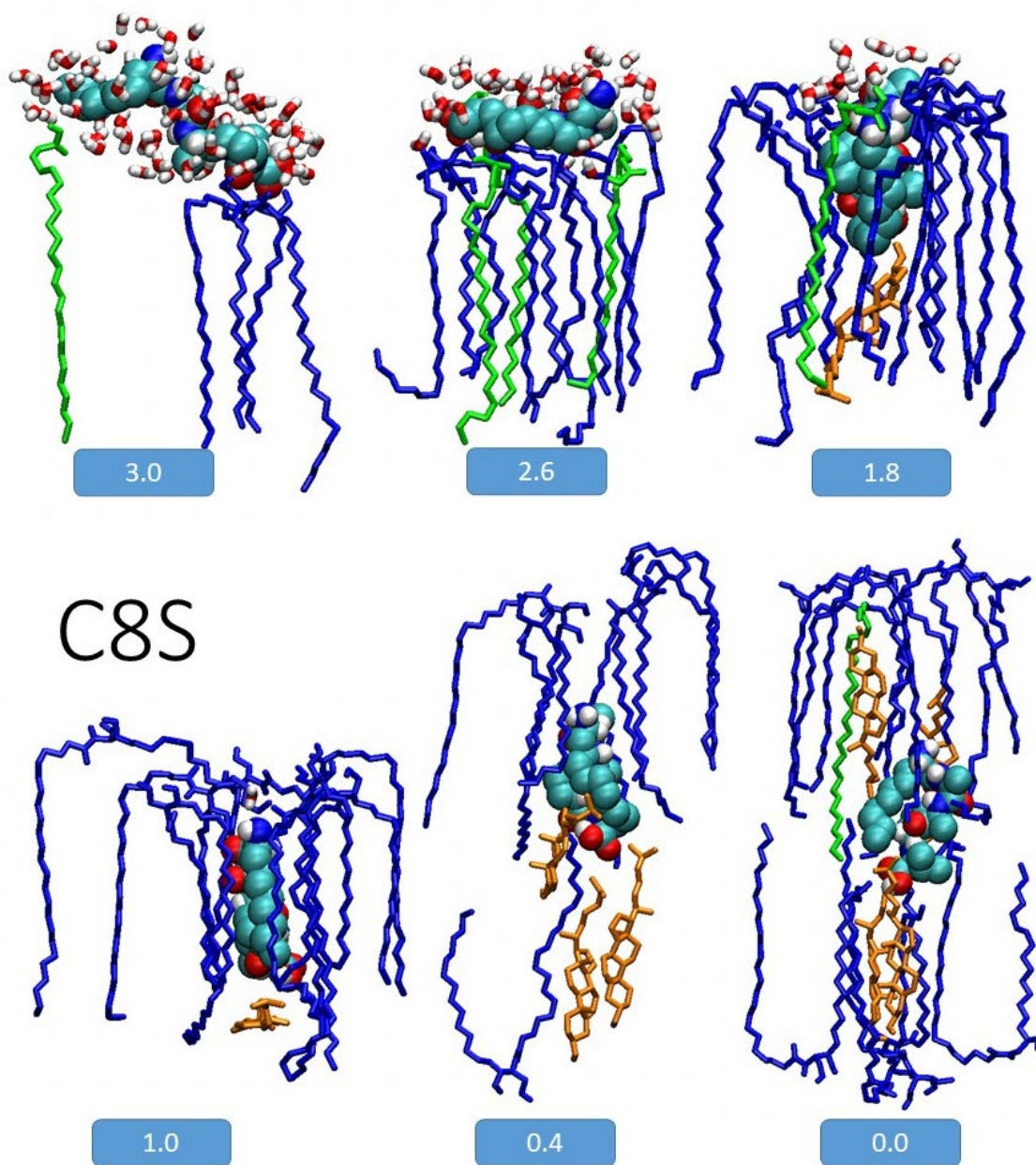
Appendix Figure 7. Selected snapshots of the pull simulation of the C8 S Laa AAPV isomer, showing that the insertion did not significantly perturb the bilayer. The values on the blue boxes represent the COM distance in nm.
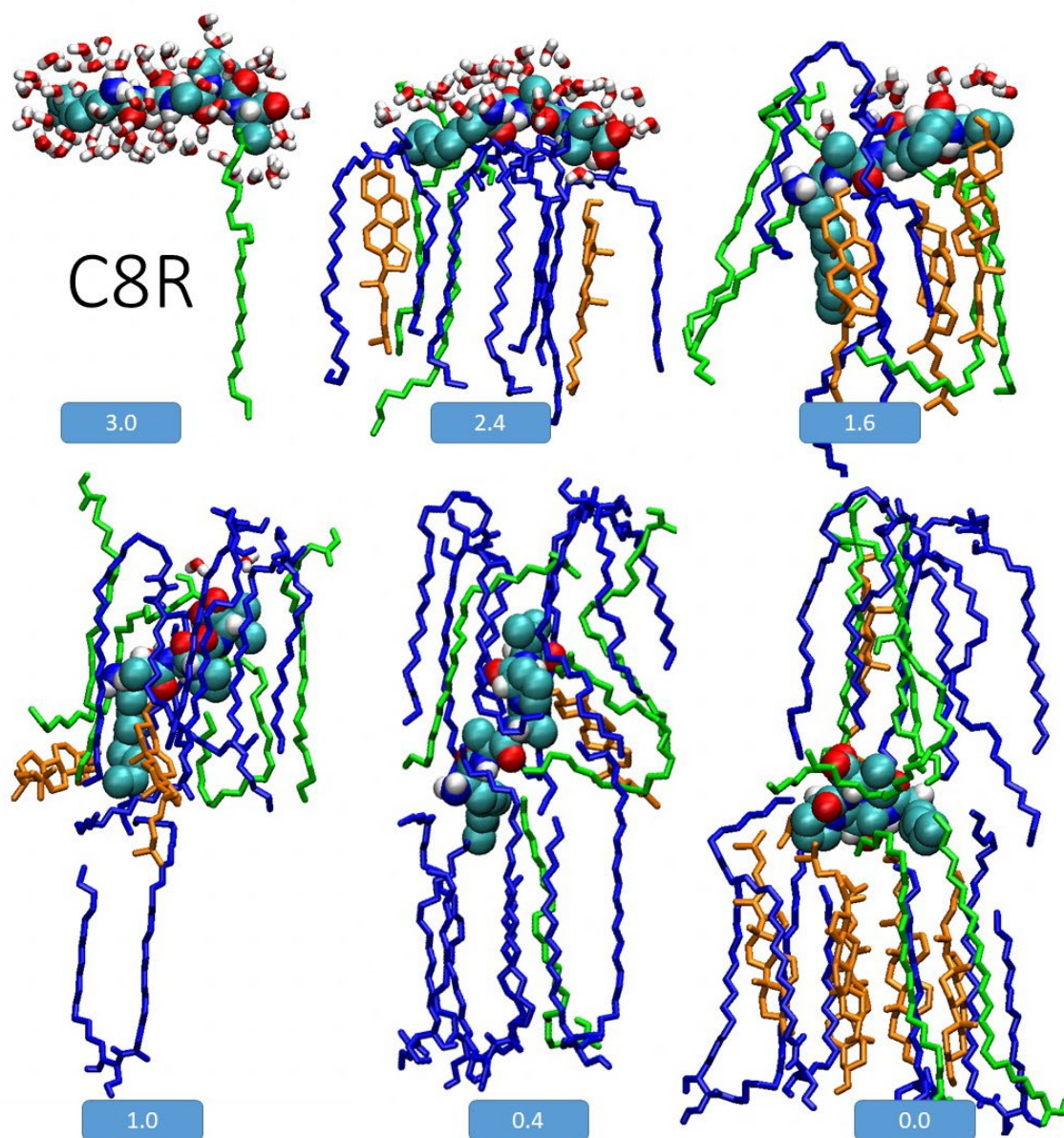
Appendix Figure 8. Selected snapshots of the pull simulation of the C8 R Laa AAPV isomer, showing that the insertion did not significantly perturb the bilayer. The values on the blue boxes represent the COM distance in nm
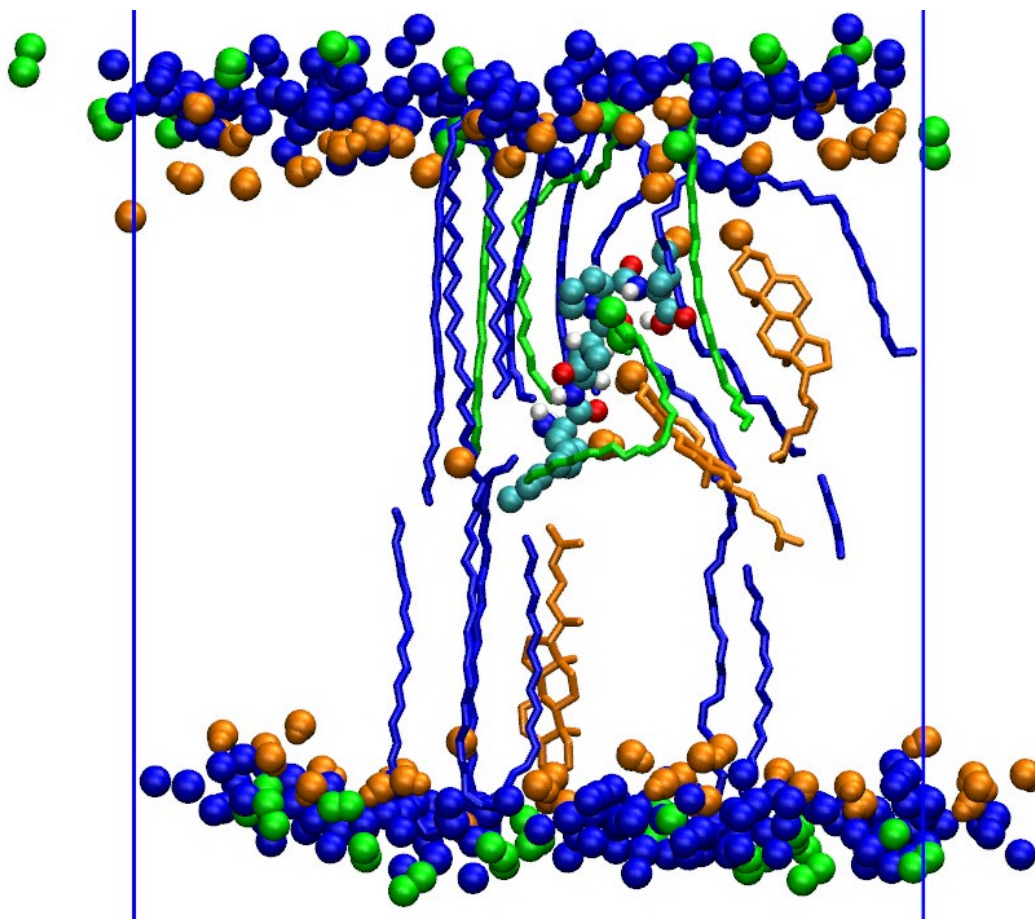
Appendix Figure 9. Snapshot of the C8 R Laa AAPV isomer obtained from the trajectory of the US-REST3 simulation where its COM was restrained at 0.6nm. It can be seen how at least three lipid head groups have been displaced.

II.   List of Conferences

WACCC2019 2nd Western Australia Computational Chemistry Conference	TALK: Permeation of short peptides across a stratum corneum model: application of a new, flexible enhanced sampling method.
MM2019 conference of the Association of Molecular Modellers of Australasia (AMMA) (Short talk)	TALK: Permeation of short peptides across a stratum corneum model: application of a new, flexible enhanced sampling method.
1WBDS-LA 1st Latin American Congress Of Women In Bioinformatics And Data Science	TALK: Molecular simulation of the permeation of short peptides across a model of the skin's lipid barrier.
GCC2020 16th German Conference On Cheminformatics And SAMPL Satellite Workshop – Virtual Edition	TALK: Molecular simulations and enhanced sampling of the permeation of short peptides across a model of the skin barrier.
ASB2020 44th Meeting Of Australian Society For Biophysics ECR symposium	TALK: Molecular simulations and enhanced sampling for the permeation of short peptides across a model of the skin barrier.
MM2021 conference of the Association of Molecular Modellers of Australasia (AMMA)	POSTER: Lipidation of bioactive peptides: Effect of lipid-tail length on transdermal permeability.

III. Derivation of REST3

The following text is taken *verbatim* from the manuscript titled "Selective replica-exchange with solute tempering (REST3) for the prediction of the interactions of small molecules with lipid bilayers" for which I am second author. The attribution statement for this work is included in the corresponding section of this thesis. As indicated then, this part of the work was conceptualised and developed by RLM and CM and is included here to provide the reader with details on the derivation and the implementation of the method.

Theoretical derivation

In REST2, the potential energy (*E*) of a replica is divided into three distinct contributions, each scaled by a separate scaling factor (126, 175) defined by

$$E(X) = \frac{\beta_i}{\beta_0} E_{mm}(X) + \sqrt{\frac{\beta_i}{\beta_0}} E_{ms}(X) + E_{ss}(X) \qquad (1)$$

where *X* indicates the position coordinates of the system, E_{mm} is the small molecule self-interaction energy, E_{ms} is the small molecule-solvent intermolecular interaction energy, E_{ss} is the solvent-solvent intermolecular interaction energy and β_i is $1/k_bT_i$, where *i* refers to the replica number. For the ground (unscaled) replica *i* = 0 and all other replicas, the scaling factor for each term is related to the virtual temperature (β_i) of replica *i*. Using the extended detailed balance condition (232) given by

$$p_i(X_i)p_j(X_j)p(X_i \rightarrow X_j) = p_i(X_j)p_j(X_i)p(X_j \rightarrow X_i). \qquad (2)$$

Considering that the probability of finding the system with Hamiltonian *i* and coordinates X_i is given by

$$p_i(X_i) = e^{-\beta_i E_i(X_i)} \qquad (3)$$

equations 3 and 1 can be substituted into equation 2 to obtain the transition probability ratio

$$\frac{p(X_i \rightarrow X_j)}{p(X_j \rightarrow X_i)} = e^{-\Delta_{ij}} \qquad (4)$$

where

$$\Delta_{ij} = (\beta_i - \beta_j)[(E_{mm}(X_j) - E_{mm}(X_i)) + \frac{\sqrt{\beta_0}}{\sqrt{\beta_i} + \sqrt{\beta_j}}(E_{ms}(X_j)$$
$$- E_{mw}(X_i))] \tag{5}$$

In REST3, the solvent term can be divided into multiple components as required (e.g., membrane, water, ions, etc.), with each cross-term scaled independently. Furthermore, each of the energy terms in equation 1 is further divided into its underlying energy contributions (bonded, electrostatic and vdW). This allows controlling the strength of the different types of interactions. For example, membrane-membrane and membrane-solvent interactions can be left unperturbed, while electrostatic interactions of the molecule-membrane component may be selectively scaled. In membrane-molecule systems such control is critical because a small change in membrane-membrane interactions may become amplified by the large magnitude of these interactions, leading to destabilization of the entire membrane. At the same time, full membrane-peptide interactions cannot be retained in classical REST2 implementation without reducing peptide-peptide interactions to almost zero. It is then crucial to decouple the scaling of these two contributions flexibly.

Let us take one of the terms of the Hamiltonian in the case of a small molecule-solvent system, the intermolecular interaction energy E_{ms}, which is defined as:

$$E_{ms}^{REST3} = \lambda_{ms,bond}E_{ms,bond} + \lambda_{ms,elec}E_{ms,elec} + \lambda_{ms,vdW}E_{ms,vdW} \tag{6}$$

where each $\lambda_i = \beta_i/\beta_0$ is the associated scaling factor for the corresponding energy contribution. It follows that the Δ_{ij} for REST3 does not depend on the terms that are left unscaled in the equation. For example, if all of the λ parameters are set to 1 except for the small molecule-solvent intermolecular terms, the resulting Δ_{ij} simply reduces to:

$$\Delta_{ij}^{REST3} = (\beta_i - \beta_j)[E_{ms(X_j)} - E_{ms(X_i)}] \tag{7}$$

As a result, the terms of the equation that are to be ignored by the replica-exchange method (in this case, all terms except the small molecule-solvent terms) are left unscaled with $\lambda = 1$, enhancing the exchange probability between two replicas several-fold in the case of systems where the energy is dominated by the solvent. An outline of the algorithmic and practical implementation of this method in GROMACS 4.6.7 can be found below.

Implementation of REST3 in GROMACS 4.6.7

Several GROMACS modules were modified, including non-bonded routines specific to SSE 4.2 and AVX 256 architectures, user definitions and distributed communication. Routines specific to replica exchange were modified to include specification of scaling coefficients related to pair-wise interactions, energy rules that may lead to a successful replica exchange, and modules that update the calculation of scaled electrostatics and van der Waals interactions. The current implementation only supports the reaction field method for non-bonded interactions. The input requires the user to specify the lower triangular matrix of possible interaction λ for both electrostatic and van der Waals energies. These matrices are broadcast to all nodes participating in the simulation. Below is a sample specification of related user input:

```
; Compound #mols
Protein_X       1
POPC            128
SOL             9955
NA              28
CL              32


[ scale_vdw ]
; Specify this section after 'molecules' section`
1.0
0.8 1.0
1.0 1.0 0.2
1.0 1.0 1.0 0.0
1.0 1.0 1.0 1.0 1.0


[ scale_q ]
; Lower triangular matrix includes the diagonal
1.0
0.8 0.2
0.2 0.0 1.0
1.0 1.0 1.0 1.0
1.0 1.0 1.0 1.0 1.0
```

GROMACS involves a master-slave communication protocol, wherein decisions related to exchange criterion and broadcasting replica exchange coordinates rest with the master. Before the exchange, GROMACS follows an odd-even check between replicas and designates all possible replica pairs that fall in the criterion for

exchange. Owing to costs involved in the gathering of the energy of each replica at the end of each time step, the routine only computes and exchanges replicas at every exchange attempt (Nreplex). Routines that are involved in the calculation of non-bonded interactions update both the scaled forces as well as the energies. With respect to the calculation of non-bonded electrostatics, due to possible complications that could arise due to charge imbalance, only energies and forces were modified with scaled electrostatic interactions. A full version of the modified GROMACS source is available at https://github.com/curtinic/gromacs.

IV. Copyrights of Figures

This Agreement between Ms. Lanie Ruiz-Perez ("You") and Elsevier ("Elsevier") consists of your license details and the terms and conditions provided by Elsevier and Copyright Clearance Center.

License Number	5062420050452
License date	May 05, 2021
Licensed Content Publisher	Elsevier
Licensed Content Publication	International Journal of Pharmaceutics
Licensed Content Title	Enhanced transdermal delivery of phenylalanyl-glycine by chemical modification with various fatty acids
Licensed Content Author	Akira Yamamoto,Kazunari Setoh,Masahiro Murakami,Masaru Shironoshita,Takumi Kobayashi,Kayoko Fujimoto,Naoki Okada,Takuya Fujita,Shozo Muranishi
Licensed Content Date	Jan 2, 2003
Licensed Content Volume	250
Licensed Content Issue	1
Licensed Content Pages	10
Start Page	119
End Page	128
Type of Use	reuse in a thesis/dissertation
Portion	figures/tables/illustrations
Number of figures/tables/illustrations	1
Format	electronic
Are you the author of this Elsevier article?	No
Will you be translating?	No
Title	Molecular dynamics simulation of the permeation of lipid-conjugated peptides through the stratum corneum
Institution name	Curtin University
Expected presentation date	Jul 2021
Portions	Fig. 2. Permeation profiles of Phe-Gly and its acyl derivatives across the intact and stripped skin.
	Ms. Lanie Ruiz-Perez Kent St, Bentley WA 6102
Requestor Location	
	Perth, 6102 Australia Attn: Ms. Lanie Ruiz-Perez
Publisher Tax ID	GB 494 6272 12
Total	0.00 AUD

This Agreement between Ms. Lanie Ruiz-Perez ("You") and Springer Nature ("Springer Nature") consists of your license details and the terms and conditions provided by Springer Nature and Copyright Clearance Center.

License Number	5062420661634
License date	May 05, 2021
Licensed Content Publisher	Springer Nature
Licensed Content Publication	AAPS PharmSciTech
Licensed Content Title	Validation of a Static Franz Diffusion Cell System for In Vitro Permeation Studies
Licensed Content Author	Shiow-Fern Ng et al
Licensed Content Date	Sep 15, 2010
Type of Use	Thesis/Dissertation
Requestor type	academic/university or research institute
Format	electronic
Portion	figures/tables/illustrations
Number of figures/tables/illustrations	1
Will you be translating?	no
Circulation/distribution	1 - 29
Author of this Springer Nature content	no
Title	Molecular dynamics simulation of the permeation of lipid-conjugated peptides through the stratum corneum
Institution name	Curtin University
Expected presentation date	Jul 2021
Portions	Fig. 1. a Sketch of typical Franz cell (tailor-made) and b diagram to indicate the physical characteristics investigated.
Requestor Location	Ms. Lanie Ruiz-Perez Kent St, Bentley WA 6102 Perth, 6102 Australia Attn: Ms. Lanie Ruiz-Perez
Total	0.00 AUD

This Agreement between Ms. Lanie Ruiz-Perez ("You") and John Wiley and Sons ("John Wiley and Sons") consists of your license details and the terms and conditions provided by John Wiley and Sons and Copyright Clearance Center.

License Number   5062421438249

License date	May 05, 2021
Licensed Content Publisher	John Wiley and Sons
Licensed Content Publication	Wiley Interdisciplinary Reviews - Nanomedicine and Nanobiotechnology
Licensed Content Title	Drug delivery through the skin: molecular simulations of barrier lipids to design more effective noninvasive dermal and transdermal delivery systems for small molecules, biologics, and cosmetics
Licensed Content Author	Marianna Foldvari, Mohammad Kohandel, Siv Sivaloganathan, et al
Licensed Content Date	May 18, 2011
Licensed Content Volume	3
Licensed Content Issue	5
Licensed Content Pages	14
Type of use	Dissertation/Thesis
Requestor type	University/Academic
Format	Electronic
Portion	Figure/table
Number of figures/tables	1
Will you be translating?	No
Title	Molecular dynamics simulation of the permeation of lipid-conjugated peptides through the stratum corneum
Institution name	Curtin University
Expected presentation date	Jul 2021
Portions	Fig 4. Schematic representation of the umbrella sampling technique.
	Ms. Lanie Ruiz-Perez Kent St, Bentley WA 6102
Requestor Location	
	Perth, 6102 Australia Attn: Ms. Lanie Ruiz-Perez
Publisher Tax ID	EU826007151
Total	0.00 AUD

JOHN WILEY AND SONS LICENSE
TERMS AND CONDITIONS
Jul 05, 2021

This Agreement between Ms. Lanie Ruiz-Perez ("You") and John Wiley and Sons ("John Wiley and Sons") consists of your license details and the terms and conditions provided by John Wiley and Sons and Copyright Clearance Center.

License Number	5102430621437
License date	Jul 05, 2021
Licensed Content Publisher	John Wiley and Sons
Licensed Content Publication	ChemPhysChem
Licensed Content Title	Molecular Dynamics Simulation of Small Molecules Interacting with Biological Membranes
Licensed Content Author	Ricardo L. Mancera, Evelyne Deplazes, Lanie Ruiz-Perez, et al
Licensed Content Date	Jun 22, 2020
Licensed Content Volume	21
Licensed Content Issue	14
Licensed Content Pages	29
Type of use	Dissertation/Thesis
Requestor type	Author of this Wiley article
Format	Print and electronic
Portion	Figure/table
Number of figures/tables	2
Will you be translating?	No
Title	Molecular dynamics simulation of the permeation of lipid-conjugated peptides through the stratum corneum
Institution name	Curtin University
Expected presentation date	Jul 2021
Portions	Figure 4. Lipid phase transition from gel to fluid phase induced by an increase in temperature. Figure 5. The four-region model for a phospholipid bilayer in full hydration.
Requestor Location	Ms. Lanie Ruiz-Perez Kent St, Bentley WA 6102 Perth, 6102 Australia Attn: Ms. Lanie Ruiz-Perez
Publisher Tax ID	EU826007151
Total	0.00 AUD

ELSEVIER LICENSE
TERMS AND CONDITIONS
Jul 05, 2021

180

This Agreement between Ms. Lanie Ruiz-Perez ("You") and Elsevier ("Elsevier") consists of your license details and the terms and conditions provided by Elsevier and Copyright Clearance Center.

License Number	5102440010281
License date	Jul 05, 2021
Licensed Content Publisher	Elsevier
Licensed Content Publication	Journal of Investigative Dermatology
Licensed Content Title	Structural Investigations of Human Stratum Corneum by Small-Angle X-Ray Scattering
Licensed Content Author	Joke A Bouwstra,Gert S Gooris,Joop A van der Spek,Wim Bras
Licensed Content Date	Dec 1, 1991
Licensed Content Volume	97
Licensed Content Issue	6
Licensed Content Pages	8
Start Page	1005
End Page	1012
Type of Use	reuse in a thesis/dissertation
Portion	figures/tables/illustrations
Number of figures/tables/illustrations	2
Format	both print and electronic
Are you the author of this Elsevier article?	No
Will you be translating?	No
Title	Molecular dynamics simulation of the permeation of lipid-conjugated peptides through the stratum corneum
Institution name	Curtin University
Expected presentation date	Jul 2021
Portions	Figure 2 Figure 3
Requestor Location	Ms. Lanie Ruiz-Perez Kent St, Bentley WA 6102 Perth, 6102 Australia Attn: Ms. Lanie Ruiz-Perez
Publisher Tax ID	GB 494 6272 12
Total	0.00 AUD

ELSEVIER LICENSE
TERMS AND CONDITIONS
Jul 05, 2021

This Agreement between Ms. Lanie Ruiz-Perez ("You") and Elsevier ("Elsevier") consists of your license details and the terms and conditions provided by Elsevier and Copyright Clearance Center.

License Number	5102441183034
License date	Jul 05, 2021
Licensed Content Publisher	Elsevier

Licensed Content Publication	Biophysical Chemistry
Licensed Content Title	The microstructure of the stratum corneum lipid barrier: Mid-infrared spectroscopic studies of hydrated ceramide:palmitic acid:cholesterol model systems
Licensed Content Author	Patrick Garidel,Bettina Fölting,Ingrid Schaller,Andreas Kerth
Licensed Content Date	Aug 1, 2010
Licensed Content Volume	150
Licensed Content Issue	1-3
Licensed Content Pages	13
Start Page	144
End Page	156
Type of Use	reuse in a thesis/dissertation
Portion	figures/tables/illustrations
Number of figures/tables/illustrations	1
Format	both print and electronic
Are you the author of this Elsevier article?	No
Will you be translating?	No
Title	Molecular dynamics simulation of the permeation of lipid-conjugated peptides through the stratum corneum
Institution name	Curtin University
Expected presentation date	Jul 2021
Portions	Fig. 13. Schematic representation of the stratum corneum and stratum corneum lipid structure.
Requestor Location	Ms. Lanie Ruiz-Perez Kent St, Bentley WA 6102 Perth, 6102 Australia Attn: Ms. Lanie Ruiz-Perez
Publisher Tax ID	GB 494 6272 12
Total	0.00 AUD

This Agreement between Ms. Lanie Ruiz-Perez ("You") and Elsevier ("Elsevier") consists of your license details and the terms and conditions provided by Elsevier and Copyright Clearance Center.

License Number	5102441441320
License date	Jul 05, 2021
Licensed Content Publisher	Elsevier
Licensed Content Publication	Biophysical Journal
Licensed Content Title	Disposition of Ceramide in Model Lipid Membranes Determined by Neutron Diffraction
Licensed Content Author	D. Groen,G.S. Gooris,D.J. Barlow,M.J. Lawrence,J.B. van Mechelen,B. Demé,J.A. Bouwstra

Licensed Content Date	Mar 16, 2011
Licensed Content Volume	100
Licensed Content Issue	6
Licensed Content Pages	9
Start Page	1481
End Page	1489
Type of Use	reuse in a thesis/dissertation
Portion	figures/tables/illustrations
Number of figures/tables/illustrations	1
Format	both print and electronic
Are you the author of this Elsevier article?	No
Will you be translating?	No
Title	Molecular dynamics simulation of the permeation of lipid-conjugated peptides through the stratum corneum
Institution name	Curtin University
Expected presentation date	Jul 2021
Portions	Figure 6. (B) Symmetric arrangement of fully extended dCER NS molecules in the unit cell of the SPP. (C) Symmetric arrangement in the unit cell with dCER NS in the hairpin configuration.
Requestor Location	Ms. Lanie Ruiz-Perez Kent St, Bentley WA 6102 Perth, 6102 Australia Attn: Ms. Lanie Ruiz-Perez
Publisher Tax ID	GB 494 6272 12
Total	0.00 AUD

SPRINGER NATURE LICENSE
TERMS AND CONDITIONS
Jul 05, 2021

This Agreement between Ms. Lanie Ruiz-Perez ("You") and Springer Nature ("Springer Nature") consists of your license details and the terms and conditions provided by Springer Nature and Copyright Clearance Center.

License Number	5102450496591
License date	Jul 05, 2021
Licensed Content Publisher	Springer Nature
Licensed Content Publication	Journal of Biological Physics
Licensed Content Title	The Lipid Organisation of the Skin Barrier: Liquid and Crystalline Domains Coexist in Lamellar Phases
Licensed Content Author	J. Bouwstra et al
Licensed Content Date	Jan 1, 2002
Type of Use	Thesis/Dissertation
Requestor type	academic/university or research institute
Format	print and electronic

Portion	figures/tables/illustrations
Number of figures/tables/illustrations	1
Will you be translating?	no
Circulation/distribution	1 - 29
Author of this Springer Nature content	no
Title	Molecular dynamics simulation of the permeation of lipid-conjugated peptides through the stratum corneum
Institution name	Curtin University
Expected presentation date	Jul 2021
Portions	Figure 7. Based on the electron density profile calculated from diffraction peaks attributed to the LPP. Base upon this molecular model the 'sandwich model' has been proposed.
Requestor Location	Ms. Lanie Ruiz-Perez Kent St, Bentley WA 6102 Perth, 6102 Australia Attn: Ms. Lanie Ruiz-Perez
Total	0.00 AUD

This Agreement between Ms. Lanie Ruiz-Perez ("You") and Elsevier ("Elsevier") consists of your license details and the terms and conditions provided by Elsevier and Copyright Clearance Center.

License Number	5102450873746
License date	Jul 05, 2021
Licensed Content Publisher	Elsevier
Licensed Content Publication	Journal of Investigative Dermatology
Licensed Content Title	The Human Skin Barrier Is Organized as Stacked Bilayers of Fully Extended Ceramides with Cholesterol Molecules Associated with the Ceramide Sphingoid Moiety
Licensed Content Author	Ichiro Iwai,HongMei Han,Lianne den Hollander,Stina Svensson,Lars-Göran Öfverstedt,Jamshed Anwar,Jonathan Brewer,Maria Bloksgaard,Aurelie Laloeuf,Daniel Nosek,Sergej Masich,Luis A. Bagatolli,Ulf Skoglund,Lars Norlén
Licensed Content Date	Sep 1, 2012
Licensed Content Volume	132
Licensed Content Issue	9
Licensed Content Pages	11
Start Page	2215
End Page	2225
Type of Use	reuse in a thesis/dissertation
Portion	figures/tables/illustrations
Number of figures/tables/illustrations	1

Format	both print and electronic
Are you the author of this Elsevier article?	No
Will you be translating?	No
Title	Molecular dynamics simulation of the permeation of lipid-conjugated peptides through the stratum corneum
Institution name	Curtin University
Expected presentation date	Jul 2021
Portions	Figure 5. Atomic three-dimensional (3D) model of the repeating unit composed of two mirrored subunits, each composed of one fully extended CER, one CHOL, and one FFA molecule.
Requestor Location	Ms. Lanie Ruiz-Perez Kent St, Bentley WA 6102 Perth, 6102 Australia Attn: Ms. Lanie Ruiz-Perez
Publisher Tax ID	GB 494 6272 12
Total	0.00 AUD

ELSEVIER LICENSE
TERMS AND CONDITIONS
Jul 05, 2021

This Agreement between Ms. Lanie Ruiz-Perez ("You") and Elsevier ("Elsevier") consists of your license details and the terms and conditions provided by Elsevier and Copyright Clearance Center.

License Number	5102451068334
License date	Jul 05, 2021
Licensed Content Publisher	Elsevier
Licensed Content Publication	Biophysical Journal
Licensed Content Title	The Permeability Enhancing Mechanism of DMSO in Ceramide Bilayers Simulated by Molecular Dynamics
Licensed Content Author	Rebecca Notman,Wouter K. den Otter,Massimo G. Noro,W.J. Briels,Jamshed Anwar
Licensed Content Date	Sep 15, 2007
Licensed Content Volume	93
Licensed Content Issue	6
Licensed Content Pages	13
Start Page	2056
End Page	2068
Type of Use	reuse in a thesis/dissertation
Portion	figures/tables/illustrations
Number of figures/tables/illustrations	1
Format	both print and electronic
Are you the author of this Elsevier article?	No
Will you be translating?	No

Title	Molecular dynamics simulation of the permeation of lipid-conjugated peptides through the stratum corneum
Institution name	Curtin University
Expected presentation date	Jul 2021
Portions	Figure 5. Snapshots from the simulation of the bilayer at 283 K showing examples of the different conformations adopted by the ceramide molecules in the bilayer.
Requestor Location	Ms. Lanie Ruiz-Perez Kent St, Bentley WA 6102 Perth, 6102 Australia Attn: Ms. Lanie Ruiz-Perez
Publisher Tax ID	GB 494 6272 12
Total	0.00 AUD

This Agreement between Ms. Lanie Ruiz-Perez ("You") and Elsevier ("Elsevier") consists of your license details and the terms and conditions provided by Elsevier and Copyright Clearance Center.

License Number	5113430572476
License date	Jul 21, 2021
Licensed Content Publisher	Elsevier
Licensed Content Publication	Biophysical Journal
Licensed Content Title	Lateral diffusion of small compounds in human stratum corneum and model lipid bilayer systems
Licensed Content Author	M.E. Johnson,D.A. Berk,D. Blankschtein,D.E. Golan,R.K. Jain,R.S. Langer
Licensed Content Date	Nov 1, 1996
Licensed Content Volume	71
Licensed Content Issue	5
Licensed Content Pages	13
Start Page	2656
End Page	2668
Type of Use	reuse in a thesis/dissertation
Portion	figures/tables/illustrations
Number of figures/tables/illustrations	2
Format	both print and electronic
Are you the author of this Elsevier article?	No
Will you be translating?	No

Title	Molecular dynamics simulation of the permeation of lipid-conjugated peptides through the stratum corneum
Institution name	Curtin University
Expected presentation date	Jul 2021
Portions	FIGURE 1 Chemical structures of the fluorescent probes examined in this paper. FIGURE 3 Diffusion coefficients of the fluores- cent probes in SCE lipid bilayers, as measured by the video FRAP technique at 270C, versus the probe molecular weight.

Ms.   Lanie   Ruiz-Perez

Kent   St,   Bentley   WA   6102

Requestor Location

Perth,   6102
Australia
Attn: Ms. Lanie Ruiz-Perez

Publisher Tax ID	GB 494 6272 12
Total	0.00 AUD

JOHN   WILEY   AND   SONS   LICENSE TERMS AND CONDITIONS

Jul 21, 2021

License Number		5113450147668
License date		Jul 21, 2021
Licensed Publisher	Content	John Wiley and Sons
Licensed Publication	Content	Photochemistry and Photobiology
Licensed Title	Content	Derivatives of 5-Aminolevulinic Acid for Photodynamic Therapy: Enzymatic Conversion into Protoporphyrin
Licensed Author	Content	Gerard M. J. Beijersbergen Henegouwen, Willem Akkermans, Joris Kloek
Licensed Date	Content	Jan 2, 2008
Licensed Volume	Content	67
Licensed Issue	Content	1
Licensed Pages	Content	5
Type of use		Dissertation/Thesis

Requestor type	University/Academic
Format	Print and electronic
Portion	Figure/table
Number of figures/tables	2
Will you be translating?	No
Title	Molecular dynamics simulation of the permeation of lipid-conjugated peptides through the stratum corneum
Institution name	Curtin University
Expected presentation date	Jul 2021
Portions	Figure 1. Structures of ALA and the derivatives that were synthe- sized and tested in this study. Figure 2. Fluorescence of PpIX, induced by 0.50 mM ALA or one of its derivatives in intact cells.

Requestor Location

Ms. Lanie Ruiz-Perez
Kent St, Bentley WA 6102

Perth, 6102
Australia
Attn: Ms. Lanie Ruiz-Perez

Publisher Tax ID	EU826007151
Total	0.00 AUD

License Number	5113450963955
License date	Jul 21, 2021
Licensed Content Publisher	Springer Nature
Licensed Content Publication	Theoretical Chemistry Accounts
Licensed Content Title	Permeability of 5-aminolevulinic acid oxime derivatives in lipid membranes
Licensed Content Author	Emma S. E. Eriksson et al
Licensed Content Date	Jan 7, 2016
Type of Use	Thesis/Dissertation
Requestor type	academic/university or research institute
Format	print and electronic
Portion	figures/tables/illustrations

Number of figures/tables/illustrations	2
Will you be translating?	no
Circulation/distribution	1 - 29
Author of this Springer Nature content	no
Title	Molecular dynamics simulation of the permeation of lipid-conjugated peptides through the stratum corneum
Institution name	Curtin University
Expected presentation date	Jul 2021
Portions	Fig. 1 Structures Fig. 6 Free energy profiles and

Ms. Lanie Ruiz-Perez
Kent St, Bentley WA 6102

Requestor Location

Perth, 6102
Australia
Attn: Ms. Lanie Ruiz-Perez

Total	0.00 AUD

This Agreement between Ms. Lanie Ruiz-Perez ("You") and John Wiley and Sons ("John Wiley and Sons") consists of your license details and the terms and conditions provided by John Wiley and Sons and Copyright Clearance Center.

License Number	5113451368436
License date	Jul 21, 2021
Licensed Content Publisher	John Wiley and Sons
Licensed Content Publication	Chirality
Licensed Content Title	Chiral combinatorial preparation and biological evaluation of unique ceramides for inhibition of sphingomyelin synthase
Licensed Content Author	Kenji Monde, Yoshiko Suga, Yuta Murai, et al
Licensed Content Date	Jan 22, 2020
Licensed Content Volume	32
Licensed Content Issue	3

Licensed Content Pages	6
Type of use	Dissertation/Thesis
Requestor type	University/Academic
Format	Print and electronic
Portion	Figure/table
Number of figures/tables	1
Will you be translating?	No
Title	Molecular dynamics simulation of the permeation of lipid-conjugated peptides through the stratum corneum
Institution name	Curtin University
Expected presentation date	Jul 2021
Portions	Figure 1 De novo pathway of endogenous (D)-erythro sphingosine and unnatural stereoisomers of sphingosine, (L)-erythro, (D)-threo, and (L)-threo sphingosines

Requestor Location	Ms. Lanie Ruiz-Perez Kent St, Bentley WA 6102
	Perth, 6102 Australia Attn: Ms. Lanie Ruiz-Perez
Publisher Tax ID	EU826007151
Total	0.00 AUD

License Number	5114540469645
License date	Jul 22, 2021
Licensed Content Publisher	Elsevier
Licensed Content Publication	Journal of Controlled Release
Licensed Content Title	A method to predict the transdermal permeability of amino acids and dipeptides through porcine skin
Licensed Content Author	Ruey-Yih Lin,Ching-Wen Hsu,Wen-Yih Chen
Licensed Content Date	Feb 1, 1996
Licensed Content Volume	38
Licensed Content Issue	2-3
Licensed Content Pages	6

Start Page	229
End Page	234
Type of Use	reuse in a thesis/dissertation
Portion	figures/tables/illustrations
Number of figures/tables/illustrations	1
Format	both print and electronic
Are you the author of this Elsevier article?	No
Will you be translating?	No
Title	Molecular dynamics simulation of the permeation of lipid-conjugated peptides through the stratum corneum
Institution name	Curtin University
Expected presentation date	Jul 2021
Portions	Fig. 1. Permeability (Kp) of amino acids and dipeptides on the space of PEG/Na2S04 aqueous two-phase partition coefficient (K), and molecular weight (MW).
Requestor Location	Ms. Lanie Ruiz-Perez Kent St, Bentley WA 6102 Perth, 6102 Australia Attn: Ms. Lanie Ruiz-Perez
Publisher Tax ID	GB 494 6272 12
Total	0.00 AUD

Order Date	24-Jul-2021	**Type of Use**	Republish in a thesis/dissertation
Order License ID	1135582-1		
ISSN	1744-6848	**Publisher**	ROYAL SOCIETY OF CHEMISTRY
		Portion	Image/photo/illustration

LICENSED CONTENT

Publication Title	Soft matter	**Rightsholder**	Royal Society of Chemistry
Article Title	Water permeation through stratum corneum lipid bilayers from atomistic simulationsThis paper is part of a Soft Matter themed issue on Modelling of soft matter. Guest editor: Mark Wilson.	**Publication Type**	e-Journal
		Start Page	4549
		Issue	22
		Volume	5
		URL	http://www.rsc.org/Publishing/Journals/sm/index.asp
Author/Editor	Royal Society of Chemistry (Great Britain)		
Date	06/01/2005		
Language	English		
Country	United Kingdom of Great Britain and Northern Ireland		

REQUEST DETAILS

Portion Type	Image/photo/illustration	**Distribution**	Worldwide
Number of images / photos / illustrations	2	**Translation**	Original language of publication

ACS Publications
Most Trusted. Most Cited. Most Read.

Molecular Dynamics Simulation Study of Permeation of Molecules through Skin Lipid Bilayer

Author: Rakesh Gupta, D. B. Sridhar, Beena Rai

Publication: The Journal of Physical Chemistry B

Publisher: American Chemical Society

Date: Sep 1, 2016

Copyright © 2016, American Chemical Society

Order Date	26-Jul-2021	**Type of Use**	Republish in a thesis/dissertation
Order License ID	1135888-1		
ISSN	1463-9084	**Publisher**	ROYAL SOCIETY OF CHEMISTRY
		Portion	Chart/graph/table/figure

LICENSED CONTENT

Publication Title	Physical chemistry chemical physics	**Publication Type**	e-Journal
		Start Page	2162
Article Title	Permeation pathways through lateral domains in model membranes of skin lipids.	**End Page**	2174
		Issue	4
		Volume	20
Author/Editor	Royal Society of Chemistry (Great Britain)	**URL**	http://firstsearch.oclc.org/journal=1463-9076;screen=info;ECOIP
Date	01/01/1999		
Language	English		
Country	United Kingdom of Great Britain and Northern Ireland		
Rightsholder	Royal Society of Chemistry		

REQUEST DETAILS

Portion Type	Chart/graph/table/figure	**Distribution**	Worldwide
Number of charts / graphs / tables / figures requested	4	**Translation**	Original language of publication
		Copies for the disabled?	No
Format (select all that apply)	Print, Electronic	**Minor editing privileges?**	No
Who will republish the content?	Academic institution	**Incidental promotional use?**	No
Duration of Use	Life of current edition	**Currency**	AUD
Lifetime Unit Quantity	Up to 499		
Rights Requested	Main product		

NEW WORK DETAILS

Title	Molecular Dynamics Simulation of the Permeation of Lipid-Conjugated Peptides through the Stratum Corneum	**Institution name**	Curtin University
		Expected presentation date	2021-08-01

Phase Diagram of a Stratum Corneum Lipid Mixture

Author: Maren Podewitz, Yin Wang, Paraskevi Gkeka, et al

Publication: The Journal of Physical Chemistry B

Publisher: American Chemical Society

Date: Nov 1, 2018

Copyright © 2018, American Chemical Society